Jennifer Helen Chandler

Characterisation of the stator complexes of the *Escherichia coli* flagellar motor

Merton College

University of Oxford

Thesis submitted for the Degree of Doctor of Philosophy

Trinity Term 2006

Abstract

Characterisation of the stator complexes of the *Escherichia coli* flagellar motor

Jennifer Helen Chandler
Merton College
University of Oxford

Submitted for the Degree of Doctor of Philosophy
Trinity Term 2006

The stator of the *Escherichia coli* flagellar motor consists of a ring of membrane-bound proton-conducting MotA / MotB complexes encircling the rotor, which are anchored to the cell wall via MotB. Protonation and de-protonation of Asp-32 of MotB is thought to induce conformational changes in MotA, altering the electrostatic interactions between charged residues of MotA and the rotor protein FliG, which are thought to play a role in torque-generation.

Previously, expression of wild type MotA or MotB in the corresponding mutant background resulted in ~ 8 step-wise increments in speed, as successive stator complexes integrated into the motor. To clarify stator complex stoichiometry, various dominant-defective point mutant MotBs (D32*) were expressed in a wild type background. Step-wise decreases in speed were not observed, indicating that mutant stator complexes had a much lower affinity for the motor than their wild type counterparts. Hence, stator complex stoichiometry could not be determined using this technique.

Chromosomal *motB* was replaced with *gfp-motB*, which allowed expression of the fusion protein at wild type levels. GFP-MotB was functional, motor-localised and fluorescent, as revealed by TIRFM (Total Internal Reflection Fluorescence Microscopy. Surprisingly, GFP-MotB (an anchored component of the motor), was found to diffuse in the membrane and exchange rapidly between a membrane pool and the motor, as revealed by FRAP (Fluorescence Recovery After Photobleaching). Characterisation of single GFP molecule photobleaching enabled quantification of membrane and motor-bound GFP-MotBs under physiological conditions. The membrane pool consisted of approximately 200 GFP-MotBs, which diffused at ~ 0.008 $\mu m^2 s^{-1}$. The motor contained 22 ± 7 GFP-MotBs (i.e. ~ 11 stator complexes) which had a rate constant on the order of 0.03 s^{-1}: the dwell time of a given stator in the motor was estimated to be 30 s.

Motor proteins MotA, FliG and FliM were fused to YFP, with the aim of doing FRET (Fluorescence Resonance Energy Transfer). However, MotA-YFP (and YFP-MotA) was undetectable using western blotting and TIRFM; FliG-YFP was fluorescent and motor-localised but non-functional whereas FliM-YFP was functional, fluorescent and motor-localised. FRET between rotor and stator components will now be possible.

Declaration

The work in this thesis was performed in the Microbiology Unit, Department of Biochemistry (University of Oxford) and in the Clarendon Laboratory, Department of Physics (University of Oxford) from October 2002 until April 2006, under the supervision of Prof. J. P. Armitage and Dr. R. M. Berry. All work in this thesis is my own unless otherwise stated and has not been submitted for a degree at this or any other university.

Acknowledgments

I would like to thank my supervisors Prof. Judy Armitage and Dr. Richard Berry for giving me the opportunity to work their laboratories and for their guidance and encouragement thoughout this project. I am also grateful to all members of both laboratories, both past and present, for their enthusiasm and support. I give my sincere thanks to Dr George Wadhams for his unstinting help and kindness. I am also appreciative of the contributions of Dr Mark Leake to the data presented in Chapter 5. I would especially like to thank my Mum, Dad and Steven for their love and support (and money!).

The work presented in this thesis was funded by the MRC and Oxford Bionanotechnology Interdisciplinary Research Council.

Abbreviations

3-D	three-dimensional
A	adenine
Amp	ampicillin
APS	ammonium persulphate
Ar	argon
ATP	adenosine triphosphate
bp	base pairs
BSA	bovine serum albumin
C	cytosine
CCD	charged-coupled device
CCW	counter-clockwise
CFP	cyan fluorescent protein
che	chemotaxis
CM	chloramphenicol buffer
CW	clockwise
DIC	differential interference microscopy
DIG	digoxigenin
DMSO	dimethyl sulphoxide
DNA	deoxyribonucleic acid
dNTP	deoxynucleoside 5’-phosphate
DTT	DL-dithiothreitol
E	glutamate
ECFP	enhanced cyan fluorescent protein
EDTA	ethylenediaminetetraacetic acid
EGFP	enhanced green fluorescent protein
EM	electron microscopy
EYFP	enhanced yellow fluorescent protein
FLAP	fluorescence loss after photobleaching
FRAP	fluorescence recovery after photobleaching
FRET	fluorescence resonance energy transfer
G	guanine
GFP	green fluorescent protein
IFT	intra-flagellar transport
IPTG	isopropyl β-D-thiogalactosidase
Kan	kanamycin
kb	kilobase
kDa	kilodalton
LB	Luria-Bertani
LBA	Luria-Bertani agar
MCP	methyl-accepting chemotaxis protein
MCS	multiple-cloning site
NA	numerical aperture
Nal	nalidixic acid
Namf	sodium-motive force

Ni-NTA	nickel-nitrilotriacetic acid
OD	optical density
ORF	open reading frame
pmf	proton-motive force
P_i	inorganic phosphate
PAGE	polyacrylamide gel electrophoresis
PBS	phosphate buffered saline
PCR	polymerase chain reaction
QPD	quadrant photodiode
^{R}	resistance
RI	refractive index
RNA	ribonucleic acid
^{S}	sensitivity
SDS	sodium dodecyl sulphate
SSc	salt sodium citrate
Suc	sucrose
T	thymine
TB	tryptone broth
TBE	tris-borate-EDTA buffer
TE	tris-HCL/EDTA buffer
TEM	transmission electron microscope
TEMED	N, N, N’, N’-tetramethylethylenediamine
Tet	tetracycline
Tris	2-amino-2-(hydroxymethyl)-1, 3-propandiol
TTSS	type III secretion system
UV	ultraviolet
X-gal	5-bromo-4-chloro-3-indolyl-β-D-galactopyranoside
XFP	cyan, green, or yellow fluorescent protein
YFP	yellow fluorescent protein

Table of contents

List of figures 11

List of tables 13

1 Introduction 14
- 1.1 Rotary motors 14
  - 1.1.1 F_1F_0-ATPase 14
    - 1.1.1.1 The binding-change mechanism 16
    - 1.1.1.2 Coupling proton-flow through F_0 to γ-subunit rotation 18
- 1.2 Eukaryotic and bacterial flagella 20
  - 1.2.1 Eukaryotic flagella 20
  - 1.2.2 Bacterial flagella 21
- 1.3 Chemotaxis 22
  - 1.3.1 The chemotaxis signalling pathway 23
- 1.4 The importance of motility and chemotaxis 26
- 1.5 Flagellar gene expression 27
- 1.6 Structure of the bacterial flagellum 29
  - 1.6.1 The filament 30
  - 1.6.2 The hook 31
  - 1.6.3 The basal body 31
- 1.7 The motor 32
  - 1.7.1 The rotor 32
    - 1.7.1.1 FliM 32
    - 1.7.1.2 FliG 33
  - 1.7.2 The stator 35
    - 1.7.2.1 Stator localisation 37
    - 1.7.2.2 Stator ion channels 38
      - 1.7.2.2.1 Proton-motive force (pmf) 40
    - 1.7.2.3 The structures of MotA and MotB 40
    - 1.7.2.4 Mutant MotB*s 43
    - 1.7.2.5 Chimera stators 44
    - 1.7.2.6 Stator complex stoichiometry 46
  - 1.7.3 Resurrection experiments 49
    - 1.7.3.1 New technologies 51
    - 1.7.3.2 Optical trapping 53
      - 1.7.3.2.1 Physics of optical trapping 54
  - 1.7.4 Models of motor rotation 56
    - 1.7.4.1 Powerstroke or thermal ratchet? 58
- 1.8 Bacterial protein localisation and dynamics 60
  - 1.8.1 Green Fluorescent Protein (GFP) 61
    - 1.8.1.1 Fluorescence Resonance Energy Transfer (FRET) 62
  - 1.8.2 Fluorescence Recovery After Photobleaching (FRAP) 64
  - 1.8.3 Calculated diffusion co-efficients (*D*) 66

1.8.4 Total Internal Reflection Fluorescence Microscopy (TIRFM) 66
1.9 Aims of this study 67

2 Materials and Methods 69
2.1 Strains and plasmids 69
2.1.1 Storing strains 71
2.2 Molecular genetic techniques 72
2.2.1 Preparing plasmid DNA 72
2.2.2 Preparing chromosomal DNA 72
2.2.3 Transforming *E. coli* 73
2.2.3.1 Calcium-chloride competent cells 73
2.2.3.2 Electro-competent cells and electroporation 74
2.2.4 Restriction digests 74
2.2.5 DNA electrophoresis 74
2.2.6 Purifying DNA fragments 75
2.2.7 Blunting of cohesive DNA ends 75
2.2.8 De-phosphorylating DNA 75
2.2.9 PCR (Polymerase Chain Reaction) 76
2.2.9.1 Overlap-extension PCR 77
2.2.10 Sequencing DNA 77
2.2.11 Ligating DNA 78
2.2.12 Southern blotting 78
2.2.13 Digoxigenin labelling of DNA probes for Southern blotting 78
2.2.14 Chromosomal gene replacement using suicide vectors 79
2.2.14.1 Allelic exchange using pDS132 79
2.2.14.2 Allelic exchange using pKO3 80
2.2.15 Over-expressing and purifying EGFP 81
2.2.16 SDS-PAGE / western blotting 82
2.2.16.1 Preparing acetone powder 83
2.3 Phenotypic analysis of strains 84
2.3.1 Growth rates 84
2.3.2 Swarm plates 84
2.3.3 Preparing motile cells 85
2.3.4 Tunnel slides 85
2.3.5 Stuck-cells bead assay 86
2.3.5.1 Home-built optical trap 86
2.3.6 Tethering cells for fluorescence microscopy 87
2.3.6.1 TIRFM apparatus 87
2.3.7 Transmission Electron Microscopy (TEM) 89

3 Mutant MotB stator complexes 90
3.1 Resurrection experiments 90
3.2 De-resurrection experiments 90
3.3 Mutant MotB*s 91
3.4 Experimental strains 94
3.5 Swarm plate analysis of RP437 expressing mutant MotB* 94

3.5.1 Growth rates of RP437 expressing mutant MotB* 96
3.6 Confirming mutant MotB* expression 97
3.7 Rotation rates of RB6 expressing mutant MotB* 98
3.7.1 Analysis programmes 99
3.7.2 Determining an optimal concentration of inducer 99
3.8 Over-expressing mutant MotB* prior to flagellar assembly 102
3.9 De-resurrection experiments 104
3.10 Resurrecting a stopped (locked) motor 111
3.11 Integrating *fliC*st into the genome 113
3.11.1 Constructing a *fliC*st strain 114
3.11.2 Phenotypic assessment of *fliC*st strains 119
3.12 Chapter discussion 119

4 Visualising GFP-MotB in the flagellar motor 122
4.1 Constructing Green Fluorescent Protein (GFP) fusion proteins 122
4.2 GFP-tagging of MotB 123
4.3 Constructing a *gfp-motB* strain 125
4.4 Western blot analysis of *gfp-motB* strain JHC1 130
4.5 Swarm plate analysis of JHC1 131
4.5.1 Growth rate of JHC1 132
4.6 Stuck-cell bead analysis of JHC1 133
4.7 Visualising GFP-MotB in the motor 134
4.7.1 TIRFM of JHC1 135
4.8 Chapter discussion 138

5 Measuring GFP-MotB stoichiometry and exchange in single, functioning motors 140
5.1 Visualising GFP-MotB in the motor 140
5.2 Fluorescence Recovery After Photobleaching (FRAP) 140
5.3 Visualising and counting single surface-immobilised GFP molecules 141
5.3.1 Over-expression and purification of EGFP 141
5.3.2 Visualising individual GFP molecules 142
5.3.3 Single-step photobleaching of individual GFP molecules 143
5.4 Separating motor and background components of fluorescence 143
5.5 Step-wise photobleaching of motors 146
5.6 Counting fluorophores 148
5.6.1 Computer simulations 149
5.7 Recovery of fluorescence in the motor 153
5.7.1 Photobleaching and image acquisition 155
5.7.2 GFP-MotB exchange in the motor 155
5.8 Fluorescence recovery in the motor in the absence and presence of nutrient. 156
5.9 Fluorescence recovery when protein synthesis is inhibited 157
5.10 Fast exchange of GFP-MotB in the motor 159
5.10.1 Photobleaching in FRAP and FLAP experiments 160
5.11 Chapter discussion 162

6 Fluorophore tagging of motor components MotA, FliG and FliM 164
6.1 Fluorescence Resonance Energy Transfer (FRET).. 164
6.2 Tagging MotA, FliG and FliM with fluorophores 164
6.3 Fluorophore-labelling of MotA.. 165
6.3.1 N-terminal GFP-labelling of MotA 165
6.3.2 C-terminal YFP-labelling of MotA... 169
6.4 Confirming genomic replacement of *motA* with *gfp-motA* or *motA-yfp*......... 172
6.5 Phenotypic analysis of *gfp-motA* and *motA-yfp* strains................................. 174
6.6 Epifluorescence and TIRFM of *gfp-motA* and *motA-yfp* strains..................... 176
6.7 Western blot analysis of *gfp-motA* and *motA-yfp* strains 177
6.8 YFP-labelling of FliM and FliG 179
6.8.1 Constructing a *fliM-yfp* strain 180
6.8.2 Constructing a *fliG-yfp* strain... 181
6.9 Confirming chromosomal gene replacement 182
6.10 Swarm plate analysis of *fliM-yfp* strains.. 183
6.11 Epifluorescence and TIRF microscopy of *fliM-yfp* strains 185
6.11.1 Swarm plate analysis of *fliG-yfp* strains 187
6.12 Epifluorescence and TIRF microscopy of *fliG-yfp* strains 189
6.13 Chapter discussion 190
6.13.1 N-terminal labelling.. 190
6.13.2 C-terminal labelling of motor components MotA, FliG and FliM 192

7 Discussion 195
7.1 De-resurrection experiments... 195
7.2 Fluorophore tagging of motor components.. 196
7.3 Determining the number of stator complexes by TIRFM and FRAP............ 197

8 Publications 199

9 References... 200

10 Appendices... 219
Appendix A 219
Appendix B 223
Appendix C 223
Appendix D 224
Appendix E 224
Appendix F.. 224
Appendix G 224
Appendix H 225
Appendix I 225
Appendix J 225
Appendix K... 226
Appendix L 226
Appendix M 226
Appendix N 227

List of figures

Figure 1.1 A structural model of F_1F_0-ATPase
Figure 1.2 The binding-change mechanism of F_1F_0-ATPase
Figure 1.3 Proton flow through F_0 directly powers rotation of the *c*-ring
Figure 1.4 The 9 + 2 microtubule structure found in eukaryotic cilia and flagella
Figure 1.5 The swimming phases of *E. coli*
Figure 1.6 The chemotaxis signal transduction pathway used by enteric bacteria
Figure 1.7 Flagellar gene expression
Figure 1.8 The structure of the composite *E. coli* flagellum
Figure 1.9 The crystal structure of FliG
Figure 1.10 The stators of *E. coli* and *Vibrio* spp. in the cytoplasmic membrane
Figure 1.11 A freeze-fracture image from *Salmonella* showing a ring of putative stator complexes
Figure 1.12 Functionally important residues in MotA, MotB and FliG
Figure 1.13 Wild type and chimera stator complexes
Figure 1.14 Putative arrangement of membrane segments in the MotA_4: MotB_2 stator complex
Figure 1.15 Torque-restoration in a tethered *motA* cell expressing wild type *motA* from an inducible plasmid
Figure 1.16 Three methods of measuring individual flagellar motor rotation
Figure 1.17 An optical trap
Figure 1.18 Three models of flagellar motor rotation
Figure 1.19 The torque-rotation rate curve of the *E. coli* flagellar motor
Figure 1.20 The structure of Green Fluorescent Protein (GFP)
Figure 1.21 Fluorescence Recovery After Photobleaching (FRAP)
Figure 1.22 Total Internal Reflection Fluorescence Microscopy (TIRFM)

Figure 2.1 Suicide vectors pDS132 and pKO3
Figure 2.2 A tunnel slide
Figure 2.3 TIRFM apparatus

Figure 3.1 Membrane topology of MotB
Figure 3.2 Structures of the amino acids used to replace D32 of MotB
Figure 3.3 Swarm plate analysis of RP437 expressing MotB D32* from pJZ18
Figure 3.4 Anti-MotB western blot of cells grown in the presence and absence of IPTG
Figure 3.5 An electron micrograph of RB6 pFD313 with a bead (probably) adsorbed to a sheared flagellar filament
Figure 3.6 Determining of an optimal concentration of IPTG sufficient to produce a stopped (locked) motor
Figure 3.7 The effect of over-expressing mutant MotB* prior to flagellar assembly
Figure 3.8 A bead rotation rate trace from strain RB6 pJZ18 MotB D32wt in the presence of IPTG
Figure 3.9 Step-wise transient fluctuations in bead rotation rate
Figure 3.10 Anti-MotB western blot analysis of the cellular levels of MotB from strains incubated with IPTG for 30 and 60 min
Figure 3.11 Exposure to IPTG for 90 min in a flow-cell
Figure 3.12 Exposure to IPTG for 2 h in a flow-cell with nutrient
Figure 3.13 Resurrecting stopped (locked) motors
Figure 3.14 Integration of *fliC*st onto the chromosome of YS34 and RP5232
Figure 3.15 A Southern blot of strains RP5232 and YS34 transformed with pDS-*fliC*st

Figure 4.1 Excitation and emission spectra of EGFP.
Figure 4.2 A Mot stator complex with a predicted stoichiometry of MotA_4: $(\mathrm{GFP\text{-}MotB})_2$
Figure 4.3 Construction of *gfp-motB* strain JHC1
Figure 4.4 Southern blot of RP437 transformed with p*gfp-motB*

Figure 4.5 Anti-MotB western blot analysis of JHC1 and RP437
Figure 4.6 Assessing the chemotactic ability of strain JHC1
Figure 4.7 Rotation rates of beads adsorbed to JHC1 and RP437
Figure 4.8 TIRFM of motile JHC1
Figure 4.9 TIRFM of JHC1 and RP437

Figure 5.1 A theoretical FRAP experiment
Figure 5.2 Slow fluorescence recovery after whole-cell photobleaching of JHC1
Figure 5.3 Fluorescence recovery in both the motor and background components of JHC1
Figure 5.4 Fluorescence recovery at the motor and in the background components of JHC1 when protein synthesis was suppressed
Figure 5.5 Over-expression and purification of GFP
Figure 5.6 Photobleaching of single-surface immobilised GFP molecules by continuous TIRF
Figure 5.7 Continuous (averaged) TIRF photobleach traces of motor and background components
Figure 5.8 Photobleaching by continuous TIRF of total fluorescence intensity of JHC1 and RP437
Figure 5.9 Histogram of normalised sizes of all steps found by the Chung-Kennedy algorithm in the total intensity traces
Figure 5.10 TIRF photobleaching traces of three individual JHC1 cells separated into motor and background components
Figure 5.11 Testing fluorophore counting
Figure 5.12 Testing fluorophore counting using simulated data
Figure 5.13 Histograms for pooled tethered and fixed cell JHC1 data
Figure 5.14 A histogram estimating the number of GFP-MotB molecules per motor
Figure 5.15 Focussed laser FRAP and FLAP
Figure 5.16 Successive TIRFM images of a JHC1 cell before and after photobleaching
Figure 5.17 Focussed laser FRAP and FLAP of JHC1

Figure 6.1 The structure of MotA
Figure 6.2 *egfp-motA* strain construction
Figure 6.3 *motA-eyfp* strain construction
Figure 6.4 Southern blots of RP437 transformed with either p*gfp-motA* or p*motA-yfp*
Figure 6.5 Swarm plate analysis of *motA-yfp* and *gfp-motA* strains
Figure 6.6 Swarm plate analysis of cells of flares from strain JHC2.27
Figure 6.7 Epifluorescence microscopy images of *motA-yfp* and *gfp-motA* strains
Figure 6.8 Western blot analysis of *motA-yfp* and *gfp-motA* strains
Figure 6.9 *fliM-eyfp* construct used to replace chromosomal *fliM*
Figure 6.10 *fliG-eyfp* construct used to replace chromosomal *fliG*
Figure 6.11 Southern blots of RP437 transformed with either p*fliG-yfp* or p*fliM-yfp*
Figure 6.12 Swarm plate analysis of *fliM-yfp*
Figure 6.13 Epifluorescence microscopy images of *fliM-yfp* strains
Figure 6.14 TIRFM images of *fliM-yfp* strains
Figure 6.15 Swarm plate analysis of *fliG-yfp* strains
Figure 6.16 Epifluorescence images of *fliG-yfp* strains
Figure 6.17 TIRFM images of *fliG-yfp* strains

List of tables

Table 2.1 *E. coli* strains used in this study
Table 2.2 Plasmids used in this study
Table 3.1 Summary of how the various amino acid substitutions of D32 of MotB differ to aspartic acid (D) in terms of size and protonatability
Table 5.1 Photobleaching parameters for different cellular components of fluorescence

1 Introduction

Cells have evolved a great variety of proteins capable of producing force and motion; such molecular motors can be divided into two groups: linear motors which move along filamentous structures inside the cell (not discussed in this work) and rotary motors.

1.1 Rotary motors

Two rotary motors have been identified: the bacterial flagellar motor and the ATP synthesising enzyme, F_1F_0-ATPase (also called ATP synthase)[1].

Studies of the bacterial flagellar motor and F_1F_0-ATPase are of medical and industrial importance and are of great interest because of their ability to convert electrochemical energy into mechanical energy.

Potential applications of the bacterial flagellar motor include microfluidic devices whereby isolated flagellated vesicles or cells (tethered to a surface via flagellar filaments) could be used to move liquids through nanodevices by regulated flagellar rotation. If such devices are to be developed using isolated motors, the structure and function of the motor needs to be fully understood.

1.1.1 F_1F_0-ATPase

In bacteria, chloroplasts and mitochondria, F_1F_0-ATPase converts proton-motive force (pmf) into rotary motion that in turn is coupled to ATP synthesis. In some bacteria, under certain growth conditions, when operating in the reverse direction, F_1F_0-ATPase generates pmf at the expense of ATP hydrolysis (Figure 1.1).

F_0 is a membrane-embedded proton-channel that generates torque by employing pmf, providing the energy required for ATP synthesis by extramembranous F_1[2,3]. F_0 comprises three types of subunit with a stoichiometry (in eubacteria) of $a_1b_2c_{10\text{-}11}$ [4,5]. F_1 is the smallest rotary motor known in nature, less than 10 nm in diameter, composed of five different polypeptides ($\alpha_3\beta_3\gamma\delta\varepsilon$). When F_1 is isolated, it functions as an ATP hydrolase. The rotor consists of the *c*-ring and γε-stalk, and the stator comprises remainder of the molecule. The γ-subunit has a coiled-coil structure that is tightly attached to the *c*-subunit ring of F_0 and breaks the symmetry of the $(\alpha\beta)_3$ hexamer: each β-subunit is distinct by virtue of its interaction with a different face of the γ–subunit. The number of *c*-subunits in *E. coli* may vary depending on the carbon source[6,7]. The *c*-subunits form α-helical hairpins which contain a conserved Asp (Asp-61) believed to participate in proton conduction. The *a*- and *c*-subunits contain other residues essential for proton conduction[5,8-12]. Protonation of these residues is believed to generate conformational changes in F_1 [13] through rotation of the *c*-ring and the associated γ-subunit[14].

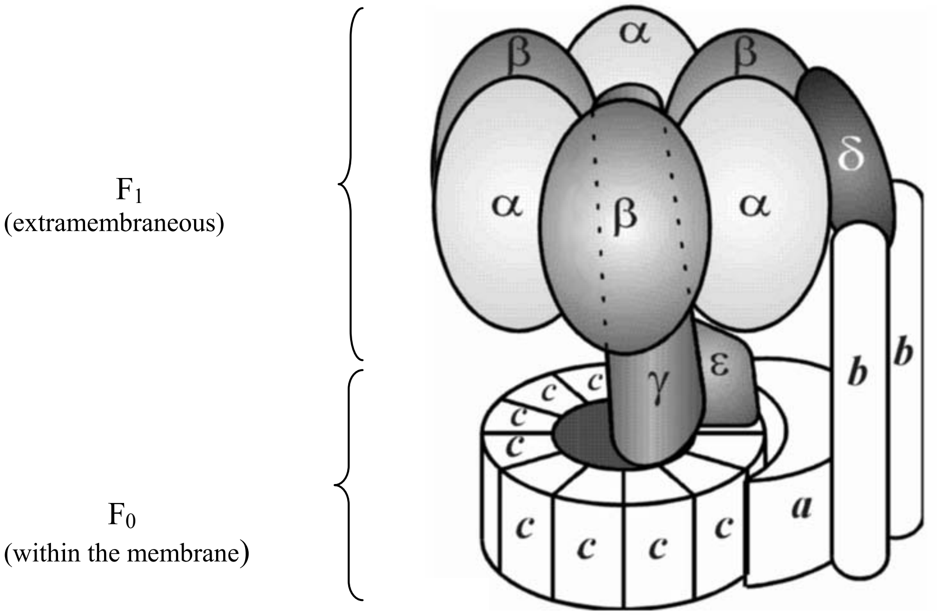

Figure 1.1: A structural model of F_1F_0-ATPase. F_0 is embedded in the membrane, whilst F_1 protrudes. The central γ-subunit projects inside the $(\alpha\beta)_3$ hexamer, and ATP hydrolysis powers rotation of the γ-subunit about its long axis. The exact stoichiometry of the *c*-ring is unknown but estimates predict between 10 and 14 *c*-subunits. Taken from www.biologie.uni-osnabrueck.de/biophysik/Feniouk/Gallery.html

1.1.1.1 The binding-change mechanism

The binding-change mechanism of F_1F_0-ATPase rotation predicts that energy released by the downhill movement of protons through F_0 directly powers rotation of the asymmetric γ-, δ- and ε-subunits, and the *c*-ring, relative to the fixed $(\alpha\beta)_3$ hexamer and *a*-subunits. This movement is believed to cause cyclical changes in the conformations of the catalytic nucleotide-binding sites in the β-subunits, endowing them with different nucleotide affinities[15,16] (Figure 1.2). One β-subunit binds ATP tightly (the T, or Tight-conformation), the second β-subunit binds ADP and P_i loosely and cannot release bound nucleotides (the L, or Loose-conformation). The final β-subunit can release a bound nucleotide (the O, or Open-conformation). Interconversion of these three conformations is driven by γ-subunit rotation. When the γ-subunit is rotated 120º counter-clockwise (CCW) (probably in 80º and 40º sub-steps[17]) the following transitions occur: T → O, allowing ATP release, L → T allowing the transition of bound ADP and P_i into ATP, and finally, O→ L, trapping the bound ADP and P_i. The binding of ADP and P_i to the new O-conformation completes the cycle (Figure 1.2).

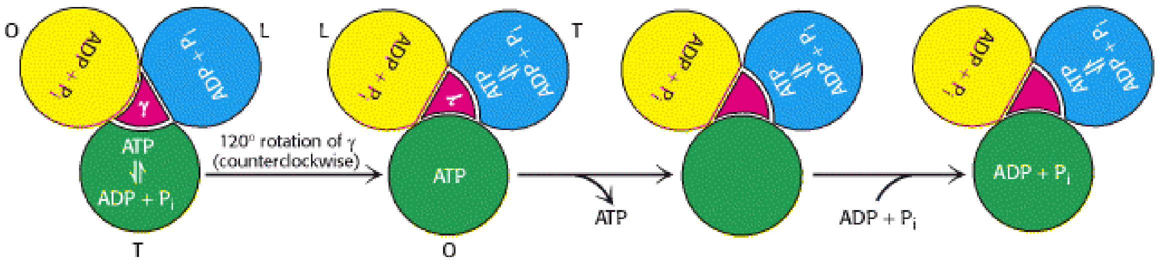

Figure 1.2: The binding-change mechanism of F_1F_0-ATPase. Energy released by the downhill movement of protons through F_0 is thought to directly power rotation of the asymmetric γ-, δ- and ε-subunits, and the *c*-ring, relative to the fixed $(\alpha\beta)_3$ hexamer and *a*-subunits, resulting in cyclical changes in β-subunits conformations, endowing them with different nucleotide affinities. When the γ-subunit is rotated 120º CCW (probably in 80º and 40º sub-steps), the following transitions occur: the subunit in the T (tight) conformation contains newly synthesised ATP which cannot be released, is converted into the O (open) conformation which can release ATP and then binds ADP and P_i to begin a new cycle.
Taken from www.ncbi.nlm.nih.gov/books/bv.fcgi?call=bv.View..ShowSection&rid=stryer

The symmetries of F_1 (3-fold) [2,18] and the *c*-ring (~ 8 - 14-fold)[19] do not match, this may facilitate rotation by avoiding deeper energy minima that would accompany matching symmetries. A non-integral proton: ATP ratio suggests there is some degree of elasticity in the γ-subunit, so that the stepping of the *c*-ring (~ 10 steps per rotation) can be matched to the stepping of F_1 (3 steps per rotation). The proton: ATP ratio is probably non-integral and lies between three and four, which corresponds to measured proton: ATP ratios[20,21].

1.1.1.2 Coupling proton-flow through F_0 to γ-subunit rotation

The *a*-subunit is thought to contain two proton half-channels that do not completely span the membrane, thus, protons can pass into either channel, but cannot traverse the membrane entirely (Figure 1.3). The *a*-subunit directly adjoins the *c*-ring, with each half-channel directly interacting with one *c*-subunit. Asp-61 (of a *c*-subunit) is neutral when in contact with the hydrophobic part of the membrane but becomes charged in the half-channel when it gives up its proton. *c*-ring rotation is prevented because rotation would move a charged aspartate into the hydrophobic membrane. Protons can move through either half-channel to protonate an aspartate, but are more likely to pass through the cytosolic half-channel because of the membrane potential (+ 0.14 V) and lower proton concentration in the matrix. Protonation of the aspartate to its neutral form results in clockwise (CW) rotation of the *c*-ring moving the newly protonated asparate into membrane contact, moving the charged aspartate from the matrix half-channel to the cytosolic half-channel, and moves a different protonated aspartate from contact with the membrane to the matrix half-channel. Protons can dissociate from aspartate through the half-channel into the matrix. Arg-210 of the *a*-subunit is believed to facilitate proton-dissociation. Each proton moves through the membrane by riding around on the rotating *c*-ring to exit through the matrix half-channel.

As the *c*-ring rotates, the γ- and ε-subunits rotate inside the $(\alpha\beta)_3$ hexamer, which are prevented from rotating by the two *b*-chains and δ-subunit. Each 360° rotation of the γ-subunit results in the synthesis of three ATP molecules, hence if there 10 *c*-subunits (as was observed in the crystal structure of yeast mitochondrial ATP synthase[22-24]), each ATP generated requires the transport of 10 / 3 = 3.33 protons.

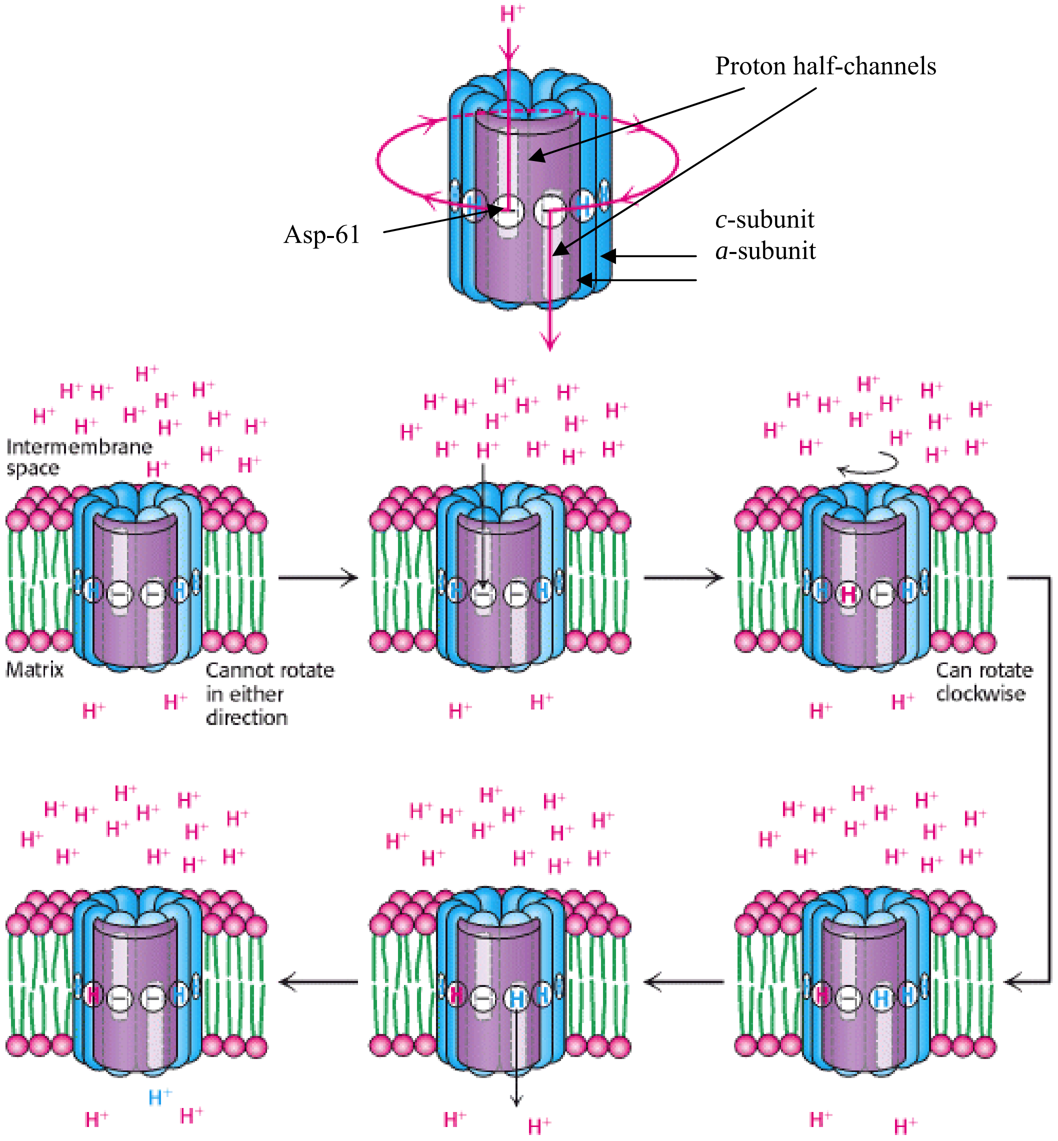

Figure 1.3: Proton flow through F_0 directly powers rotation of the *c*-ring. (Top) The *c*-subunit (blue) has two membrane-spanning helices; the second helix contains Asp-61 which lies on the centre of the membrane. The structure of the *a*-subunit (red) has not yet been determined, but is thought to contain two half-channels that individually do not allow protons to completely traverse the membrane. (Bottom) A proton enters from the intermembrane space into the cytosolic half-channel to neutralise the charge on Asp-61 of a *c*-subunit. The *c*-ring can then rotate CW by one *c*-subunit, when the charge is neutralised, moving an aspartate into the matrix half-channel. This proton can then dissociate into the matrix, which is facilitated by Arg-210 of the *a*-subunit, thus resetting the system. Taken from www.ncbi.nlm.nih.gov/books/bv.fcgi?call=bv.View..ShowSection&rid=stryer

1.2 Eukaryotic and bacterial flagella

Eukaryotic and bacterial flagella have different evolutionary origins and structures; they are classic examples of analogy rather than homology;

1.2.1 Eukaryotic flagella

Eukaryotic flagella are complex cellular projections that beat, whereas bacterial flagella rotate. Eukaryotic flagella comprise of a bundle of nine fused pairs of microtubule doublets surrounding two central singlet microtubules, called the “9 + 2” structure or axoneme (Figure 1.4). At the base of the flagellum is a basal body which is the microtubule-organising centre for the flagellar microtubules. Dynein arms protrude from each microtubule doublet to the adjacent microtubule and are responsible for flagellar beating. Force produced by the dynein arms through ATP hydrolysis cause the microtubule doublets to slide against each other and the flagellum as a whole to bend.

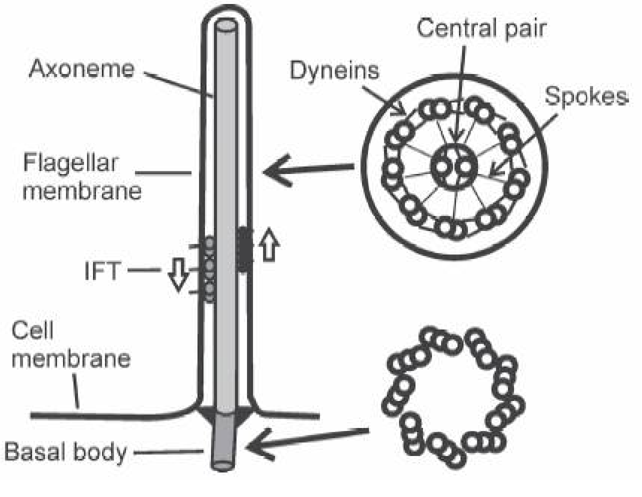

Figure 1.4: The 9 + 2 microtubule structure found in eukaryotic cilia and flagella. The basal body lacks central dyneins, and the entire flagellum is encased by the plasma membrane. IFT = Intra-Flagellar Transport. Taken from www.upstate.edu/cdb/mitcheld/publications/Jekey_Mitchell.pdf

Eukaryotic cilia and flagella share a common structure; there is no physiological difference between them except length: cilia are shorter than flagella. The entire flagellum is encased in the plasma membrane. Transport of axonemal subunits, transmembrane receptors and other proteins inside the flagellum is known as Intra-Flagellar Transport (IFT) and is essential for the assembly and maintenance of eukaryotic flagella[25].

Some theories of eukaryotic flagella evolution propose that they developed from pre-existing eukaryotic cytoskeleton components as an extension of the mitotic-spindle apparatus[26]. Another theory suggests that they evolved from ectosymbiotic spirochetes on the surface of the eukaryotic host but the absence of tubulin and axonemal dynein in modern spirochetes makes this theory unlikely[27,28].

1.2.2 Bacterial flagella

Bacterial flagella are semi-rigid helical structures about 18 nm in diameter and up to 10 μm in length. They are rotated at their base by a motor which employs an ion-motive force, usually pmf, to drive the cell forward at speeds of about 25 μm s^{-1}.

Flagellated species of bacteria differ in their distribution of flagella: a single flagellum at the cell pole is called monotrichous flagellation; flagella at one or both poles of the cell is called polar flagellation; a bundle of flagella at one or both cell poles is called lophotrichous flagellation and flagella distributed randomly over the cell surface is called peritrichous flagellation.

Bacterial flagella comprise three distinct regions: the filament, hook and basal body (see section 1.6). The filament is a semi-rigid helix that when rotating propels the cell with the hook acting as a universal joint connecting the filament to the basal body which contains the rotary flagellar motor.

The synthesis of bacterial flagella is energetically expensive, involving the ordered expression of ~ 50 genes. The ability of a motile cell to move in response to a concentration gradient of a specific chemical (chemoeffector) confers a selective advantage to the cell, allowing it to move to environments more favorable for growth, this process is known as chemotaxis[29].

1.3 Chemotaxis

Bacteria are too small to sense a concentration gradient along their length, so they sample their environment temporally. Current chemoeffector levels are compared to those moments ago, enabling the cell to compare concentrations over several body lengths[30].

E. coli moves around its environment in a three-dimensional (3-D) ‘random walk’ consisting of ‘runs’ of smooth swimming interspersed with brief ‘tumbles’ (Figure 1.5A). During a run, the six or so flagella rotate CCW to form a bundle[31,32] propelling the cell forward (Figure 1.5B); tumbles are caused by the flagellar bundle disassembling as a result of some flagellar motors switching independently to CW rotation (Figure 1.5C). During tumbles, Brownian motion re-orientates the cell in another direction, when the bundle reforms, the cell is usually pointing in another direction[33-35]. In the presence of attractants (e.g. nutrients) or repellents (e.g. toxins), the 3-D random walk becomes biased. When swimming in a favourable direction, the frequency of tumbling is reduced; conversely, when swimming in an unfavourable direction, the frequency of tumbling is increased, allowing the bacterium to accumulate in favourable growth environments (Figure 1.5A).

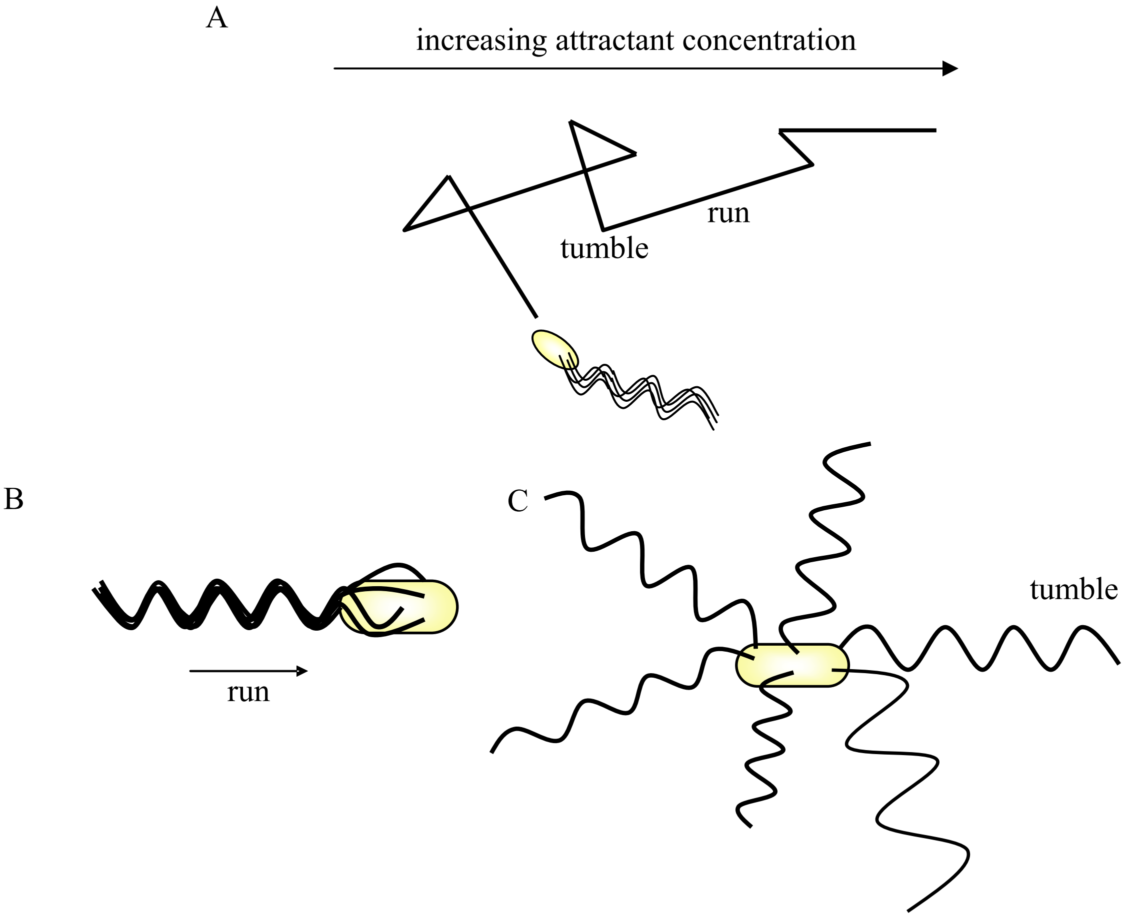

Figure 1.5: The swimming phases of *E. coli*. (A) A biased 3-D random walk. When swimming up an attractant concentration gradient, the tumbling frequency decreases, resulting in accumulation in environments favourable for growth. (B) CCW rotation results in the formation of a flagellar bundle which propels the cell forward, resulting in a run. (C) A switch to CW rotation in one or more flagellar motors results in the bundle flying apart, causing re-orientation of the cell body.

1.3.1 The chemotaxis signalling pathway

Chemoeffectors are detected via the periplasmic domains of Methyl accepting Chemotaxis Proteins (MCPs). Ligand binding activates the MCP by inducing a conformational change in the transmembrane domain of the MCP, resulting in activation of an intracellular signalling cascade (a phosphotransfer system) using phosphoryl groups as the signalling currency (Figure 1.6). The conformational change in the MCP is transmitted through the adaptor protein CheW to the histidine kinase CheA, both of which are bound to the cytoplasmic domain of the MCP[36]. When an attractant leaves or a repellent binds to an MCP, CheA autophosphorylates, which in turn phosphorylates the response regulators CheY and CheB[37-39]. CheY-P undergoes a conformational change enabling it to bind to the motor switch protein FliM (see section 1.7.1.1 for more on FliM) and induce tumbling; this binding is thought to reduce the free energy of the CW state relative to the CCW state. Although CheY-P de-phosphorylates spontaneously, in *E. coli*, CheZ helps terminate the signal by de-phosphorylating CheY-P more rapidly[40]. In the absence of CheY-P, motors rotate exclusively CCW. CW rotation is observed in Δ*cheY* cells when the temperature is reduced to 0 °C, indicating an entropic contribution to the free energy difference between the CW and CCW states[41]. Unstimulated cells switch on average about once a second, an interval required to allow gradient sensing. Curved swimming patterns plus Brownian motion mean that even when apparently swimming smoothly, cells are randomised within 10 s. Switching occurs at random intervals which are not correlated in motors of the same cell[42,43]. The motor can switch between CW and CCW rotation within 10 ms in tethered cells and within 1 ms in single filaments[44,45].

To allow gradient sensing, the CheY-P signal must be terminated rapidly, and this is achieved by CheZ. In addition, the receptor signalling state must be reset. This is achieved by regulating methylation of specific glutamate residues on the cytoplasmic domain of the MCPs. This process, adaptation, involves two proteins: the methyltransferase CheR which is constitutively active[46-48], and the methylesterase CheB[49], whose activity is increased 100-fold when phosphorylated by CheA-P[40,50,51].

When the level of attractant bound to the MCP falls, the phosphotransfer signalling pathway is activated: CheA autophosphorylates, CheA-P is then de-phosphorylated by CheY and CheY-P binds to FliM resulting in CW rotation and tumbling. A negative feedback loop is also activated: CheB also de-phosphorylates CheA-P resulting in elevated levels of CheB-P which de-methylate MCPs, reducing the ability of the MCP to activate CheA. This results in re-setting the signalling pathway so the cell can respond to any subsequent change in attractant level. Differences in excitation and adaptation times allow bacteria to have a memory of past environments.

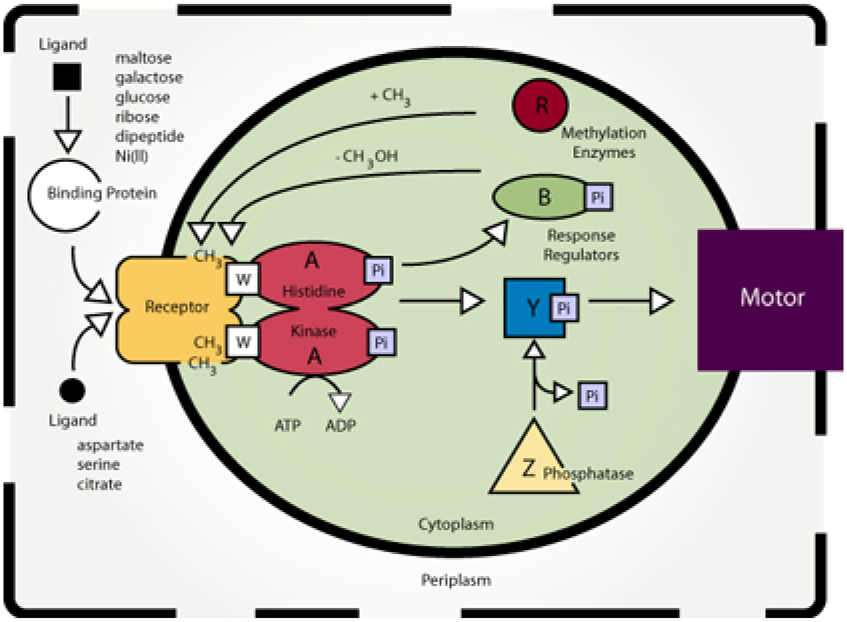

Figure 1.6: The chemotaxis signal transduction pathway used by enteric bacteria such as *E. coli* to sense and respond to chemoeffector gradients in their environment. Ligands either bind to receptors (MCPs) directly or to their corresponding periplasmic-binding proteins which in turn bind to the periplasmic domain of MCPs. MCPs span the cytoplasmic membrane and have an intracellular signalling domain and form ternary complexes with CheA and CheW to generate signals to control the direction of flagellar motor rotation. A decrease in attractant bound to the MCP results in the autophosphorylation of CheA, which transfers the phosphoryl residue to CheY. CheY-P binds to the motor switch protein FliM resulting in CW rotation and tumbling. CheZ terminates the signal by de-phosphorylating CheY-P in less than 1 s. Adaptation is bought about in 5 - 10 s by CheR and CheB by varying the methylation state of the MCP. The cytoplasmic chemotaxis (Che) signalling proteins are identified by single letters e.g., A = CheA. P_i = phosphate, CH_3 = methyl group, ATP = adenosine triphosphate, ADP = adenosine diphosphate. Taken from [52].

1.4 The importance of motility and chemotaxis

Motility and chemotaxis have been implicated in pathogenesis, symbiosis and biofilm formation. The flagellar basal body is closely related to the Type III Secretion System (TTSS)[53] used by pathogenic species to deliver effector proteins into their host. Several TTSS proteins have homology to flagellar export proteins, which led to the suggestion that TTSS evolved from flagella. Mutations in flagellar genes have been shown to attenuate the virulence of several human pathogens including *Burkholderia cepacia*[54], *Campylobacter jejuni*[55], *Helicobacter pylori*[56] and *Pseudomonas aeruginosa*[57,58]. Mutations in the flagellar filament protein (FliC) of *C. jejuni*, which normally acts as an adhesin by directly interacting with host ligands[59], reduces virulence, as can mutations in the mucin-binding flagellar cap protein of *P. aeruginosa*[57,58,60]. Non-motile or non-chemotactic *H. pylori* are unable to cause gastric ulcers because they cannot colonise the gastric mucosa *in vivo*[61].

Flagella and motility have a role in the formation of several symbiotic relationships, such as the symbiosis between the bioluminescent marine bacterium *Vibrio fischeri* and the Hawaiian squid *Euprymna scolopes*[62,63]. Newly hatched juvenile *E.*

scolopes are colonised by motile *V. fischeri* whereas nonmotile *V. fischeri* are unable to do this[64].

Flagella are not absolutely required for, but facilitate, the formation and development of biofilms, as seen in *E. coli*[65], *V. cholerae*[66] and *P. aeruginosa*[67]. Beneficial biofilms include those in sewage treatment bioreactors and legume root nodules (where they are involved in symbiotic nitrogen fixation); disadvantageous biofilms include those that form on medical implants and contact lenses where they can cause blockages and / or infections.

1.5 Flagellar gene expression

Approximately 50 genes are involved in the assembly and operation of a bacterial flagellum, with less than 20 genes encoding proteins found in the mature organelle, indicating that the majority of these genes are involved in controlling transcription and / or assembly of flagella[68]. Expression and assembly of flagellar components must be tightly controlled because protein products are required in numbers ranging from under ten to many thousands in the final structure. Flagellar components employ either the Sec or type III flagellar export pathway for export and assembly (the majority of the flagellar proteins located beyond the cytoplasmic membrane utilise the type III flagellar export pathway).

In *E. coli*, 15 operons code for flagellar proteins and a few operons code for chemotaxis (Che) proteins. These operons are expressed in a hierarchy (Figure 1.7); if any gene necessary for an early step in assembly is disrupted, then genes needed later in assembly are not expressed. The order of expression corresponds to the spatial position of the gene products, from the cytoplasmic to the extracellular side[69] (Figure 1.8) .

There are three classes of flagellar operons: the master operon, *flhDC,* Class 2 and Class 3. The master operon, *flhDC*, controls expression of Class 2 operons which in turn control the expression of Class 3 operons. Class 2 and 3 operons have related, but distinct promoter sequences, sharing a - 10 consensus sequence but not the - 35 site. Control of Class 3b operons (encoding proteins required late in flagellum assembly, e.g. filament subunits and motor proteins) is via the interaction of FliA (σ^F, a flagella-specific sigma factor), and the exported anti-sigma factor FlgM. When FlgM is in the cell, operons requiring σ^F are not expressed. When FlgM is exported from the cell, on completion of the hook, σ^F can induce expression of the Class 3b operons.

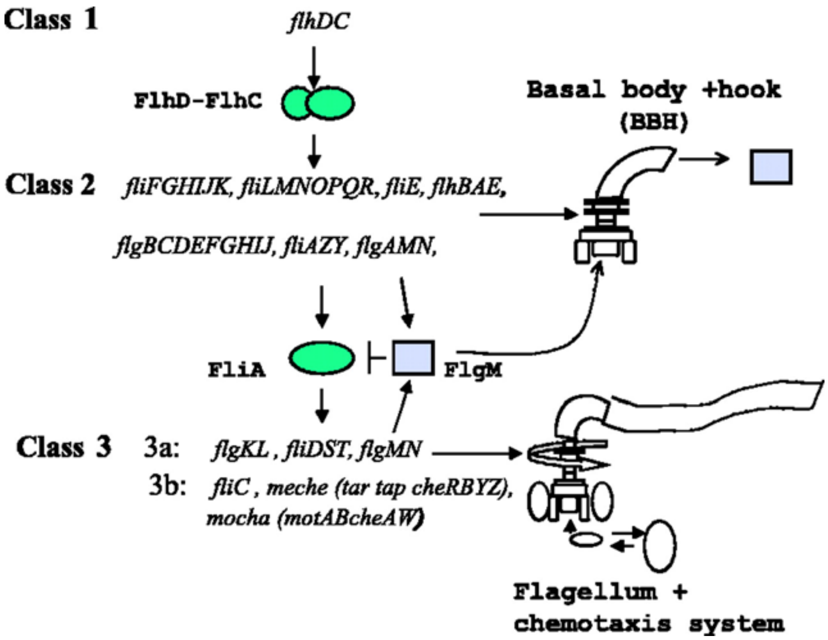

Figure 1.7: Flagellar gene expression. There are three classes of operons required for flagellar assembly, the master operon *flhDC*, and Class 2 and Class 3 operons, whose expression is hierarchal. The order of expression corresponds to the spatial position of the gene products, from the cytoplasmic to the extracellular side. Taken from [70].

1.6 Structure of the bacterial flagellum

Bacterial flagella comprise six parts comparable to man-made motors: a rotor, stator, drive shaft, bushing, universal joint and a propeller. The flagellum is composed of three regions: the filament, hook and basal body (Figure 1.8).

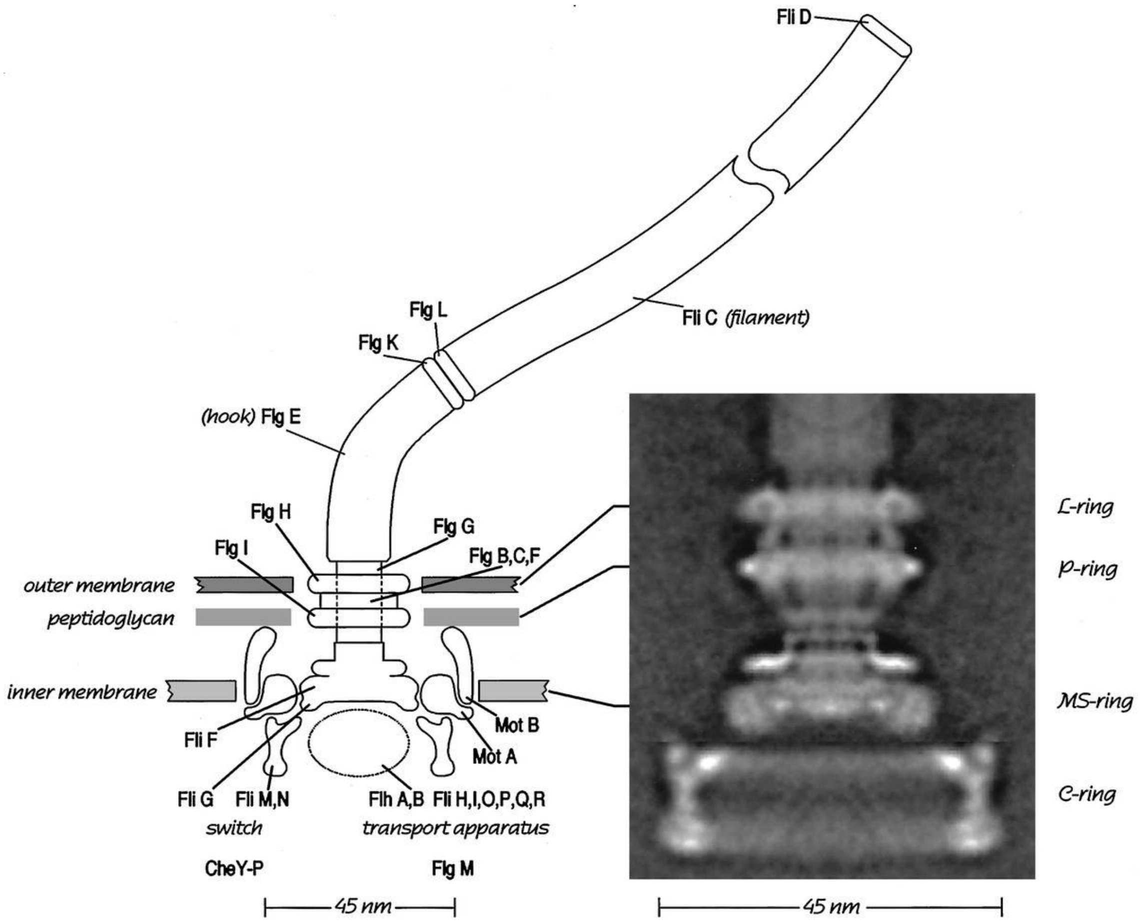

Figure 1.8: An *E. coli* flagellum spanning the cell envelope. Torque is generated by interactions between the C-ring and the (MotA and MotB) stator complexes as protons are translocated across the cytoplasmic membrane. The L- and P-rings are absent in Gram-positive bacteria. Taken from [71].

1.6.1 The filament

The filament functions as a propeller and is 5 - 10 μm in length, and ~ 20 nm in diameter. Up to 20,000 FliC (flagellin) subunits are exported through the 3 nm diameter channel in the filament and polymerise at the distal end of the growing filament. In contrast to the hook, there is no apparent length-control mechanism. Long filaments are easily broken, but they can re-grow because of continuous export of the capping protein (FliD)[72], which co-ordinates polymerisation of FliC subunits[73,74]. The FliC subunits form eleven parallel rows or protofilaments on the flagellums' cylindrical surface. When all the protofilaments are the same length, the flagellum is a straight rod; however, when some of the protofilaments are long (L-type) and some are short (R-type), the filament coils to form a helix[75-77]. The cap protein (FliD) prevents loss of FliC subunits to the medium. FliD has an annular pentameric structure with flat 'top' domains and relatively flexible 'leg' domains[78,79] which allow accommodation of the different vertical positions of the FliC subunits which are arranged like a spiral staircase with approximately five and a half subunits per turn.

The N- and C- termini of FliC subunits are highly conserved across bacterial species and are folded towards the centre of the filament and are involved in polymerisation whilst the central domain is highly variable, antigenic and solvent exposed[76].

1.6.2 The hook

The hook acts as a flexible coupling or universal joint between the filament and the basal body allowing bundle formation in peritrichously flagellated bacteria[80] and is involved in the transmission of motor torque to the filament.

Like FliC, FlgE hook subunits (~ 120 copies) are exported through a central channel in the hook and polymerise into eleven protofilaments[81]. Two hook-filament junction proteins, FlgK and FlgL connect the filament to the hook and serve as adaptors between the different lattice patterns[82-84]. A rod connects the hook to the basal body, which passes through the L- and P-rings (these two rings are absent in Gram-positive bacteria).

1.6.3 The basal body

The basal body acts as a drive shaft and bushing and is the term used for all the cytoplasmic and membrane-bound flagellar machinery, and includes the motor. A rod connects a series of rings: the outer membrane L-ring, periplasmic P-ring, integral membrane MS-ring and cytoplasmic C-ring[85-87]. The L- and P-rings do not rotate but act as bushings, allowing transmission of motor torque to the hook, then the filament; through the outer membrane and peptidoglycan, protecting the cell from potential structural damage as a result of rapid filament rotation.

1.7 The motor

The motor is part of the basal body and is ~ 45 nm in diameter, and comprises a rotor, (C-ring, MS-ring, rod and filament), which rotates, and the anchored torque-generating stator complexes. In *E. coli*, the stator complexes are thought to consist of multiple copies of the integral membrane proteins, MotA and MotB arranged in a ring around the rotor[88-90].

1.7.1 The rotor

The C-ring (or 'switch complex') was discovered when membrane extracts were subjected to smaller extremes of pH and ionic strength[91-93]. The switch complex extends ~ 15 nm into the cytoplasm and is made up of multiple copies of the peripheral membrane proteins FliG, FliM and FliN (copy numbers per motor are ~ 25 [94,95], ~ 34 [95,96] and ~ 110 [95] respectively).

1.7.1.1 FliM

FliM (37.9 kDa) is the target for the output of the chemosensory signalling pathway, CheY-P, which when bound to FliM results in CW rotation[97-100] (see section 1.3). The conserved acidic residue Glu-150 of FliM is essential for proper CW / CCW motor bias[101]. Mutations in *fliM* cause paralysis. FliM and FliN are located separately from the Mot stator complexes but interact with each other[102-104]. Under-expression of FliM results in fewer flagella per cell than wild type, most of which are defective, producing sub-normal average torque and fluctuate rapidly in speed. Speed fluctuations indicate that stable operation requires most, possibly all, of the normal complement of ~ 34 FliM[103]. Over-expression of FliM impairs motility, chiefly by sequestering FliN[104,105]. FliN is probably not involved directly in either torque-generation or switching, and may act as a stabilising protein or be involved in flagellar export[104,106]. Interestingly, in *Bacillus subtilis,* FliN is replaced by FliY, which resembles a fusion between FliM and FliN (in addition to a classical FliM)[107] .

Cryo-electron microscopy revealed ~ 34-fold rotational symmetry of the C-ring, of which FliM is a part, but appears to vary between specimens (± 2)[108,109]. FliM has been visualised as discrete spots on the sides of cells by expressing the fusion protein FliM-YFP (Yellow Fluorescent Protein) from an inducible plasmid in a deletion background[110]. FliM-YFP localisation was not observed in an *flhDC* mutant strain, where flagellar synthesis does not occur (see section 1.5 for more on flagellar gene expression); nor was it observed in the absence of FliG, in support of a mediatory role for FliG in FliM attachment; FliN is not required for FliM localisation as long as FliG is present[110].

1.7.1.2 FliG

FliG (36.8 kDa) is involved in torque-generation together with the Mot stator complexes[111]. Mutations in *fliG* that result in assembled but paralysed flagella all cluster on a prominent ridge in the C-terminal domain of FliG[111-113]. Mutagenesis of this region revealed three residues important for torque-generation: Arg-281, Asp-288 and Asp-289[114]; this region is believed to interact with the stator protein MotA because FliG molecules lacking the C-terminal domain fail to bind to MotA (MotA also binds weakly to FliM)[115] (see section 1.7.2.3 for more on the interaction of MotA / FliG). The crystal structure of the C-terminal and middle domains of FliG from *Thermotoga maritima* (FliG$_{MC}$) revealed two compact, globular domains connected by an α-helix and a short segment with extended structure that contains two well-conserved Gly residues which may provide flexibility[113] (Figure 1.9A). Cross-linking studies predict that the FliG$_C$ domains are at an outer radius, where they interact with the stator, whilst the FliG$_M$ domains are nearer the MS-ring[109,116] (Figure 1.9B). The conserved acidic residue Glu-125 of FliG is essential for flagellar assembly[101].

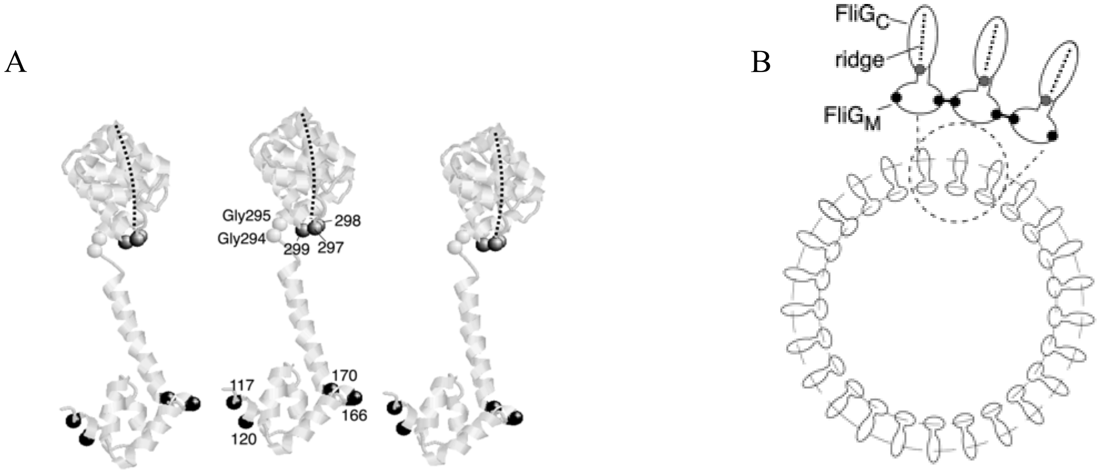

Figure 1.9: The crystal structure of FliG and its putative arrangement in the C-ring. (A) Three copies of FliG$_{MC}$ protein from *T. maritima* (with *E. coli* residue numbers). Space-filled α-carbons represent the Gly-Gly motif and the positions giving high-yield cross-linking. Residues 117 and 120 of one subunit are near 166 and 170 of the adjacent subunit of the FliG$_M$ domain. The prominent C-terminal charge-bearing ridge is indicated with a dashed line, and is in a radial direction relative to the axis of the flagellum, which is important for torque-generation. (B) Putative FliG subunit arrangment, viewed along the axis of rotation. In order to interact with the MS-ring, the FliG$_M$ domains have an inner position, whilst the FliG$_C$ domains have an outer position to allow interaction with the stator complexes. FliG$_C$ = C-terminal domain; FliG$_M$ = middle domain. Taken from [116].

A recent electron microscopic reconstruction of the MS-ring (FliF) based upon scanning transmission electron microscopy[81] and ^{35}S labelling[117], showed ~ 26-fold symmetry[94]. The ratio of FliF: FliG is thought to be 1: 1, because when FliF and FliG are expressed as a single fusion protein, functional flagella assemble[118]. The 26-fold symmetry of MS-ring is more pronounced when associated with FliG. Thus, while the subunit number might vary slightly among specimens, a typical motor has close to 26 copies of FliG. FliG may bind to FliF[119,120]; FliM and FliN bind to each other[99,115,120]. Functional and partially functional fusion proteins have been constructed: FliF / FliG[118,121], FliM / FliN[122] but not FliG / FliM[123]. *In vitro*, FliG, FliM and FliN all self-associate and bind to each other in all pair-wise combinations[115].

1.7.2 The stator

In *E. coli*, the stator complexes comprise multiple copies of the cytoplasmic membrane proteins, MotA and MotB, which together form membrane proton-conducting channels[124-129] (Figure 1.10A). MotA and MotB are not necessary for flagellar assembly, and mutants in either protein are paralysed[130]. Mot proteins bind to each other and can be co-isolated via an affinity tag on MotB[115].

The precise structures of MotA and MotB, and the complexes they form are unknown; the combination of membrane and cytoplasmic segments presents significant problems to protein crystallography.

MotA (32 kDa) is believed to have four transmembrane domains and a large cytoplasmic domain[131-133]. MotB (34.2 kDa) has an N-terminal transmembrane domain and most of the protein is in the periplasm[134,135], which contains a putative peptidoglycan-binding motif[136], believed to anchor the stator complex to the cell wall (Figure 1.10A)[135]. Mutations near the putative peptidoglycan-binding domain of MotB appear to misalign the rotor and stator. The stator complex needs to be anchored for torque-delivery to the filament[137]. Intergenic suppression studies suggest that MotA and MotB interact via their periplasmic domains and together are considered the stator[125,138].

Some marine and alkaliphilic species of bacteria employ sodium-motive force (Namf) to drive rotation of the flagellar motors and are thought to function in a similar manner to proton-driven motors[139-141]. *V. alginolyticus* has two types of flagella: lateral proton-driven flagella which are expressed when the cell is associated with a surface, and a polar sodium-driven flagellum which is expressed in open oceans[142,143]. The stators of the sodium-driven motor of *V. alginolyticus* are composed of PomA and PomB (Figure 1.10B), which form complexes[144,145] and have sequence and structural homology to MotA and MotB respectively. *E. coli* MotA and MotB are capable of restoring motility in Δ*pomAB V. alginolyticus*. Namf can easily be manipulated using specific sodium-channel inhibitors, amiloride[146] and phenamil[147], making study of the sodium-driven motors easier than of the study proton-driven motors.

The sodium-driven stator contains two outer membrane proteins, MotX and MotY which are needed together with PomA and PomB for torque-generation[144] (Figure 1.10B). MotX and MotY have only been identified in *Vibrio* spp. and their role(s) are unclear[148,149].

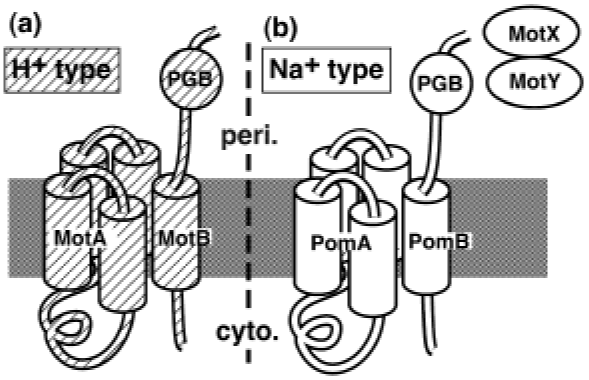

Figure 1.10: Proton and sodium-driven stators. (A) The stators of the proton-driven *E. coli* motor in the cytoplasmic membrane. MotA and MotB comprise the proton-driven stator of *E. coli*. (B) Four motor proteins, MotX, MotY, PomA, and PomB comprise the stator of the sodium-driven polar flagellum of *Vibrio* spp. MotX and MotY are thought to be located in the outer membrane, but their exact role(s) are unclear. MotA and PomA each have four transmembrane domains, whilst MotB and PomB have only one. Only one copy of each protein is shown for simplicity, stator complexes are thought to have a stoichiometry of $MotA_4$: $MotB_2$ (or $PomA_4$: $PomB_2$) (section 1.7.2.6). peri = periplasm; cyto = cytoplasm. Taken from [150].

Rizzotti[151] suggested that stator proteins may have evolved from the *c*-subunit stator protein of F_1F_0-ATPase (see section 1.1.1 for more on F_1F_0-ATPase). However, MotA and MotB (and PomA and PomB) show homology with a widespread family of proteins that couple ion-motive force to a wide variety of membrane transport processes, namely ExbBD[152], TonB and TolQR [153] and it is much more likely that these proteins are their direct ancestors.

1.7.2.1 Stator localisation

While isolation of the rotor complex is relatively straightforward, the stator proteins remain in the membrane and do not fractionate with the rest of the hook–basal body complex[130]. Evidence for stator localisation is indirect but electron microscopy and freeze-fracture studies suggest they form a ring of 'studs' around the MS-ring of the basal body. 14 - 16 studs were observed at the poles of *Aquaspirillum serpens*[154] (similar numbers were seen in *Streptococcus*), 10 - 12 studs were observed in *E. coli* [89]; and ~ 12 studs were observed in *Salmonella* and *Bacillus* spp. [90,155] (Figure 1.11). The discrepancy in the number of studs observed could reflect real variability or be artifacts of technique. Occasionally fewer studs were observed in *E. coli* but wild type *E. coli* motors may have fewer than the full complement of torque generators as judged by torque measurments[156]. Putative stator complex studs are not observed in either Δ*motA* or Δ*motB* mutants;

however, when *motA* and *motB* are restored on inducible plasmids in Δ*motA* and Δ*motB* mutants respectively, the studs return; indicating that both MotA and MotB are required for their formation.

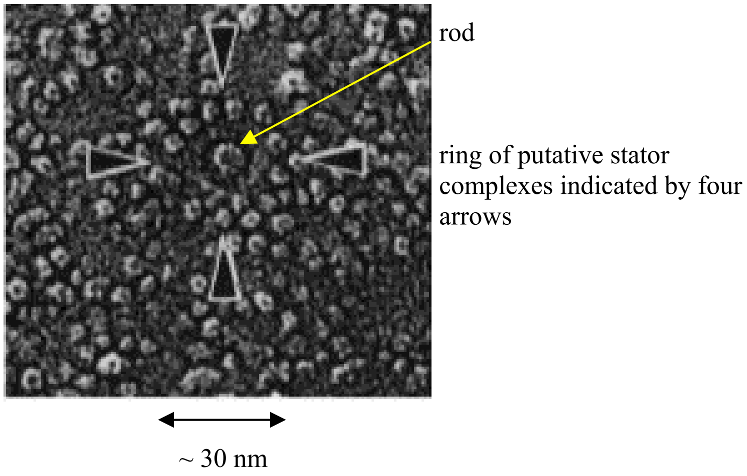

Figure 1.11: A freeze-fracture image from *Salmonella* fractured through the cytoplasmic membrane showing a circular array of membrane-embedded particles thought to be the MotA and MotB stator complexes. The larger particle in the centre is the cell-proximal part of the rod. The inner diameter of this particle ring is about 30 nm, indicated by the arrows. Taken from [89].

1.7.2.2 Stator ion channels

Early studies involving indirect mutant studies and sequence analysis predicted that MotA alone formed the proton-channel, with MotB anchoring the Mot complex to the peptidoglycan[124,132,138,157,158]. The consensus now is that MotA and MotB together form the channel[127] with water molecules facilitating the transit of protons [126]. Certain mutations in *motB* can be suppressed by mutations in *motA*[125] and many pairs of mutations in *motA* and *motB* are strongly synergistic, being tolerated singly but abolishing function when present together[138].

Over-expression studies of wild type and mutant MotA[124] found that over-expression of wild type MotA suppressed growth, perhaps by rendering the membrane leaky to protons, whilst mutant MotA did not. However, when the proton conductance of membrane vesicles prepared from wild type cells were compared to vesicles containing dominant non-functional MotA from paralysed mutants, there was no major difference in conductance[124]. Mutants were found that generated normal torque at low speed but abnormally low torque at high speed; at high speed they displayed altered hydrogen isotope effects, indicating that MotA is involved in proton transfer[124] (D_2O is approximately 20 % more viscous than H_2O, the associated small increase in load did not affect swimming speeds) . These mutations map primarily to the cytoplasmic domain[132]. However, these data have been mis-interpreteted and may reflect the reduced transport of D_2O into the periplasm (Howard Berg, personal communication).

Stolz and Berg[127] found that over-expression of a fusion protein containing the N-terminal 60 residues of MotB joined to a polar 50 residue sequence encoded by an open reading frame from pBR322, impaired growth when MotA was present due to proton-leakage, indicating that the MotB membrane-spanning fragment activates the proton-channel[127].

However, Wilson and Macnab[159,160] found that over-expressing MotA (~ 50-fold) caused only a moderate reduction in growth and motility, arguing against MotA having an intrinsic ability to conduct protons across the membrane since large amounts of protons would be expected to collapse the pmf and thus inhibit growth[159,160].

When MotA was over-expressed, the amount of MotA found in the cytoplasmic membrane was much larger than the amount that could be accommodated by the flagella[159]. MotA over-expressed alone incorporated into the membrane, whereas when MotB was over-expressed, it was unstable unless MotA was also over-expressed[160] and the majority accumulated in the cytoplasm; perhaps stable insertion of MotB into the membrane requires the presence of MotA[134]. Similarly, PomB requires PomA for stability. Van Way *et al*[161] proposed that MotA and MotB co-insert as a stable intermediate into the membrane with the periplasmic tail of MotB blocking the proton-channel until the stator complex is orientated properly at the periphery of the rotor, once the tail binds to the peptidoglycan, it opens the channel[161].

1.7.2.2.1 Proton-motive force (pmf)

1000 protons are thought to flux through the motor per revolution, so theoretically a cell rotating at 100 Hz would conduct protons at a rate of 10^5 protons s^{-1} [80,162]. Early work suggested a threshold pmf for rotation[163] but more recent work indicates that rotation rates are proportional to pmf all the way to zero pmf[164]. Flagellar rotation rate is directly proportional to pmf over the full physiological range (up to -180 mV)[165-167].

1.7.2.3 The structures of MotA and MotB

The sequences of MotB show little homology across species; the best conservation is interestingly in the membrane-spanning domain and there is no consensus membrane-insertion signal sequence[134]. The region linking the membrane-spanning domain to the peptidoglycan-binding motif is variable in length and sequence. MotB contains one absolutely essential and conserved residue, Asp-32 (Asp-24 in PomB) on the cytoplasmic face of the transmembrane domain. This is critical for proton-translocation and rotation (or sodium-translocation in *Vibrio* spp.)[101,138,157]. Protonation of Asp-32 is believed to induce a conformational change in the stator complex, thought to be an important part of the torque-generating cycle of the motor[152] (see section 1.7.4 for more about models of rotation). Elements regulating ion-flow are likely to be in the middle-third of the channel[129].

The large cytoplasmic loop of MotA (between transmembrane helices 2 and 3) is better conserved than the cytoplasmic domain of MotB, and contains four functionally important residues Pro-173, Pro-222, Arg-90 and Glu-98. Pro-173 and Pro-222 may be involved in protein stabilisation and regulation of conformational changes coupled to the protonation / de-protonation of Asp-32 of MotB[158,168]. Pro-173 and Pro-222 are thought to be located near Asp-32 [168]. Arg-90 and Glu-98 are thought to be directly involved in torque-generation by interacting electrostatically with charged residues or permanent dipoles on the C-terminus of the rotor protein FliG, (possibly Arg-281, Asp-288 and Asp-289)[114,158,169] (Figure 1.12). Charge appears to be their key property. The conserved Glu-150 residue and the lesser conserved Glu-102 and Glu-106 residues of MotA may also be involved in torque-generation[158]. Neutralisation or reversal of charge of these residues on MotA, MotB and FliG severely impairs swimming, suggesting that there is an electrostatic interaction between the rotor and stator, although it could simply affect the conformation of the proteins which may impede rotation if torque is coupled by a steric interaction between these domains. The conserved charged residues of FliG and MotA have been replaced singly and in pairs and tested on swarm plates for strong suppression or synergism of movement[169]. No single electrostatic interaction was found to be critical for torque-generation, but it did reveal that Asp-289 and Asp-288 on FliG interact with Arg-90 of MotA, and Arg-281 on FliG interacts with Glu-98 of MotA. Substitution of a neutral residue had less of an effect than one of opposite charge. The exact role of these interactions is still unknown, but their strength may be increased if water is excluded from the interface.

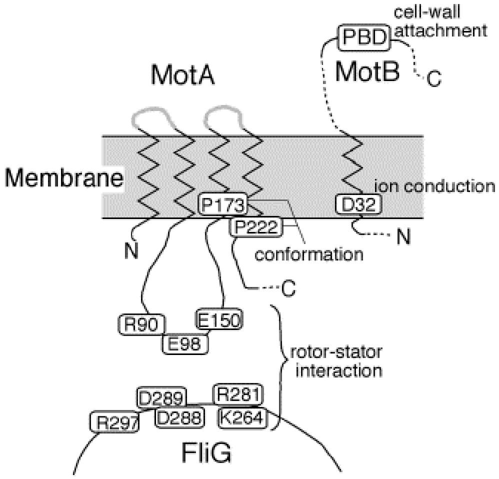

Figure 1.12: Functionally important residues in MotA, MotB and FliG. The combination of cytoplasmic and membrane segments in MotA and MotB hinders their crystallisation, so the predicted structures are estimated from sequence analysis and cross-linking studies. Dashed segments in MotA and MotB are dispensable for rotation. Taken from [170].

In summary, protonation of Asp-32 of MotB is believed to cause a conformational change in the stator complex which modulates the conformation of MotA, altering the interaction of the charge-bearing cytoplasmic loop of MotA with a complementary charged region in the C-terminal domain of FliG (FliG$_C$). Mutation of Asp-32 or Pro-173 alters the susceptibility of MotA to proteolysis, providing additional evidence for changes in its conformation[152].

1.7.2.4 Mutant MotB*s

Asp-32 (D32) of MotB is the only conserved acidic residue in all five motor proteins (MotA, MotB, FliG, FliM and FliN) believed to be essential in torque-generation. To determine what features of the D32 side chain are important in regulating conformation of the Mot stator complex, various MotB D32* substitutions were made, all of which were non-motile except the D32E substitution[152,171]. The corresponding mutation in *S. enterica* serovar typhimurium (D33E) also permitted partial function[172]. These proteins were not grossly mis-folded because they accumulated to levels at least as high as those of wild type MotB and had strong dominant-negative effects suggesting that these mutant MotB*s retained the ability to be installed in the motor. Conformational changes in the stator complexes were assessed by examining the pattern of MotA fragments produced during trypsin digestion of membrane vesicles containing MotA together with either wild type or mutant MotB* (trypsin cuts at Arg-66 (or 67) and Arg-131 in the cytoplasmic loop of MotA).

Small, uncharged replacements of MotB D32 (D32N, D32A, D32G, D32S and D32C) caused significant conformational changes in MotA, as evidenced by a change in the pattern of proteolytic fragments, however, medium-sized replacements (D32L, D32E and D32R) irrespective of charge did not cause a conformational change. A protonated Asp (whereby the side-chain is neutralised and a hydrogen-bond donor is introduced) is between D32N and D32S in terms of charge and size, both of which caused a conformational change. The magnitude of dominant-negative effects were quantified by expressing the mutant MotB* from an inducible plasmid on swarm plates, and was found to vary with mutation following the sequence A ~ N > E > R. Thus the most strongly dominant mutations the ones that produced the largest effects on conformation in limited-proteolysis experiments. The negative side-chain charge and / or the ability to bind protons appear to be the most important features of D32.

1.7.2.5 Chimera stators

Several chimeric stators across species have been constructed, and showed that torque-generation is independent of the translocating ion[148,149,173]. The stators of *Vibrio* spp. contain two outer membrane proteins MotX and MotY[174-176] and the cytoplasmic proteins PomA and PomB (MotA and PomB homologues respectively) which are needed for torque-generation. However, the role(s) of MotX and MotY are unclear (Figure 1.13B). MotY has some homology to MotB and PomB in that it has a putative peptidoglycan-binding motif at its C-terminus, whereas MotX shows no homology to MotA or PomA[177]. Suggested roles for MotX and MotY include sodium-recognition, a sodium-channel, viscosity sensor, a stabiliser for PomA and PomB, or a bearing for high speed rotation.

MotA and MotB from *Rhodobacter sphaeroides* do not complement Δ*pomAB* in *V. alginolyticus*, nor do PomA and PomB support torque-generation without MotX and MotY[177]. However, MotA from *R. sphaeroides* can replace PomA in *V. alginolyticus* and can function together with PomB and MotX and MotY as a sodium-driven motor[172]. MomB^R is a chimeric stator protein composed of the N-terminus of MotB from *R. sphaeroides* fused to the C-terminus of PomB from *V. alginolyticus*, which functions as a sodium-driven motor with PomA and MotX and MotY in *V. alginolyticus*[150]. Similarly, MomB^E is a chimera protein composed of the N-terminus of *E. coli* MotB fused to the C-terminus of PomB, and supports sodium-driven motility with MotA, MotB and MotX in *E. coli*[148] (Figure 1.13D).

Mutant *V. cholerae*: (Δ*pomA* Δ*pomB* Δ*motX* Δ*motY*) become motile when expressing *motA* and *motB* and their resultant motors are proton-driven[177]. However, *E. coli* deleted for Δ*motAB* when expressing PomA and PomB are non-motile. However, if the C-terminus of PomB is replaced by the C-terminus of MotB (called PotB), the resulting proton-driven motor (with PomA) is functional with or without MotX and MotY in *V. alginolyticus*[150] (Figure 1.13C). PotB supports sodium-driven motility in Δ*motB E. coli* cells, and the swimming speed was even higher than with the original MotA and MotB stator of *E. coli*[150].

These results collectively suggest that the C-terminus of PomB is not necessary for sodium-driven motility in a PomA and PomB stator but it can convert a MotA and MotB proton-driven motor into a sodium-driven motor. These results indicate that the cytoplasmic and transmembrane domains of PomA and PomB are sufficient for sodium-driven motility.

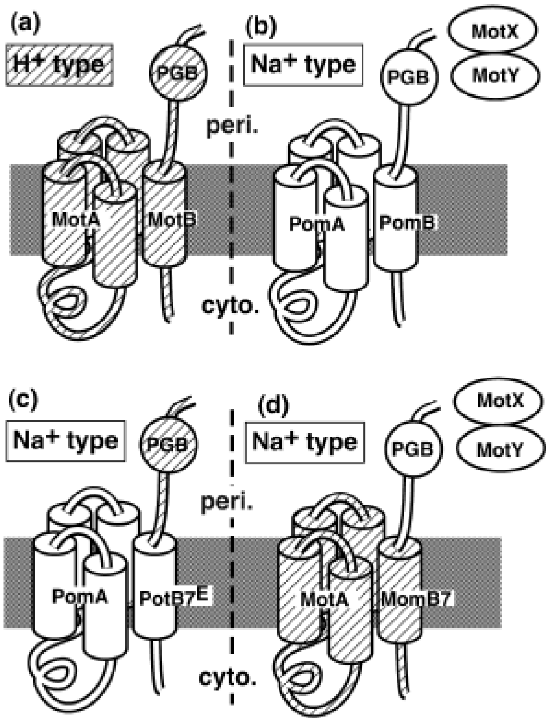

Figure 1.13: Wild type and chimera stator complexes (note that only one copy of MotA or PomA is drawn for simplicity). Hatched regions signify an *E. coli* origin; white regions signify a *Vibrio* spp. origin. (A) The *E. coli* stator comprises MotA and MotB, which together conduct protons to power flagellar rotation. (B) The *Vibrio* spp. polar stator conducts sodium ions to power flagellar rotation. MotX and MotY are thought to reside in the outer membrane, and are necessary for torque-generation in *Vibrio* spp., but their exact role(s) are unclear. (C) PotB is a chimeric stator protein composed of the N-terminal transmembrane domain of PomB fused to the periplasmic domain of *E. coli* MotB. Surprisingly, PotB functions with PomA as a sodium-motor component not only in *V. alginolyticus* but also in *E. coli.* (D) MomB7 is a chimeric stator protein composed of the transmembrane domain of MotB fused to the periplasmic domain of PomB, which functions as a sodium-driven motor in *V. alginolyticus,* but is non-motile in *E. coli*. PGB = peptidoglycan-binding motif; peri = periplasm; cyto = cytoplasm. Taken from [126,138].

1.7.2.6 Stator complex stoichiometry

The stoichiometries of MotA and MotB in a stator complex is not known for certain; early work suggested $MotA_1$: $MotB_1$[129]. However, MotA can be cross-linked to form stable tetramers and MotB can cross-link to form stable dimers (which does not require the presence of MotA)[145,178]. ^{35}S-radiolabeling of purified MotA and MotB complexes show that MotA and MotB are present in a 2: 1 ratio[160]; however immunoprecipitation experiments estimated a four-fold excess of MotA over MotB in wild type cells (600 ± 250 copies of MotA, versus 150 ± 70 copies of MotB)[179]. MotA and MotB are co-transcribed and coupled translationally from the *mocha* operon (which also contains CheA and CheW)[131,160]; the last four bases of *motA* overlap with the first four bases of *motB*, and this may be important in controlling the relative stoichiometries between the two gene products[160].

PomA and PomB each form stable homodimers and purify as a complex with a molecular weight corresponding to a stoichiometry of PomA_4: PomB_2[178]. A tandem PomA dimer (two *pomA* genes fused together) produced a single functional polypeptide *in vitro*[180]. Recent sizing-chromatography experiments of PomA and PomB[129] predicted a stator complex stoichiometry of A_4: B_2 [129] (Figure 1.14). Targeted disulphide cross-linking experiments of MotA and MotB indicate that Asp-32 of each MotB lies on an opposite face of the dimer, suggesting two independent proton-channels per MotA_4: MotB_2 stator complex.

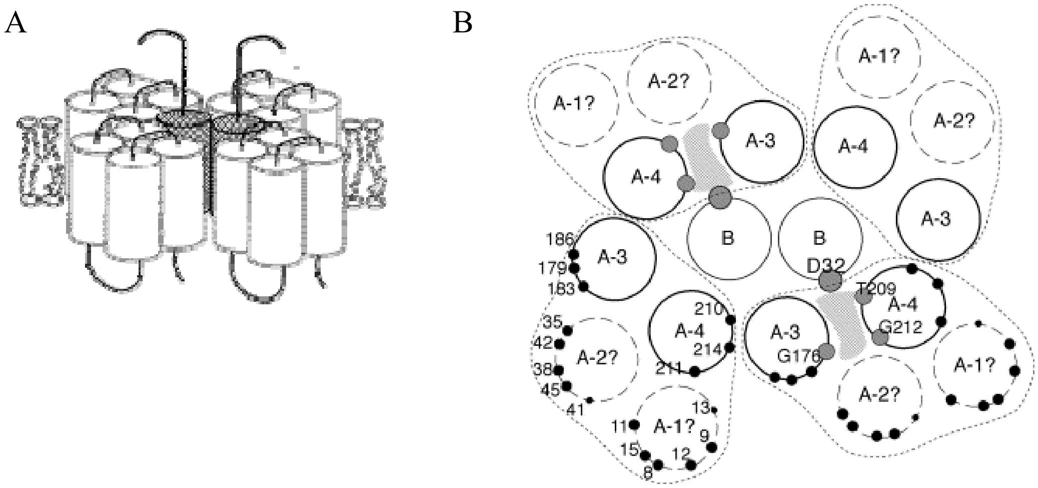

Figure 1.14: Putative arrangement of membrane segments in the $MotA_4$: $MotB_2$ complex. (A) Stator complex viewed in the plane of the membrane. (B) Stator complex viewed from the periplasmic side of the membrane. Dashed lines enclose the four transmembrane segments within each MotA subunit. Segments A1 and A2 of MotA lie on the outside of the complex. Asp-32 of each MotB (large gray circles) are widely separated and most likely function in two distinct proton-channels, indicated by crosshatching. Small grey circles indicate three conserved residues that might face into the channel(s). Positions where tryptophan replacements were tolerated either fully (large black circles) or partially (small black circles) are indicated; Trp was only tolerated in the outer half of the MotB segment towards the periplasm (not shown). Taken from[129,170].

Each proton-channel is believed to comprise eight transmembrane segments from two MotA subunits and one transmembrane segment from one MotB subunit, hence 18 transmembrane segments per stator complex (16 from four copies of MotA, and two from two copies of MotB)[181]. Patterns of cross-linking are consistent with an arrangement of a central MotB dimer surrounded by the third and fourth transmembrane segments (A3 and A4) of four MotA subunits, which are believed to flank Asp-32 of MotB (Figure 1.14)[126,138]. The channel is thought to lie between the A3 and A4 segments of a MotA subunit rather than at the interface between subunits (indicated by grey hatching). Tryptophan-scanning studies suggest that transmembrane segments A1 and A2 are lipid-exposed, whilst A3 and A4 are likely to be constrained by other membrane segments[181]. The four MotA subunits must occur in at least two non-equivalent environments because given the subunit composition $MotA_4$: $MotB_2$, the complex can have no greater than two-fold symmetry[181]. Two of the MotA subunits may have no obvious direct role in forming the channel, but they may provide a physical connection allowing the channels to act co-operatively. Two protons traversing the complex might act co-operatively to drive the conformational change(s) triggered by binding to Asp-32, implying that Asp-32 of MotB although distant from each other in the complex are actually functionally coupled. Alternatively, MotA subunits may rotate continuously around the MotB dimer or may exchange positions with each other as the complex undergoes protonation / de-protonation so that each MotA subunit samples all of the environments in the complex[154].

1.7.3 Resurrection experiments

MotA or MotB mutants have paralysed flagella[182], but they can be ‘resurrected’ through induced expression of wild type genes carried on plasmids[183]. In early resurrection experiments, the composition of the torque-generating units was determined by inducing expression of a wild type *motA* or *motB* in a mutant background. Block and Berg[183] expressed wild type *motB* from an inducible plasmid in a paralysed *motB* mutant (strain RP3087) using tethered cells and found that by measuring increasing rotation of the tethered cell bodies, the motor torque was restored in approximately seven steps, although they suggested as many as 16 steps could be inferred from the final rotation rates obtained. Incorporation into the motor is thought to be reversible because downward steps in rotation rate were also seen[156]. This work indicated that MotB is a component of the torque-generating units. Given that the background strain was a point mutant, it was not known whether defective copies of MotB were present in the motor prior to induction; it is possible that the increments in torque were in fact displacement of torque-generating units rather than simple incorporation.

Blair and Berg[156] extended their study to *motA* (Figure 1.15) and *motB* point (RP5037 as above) and deletion mutants and found that torque increments were the same for incorporation of MotA and MotB. Step-wise decreases in torque were common in deletion mutants, but rare in point mutants, implying that in point mutants defective Mot proteins may be present in the motor before resurrection, delaying incorporation of functional copies, suggesting there is competition between Mot proteins for binding to a limited number of sites[156]. The step-wise increments in torque were of equal size in both CW and CCW directions, implying that each torque-generator can drive the motor with equal force in either direction. The torque measured in wild type motors was only approximately five times that for a one-generator motor, whereas following complete resurrection, this factor was about eight[89,90,154,155]. Together with the observation of 10 - 12 studs (putative MotA and MotB complexes) in electron microscopy / freeze-fracture studies[156] (see section 1.7.2.1) this suggests that a cell harvested in exponential phase may not possess a full complement of torque-generators or freeze fracture studs were not all stator components.

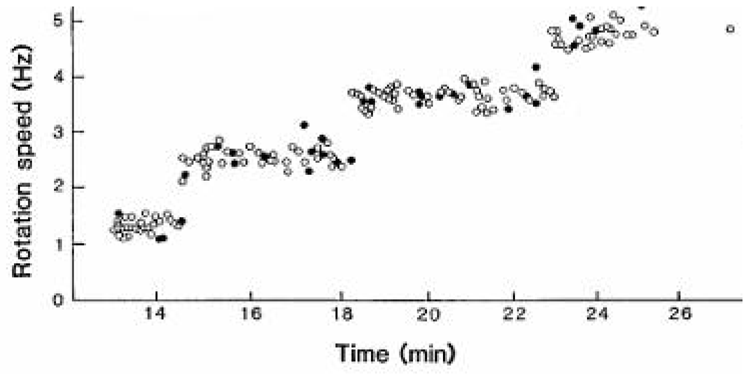

Figure 1.15: Torque-restoration in a tethered *motA* cell (strain MS5037) expressing wild type *motA* from an inducible plasmid. Inducer IPTG was added at time zero. Black data points represent CW rotation; white data points represent CCW rotation. Taken from [184].

Muramoto *et al*[184] observed step-wise decreases in rotation rate of the sodium–driven motors of tethered *V. alginolyticus* after UV irradiation in the presence of the photoreactive analogue of amiloride, a known inhibitor of sodium-channels[156,182,183,185]. This was interpreted as the successive inactivation of independent stator units upon the irreversible binding of amiloride, and suggested between 5 – 9 stator complexes per motor.

Early resurrection experiments tethered cells to glass coverslips via flagellar filaments using anti-filament antibody, to measure cell body rotation (Figure 1.16A)[80]. Only slow rotation can be measured in tethered cells because of the high load on the rotating cell body, they spin at ~ 10 Hz. The motor generates considerably less torque in a swimming cell than in a tethered cell because the frictional drag co-efficient of the swimming cell body rolling around it long axis is less than that of a tethered cell rotating like a propeller[186,187]. Rotation rates of tethered cells vary with load. The mechanics of flagellar rotation are dominated by the viscosity of the surrounding media rather than inertia. The Reynold's number is very low (~ 10^{-4}), so flagellar filaments generate thrust by using viscous drag. When the cell rotates the helical filament, it has to push as well as twist, so as a result the cell body counter-rotates.

1.7.3.1 New technologies

Recently, new technology has become available allowing rotation to be measured under more realisitic conditions. Electrorotation is an extension of the tethered cell technique allowing controlled external torque to be applied to the motor by using electric fields rotating at megahertz frequencies[188]. Rotation rates unobtainable in cells rotating under their own power can be studied using this technique, and the motor can be made to rotate backwards by reversing the field. The actual rotation rate of the motor can be measured using either video microscopy or a photodetector-based technique. The latter has the advantage of much higher temporal resolution and are necessary if rotation rates above 30 Hz are to be measured. Laser-dark field microcopy is a technique which allows fast flagellar rotation of free-swimming cells to be measured (Figure 1.16B).

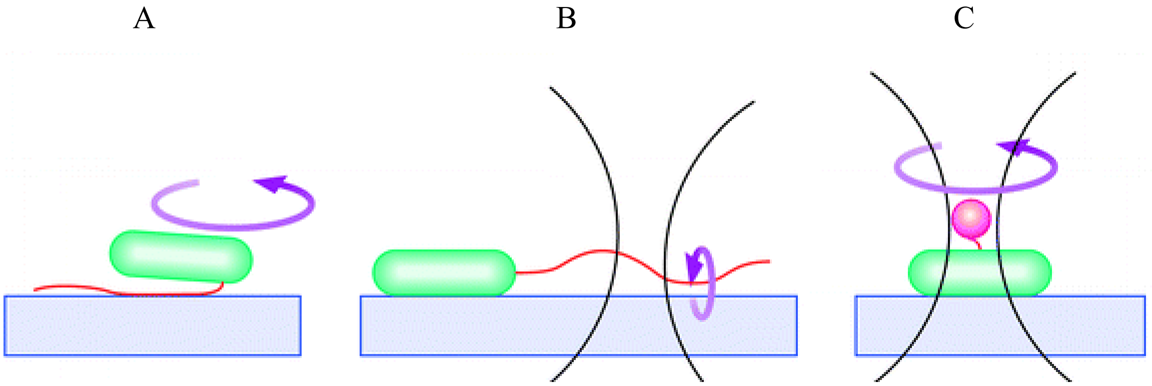

Figure 1.16: Three methods of measuring individual flagellar motor rotation. (A) Tethered cells, whereby the cell is attached to a glass slide via a flagellum and rotation of the cell body is measured. (B) Laser dark-field microscopy allows measurement of fast flagellar rotation. (C) Beads attached to flagellar stubs serve as markers of rotation in an optical trap. Taken from www.els.net

Ryu *et al*[188] developed a new motor assay whereby cell bodies are stuck to a glass surface using poly-L-lysine, and polystyrene beads of varying diameters are adsorbed to filament stubs which serve as markers of rotation in an optical trap[189] (see section 1.7.3.1 for more about optical traps) (Figure 1.16C). This regime reduces the load on the motor and allows rotation rates similar to those observed during free swimming to be measured.

At high load, (bead diameter 1 μm) increases in rotation rate were linear with the torque-generator number. At low load, (bead diameter 0.3 μm) the limiting rotation rate of the bead (and therefore the motor) was independent of the torque-generator number at vanishing load where the total load, hence the torque, on the motor is close to zero and is roughly equivalent to a motor in a free swimming cell where one unit turns the motor as rapidly as many. This result indicated that each unit may remain attached in the motor for most of its mechano-chemical cycle; indicating that the torque-generating stator complexes have a high-duty ratio[188].

More recent experiments whereby flagellar motors recovered after being disrupted either mechanically[190], electrically[167] or electrochemically[191], observed rotation rate increases that were less than one-eighth of the maximum rotation rate seen for the same cell. Recent torque-restoration experiments[192] also observed two different step sizes, approximately one-eighth ('full step') and one-sixteenth ('half-step') of the maximum rotation rate, indicating that each stator complex may be a dimer of two independent torque-generating monomers. They also demonstrated that motors can contain at least 11 stator complexes and found that rotation rate increments at high numbers of torque-generators were smaller than those at low numbers, indicating that not all units in a fully induced motor are equivalent (in contrast to earlier work).

1.7.3.2 Optical traps

Optical trapping is a technique that focuses low power laser through a high numerical aperture (NA) objective to trap and manipulate small (nm-scale) dielectric objects in 3-D. The trapped particle can be moved using the laser beam; hence, the laser is often referred to as an 'optical tweezer'.

Early work on optical trapping was carried out by Ashkin *et al*[193]. In 1987, bacteria and viruses were trapped using a 514.5 nm Ar (argon) laser[194], however, the cells died. Later, a 1064 nm Nd:YAG (neodymium-doped yttrium aluminum garnet) laser was used that did not appear to cause any significant cell damage[195]. Continuous trapping using a 1064 nm wavelength inflicts a low level of photodamage to the specimen and has been shown to have no effect on intracellular pH or DNA[196]; however there is a local temperature increase at the focus (2 °C per 100 mW of 1064 nm wavelength trapping power).

Optical trapping is a relatively cheap non-invasive technique which is easy to use and the set-up is easily integrated into microscope imaging systems as the laser light can simply be routed through the optics of the microscope. The spatial resolution is excellent (10 nm – 100 μm) and confers a large degree of accuracy in the manipulation of small objects.

Optical tweezers have been used to stretch DNA to its full length[197], manipulate organelles[198] and measure the minute forces and nanometre displacements of molecular motors such as kinesin[137].

1.7.3.2.1 Physics of optical trapping

The laser beam is brought to a diffraction-limited focus by a high NA microscope objective lens (Figure 1.17). Particles close to the focus, with a refractive index (RI) greater than their surroundings (typically an aqueous solution) are drawn into what is essentially a potential well at the focal point (the RI of biological specimens is approximately 1.05 relative to water). The strength with which the object is held can be changed by changing the intensity of the laser.

The maximal trapping force for a 1 W laser at 1064 nm wavelength on 1 μm diameter polystyrene beads in aqueous solution is of the order of 100 pN. The force restoring a trapped particle to the centre of the trap is linearly related to its displacement within the diffraction-limited range of the focal spot. Any deviation of a trapped particle from the centre of the trap contributes a linear deflection to the transmitted laser illuminating the quadrant photo-diode (QPD). Thus the position of a particle in the trap can be precisely measured. Very fine displacement of the trapped particle may also be accomplished by adjusting the x, y, z position of the laser beam itself.

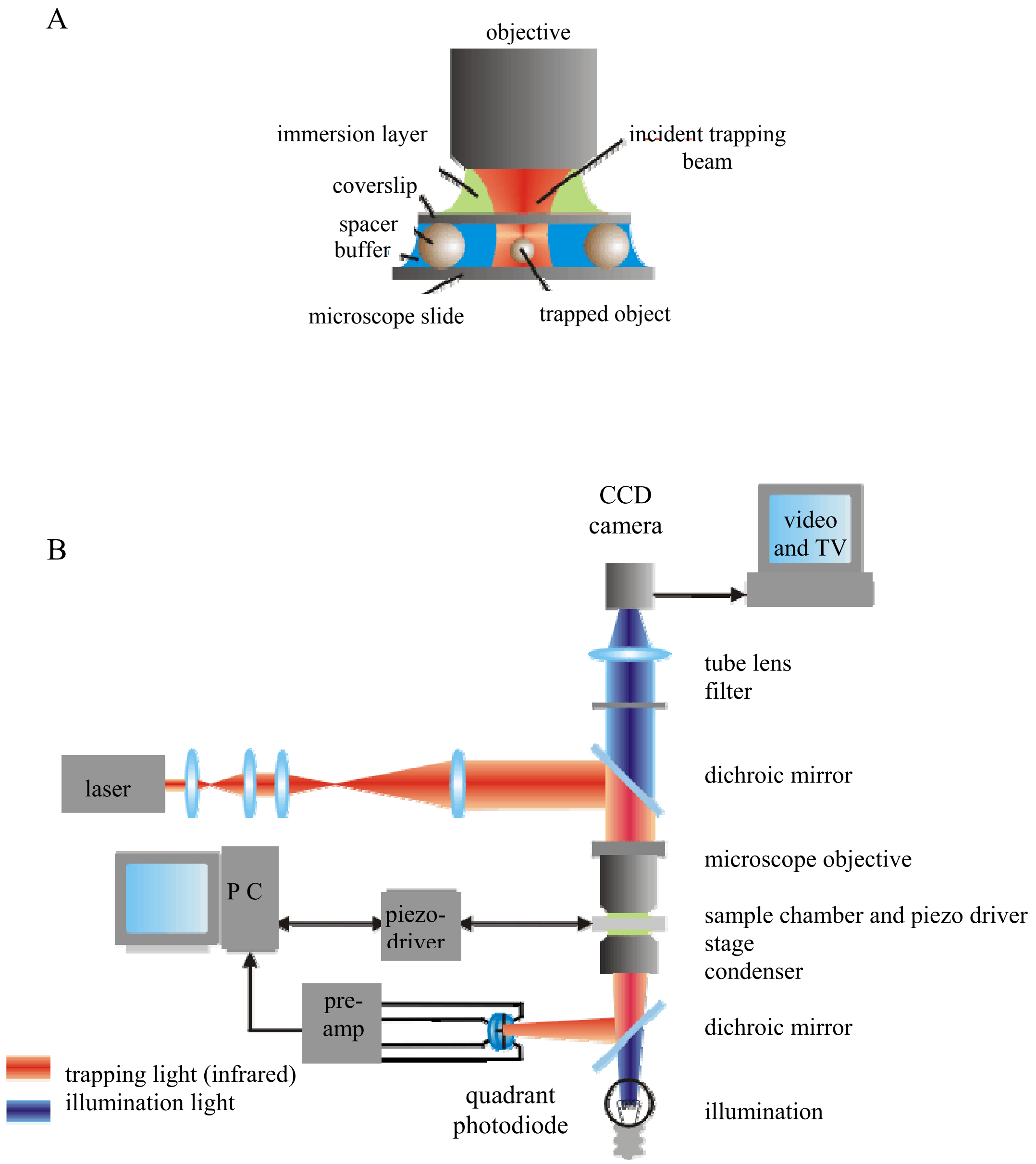

Figure 1.17: An optical trap. (A) Sample chamber in detail. (B) Optical trap set-up. Taken from www.isibrno.cz/omitec

1.7.4 Models of motor rotation

Relatively little is known about the mechanism of flagellar motor rotation compared to other molecular motors owing to the limited structural information available and the inability to study the complex *in vitro*. Most models of the bacterial flagellar motor predict that the force between the rotor and stator is either electrostatic or results from elastic deformation of components in the motor.

A credible model must be consistent with known structural features, for example, it is known that the filament, hook, rod, MS-ring and C-ring rotate relative to the stator complexes.

There are three common themes in models of motor rotation:

A. Turbine model: protons flow through stator ion-channels and electrostatically interact with helical lines of charge on the rotor protein FliG. Proton-influx makes the rotor and stator slide relative to each other, keeping lines of negative charge close to the positively charged proton, creating a dynamic electrostatic field that moves the rotor[199]. Therefore, protons interact with both the rotor and the stator. Water may be excluded from the rotor-stator interface, making the electrostatic interactions stronger (Figure 1.18A).

B. Turnstile model[114,200]: protons are deposited onto FliG from the extracellular matrix and are released into the cytoplasm only after the rotor has turned, which depends on thermal fluctuations. This model is how ATP synthase is thought to function (see section 1.1.1). However, this model is unlikely to work for the flagellar motor because no potential proton-binding sites on the rotor have been identified by mutagenesis[101] (Figure 1.18B).

C. Crossbridges and conformational change model[80]: crossbridges bind the rotor and stator and conformational changes coupled to proton-translocation pull the rotor relative to the stator and the cycle is completed by unbinding of crossbridges. In this model, the proton does not interact with the rotor, only the stator (Figure 1.18C). This model is more like an ATP-driven myosin conformational change model.

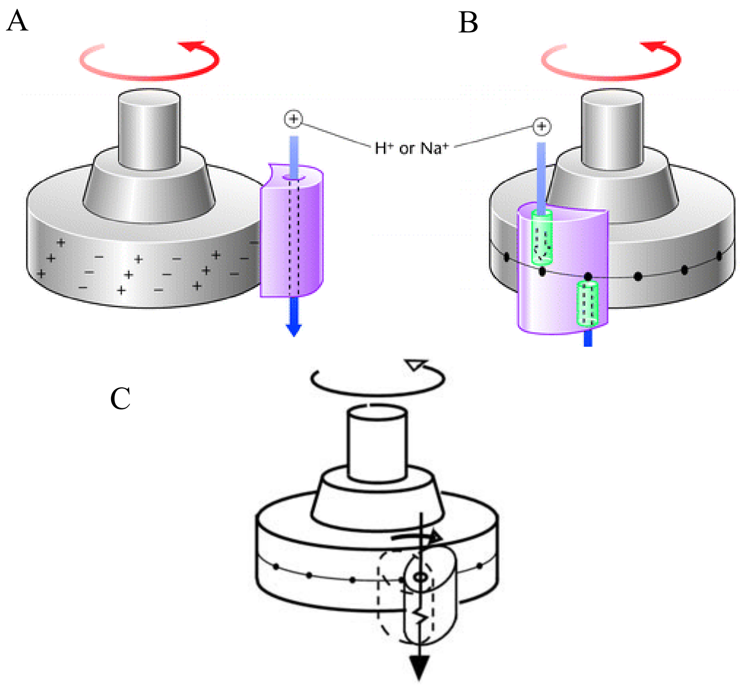

Figure 1.18: Three models of flagellar motor rotation. (A) The electrostatic proton-turbine model predicts that protons flow through the stator channels and exert electrostatic force on helical lines of charge on the rotor which keep lines of negative charge close to the proton, thus, causing the rotor to rotate as protons flow through the stator. (B) The proton-turnstile model predicts that protons are passed to a second set of channels by rotation of the rotor so that rotation and proton flow are coupled. (C) The crossbridges and conformational change model involves conformational changes in the stator complexes as protons traverse the membrane. A and B are taken from from www.els.net; C from [186,201].

1.7.4.1 Powerstroke or thermal ratchet?

It is unknown whether protons (or sodium ions) moving down their electrochemical gradients are directly involved in torque-generation. They may participate in a powerstroke in which dissipation of energy available from the electrochemical gradient and rotational work occurs synchronously (model C in the previous section). Alternatively, they may be involved indirectly in torque-generation by enabling a thermally-powered ratchet with tight coupling.

The torque-rotation rate curve serves as a test for any model of flagellar motor rotation. Torque has been measured over a wide range of rotation rates; including those at which the motor is driven backwards by electrorotation (see section 1.7.3.1). Torque exerted by the motor is approximately constant from – 100 Hz to nearly + 200 Hz (Figure 1.19). At faster rotation rates it declines approximately linearly, crossing the zero-torque line at 300 Hz. At lower temperatures, the region of transition from constant torque to declining torque (called the ‘knee’) shifts to slower rotation rates, and the rate of decline steepens[202].

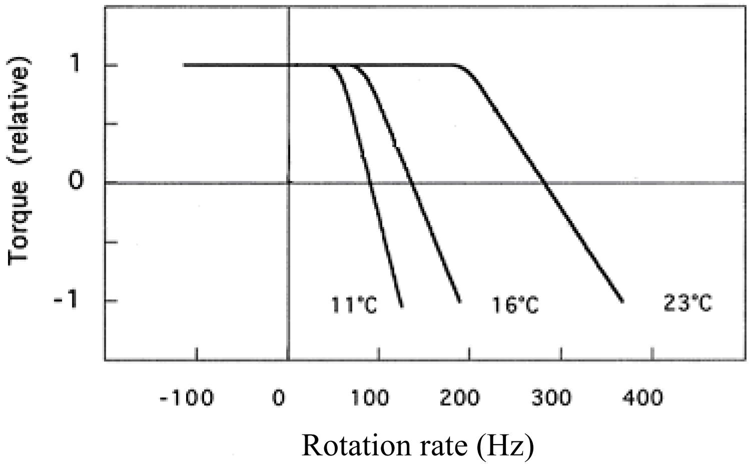

Figure 1.19: The torque-rotation rate curve for the *E. coli* flagellar motor at three temperatures obtained from electrorotation (derived from wild type strain AW405[186,203]). The torque–rotation rate relationship is linear for negative rotation rates (when the motor is pushed against its natural direction) and up to a positive rotation rate that depends upon temperature. At faster rotation rates the torque falls more steeply. Torque is shown approximately constant in the linear regime. Adapted from [142,166].

At slow rotation rates, torque is independent of temperature and physiological ion, as found previously with *Streptococcus*[204]. The observation of constant torque in tethered cells (when the motor is operating at near thermodynamic equilibrium) indicates that internal processes in the torque-generating cycle, such as proton-translocation, are not rate-limiting at rotation rates of 10 Hz or less. Torque estimates at slow rotation rates range from about 2700 pN nm[205] to 4600 pN nm[206].

At swimming rotation rates, torque is temperature-dependent[204,207], and torque is much reduced, indicating that rotation is limited by internal processes. Motor rotation rate increases six-fold as the temperature is increased from 10 °C to 40 °C [208], this is to be expected if increasing the temperature increases the rates of internal motor processes. At the ‘zero-torque speed’ (110 Hz in *Streptococcus* at 22 °C) these internal processes dissipate all the energy available to the motor and the output power goes to zero. Slowly declining torque in the slow rotation rate regime argues for a powerstroke mechanism in which the rate-limiting step depends strongly on torque and dissipates most of the available free energy. This regime would allow the torque-rotation rate curve to have a relatively flat plateau, because small changes in torque can generate large changes in rotation rate[209]. The torque-rotation curves are relatively steep[199,207], favouring a powerstroke mechanism.

The thermal-ratchet model fails the torque-rotation rate curve test[203]. At negative rotation rates, it predicts barriers to rotation (which do not exist), and at positive rotation rates, it predicts that torque falls steadily toward the zero-torque rotation rate[199]. It does not predict a constant-torque plateau or an abrupt transition from a slow-rotation rate to a fast rotation rate regime[168].

Blair *et al*[210] proposed the following cross-bridge mechanism: a proton moving in response to the pmf binds to the outward-facing Asp-32 of MotB; this drives a conformational change in the stator, a powerstroke moves the rotor forward (or stretches a spring that moves it forward) and transforms Asp-32 to an inward-facing site. Finally, proton-dissociation triggers detachment of the cross-bridge from the rotor, relaxing back into its original shape, and re-attachment to an adjacent site.

Crystallography, electron microscopy, site-directed mutagenesis and functional studies of working motors (pmf, rotation rate and torque measurements) need to be carried out in order to elucidate the mechanism of motor rotation.

1.8 Bacterial protein localisation and dynamics

Recent advances in fluorescence microscopy have provided insights into the extraordinary complexity of the sub-cellular organisation of the bacterial cell[211,212]. Many bacterial proteins require specific intracellular localisation for proper function and regulation. The challenge is to uncover the mechanisms by which proteins are localised and maintained at their proper intracellular location.

Many questions concerning flagellar localisation remain unanswered, for example: are flagella randomly located over the *E. coli* cell surface or are they actively positioned to specific sites? How do flagellar components such as the stator complexes locate and recognise the flagellum in the cytoplasmic membrane? Does the nonhomogeneity of phospholipids within the bacterial cytoplasmic membrane, where unique domains of phospholipids have been identified in polar and septal regions, have a role in protein (and possibly flagella) localization?[213]

1.8.1 Green Fluorescent Protein (GFP)

Protein expression, localisation, interaction and kinetic studies have advanced considerably through the use of fluorescent *in vivo* reporter proteins such as Green Fluorescent Protein (GFP). GFP originates from the jellyfish *Aequorea victoria* where it functions in conjunction with the photoprotein, aequorin. GFP expression is easy to detect in living cells by non-invasive approaches such as fluorescence microscopy. Wild type GFP has a minor excitation peak at 395 nm and a minor one at 475 nm and an emission peak at 509 nm.

The crystal structure of GFP to 1.9 Å resolution has been solved[213] (Figure 1.20). GFP is a single peptide of 238 amino acids, which adopts a β-can structure[214,215] consisting of 11-antiparallel β-strands forming a compact cylinder (~ 30 Å in diameter and ~ 40 Å in length). Inside the cylinder is an α-helix containing the chromophore which is completely and rigidly encapsulated. The chromophore is formed from the auto-catalytic cyclisation of residues 65 – 67 (Ser-Tyr-Gly in the native protein). Chromophore maturation takes ~ 0.5 h and requires molecular oxygen. GFP can be fused to another protein either N- or C-terminally[186] because both termini of GFP are rather flexible on the surface of the β-can, enabling GFP to fold as an autonomous unit whose structure is not significantly distorted by the fused protein.

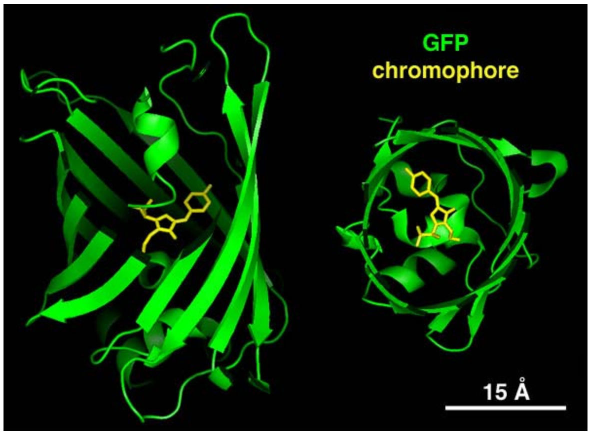

Figure 1.20: The structure of GFP. GFP has a β-can structure consisting of 11-antiparallel β-strands which form a compact cylinder containing the chromophore. Taken from www.mekentosj.com/science.fret/images/gfp.html

Many mutant variants of GFP have been engineered, such as EGFP (Enhanced GFP) which is 35 times brighter than wild type GFP. The excitation peak of EGFP is shifted to 490 nm, while the emission peak is the same as wild type GFP (509 nm). Other variants include CFP (Cyan Fluorescent Protein) and YFP (Yellow Fluorescent Protein), which can be used in Fluorescence Resonance Energy Transfer (FRET) experiments.

1.8.1.1 Fluorescence Resonance Energy Transfer (FRET)

FRET describes an energy transfer mechanism between two fluorophores, a donor (e.g. CFP) and an acceptor (e.g. YFP). For FRET to occur, the donor emission spectrum must overlap with the acceptor absorption spectrum, and they must be within 10 nm of each other. The donor fluorophore is excited at its specific fluorescence excitation wavelength; this excited state is transferred to an acceptor fluorophore by a long-range dipole-dipole coupling mechanism. The donor fluorophore then returns to its electronic ground state.

The FRET efficiency is determined by: (1) the distance between the donor and acceptor fluorophores, (2) the spectral overlap of the donor emission spectrum and the acceptor absorption spectrum, and (3) the relative orientation of the donor emission and acceptor absorption dipole moment. When the donor and acceptor fluorophores are dissociated, the donor emission is detected upon donor excitation. When the donor and acceptor fluorophores are in close proximity, (1 - 10 nm) donor emission is reduced and acceptor emission is predominately observed because of the intermolecular FRET from the donor to the acceptor. FRET can be used to quantify protein-protein interactions, protein-conformational changes and protein-complex formation.

Occasionally, fusion to XFP (cyan, green or yellow fluorescent protein) can affect the functioning of the tagged protein, possibly caused by steric hindrance imparted by the XFP-tag. However, the XFP-tag is unlikely to affect the mobility of a tagged protein, unless it interacts with other cytoplasmic or membrane proteins.

The localisation of various chemotaxis and flagellar motor proteins have been determined by fusing them to XFP, for example, Sourjik and Berg[110] over-expressed XFP-tagged CheY, CheZ, CheA and FliM from inducible plasmids and found that CheY, CheZ and CheA clustered at the cell pole in an MCP-dependent manner, whereas FliM localised as fluorescent spots on the sides of the cell.

Many proteins function in multimeric complexes, such as the flagellar motor, and investigating their organisation and dynamics is critical for understanding their function. Currently, little is understood about protein dynamics and turnover within individual complexes under natural conditions *in vivo*. A technique called FRAP (F̲luorescence

Recovery After Photobleaching) has been used to assess the dynamic properties of proteins.

1.8.2 Fluorescence Recovery After Photobleaching (FRAP)

Fluorescence Recovery After Photobleaching (FRAP) is an imaging technique whereby the fluorescence of a fluorophore is deliberately bleached by an intense flash of laser light. This so-called 'photobleaching' is performed in a defined area of a cell and recovery of fluorescence into the photobleached area by the diffusion of unbleached fluorophores is measured. Hence, the mobility and dynamics of XFP-tagged proteins within living cells can be measured (Figure 1.21).

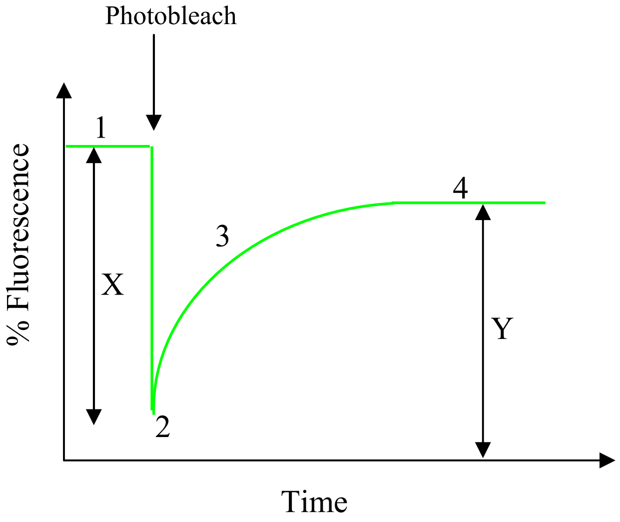

Figure 1.21: A theoretical FRAP experiment. Fluorescence is measured at the start of the experiment (1); an area of the cell sample is photobleached causing the percentage fluorescence to decrease (2). Recovery of fluorescence into the photobleached area is monitored as unbleached fluorophores diffuse into the photobleached area (3); the amount of fluorescence recovery stabilises (4). The percentage of fluorescence lost due to photobleaching is 'X' and the percentage of fluorescence recovery is 'Y'. In reality, the percentage recovery of fluorescence (Y) never reaches 100 %. The lateral mobility of the fluorophores is determined by the gradient of the curve (3). Larger gradients equate to faster fluorescence recovery and more mobile fluorophore molecules.

FRAP has been used to assess the mobility of over-expressed cytoplasmic membrane proteins TatA / B / C-GFP in *E. coli*[216], and the mobility of the light-harvesting phycobilisomes of *Synechococcus*[217]. FRAP has also been used to measure membrane fluidity by using lipid-soluble fluorescent dyes[218].

When using FRAP to calculate a diffusion co-efficient (*D)*, there are several considerations: (1) *D* are usually temperature-sensitive so a temperature-controlled microscope stage must be used. (2) FRAP has limited spatial resolution and the resulting photobleached area is larger than half the wavelength of the light because light is scattered by the sample. (3) For accurate measurements of *D*, the total size of the sample should be much greater than the size of the photobleached spot. (4) When calculating *D*, the membrane environment is assumed to be uniform over the entire measurement area. (5) The photobleach must be performed quickly and post-photobleach images must be recorded rapidly when monitoring fast-diffusing proteins. (6) Photobleached GFP molecules may 'blink' resulting in fluorescence recovery in the absence of diffusion; to control any reversible photobleaching of GFP, the FRAP conditions should be repeated in samples in which no recovery of fluorescence is expected.

FRAP measurements are often complicated by an immobile fraction and by the binding and dissociation of fluorophore-tagged proteins to and from intracellular components, resulting in longer recovery times. Kinetic models and computer simulations are useful when analysing FRAP data to determine a value for *D*, the mobile fraction, and the transport rate or binding / dissociation rate other proteins.

1.8.3 Calculated diffusion co-efficients (*D*)

The MinCDE system of *E. coli,* which locates the cell-division plane is thought to require a difference in the values of *D* between the membrane-associated and the cytoplasmic forms of MinD and MinE for its proper function[219,220]. In *Caulobacter cresentus*, PleC (90 kDa) is a single histidine kinase with four transmembrane domains, which regulates asymmetric cell division. It was replaced with *pleC-yfp* in the genome, and visualised using single-molecule fluorescence microscopy. Diffusion was observed thoughout the membrane, (as well as immobilised molecules at the cell pole); and a value of *D* was calculated for mobile PleC-YFP (not bound to the cell pole): $12 \pm 2 \times 10^{-3}$ μm^2 s^{-1} [221]. This value of *D* is near the low end of the range of *D* values calculated for eukaryotic membrane proteins; it is roughly 200 times smaller than that measured by FRAP for the cytoplasmic maltose-binding protein (72 kDa) in *E. coli* [222] Measurements of *D* eukaryotic membrane proteins using FRAP, single gold bead tracking[223,224], and single-molecule tracking techniques[225,226] have yielded values ranging from 5×10^{-3} to 500×10^{-3} μm^2 s^{-1}.

1.8.4 Total Internal Reflection Fluorescence Microscopy (TIRFM)

When light travelling through a medium with a high refractive index (such as glass) passes through a medium with a lower refractive index (such as water) the light is bent (Figure 1.22). As the angle of incidence of the light increases, the light propagated into the aqueous layer is increasingly bent until a 'critical angle' is achieved whereby light is no longer propagated. Beyond this critical angle two phenomena occur: (1) all of the propagated light is totally reflected back into the glass at the interface, (2) an evanescent field penetrates into the aqueous phase up to 200 nm deep, this decays exponentially and depends on refractive indices of the two phases, the incident angle and the wavelength of the light. Fluorophores within the evanescent field become excited by absorbing photons; hence fluorophores within this thin 200 nm region of the sample can be visualised. This technique achieves a very low signal-to-noise ratio because the majority of the sample is too far from the coverslip to be within the TIRF excitation field.

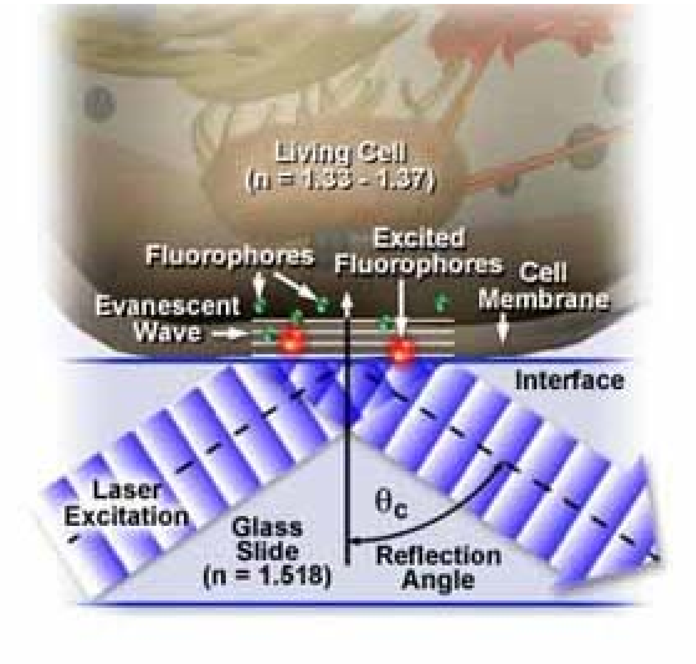

Figure 1.21: TIRFM. TIRF generates an evanescent wave approximately 200 nm into the sample, which decays exponentially. This evanescent wave is generated when the incident light is totally reflected from the interface, only fluorophores within this region are excited by the evanescent wave. n = refractive index. Taken from www.opticalanalysis.com/research_tirfm.html

1.9 Aims of this study

- To determine whether various point mutant MotBs (D32*) expressed from an inducible plasmid in a wild type background could form stator complexes and install into the motor and exert dominant-negative effects on rotation rate.

- To determine whether the various D32* substitutions (which include charge reversals and neutralisations) affect cell motility differently. To determine if a fully-functional motor could be made to slow down in a step-wise fashion ('de-resurrect') as successive mutant stator complexes incorporate into the motor.
- To determine if a stopped (locked) motor containing mutant stator complexes could resurrect in a step-wise manner when the inducer is removed and mutant MotB* is no longer expressed.
- To visualise GFP-MotB at the motor by replacing native chromosomal *motB* with *gfp-motB*. Stuck-cell bead assays, swarm plates and TIRFM would be used to confirm functionality and fluorescence.
- To quantify the number of fluorescent GFP-MotB molecules (and hence the number of stators) in the motor using TIRFM and FRAP.
- To determine whether there is GFP-MotB turnover in the motor with a membrane pool, or is the motor a stable entity? To calculate a diffusion co-efficient and a rate constant for GFP-MotB using TIRFM and FRAP.
- To replace other motor genes in the chromosome (*motA*, *fliG* and *fliM*) with fluorescently-tagged gene fusions, with the intention of doing FRET.

2 Materials and Methods

2.1 Strains and plasmids

Strains and plasmids used in this study are shown in Tables 2.1 and 2.2 respectively. *E. coli* strains were grown either with shaking in Luria-Bertani broth (LB-broth) (Appendix A) or on solid LBA plates (LB-broth containing 1.5 % agar) (Appendix A) containing the appropriate antibiotic(s) at 37 ºC, unless otherwise stated. The following antibiotics were used (when necessary):

- ampicillin / carbenicilin 100 µg / ml (in distilled water)
- chloramphenicol 34 µg / ml (in 95 % ethanol)
- kanamycin 25 µg / ml (in distilled water)
- tetracycline 10 µg / ml (in 100 % ethanol)

***E.coli* strain**	**Description**	**Source/Reference**
RB6	Δ*cheY fliC726* (parental strain KAF95)	Berg and Turner[227]
RP437	wild type for chemotaxis	A gift from John S. Parkinson, University of Utah
YS34	Δ*motA motB* Δ*cheY* Δ*pilA fliC*::*Tn10*	Lo *et al*[101]
RP5232	Δ*cheY*	A gift from John S. Parkinson, University of Utah
PS2589	*fliC*st	A gift from Jeffrey Stock, Princeton University
JHC36	*fliC*st Δ*motA* Δ*motB* Δ*cheY* Δ*pilA* (parental strain YS34)	This study
JHCE3	*fliC*st Δ*cheY* (parental strain RP5232)	This study
DH5α	cloning strain, supports blue/white selection	Gibco-BRL
BW25141	*pir*$^{+}$; used for cloning pDS132	A gift from Jeffrey

		Stock, Princeton University
JHC1	*gfp-motB* (parental strain RP437)	This study
GM2163	Dam$^-$ Dcm$^-$, useful for the production of DNA to be cut with Dam or Dcm-sensitive restriction enzymes; Cm^R	New England Biolabs
JHC2.27	*motA-yfp* (parental strain RP437)	This study
JHC3.72/ JHC3.81 / JHC3.82	*yfp-motA* (parental strain RP437)	This study
JHC4.25/ JHC4.26/ JHC4.31/ JHC4.32	*fliM-yfp* (parental strain RP437)	This study
JHC5.8/ JHC5.42/ JHC 5.44	*fliG-yfp* (parental strain RP437)	This study
M15 pREP4	expression host containing pREP4; Kn^R	Qiagen

Table 2.1: *E.coli* strains used in this study.

Plasmid	**Description**	**Source/Reference**
pJZ18-D32wt	wild type *motB*; Amp^R; P$_{tac}$	Zhou *et al*[228]
pJZ18-D32A	*motB* D32A; Amp^R; P$_{tac}$	
pJZ18-D32E	*motB* D32E; Amp^R; P$_{tac}$	
pJZ18-D32G	*motB* D32G; Amp^R; P$_{tac}$	
pJZ18-D32N	*motB* D32N; Amp^R; P$_{tac}$	
pJZ18-D32Q	*motB* D32Q; Amp^R; P$_{tac}$	
pJZ18-D32R	*motB* D32R; Amp^R; P$_{tac}$	
pJZ18-D32W	*motB* D32W; Amp^R; P$_{tac}$	
pFD313	*fliC*st encoding a 'sticky' flagellin carrying a 57 residue deletion (residues 245-301 of 497) replaced by a 6 residue linker; Cm^R	Kuwajima [229]
pUC19	high-copy number cloning plasmid; Amp^R; supports blue-white selection	New England Biolabs
pKO3	suicide vector; Cm^R; *sacB*; *repA* (Ts) origin of replication	Link *et al*[230]
pKO3-PS-*fliC*st	pKO3 carrying approximately 100 bp downstream and upstream from the start and end of *fliC*st..	This study
pDS132	suicide vector; Cm^R; *sacB*; R6K origin of replication	Philippe *et al*[231]
pDS-*fliC*st	pDS132 carrying approximately 500 bp downstream and upstream from the start and end of *fliC*st.	This study
pDFB102	*motA motB;* Amp^R; P$_{lac}$	A gift from David Blair, University of

		Utah
pECFP-N1	CFP cloning sequence with enhancements to increase fluorescence; Kan^R	BD Biosciences
pEGFP-N1	GFP cloning sequence with enhancements to increase fluorescence; Kan^R	
pEYFP-N1	YFP cloning sequence with enhancements to increase fluorescence; Kan^R	
p*gfp-motB*	pKO3 carrying *gfp-motB*	This study
pYS7	*fliC*st encoding a 'sticky' flagellin carrying a 57 residue deletion (residues 245-301 of 497) replaced by a 6 residue linker; Cm^R	A gift from Akihiko Ishijima, Nagoya University
p*gfp-motA*	pDS132 *gfp-motA*	This study
p*motA-yfp*	pDS132 *motA-yfp*	This study
p*fliM-yfp*	pDS132 *fliM-yfp*	This study
p*fliG-yfp*	pDS132 *fliG-yfp*	This study
pREP4	plasmid carrying *lacI*^{q} gene, used for reducing 'leaky' expression from the *tac* promoter of pQE-80; Kn^R	Qiagen
pQE-80	P_{tac}-based expression vector. Introduces 6 x His-tag to the N-termini of expressed proteins; Amp^R	Qiagen
pQE-80-*egfp*	pQE-80 carrying *egfp*: for the over-expression of EGFP protein	This study

Table 2.2: Plasmids used in this study.

2.1.1 Storing strains

Strains were grown to stationary phase in LB-broth with shaking and mixed with sterile 50 % glycerol in a 3: 2 ratio in a cryotube (Sarstedt) and snap-frozen in liquid nitrogen and stored at – 80 ºC.

2.2 Molecular genetic techniques

2.2.1 Preparing plasmid DNA

Small-scale preparation of plasmid DNA was carried out using the alkaline lysis method[232] (Appendix A). 1.5 ml of stationary phase culture was centrifuged and resuspended in DISH I. DISH II and DISH III were added and the mixture was centrifuged. The supernatant was decanted and the plasmid DNA was precipitated by the addition of 100 % ethanol. This mixture was incubated at - 20 ºC for 30 min. Plasmid DNA was recovered by centrifugation, washed with 70 % ethanol and air-dried at 37 ºC for 30 min. High-copy number plasmid pellets were resuspended in 50 µl sterile water containing RNAase at 20 µg / ml, whilst low-copy number plasmids were re-suspended in 20 µl of sterile water containing RNAase I.

Sequencing quality DNA and DNA for use as a template in PCR were prepared using the Hi-Speed Midi kit (Qiagen), according to their instructions. Plasmid DNA was eluted in 200 µl sterile water and stored at - 20 ºC until required.

2.2.2 Preparing chromosomal DNA

Genomic DNA was isolated from *E. coli* using a modified version of the protocol described by Giuliano *et al*[233]. 1.5 ml of stationary phase culture was centrifuged and frozen in liquid nitrogen. The cell pellet was resuspended in 0.5 ml of 65 ºC lysis buffer (Appendix A) and once cooled, 0.1 mg of proteinase K was added. This cell lysate mixture was incubated at 45 ºC for 2 h and extracted twice with 0.5 ml phenol: chloroform: isoamyl alcohol (25: 24: 1 v/v) (Biogene). Chromosomal DNA was precipitated with 1 ml of 100 % ethanol, washed in 1 ml of 70 % ethanol and dried overnight at room temperature. The DNA pellet was resuspended in 50 µl of sterile water containing RNAase I and stored at - 20 ºC until required.

2.2.3 Transforming *E. coli*

Competent cells were either prepared using the calcium-chloride method or electro-competent cell method, both of which are described in Sambrook *et al*[233].

2.2.3.1 Calcium-chloride competent cells

Calcium-chloride competent cells were prepared using the method described in Sambrook *et al*[233] and were stored at 4 ºC for up to five days prior to use. 1 ml of a stationary phase culture of *E. coli* was inoculated into 50 ml of LB-broth and incubated for 2-3 h at 37 ºC with shaking until an OD_{600} 0.4 - 0.5. Cells were centrifuged and resuspended in 10 ml ice–cold 100 mM $CaCl_2$ and incubated on ice for 30 min. Cells were re-pelleted and resuspended in 2 ml ice-cold 100 mM $CaCl_2$ and incubated on ice for a further 1 h. For transformations of supercoiled plasmids, 0.5 µg of DNA was transformed, whereas for ligations, the entire ligation mixture was transformed by incubating the DNA with 100 µl of competent cells on ice for 1 h. Cells were heat-shocked by exposing them 42 ºC for 2 min, followed by 2 min on ice. 1 ml of LB-broth was added to the heat-shocked cells and incubated at 37 ºC for 1 h to allow cells to recover and express antibiotic resistance genes. The mixture was spread onto selective

LBA plates containing the appropriate antibiotic(s) and incubated overnight at 37 ºC unless otherwise stated.

2.2.3.2 Electro-competent cells and electroporation

Electro-competent cells were prepared using the electroporation cell method as described in Sambrook *et al*[233] and stored at -80 ºC prior to use. 1 - 2 µl of DNA was added to 40 µl cells in a microfuge tube and incubated on ice for 1 min, and then the mixture was transferred to a pre-chilled electroporation cuvette. An electrical pulse was delivered at 25 µF capacitance, 2.5 kV, and 200 ohm resistance. 1 ml of SOC media (Appendix A) was added to the cell mixture which was transferred to a room-temperature microfuge tube. Cells were allowed to recover at 37 ºC for 2 h, then spread-plated onto SOB plates (Appendix A) containing the appropriate antibiotic(s).

2.2.4 Restriction digests

DNA digests using various restriction enzymes (New England Biolabs) were carried out in 20 - 50 µl volumes with the reaction buffer provided, 2 - 10 units of enzyme and BSA (if necessary), for 2 h at 37 ºC, unless the instructions stated otherwise.

2.2.5 DNA electrophoresis

DNA fragments were separated according to size using agarose gel electrophoresis. Multi-purpose agarose (Roche) was used at concentrations between 0.8 and 2 % (w/v) (depending upon the size of DNA bands expected) in 0.5 X TBE buffer

(90 mM Tris-borate, 2 mM EDTA, pH 8.0) and electrophoresed at between 100 and 145 V. Gels were stained for 20 min in 1 ng / ml ethidium bromide and visualised on a UV transilluminator (λ_{max} = 360 nm).

2.2.6 Purifying DNA fragments

DNA fragments were purified from solution or agarose gels using the GenElute Gel Extraction Kit (Sigma) according to the instructions.

2.2.7 Blunting of cohesive DNA ends

Overhanging 3' ends were removed and recessed 3' overhangs were generated using T_4 DNA polymerase (New England Biolabs) generating blunt-ended DNA fragments. Two units of enzyme were used in a final reaction volume of 40 µl and incubated at 15 ºC for 20 min. The resulting DNA solution was purified using the method described in section 2.2.6.

2.2.8 De-phosphorylating DNA

To prevent vector self-ligation during cloning of DNA fragments with two identical ends, vector DNA was de-phosphorylated using alkaline phosphatase (New England Biolabs). Two units of enzyme was used in a final reaction volume of 40 µl and incubated at 37 ºC for 90 min. The DNA was purified from solution using the method described in section 2.2.6.

2.2.9 PCR (Polymerase Chain Reaction)

PCRs were carried out either using Pfu DNA polymerase (Stratagene) or Extensor Hi-Fidelity PCR master mix (ABgene) according to the instructions in a Techgene Thermal Cycler (Techne).

The thermal cycling programme for the Extensor Hi-Fidelity PCR master mix was as follows:

step 1	Initial denaturation	94 ºC, 2 min
step 2	Denaturation	92 ºC, 10 s
step 3	Annealing	62 ºC, 30 s
step 4	Extension	68 ºC, x min*
step 5	to step 2 (10 cycles)	
step 6	Denaturation	94 ºC, 10 s
step 7	Annealing	62 ºC, 30 s
step 8	Extension	68 ºC, x min*
step 9	to step 6 (20 cycles)	
step 9	Final extension	68 ºC, 7 min

* Extension time was determined by the length of DNA sequence to be amplified (2 min if < 3 kb, 6 min if < 6 kb)

The thermal cycling programme for the Pfu DNA polymerase was as follows:

step 1	98 ºC, 4 min
step 2	98 ºC, 2 min

step 3	60 ºC, min*
step 4	72 ºC, 4 min
step 5	to step 2 (25 cycles)
step 6	72 ºC, 5 min

*1 min for every 500 bp to be amplified

2.2.9.1 Overlap-extension PCR

Overlap-extension PCR used the same conditions as described for PCR, except that the template consisted of two DNA templates. Primers used in the reaction were the N-terminal primer of one of the original PCR reactions, and the C-terminal primer of the other.

2.2.10 Sequencing DNA

DNA was sequenced by the Sequencing Service (Biochemistry Department, University of Oxford) using ThermoSequenase dye terminators (Amersham) on an ABI377 sequencer (Applied Biosystems) with BigDye version IV chemistry. DNA sequences were analysed using the Clone Manager software package (Sci Ed Central) and assembled using the Staden software package. Plasmids were supplied at a concentration of 0.5 mg / ml and primers at 32 pmol.

2.2.11 Ligating DNA

Vector and insert DNA in a ratio of about 1: 3 (total amount of DNA present 1 - 2 µg) were ligated in a reaction volume of 50 µl containing 2 µl T_4 DNA ligase (Gibco-BRL), supplied reaction buffer and 50 µM ATP, and left at 16 ºC for at least 12 h. This ligation was subsequently transformed into freshly prepared competent cells.

2.2.12 Southern blotting

Digested chromosomal DNA (10 µg) was separated on an agarose gel, depurinated, denatured, neutralised and transferred to Hybond-N membrane (Amersham) by upward capillary transfer[186]. The membrane was dried, UV fixed and pre-hybridised for at least 3 h. Hybridisation of the probe was carried out at 68 ºC in a Hybaid oven for 16 h. Bands were detected using the DIG colour detection kit (Boehringer Mannheim) (see section 2.2.13).

2.2.13 Digoxigenin labelling of DNA probes for Southern blotting

DNA for use as probes in Southern blotting were purified from agarose gels as described previously and labelled using the random hexanucleotide priming technique with the DIG DNA Labelling and Detection Kit (Boehringer Mannheim) according to the instructions.

2.2.14 Chromosomal gene replacement using suicide vectors

Genomic replacement using double homologous recombination of a suicide vector was used to produce markerless strains. Suicide vectors integrate into the genome at their target sequence by homologous recombination, and a second crossover event excises the vector backbone from the chromosome, resulting in allelic exchange.

Two types of suicide vector currently exist: those carrying the R6K replication origin, such as pDS132, and temperature-sensitive vectors such as pKO3. The first type of suicide vector can only replicate in strains producing the *pir* gene product, the π protein, whilst the second type of suicide vector can only replicate at the permissive temperature.

Integration into the chromosome is selected for by an antibiotic resistance marker (Cm^R in pKO3 and pDS132) either at the restrictive temperature or in a *pir*- background. Vector backbone excision from the chromosome is selected for by counter-selectable markers: if the vector backbone is still present on the chromosome, then the cell will die in the presence of the counter-selective compound. Both pKO3 and pDS132 use the sucrose-sensitivity system as their counter-selectable determinant. Levan saccharase encoded by the *sacB* gene from *B. subtilis* is lethal to most Gram-negative bacteria in the presence of sucrose. Thus growing on sucrose-agar plates selects for vector backbone excision, and hence, allelic exchange.

2.2.14.1 Allelic exchange using pDS132

All cloning steps were carried out in strain BW25241 (*pir*$^+$) at 37 ºC (a gift from Jeffrey Stock, Princeton University) which allowed replication of pDS132. Recombinant pDS132 carrying a target sequence was introduced into the chosen background strain by electroporation.

Electroporated cells were grown on Cm / SOB agar plates (Appendix A) at 37 ºC for 16 - 36 h, which selected for vector integration onto the chromosome. Resulting colonies were grown to stationary phase in Cm / LB-broth at 37 ºC to ensure they retained Cm^R. 100 µl of culture was centrifuged, resuspended in 100 µl LB-broth and sub-cultured into 5 ml of LB-broth and grown to stationary phase with shaking at 37 ºC, allowing cells to lose cytoplasmic pDS132. 100 µl of culture was serially-diluted in 10 mM $MgSO_4$ and spread-plated on 5 % sucrose LBA plates without NaCl, and incubated overnight at 37 ºC, allowing a second cross-over and vector excision from the chromosome. 250 colonies were replica-plated on Cm / LBA plates and 5 % sucrose LBA plates without NaCl.

Gene replacement was confirmed by Southern blotting (see section 2.2.12) and sequencing of chromosomal DNA preparations of Cm^S Suc^R colonies.

2.2.14.2 Allelic exchange using pKO3

All cloning steps were performed in strain DH5α at 30 ºC. The background strain was transformed using the $CaCl_2$ method (see section 2.2.3.1) and plated on pre-warmed Cm / LBA plates at 30 ºC and 43 ºC. 5 colonies from the 43 ºC plates were grown to stationary phase in LB-broth with shaking at 30 ºC. 100 µl of culture was centrifuged and serially-diluted into 1 ml LB-broth and spread-plated onto 5 % sucrose LBA plates at 30 ºC and Cm / LBA plates at 43 ºC. Colonies on the 5 % sucrose LBA plates were replica-plated onto Cm / LBA plates at 30 ºC and LBA plates to test for vector backbone excision. Gene replacement was confirmed by Southern blotting (see section 2.2.12) and sequencing.

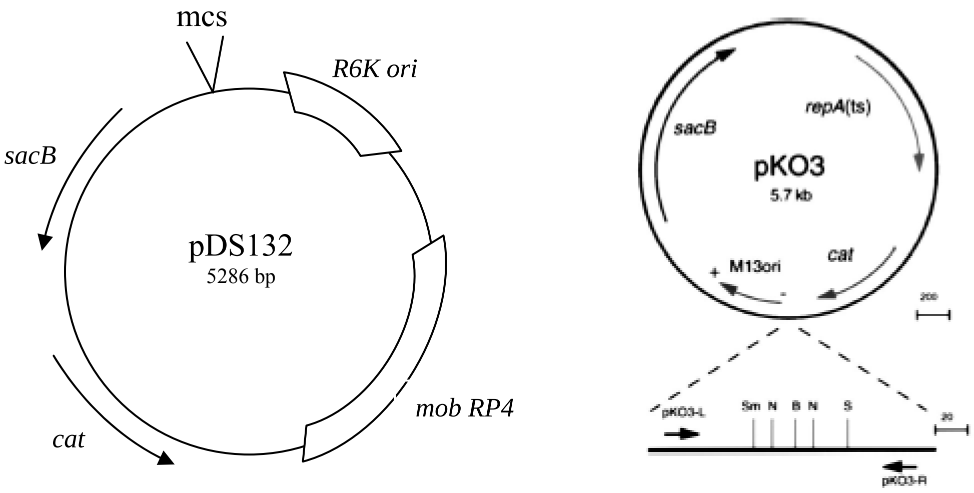

Figure 2.1: Suicide vectors pDS132 and pKO3. Both were used in this study to replace native genes in the chromosome. Both vectors carry the chloramphenicol resistance gene *cat* (Cm^R) and the counter-selectable marker *sacB* encoding levan saccharase. They carry different origins of replication: pDS132 carries an R6K origin of replication (*R6K ori*) which allows replication only in strains that produce the π protein, the product of the *pir* gene, whilst pKO3 carries the *repA* (Ts) origin of replication that has a permissive temperature of 30 ºC but is inactive at 43 ºC. The multiple-cloning site of pKO3 is enlarged and contains *Sma*I (Sm), *Not*I (N), *Bam*HI (B) and *Sal*I (S). The multiple-cloning site (mcs) of pDS132 contains *Sph*I and *Sac*I. Taken from[230] and [229].

2.2.15 Over-expressing and purifying EGFP

GFP was over-expressed and purified to use as a positive control in western blotting when hybridising with an anti-GFP antibody to detect EGFP-tagged motor proteins (Chapters 4 and 6). Details of step-wise photobleaching of individual EGFP molecules are described in Chapter 5. This enabled quantification of motor EGFP-MotBs. Purified EGFP was also used for antibody production because commercially available anti-GFP antibody is not specific.

Strain M15 pREP4 containing the expression plasmid pQE-80-*egfp* was grown to stationary phase at 37 ºC in Amp / Kan / LB-broth and sub-cultured into 500 ml Amp / Kan / 2YT media (Appendix A) with appropriate antibiotics until OD $_{600}$ 0.7, then induced overnight with 100 µM IPTG at 18 ºC. Following induction, cells were harvested by centrifugation for 15 min at 4 ºC then resuspended in lysis buffer (Appendix A). Cells were lysed by storage at -20 ºC followed by thawing and sonication (6 x 20 s full power bursts; Vibracell (Sonics & Materials Incorporated)). Lysates were centrifuged for 15 min at 4 ºC to remove insoluble material and cell debris. Lysate was filtered through a 0.45 µm filter (Millipore). Cleared lysates were applied to a Nickel-NTA agarose (Qiagen) column and equilibrated with lysis buffer. The column was washed with at least sixty column volumes of lysis buffer, and EGFP was eluted in 4.5 ml of lysis buffer (Appendix A) and collected in microfuge tubes.

Protein concentration was measured using a Bradford based assay (BioRad) using BSA as a standard. Protein purity was assessed using SDS-PAGE gels stained with Coomassie blue (Appendix A). Purified EGFP was sent to Eurogentec where it was injected into rabbits for anti-GFP antibody production; the remainder was stored at -20 ºC.

2.2.16 SDS-PAGE / western blotting

Pelleted cells were resuspended in 50 µl SDS-PAGE loading buffer (Appendix A) and heated at 110 ºC for 10 min. Samples were loaded onto 10 or 12 % polyacrylamide gels using the mini-protean II system (Biorad). Protein was transferred onto nitrocellulose membrane (APB) using the mini-protean II transfer kit. Membranes were blocked in 5 % non-fat milk (Marvel) / PBS (v/v) for 1 h at room temperature with gentle shaking or overnight at 4 % without shaking, and then washed twice with PBS. Primary antibody was diluted in 1 % non-fat milk / PBS (v/v) and added to the membrane for 1 h at room temperature, the membrane was then washed four times in 0.2 % Tween-20 / PBS (v/v). Secondary HRP-conjugated anti-rabbit antibody (DAKO) was added to the membrane, diluted 1: 1000 in 1 % non-fat milk / PBS (v/v), and incubated for 1 h at room temperature. The membrane was washed four times in 0.2 % Tween-20 / PBS (v/v) and a final time in PBS. Bands were detected using enhanced chemiluminescence solution (APB) and X-OMAT AR film (Kodak).

2.2.16.1 Preparing acetone powder

An acetone powder was used in western blotting when hydridising membranes with anti-MotA and anti-MotB antibody as both antibodies resulted in high levels of background. 500 ml of YS34 (Δ*motA* Δ*motB* Δ*cheY* Δ*pilA fliC*::*Tn10*) was grown in LB-broth with shaking at 37 ºC until an OD $_{600}$ 0.6. Cells harvested by centrifugation were resuspended in 3 ml of 0.9 % NaCl at 4 ºC. 20 ml of ice-cold acetone was added to the cell suspension and mixed vigorously and centrifuged. The supernatant was discarded and the cell pellet was resuspended with fresh ice-cold acetone and mixed vigorously, and allowed to sit at 0 ºC for 10 min. After centrifugation, the pellet was spread on a piece of filter paper and air-dried at room temperature for 30 min. The resulting acetone powder was used at a final concentration of 1 % during primary antibody incubation.

2.3 Phenotypic analysis of strains

2.3.1 Growth rates

Growth rates were determined by sub-culturing stationary phase culture 1: 100 into 50 ml LB-broth with shaking at 37 ºC and measuring OD $_{600}$ of a 1 ml sample of culture at approximately hourly intervals until stationary phase was reached. Each strain was analysed in triplicate.

2.3.2 Swarm plates

Swarming is the ability of motile cells to move through LB-broth containing 0.25 % agar (Difco, Bactoagar) and can be used as a test of chemotactic ability. As cells metabolise nutrients in the agar, they create a gradient and, if chemotactic, swim out (swarm) from the point of inoculation up the attractant gradient to regions of higher nutrient concentration, forming a large ring. Bacteria in the outer ring have consumed and swarmed to the preferred nutrient on the plate; successive rings are caused by bacteria metabolising and swarming to the remaining attractants.

Plates containing the relevant antibiotics (and / or inducer) were poured 3 h prior to inoculation. 5 µl aliquots of stationary phase culture (in LB-broth, at 30ºC) were inoculated onto the swarm plates. Plates were incubated at 30 ºC, for 8 - 48 h depending upon the strains being assessed. Each set was repeated in triplicate.

2.3.3 Preparing motile cells

E. coli was grown in T-broth (Appendix A) at 30 °C until OD $_{600}$ 0.8. 1 ml of cell suspension was centrifuged twice and resuspended in an equal volume motility buffer (to remove traces of T-broth). The cell suspension was forced 110 times between two syringes with 26-gauge needles connected by a piece of polyethylene tubing (12 cm long, 0.58 mm inner diameter), a method known as 'shearing'[228]. Turbulent flow inside the tubing shears the flagellar filaments at a random point along their length. Shearing shortens flagella so that a spinning bead is close to the cell body and does not attach itself to neighboring cells or flagella. The cell / flagella suspension was washed three times by centrifuging which pelleted the cells but not loose flagella. Cells were resuspended in 1 ml of motility buffer (Appendix A).

2.3.4 Tunnel slides

A 'tunnel slide' is a microscope glass slide with two strips of double-sided sticky tape (Sellotape) running along its longitudinal axis (Figure 2.2). Coverslips were cleaned by leaving them for 30 min in a saturated solution of 95 % ethanol and KOH and then air-dried for 30 min. A coverslip was placed on the sticky tape and firmly pressed down, ensuring there were no bubbles in the tape.

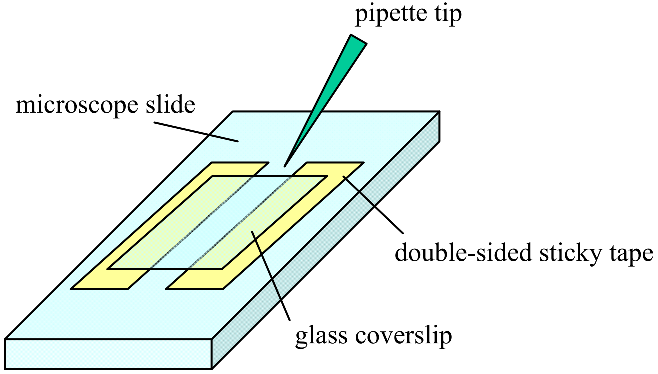

Figure 2.2: A tunnel slide used to view motile cells in an optical trap and fluorescence microscopy. The central chamber has a volume of approximately 5 μl.

Cells were either stuck to the coverlslip using poly-L-lysine (see section 2.3.5) or tethered via flagella (see section 2.3.6).

2.3.5 Stuck-cell bead assay

0.1 % (w/w) poly-L-lysine was flushed through a tunnel slide (all flushes were ~ 40 μl) and left for 15 min, followed by two flushes of motility buffer. Sheared motile cells in motility buffer were flushed through the slide and left to settle for 8 min. A flush of motility buffer removed loose cells and a polystyrene bead suspension (0.05 % w / w in motility buffer, Polybead® Polysciences) was left for 8 min to allow the beads to associate with filament stubs. A flush of motility buffer removed unadsorbed beads.

2.3.5.1 Home-built optical trap

The home-built optical trap used had a single focus 1064 nm wavelength laser (Elforlight, Northants, UK) which was broadened and steered into the back aperture of an oil-immersion microscope objective of N.A. 1.4 (CFI plan-fluor 100x, Nikon, Japan) to form the optical trap at the image plane. Any deviation of a trapped bead from the centre of the trap contributes a linear deflection to the transmitted laser which is re-collimated by a condenser lens and the back-focal-plane (BFP) of the condenser is imaged onto a quadrant photodiode (QPD) (Pin-SPOT 9DMI, UDT Sensors, CA, USA) to form a position detector. Thus positions in the trap can be precisely measured. Illumination for bright-field or DIC imaging was provided by a fibre-coupled tungsten halogen bulb which was filtered to remove short-wavelength light that damages biological specimens.

2.3.6 Tethering cells for fluorescence microscopy

To tether cells by their flagella, 5 µl of 1 / 80 dilution of stock anti-FliC antibody (a gift from David Blair, University of Utah) in PBS was added to 100 µl of sheared motile cells and ~ 10 µl of this suspension was added to a tunnel slide and left for 20 min, after which, motility buffer (containing 50 µg/ml Cm) or 10 % T-broth in motility buffer was flushed through to remove loose cells.

Tunnel slides for fluorescence microscopy had two modifications: (1) clear nail varnish was used instead of double-sided sticky tape to fix the coverslip to the glass slide because sticky tape leached fluorophores, (2) (when required) anti-FliC antibody was used to tether cells via their flagella to the coverslip to monitor cell body rotation.

A 1: 1000 suspension of 202 nm diameter latex beads (Polysciences Europe, Eppelheim, Germany) were flushed through the tunnel slide and left for 2 min to allow them to settle onto the coverslip, (to mark the coverslip) and finally washed with excess buffer. Where required, cells were incubated with chloramphenicol (50 µg / ml) for 30 min prior to shearing (once they had reached an OD_{600} 0.8).

2.3.6.1 TIRFM apparatus

A home-built inverted fluorescence microscope was used, with x100 Plan Fluor 1.45 NA oil-immersion objective lens (Nikon UK Ltd., Kingston-upon-Thames, UK) and an xyz nano-positioning stage (E-503.00, Physik Instrumente, Karlsruhe, Germany).

Brightfield illumination used a fibre-coupled tungsten-halogen lamp; laser excitation a fibre-coupled TEM00 plane-polarized multi-line argon-ion laser (Melles Griot, Rochester, NY), filtered (laser-line, 488 nm), expanded x3 and focussed onto the back-focal-plane of the objective lens via a dichroic mirror (505 nm long-pass). Controlled lateral movement of the focus equated to rotation of the emergent angle from the objective allowing switching between epifluorescence and TIRF. The field width was ~60 µm, intensity ~25 W cm^{-2}. An independent separately-shuttered excitation path allowed a proportion of the laser light to be focussed in the sample plane to a width ~0.5 µm, intensity ~130 kW cm^{-2}. Fluorescence emission was passed through the dichroic mirror, an emission filter (535 nm band-pass) and a notch rejection filter (488 nm), and imaged by a 128 x 128 pixel, cooled, back-thinned electron-multiplying charge-coupled-device camera (iXon DV860-BI, Andor Technology, Belfast, UK), ~50 nm per pixel magnification.

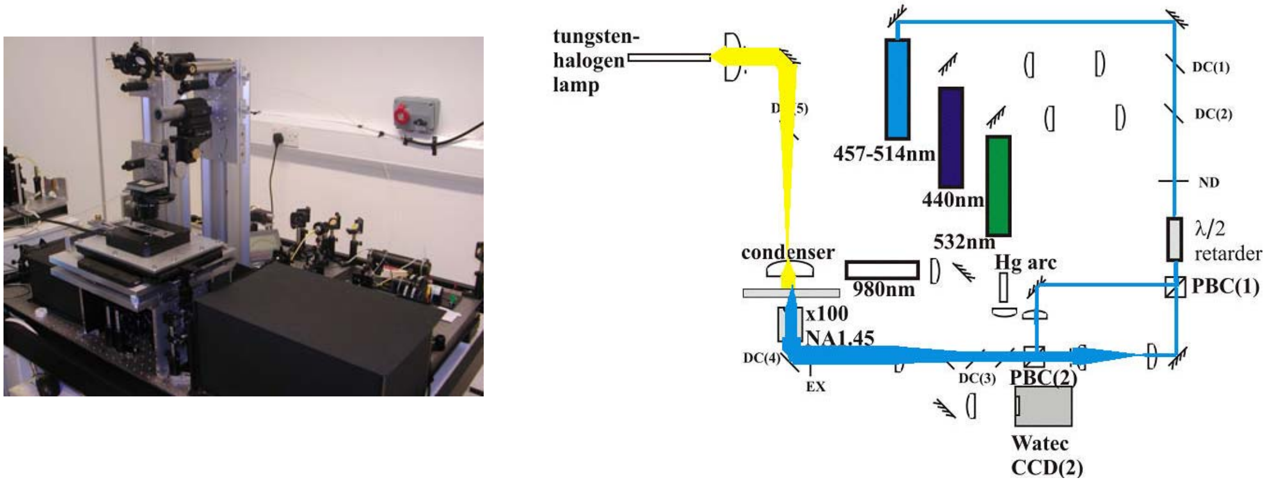

Figure 2.3: TIRFM apparatus. (A) A photo of the TIRFM apparatus used in this study, in the Biophysics Department, Clarendon Laboratory, University of Oxford. (B) A diagram of the TIRFM set-up used in this study.

2.3.7 Transmission Electron Microscopy (TEM)

Motile sheared cells of strain RB6 were resuspended in motility buffer and mixed with an equal volume of beads (0.75 μm diameter, 0.05 % w/w in motility buffer, Polybead® Polysciences) and left for 10 min in a microfuge tube. Cells were fixed and negatively stained onto EM grids by incubating 50 μl of cell suspension on the grids and leaving them for 1 h. EM grids were placed on 30 μl droplets of uranyl acetate and left for 30 s (uranyl acetate is an electron dense stain that deflects electrons and stains around the specimen). EM grids were placed on 50 μl droplets of distilled water to remove excess uranylacetate and placed onto formovar carbon coated grids for TEM observation using a Phillips 400 electron microscope..

3 Mutant MotB stator complexes

3.1 Resurrection experiments

Block and Berg[183] induced expression of wild type *motB* in a mutant *motB** background and observed torque-restoration (‘resurrection’) in approximately seven steps (each step corresponded to the successive incorporation of a stator complex into the motor). Recent resurrection experiments[192] expressed *motA* in a mutant *motA* background and demonstrated that the complete motor contains at least 11 stator complexes. They also observed two different rotation rate step sizes, approximately one-eighth (‘full step’) and one-sixteenth (‘half-step’) of the maximum rotation rate, suggesting that stator complexes may incorporate as dimers, in which each monomer can generate torque independently (see section 1.7.3 for more detail about resurrection experiments).

3.2 De-resurrection experiments

In order to quantify the number of MotBs in the motor and determine whether stator complexes exists as dimers or monomers, mutant MotB* was expressed from an inducible plasmid in a wild type background. The motor rotation rate was expected to slow down in a step-wise manner as successive mutant stator complexes incorporated into the motor. The number and size of step-wise decreases in rotation rate would indicate the number and nature of stator complexes in the motor and indicate if MotB*s incorporate as dimers or monomers. Theoretically, a full-step decrease in rotation rate would correspond to the incorporation of a stator complex containing two mutant MotB*s. A half-step decrease in rotation rate would correspond to the incorporation of either a dimer stator complex containing one mutant MotB* and one wild type MotB, or the incorporation of a stator complex monomer containing a single mutant MotB*.

3.3 Mutant MotB*s

MotB* with the critical amino acid Asp-32 (D32) mutated to a different amino acid was expressed from an inducible plasmid (pJZ18) in a wild type background. D32 lies at the cytoplasmic face of the MotB transmembrane segment (Figure 3.1) and has been shown play a critical role in proton-conductance and torque-generation[101]. Various D32 substitutions were tested for their effect on torque-generation to determine what properties of this amino acid are important for function.

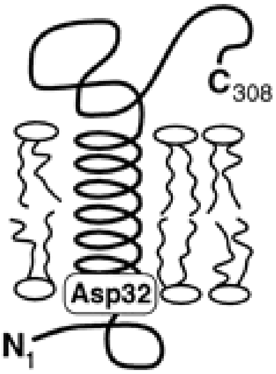

Figure 3.1: Membrane topology of MotB showing the conserved acidic residue Asp-32 (D32) which lies on the cytoplasmic face of the transmembrane segment. Taken from [168].

Substitutions of D32 with amino acids similar in charge and structure to aspartate (D) were expected to have less of an effect on motor rotation rate than substitutions with those of an opposite charge or highly different side chain structure. D32 was replaced with alanine (A), glutamate (E), glycine (G), asparagine (N), arginine (R) and tryptophan (W) (Figure 3.2).

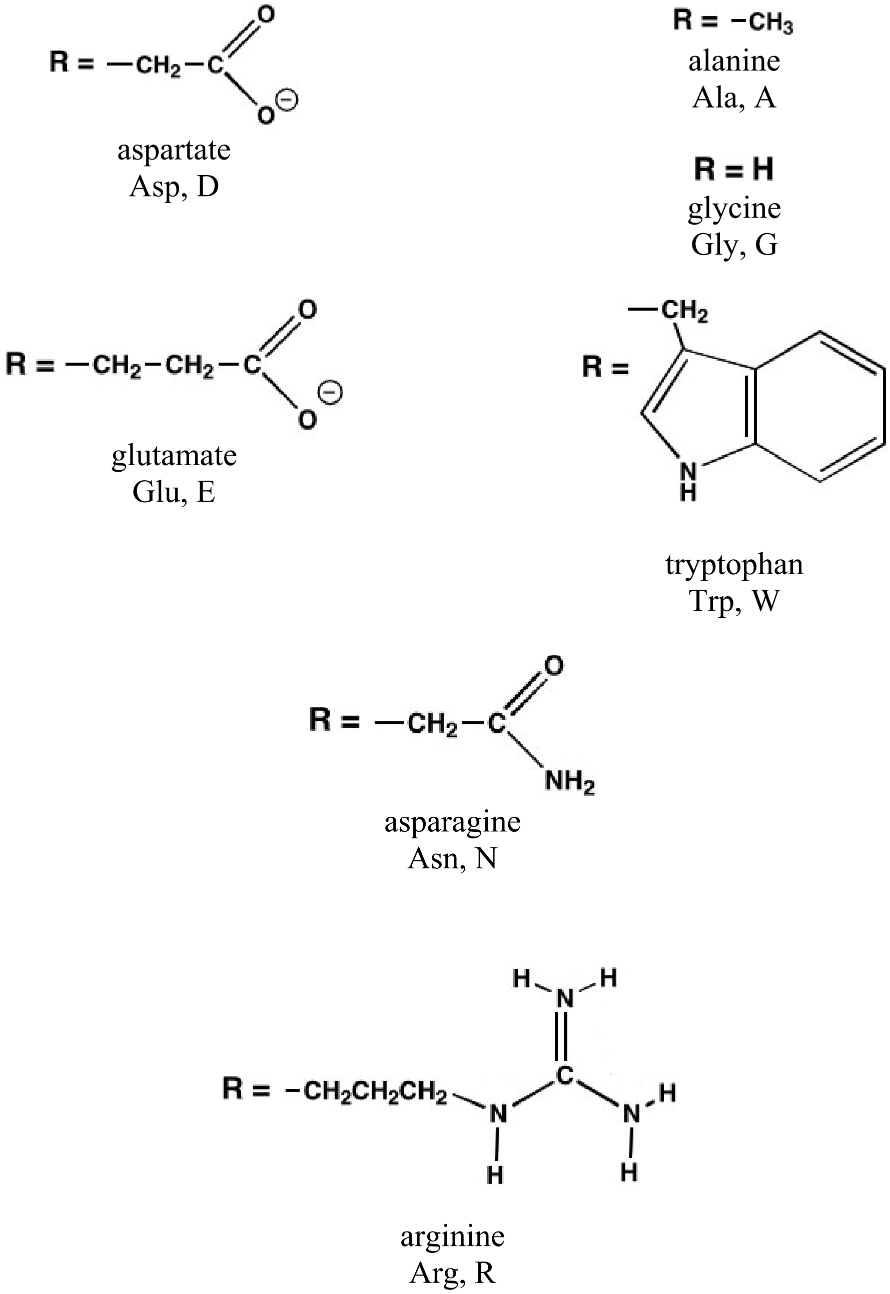

Figure 3.2: Structures of the amino acids which were substituted for D32 of MotB.

Aspartate (D) is an acidic, negatively charged amino acid with a side chain pK_a of 3.9. Glutamate (E) is closest to aspartate both in terms of charge and size; the negatively-charged side chain is one carbon larger than aspartate and has a pK_a of 4.1. The D32E substitution was not expected to affect proton-conduction owing to the negative charge, but might affect channel conformation due to the slightly larger side chain.

Asparagine (N) is an uncharged derivative of aspartate. The D32N substitution might affect proton-conduction because of the neutral charge but possibly not affect stator channel conformation due to its similarity in size to aspartate.

Arginine (R) is a basic, positively charged amino acid, with a side chain pK_a of 12.5, which is capable of undergoing very low levels of protonation. Tryptophan (W) is a large, aromatic hydrophobic amino acid which was expected to affect motor rotation severely as a result of its large size and neutral charge. Alanine (A) and glycine (G) are small hydrophobic amino acids; D32A and D32G substitutions were predicted to affect proton-conduction owing to their neutral charge, but not conformation of the stator channel owing to their small size. Table 3.1 summarises how these amino acids differ from aspartate (D) in terms of size and protonatability.

Amino acid	**Size relative to aspartate**	**Protonatable?**	**pK_a of side chain R**
D	-	YES	3.9
A	smaller	no	4.1
E	bigger	YES	-
G	smaller	no	-
N	same	no	-
R	bigger	YES	12.5
W	much bigger	no	-

Table 3.1: A summary of how the various amino acid substitutions of D32 of MotB differ to aspartate (D) in terms of size and protonatability.

3.4 Experimental strains

Strain RB6 (Δ*cheY fliC726*) carries a Δ*cheY* deletion which reduces motor switching and a chromosomal mutation in *fliC* (allele *fliC726*) with a non-flagellate phenotype. RB6 was transformed with pFD313 (Cm^R), a plasmid carrying $fliC^{st}$ encoding 'sticky' flagellin which has a deletion in the central region of the protein (residues 245-301 of 497 were replaced by a 6-residue linker), exposing the hydrophobic core, rendering the protein and hence the filament 'sticky' to surfaces such as glass. 'Sticky' filaments are still functional; $FliC^{st}$ expressed from pFD313 confers approximately 50 % of wild type swarming[228].

RB6 pFD313 was transformed further with pJZ18 (Amp^R, a derivative of pTM30 [234]) expressing either mutant MotB* (D32A, E, G, N, R, and W) or wild type (D32wt) under the control of a *tac* promoter. pJZ18 also carried the *lacI* gene encoding the *lac* repressor (a gift from David Blair, University of Utah).

3.5 Swarm plate analysis of RP437 expressing mutant MotB*

To test the negative dominance of mutant MotB*, wild type strain RP437 was transformed with pJZ18 carrying either wild type or mutant *motB**. Strain RB6 could not be tested on swarm plates because it carries a Δ*cheY* deletion rendering it non-chemotactic. Strains were grown in LB-broth with shaking until stationary phase at 30 ºC; 5 µl of culture was inoculated onto soft-agar swarm plates containing Amp and 100 µM IPTG; plates were incubated at 30 ºC for 10 h.

Strains expressing mutant MotB* from pJZ18 had slower swarm rates than the strain expressing D32wt (Figure 3.3A), indicating that these mutant MotB*s were dominant-defective proteins capable of incorporating into the motor. Wild type MotB was still expressed from the chromosome in all strains expressing mutant MotB* from pJZ18 (see section 3.6 for western blot analysis of MotB* expression). The magnitudes of the dominant-negative effects were quantified by assaying the mutants on swarm plates in triplicate (Figure 3.3B); the ascending order of negative dominance of the mutant MotB*s was: G < N < A < W < E < R.

Interestingly, cells expressing the MotB D32E and D32R substitutions had the fastest swarm rates of the mutants tested; glutamate and, to a lesser extent, arginine are capable of undergoing protonation and de-protonation (Table 3.1); it is possible that these substitutions allowed a low level of proton-conduction through the stator complex, powering rotation of the motor. Alternatively, and probably more likely, MotB D32E and MotB D32R may have had lower affinities for the motor and therefore did not displace wild type MotB.

Photos taken at 10 h

A

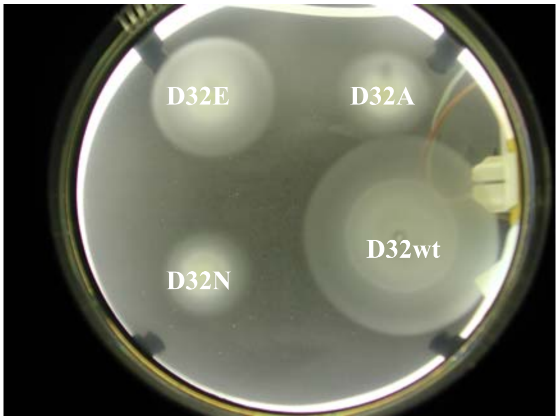

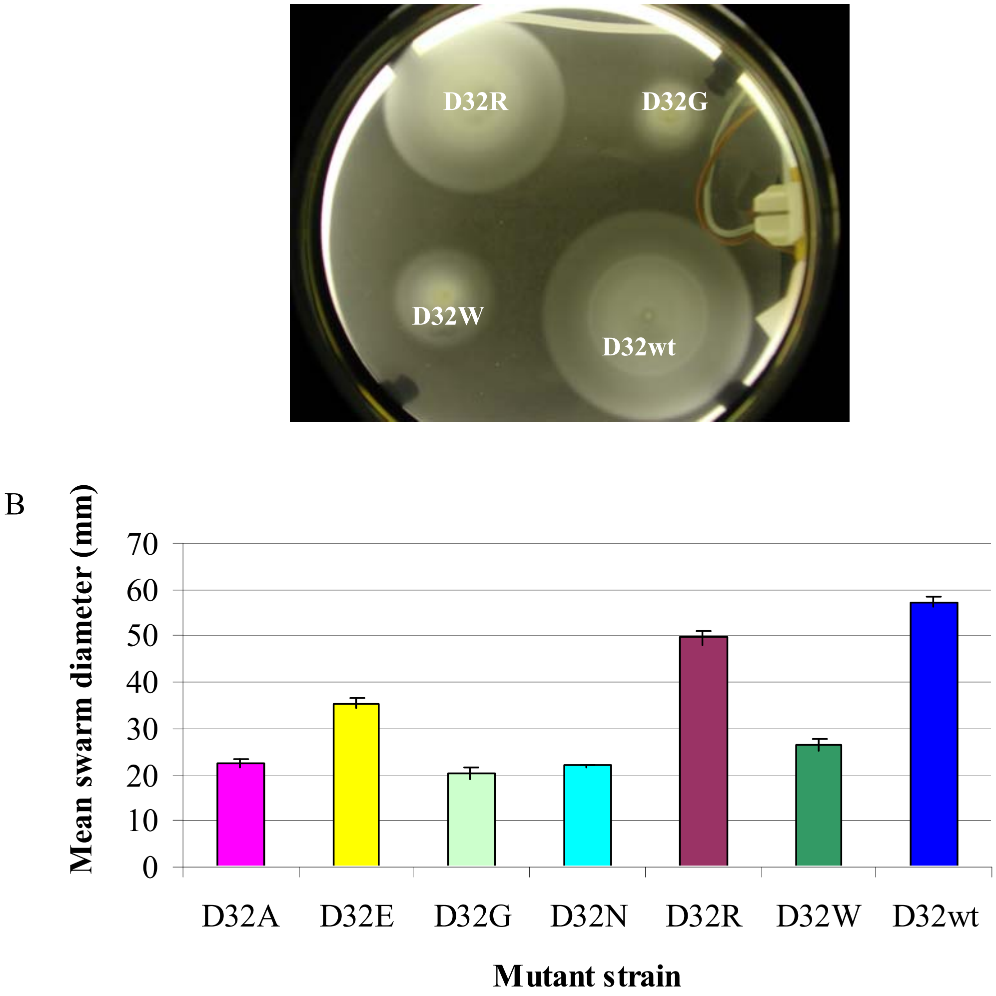

Figure 3.3: Swarm plate analysis of strain RP437 expressing mutant MotB* from pJZ18. (A) Swarming phenotypes of RP437 pJZ18 MotB D32* strains in the presence of 100 µM IPTG. Cells expressing MotB D32wt were inoculated onto both plates and plates were photographed 10 h at 30 ºC. (B) Mean swarm diameters for RP437 pJZ18 MotB D32* strains. Swarm plates were performed in triplicate and standard error bars are shown.

3.5.1 Growth rates of RP437 expressing mutant MotB*

Swarm plates rely upon both growth and taxis so it was necessary to determine whether the growth rates of strains expressing various MotB D32* differed.

0.5 ml of stationary phase culture of each RP437 pJZ18 MotB D32* strain was sub-cultured into 50 ml of LB-broth, and grown with shaking at 37 ºC. The OD $_{600}$ of a 1 ml sample of each culture was measured approximately every hour (three separate cultures of each strain were measured). There was no observable difference in growth rates between different strains (data not shown).

3.6 Confirming mutant MotB* expression

Western blotting was used to verify mutant and wild type MotB expression from pJZ18. All strains (RB6 pJZ18 MotB D32A, E, G, N, R, W and wt) were grown in T-broth containing 500 μM IPTG with shaking at 30 ºC until an OD$_{600}$ 0.6. 1 ml of culture was centrifuged and resuspended in 100 μl of SDS-PAGE loading buffer (Appendix A). Cell lysates were subjected to SDS-PAGE, blotted onto membranes and hybridised with 1 / 1000 dilution of anti-MotB antibody (a gift from David Blair, University of Utah).

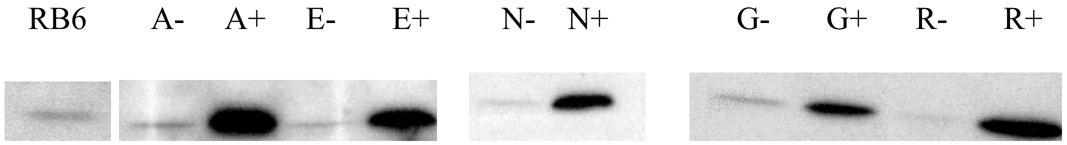

Figure 3.4: Anti-MotB western blot of cell lysates from strains grown in the presence (+) and absence (-) of 500 μM IPTG. Cell lysates were subjected to SDS-PAGE, blotted and probed with a 1 / 1000 of anti-MotB antibody. Cell lysate of the parental strain RB6 was subjected to western blotting to determine the chromosomal expression levels of wild type MotB. Cell lysates of mutant strains expressing MotB D32A, E, N, G and R are shown; strains expressing MotB D32W and D32wt displayed similar results (data not shown). A = RB6 pJZ18 MotB D32A, E = RB6 pJZ18 MotB D32E etc.

As Figure 3.4 shows, the chromosomal level of expression of wild type MotB in the parental strain RB6 was approximately equal to the level of MotB expression in strains carrying pJZ18 MotB D32* in the absence of IPTG, indicating that expression from pJZ18 was tightly regulated. The cellular levels of MotB in strains carrying pJZ18 grown in the presence of IPTG was significantly higher than the cellular levels of MotB when grown without IPTG, confirming mutant MotB* over-expression from pJZ18.

The abundance of cellular mutant MotB* may have allowed mutant MotB* to form a complex with newly expressed MotA because of the high ratio of mutant-to-wild type MotB, regardless of affinities for the motor. However, MotA and MotB are known to be transcriptionally and translationally coupled, so it is possible that mutant MotB* (expressed from pJZ18) had to rely upon diffusion and random collision with MotA in the membrane in order to form a complex. Hence, the number of mutant stator complexes may have been significantly lower than the number of wild type stator complexes even though the cellular levels of mutant MotB* were much higher than the cellular levels of wild type MotB.

3.7 Rotation rates of RB6 expressing mutant MotB*

Motile cells were sheared and cell bodies were stuck to the glass surface of a tunnel slide using poly-L-lysine. Polystyrene beads (0.75 μm diameter) were adsorbed to truncated filament stubs which acted as markers of rotation in a weak optical trap. The position of the bead was measured using back-focal plane laser interferometry[235], as described[236]. In the case of extended measurements (up to 2 h), a feedback system to a piezo-electric stage was used to compensate for drift.

Electron microscopy was used to visualise and determine the length of sheared flagellar filaments. Figure 3.5 shows a sheared RB6 pFD313 cell with a 0.75 μm diameter bead adsorbed (probably) to a truncated filament. Sheared flagellar filaments averaged between 1.5 – 2 μm in length.

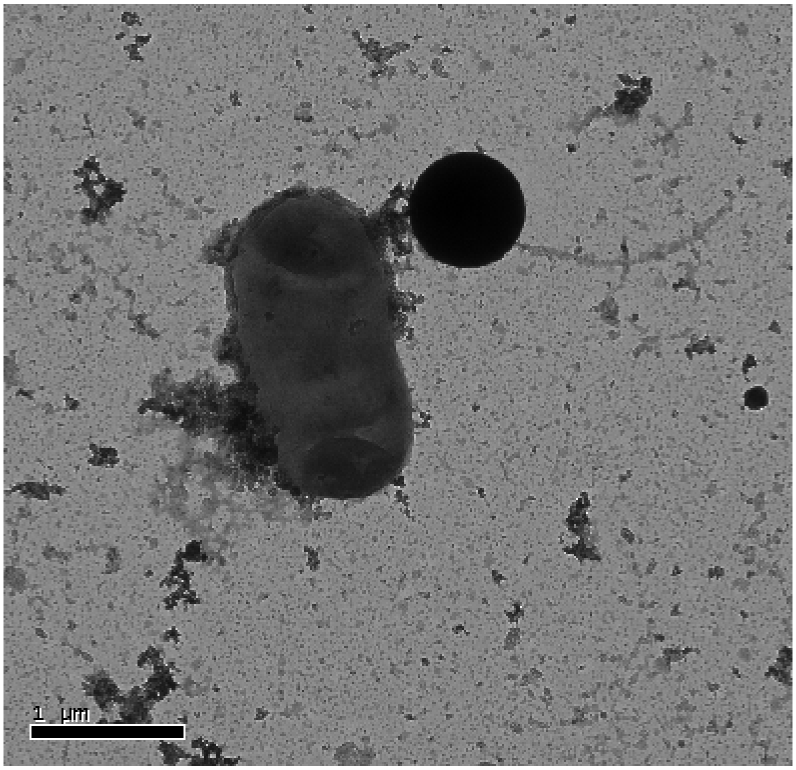

Figure 3.5: An electron micrograph of an RB6 pFD313 cell with a 0.75 diameter bead adsorbed (probably) to a sheared flagellar filament.

3.7.1 Analysis programmes

Rotation rates were obtained from power-spectra of combined (x, y) data as described[191], using data windows of length 1 s beginning at intervals of 0.1 s and multiplied by a 'flat-top' window to provide weighting towards the centre. This gave a rotation rate resolution of 1 Hz.

3.7.2 Determining an optimal concentration of inducer

Strains were grown with shaking at 30 ºC in T-broth supplemented with the inducer IPTG (0, 10, 50, 100, 300 and 500 µM) to determine what concentration of IPTG could result in stopped motors. Strains expressing MotB D32A, R and W (and D32wt) were tested as they had varying swarm rates (see section 3.4). Once an OD $_{600}$ 0.6 was reached, cells were attached in tunnel slides for a "stuck-cell" bead assay (0.75 µm diameter bead) to measure the percentage of motile cells and bead rotation rates (adsorbed to truncated flagellar filaments). All buffers used in the tunnel slides contained the appropriate concentration of IPTG. The percentage of motile cells (% spinning) was calculated as the ratio of stuck cells with adsorbed spinning beads compared to the total number of stuck cells with beads adsorbed (spinning and not spinning) in approximately 10 - 20 fields of view, depending upon the extent of cell body fixing, (which equated to 50 - 100 stuck cells) (Figure 3.6A). Rotation rates of beads adsorbed to cells grown in various concentrations of IPTG were measured using an optical trap (Figure 3.6B).

A

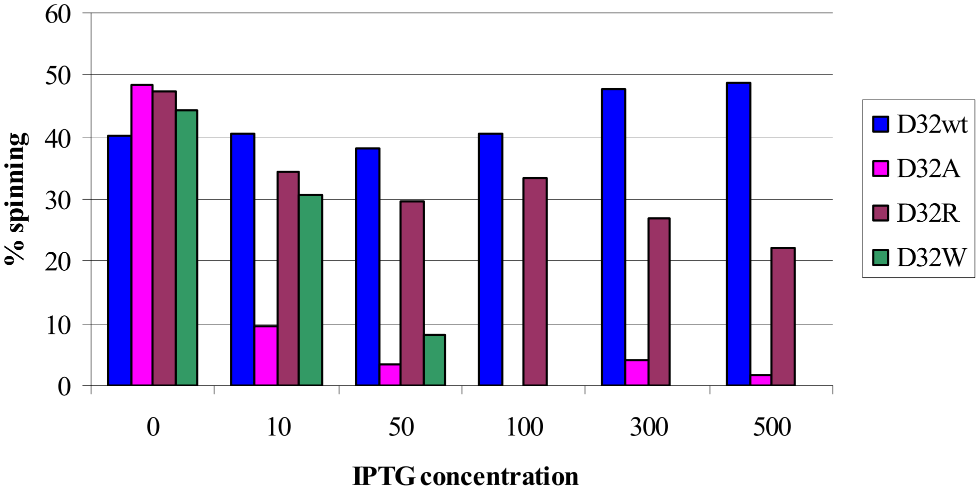

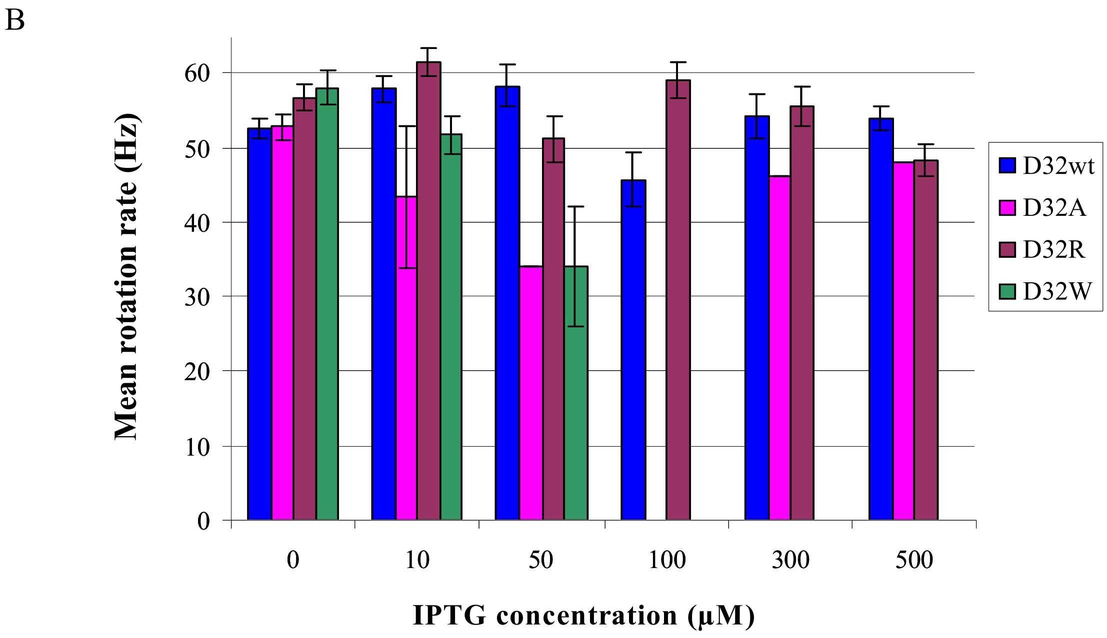

Figure 3.6: Determining of an optimal concentration of IPTG sufficient to result in stopped motors. Four strains were tested (all RB6 pJZ18 MotB D32*): three mutants (D32A, R and W), and the wild type (D32wt). Each strain was grown in the presence of various concentrations of IPTG until an OD $_{600}$ 0.6. Cells were stuck in a tunnel slide using poly-L-lysine and beads of 0.75 μm diameter were used as markers of rotation in a weak optical trap. (A) The percentage of motile cells was calculated as the ratio of cells with an adsorbed spinning bead compared to the total number of stuck cells with beads attached, spinning and not spinning. (B) Mean bead rotation rate of cells grown in various concentrations of IPTG. Bead rotation rates on individual cells were measured in an optical trap and averaged for the population. Standard error bars are shown.

The percentage of cells with a rotating bead attached on cells of the strain expressing MotB D32wt was approximately constant when grown in various concentrations of IPTG. However, the percentage of motile cells expressing mutant MotB* from pJZ18 (D32A, R and W) changed in an IPTG-dependent fashion. High concentrations of IPTG resulted in fewer motile cells. Cells expressing MotB D32W were non-motile at IPTG concentrations of 100 μM and higher; those expressing MotB D32A displayed very poor motility at high concentrations of IPTG. Surprisingly, whilst the percentage of motile cells expressing MotB D32R decreased in an IPTG-dependent manner, at 500 μM IPTG, the percentage of motile cells was approximately half the percentage of motile cells expressing MotB D32wt. MotB D32R may have had a much lower affinity for the motor than MotB D32A and D32W. The motor may have had a preference for wild type stator complexes and only occasionally incorporated a MotB D32R stator complex because of the high ratio of mutant-to-wild type MotB (presumably mutant and wild type stator complexes compete for binding in the motor). A lower affinity for the motor could be explained by the introduction of a positive charge into the stator complex which may distort the complex structure significantly or affect the ability of MotB D32R to form a complex with MotA.

Interestingly, even though the percentage of motile cells expressing mutant MotB* decreased with increasing IPTG concentration, the bead rotation rates of cells expressing mutant MotB* and wild type MotB were similar and independent of IPTG concentration. Motors in cells expressing mutant MotB* from pJZ18 were expected to contain both a mixture of wild type and mutant stator complexes because wild type MotB was also expressed from the chromosome. Motors with higher numbers of mutant stator complexes were expected to have lower rotation rates than those with higher numbers of wild type stator complexes. However, the absence of slow and intermediate rotation rates suggests that the motor may function only if all the stator complexes are wild type, and the presence of one mutant stator complex may be sufficient to lock the motor.

3.8 Over-expressing mutant MotB* prior to flagellar assembly

Rather than inducing mutant MotB* expression in a growing colony, IPTG was added before growth was initiated. This would result in high levels of mutant MotB* when cells emerge from the non-motile lag phase and start to synthesise flagella. Mutant and wild type strains (D32A, E, G, N, R, W and wt) were grown with shaking in T-broth containing 500 µM IPTG, at 30 ºC until an OD $_{600}$ 0.6. The stuck-cell bead assay was used to determine the percentage of motile cells. The percentage of cells with spinning beads is shown in Figure 3.7A. The average bead rotation rates for all strains are shown in Figure 3.7B.

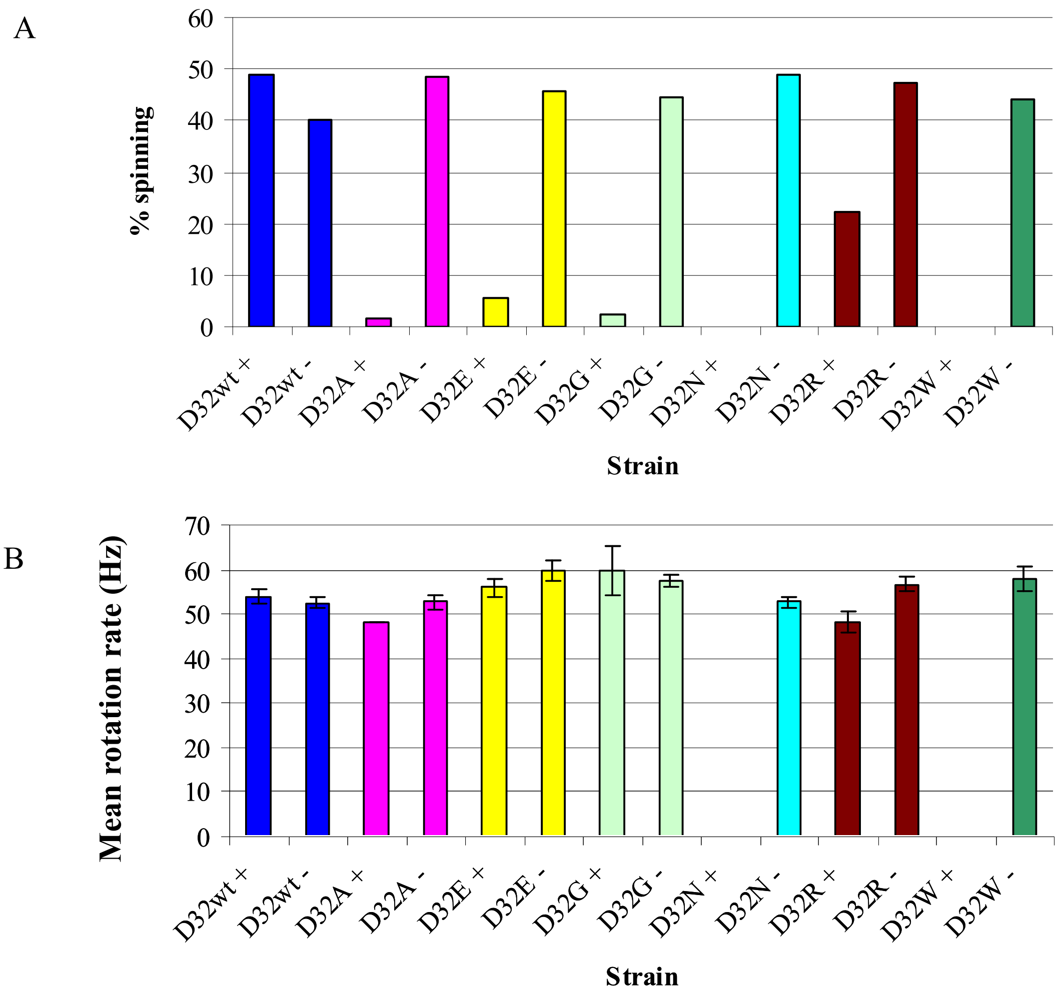

Figure 3.7: The effect of over-expressing mutant MotB* prior to flagellar assembly. Cells were grown in 500 µM IPTG until an OD $_{600}$ 0.6 and stuck in tunnel slides for a stuck-cell bead assay. (A) The percentage of cells with rotating beads (% spinning) is shown for all strains grown in the presence (+) and absence of (-) 500 µM IPTG. (B) The average bead rotation rates of each strain grown in the presence (+) and absence of 500 µM IPTG (-). Standard error bars are shown.

The percentage of motile cells of all strains expressing mutant MotB* grown in the presence of 500 µM IPTG was significantly lower than the percentage of motile cells grown without IPTG. Strains expressing MotB D32N and D32W were completely non-motile, and very few motile cells were observed in strains expressing MotB D32A, E and G. These results once again indicate that all the mutant MotB* stator complexes tested in this study were capable of installing into the motor and exerting their dominant-negative effects. The percentage of motile cells expressing MotB D32R again was highest of the mutants tested, possibly because MotB D32R had a much lower affinity for the motor than the other mutant MotB*s tested.

3.9 De-resurrection experiments

Cells were grown in T-broth until OD_{600} 0.6 with shaking at 30 ºC, stuck in tunnel slides and exposed to 500 µM IPTG for 90 min. The rotation rate of a bead adsorbed to an individual cell of each strain was monitored during incubation with IPTG (performed in triplicate). Rotation rate was expected to decrease in a step-wise manner as successive mutant stator complexes incorporate into the motor. It was thought that this technique may allow slow and intermediate rotation rates not seen previously to be observed.

No cells expressing any mutant MotB* de-resurrected (slowed down) in a step-wise manner. The bead rotation rates of approximately one in three mutant and wild type cells decreased in a non-step-wise manner both in the presence and absence of 500 µM IPTG, suggestive of de-energisation. Figure 3.8 shows a bead rotation rate trace for a cell expressing MotB D32wt in the presence of 500 µM IPTG. IPTG was flushed through the tunnel slide at time zero. The decrease in rotation rate observed between 2000 s and 2800 s is not step-wise, suggestive of de-energisation rather than wild type stator complexes being replaced in the motor. Such putative de-energisation traces were observed in cells carrying pJZ18 MotB D32wt in the absence of IPTG, and in cells carrying pJZ18 MotB D32* both in the presence and absence of IPTG.

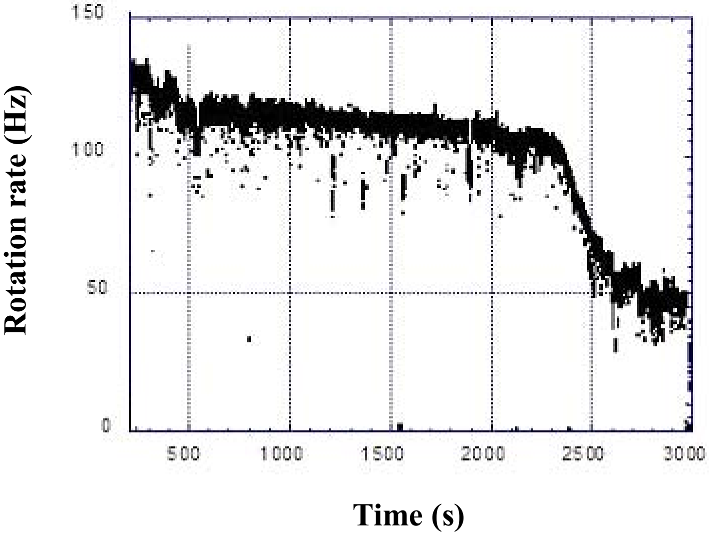

Figure 3.8: A bead rotation rate trace from a cell expressing MotB D32wt in the presence of 500 μM IPTG. IPTG was flushed though the slide at time zero. The rotation rate of a bead attached to an individual cell was monitored from 200 s until 3000 s. Bead rotation rate was measured by using a weak optical trap. The decrease in rotation rate is non-step-wise and suggestive of de-energisation.

Figure 3.9A shows a section of a 90 min trace of a cell again expressing MotB D32wt in the presence of IPTG. However, in this trace, the bead rotation rate fluctuated in a step-wise manner; which may correspond to wild type stator complexes transiently leaving the motor, resulting in a decrease in rotation rate. Step-wise fluctuations in bead rotation rate were also observed in strains expressing MotB* (Figure 3.9B) which may be the result of wild type stator complexes transiently leaving the motor, rather than the incorporation of mutant stator complexes into the motor, because of the absence of slow and intermediate rotation rates observed in the previous experiments. Step-wise fluctuations in bead rotation rate were observed in all strains (including D32wt) both in the presence and absence of IPTG.

Occasionally in traces of the bead rotation rate of cells expressing mutant MotB*, beads stopped rotating for approximately 1 - 20 s (Figure 3.9B). Such stops were seldom observed in bead rotation rate traces from the strain expressing MotB D32wt. These stops may be the result of a mutant stator complex incorporating into the motor, transiently locking the motor, until it leaves or is displaced by a wild type stator complex. Alternatively, albeit unlikely, these stops may be the result of the bead transiently attaching to the coverslip, or they may be pauses in rotation.

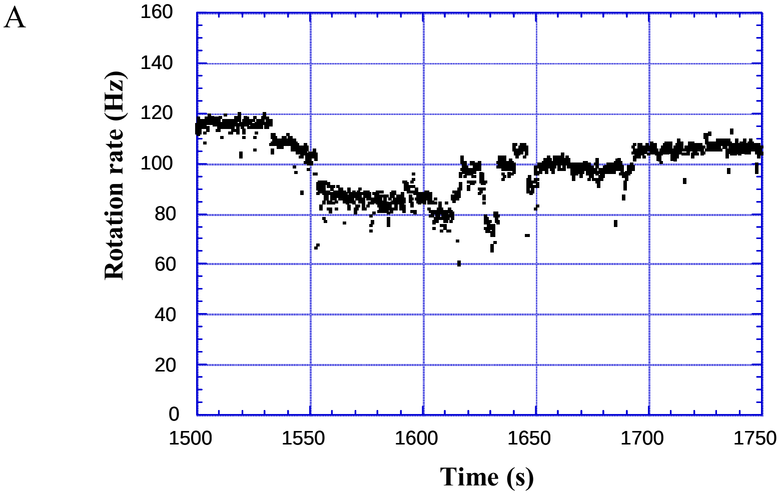

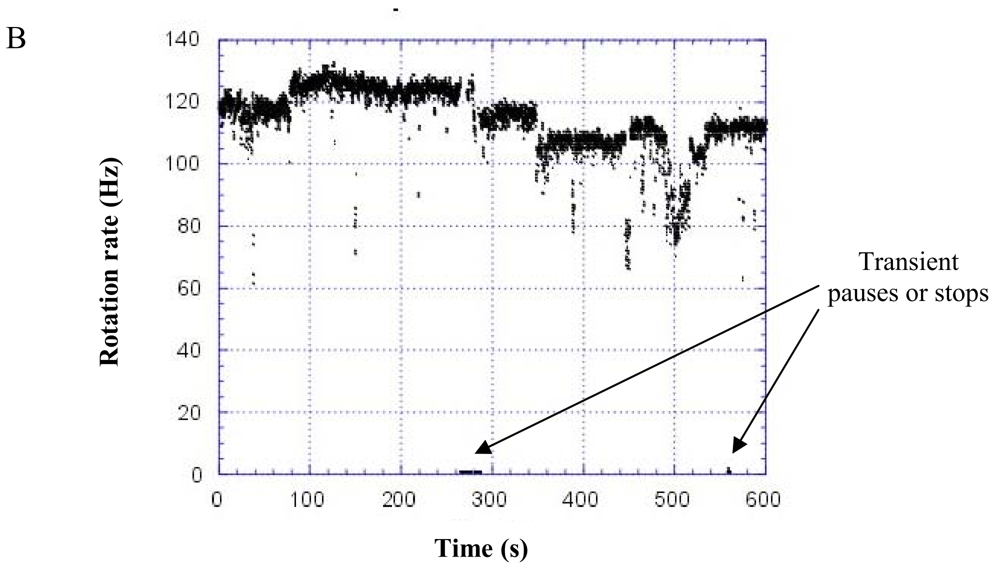

Figure 3.9: Step-wise fluctuations in bead rotation rate. (A) A section of a 90 min bead rotation rate trace of a cell (RB6) expressing MotB D32wt in the presence of 500μM IPTG. Only 1500 s to 1750 s of the trace is shown; the remainder of the trace up to 90 min is similar (not shown). (B) A bead rotation rate trace of a cell (RB6) expressing MotB D32A in the presence of 500μM IPTG. The rotation rate of a bead attached to a single cell was monitored from time zero. Transient pauses or stops in rotation are indicated.

Western blotting was used to verify mutant MotB* expression from pJZ18 during the 90 min incubation with 500 μM. All strains were grown in T-broth with shaking at 30 ºC until an OD $_{600}$ 0.6, then 500 μM IPTG was added to the culture. After 30 min, 1 ml of culture was centrifuged and resuspended in 100 μl of SDS-PAGE buffer, and a further 1 ml of culture was taken after 60 min incubation with IPTG. Cell lysates were subjected to electrophoresis, blotted and probed with a 1 / 1000 dilution of anti-MotB antibody. As shown in Figure 3.10, incubating cells in 500 μM IPTG for 30 min was sufficient to produce an excess of mutant MotB* compared to the chromosomal wild type MotB.

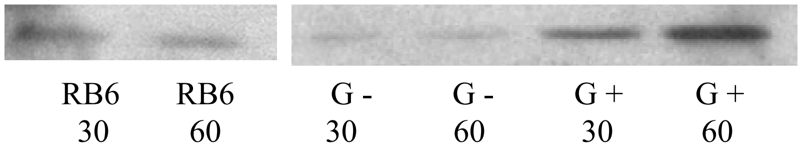

Figure 3.10: Anti-MotB western blot analysis of the cellular levels of MotB from strains incubated with IPTG for 30 and 60 min. Cell lysates from all mutant strains, D32wt and parental strain RB6 were subjected to SDS-PAGE, blotted and probed with 1 / 1000 dilution of anti-MotB antibody. 1 ml samples of cultures were harvested after 30 and 60 min growth in IPTG. Samples were also taken from cultures grown in the absence of IPTG after 30 min and 60 min. Western blots for strains RB6 and D32G are shown. All other mutants and D32wt displayed very similar results, data not shown. (-) = absence of IPTG, (+) = presence of 500 µM IPTG.

To eliminate the possibility of oxygen starvation, the tunnel slides were modified by attaching tubes at both ends of the central chamber allowing a continuous gentle flow of buffer over stuck cells. Once cells were stuck to the glass of the 'flow-cell', motility buffer containing 500 µM IPTG was continuously and slowly flowed through the chamber. As before, bead rotation rates of individual cells were monitored but no mutant cells de-resurrected in a step-wise manner, and again, putative de-energisation and step-wise fluctuations in bead rotation rate were observed.

To determine the effect of exposure to IPTG for 90 min on the cell population of each strain, the percentage of motile cells and rotation rates were measured for mutant (D32A, E, R and W) and wild type (D32wt) strains (Figure 3.11A, B).

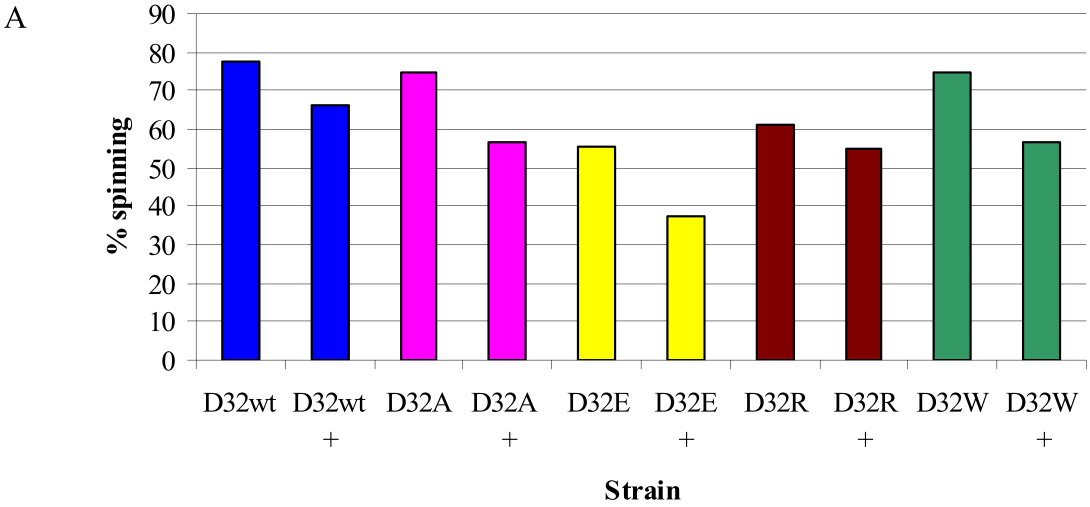

B

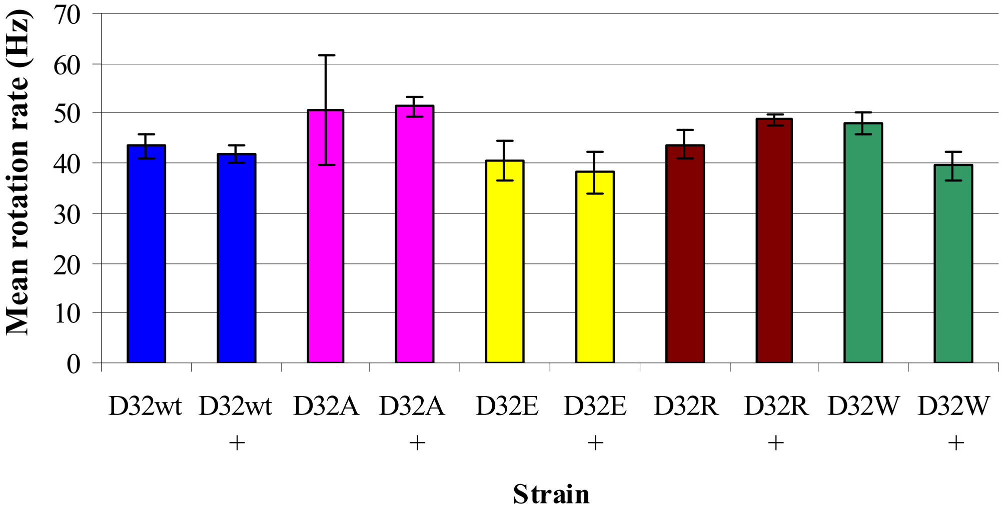

Figure 3.12: The effect of exposure to IPTG for 90 min in a flow-cell. Cells were grown in T-broth with shaking at 30 ºC until an OD $_{600}$ 0.6, and stuck in a flow-cell. 500 µM IPTG was continuously flowed through the flow-cell chamber for 90 min. (A) The percentage of motile cells of mutants (D32A, E, R, and W) and wild type (D32wt) were calculated prior to the flow of IPTG and after 90 min of continuous flow of 500 µM IPTG. (B) Average bead rotation rates of mutant and wild type strains measured prior to the flow of IPTG and after 90 min of continuous flow of 500 µM IPTG. Standard error bars are shown. (+) = IPTG, (-) = no IPTG.

The percentage of motile cells expressing mutant MotB* after exposure to 500 µM IPTG for 90 min in a flow-cell decreased slightly, but not significantly more than the decrease observed in cells expressing MotB D32wt. The reduction in the number of motile cells may have been the result of de-energisation as a result of nutrient starvation.

To eliminate the possibility of nutrient starvation, motility buffer in the flow-cell was supplemented with 10 % T-broth, and incubation with 500 µM IPTG was increased to 2 h. Individual bead rotation rates were monitored for 2 h during the exposure to IPTG. Again, no mutant cells de-resurrected in a step-wise manner. Albeit less frequently, putative de-energisation traces in rotation rate were observed for all strains both in the presence and absence of IPTG.

The percentage of motile cells in the flow-cell containing 10 % T-broth decreased slightly after 2 h in all strains (Figure 3.12A). The decrease in the percentage of motile cells expressing mutant MotB* were not significantly different to the decrease observed in cells expressing MotB D32wt. Once again, the average rotation rate of cells before and after exposure to IPTG / T-broth was not significantly different (Figure 3.12B).

The lack of any step-wise de-resurrections of any cell expressing mutant MotB* with or without 10 % T-broth, and the absence of any significant decrease in the percentage of motile cells suggests that either mutant MotB* had a lower affinity for binding to MotA in a pre-motor complex before the stator bound to the motor, or that mutant stator complexes themselves had a lower affinity for the motor.

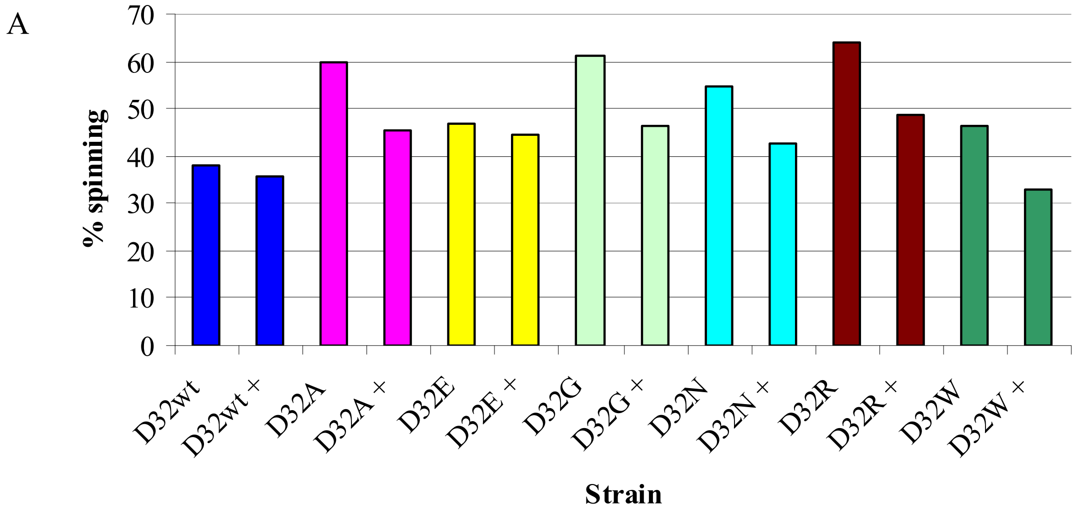

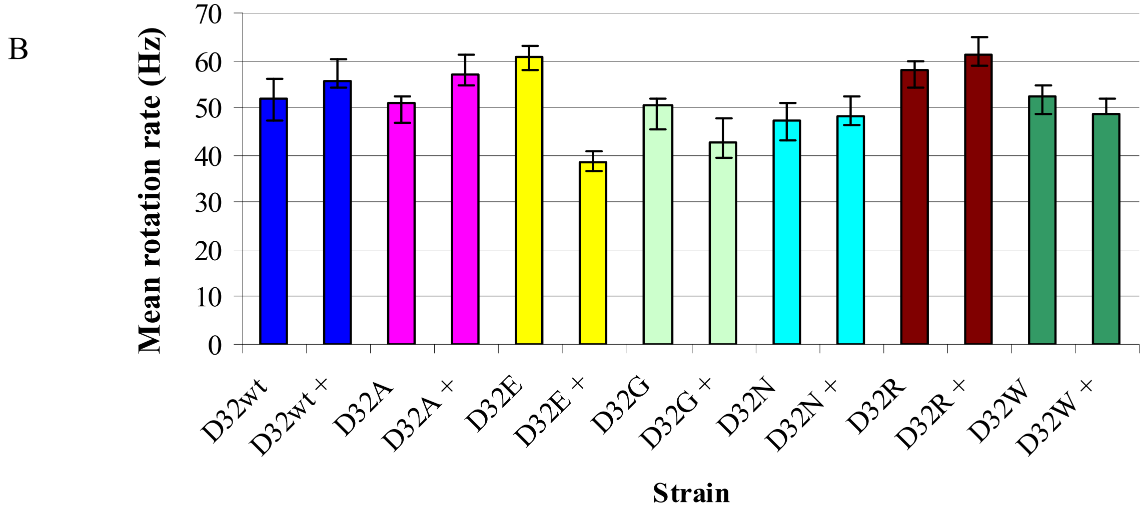

Figure 3.12: The effect of exposing each strain to 500 µM IPTG for 2 h in a flow-cell containing motility buffer supplemented with 10 % T-broth. (A) The percentage of motile cells for all strains were measured both prior to the flow of IPTG / T-broth and after 2 h. (B) Average bead rotation rates for all strains both prior to the flow of IPTG / T-broth and after. Standard error bars are shown.

3.10 Resurrecting a stopped (locked) motor

To determine whether it was possible to resurrect a stopped motor containing at least one mutant stator complex using wild type MotB, all strains were grown in 500 µM IPTG until an OD $_{600}$ 0.6 and stuck in a flow-cell. All buffers contained 500 µM IPTG. The percentage of motile cells of each strain and bead rotation rates were measured when cells were first attached in the flow-cell and after 90 min continuous flow of motility buffer (without IPTG) (Figure 3.13A, B).

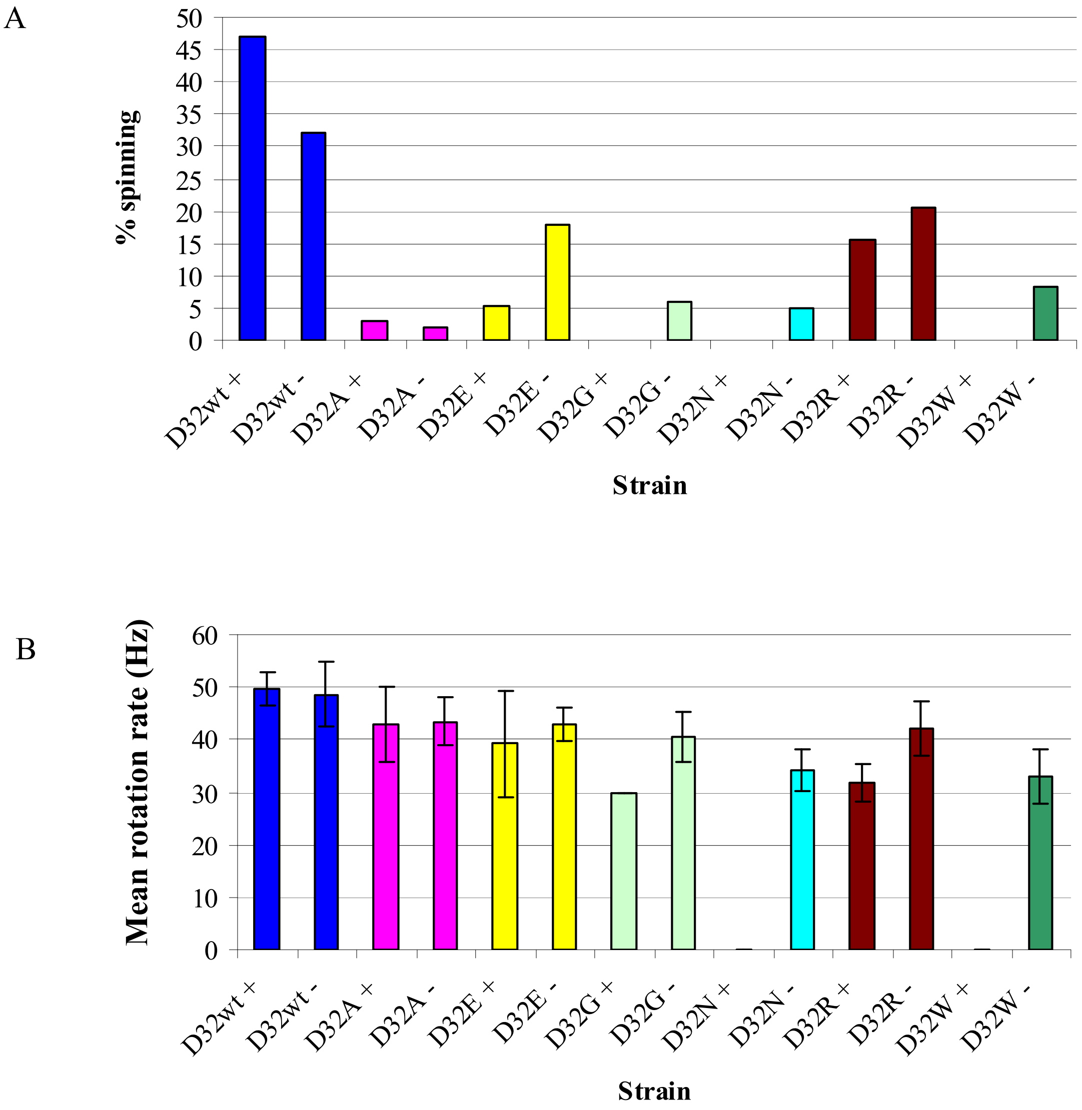

Figure 3.13: Resurrecting stopped (locked) motors. All strains were grown in T-broth containing 500 µM IPTG, with shaking at 30 ºC until an OD $_{600}$ 0.6. Cells were stuck to the glass of a flow-cell using the stuck-cell bead assay and the percentage of motile cells was measured when cells were in the flow-cell at time zero and after 2 h of continuous flow of motility buffer containing 10 % T-broth (and no IPTG). Standard error bars are shown.

The increase in the percentage of motile cells expressing mutant MotB* suggests that it was possible to resurrect a stopped motor containing mutant stator complexes with wild type MotB. Motors of non-motile cells may have stopped because they contained only one mutant stator complex or possibly several. The absence of slow and intermediate rotation rates in earlier experiments, and the brief pauses in rotation suggests that the presence of one mutant stator complex may be sufficient to paralyse a functioning motor. Hence, a stopped motor may resurrect if the single mutant stator complex is displaced from the motor by a wild type stator complex. Incubation in the flow-cell for 2 h in the absence of IPTG may be sufficient for excess mutant MotB* to be degraded; MotB has been shown to be degraded under conditions where it exceeded the levels of MotA during pulse-chase experiments, indicating that it requires MotA for stability[160]. The observation of a decrease in the percentage of motile cells expressing MotB D32 wt over the 2 h interval, suggests that the increase in the percentage of motile mutant cells from zero to over 20 % in some mutants, is significant. Cells expressing MotB D32E showed the largest increase in the percentage of motile cells of all mutant strains tested, possibly because MotB D32E was degraded faster than other mutant MotB*s, or it may have had a lower affinity for the motor. These results indicate that it is possible to resurrect a stopped (locked) motor containing at least one mutant stator complex and there is exchange at the motor, indicating that a synthesised motor is not necessarily a stable entity.

3.11 Integrating *fliC*st onto the genome

In order to investigate the stator complexes further through resurrection and de-resurrection experiments, a strain was created which carried *fliC*st on the chromosome; (previously expressed from pFD313) (see section 3.3). The removal of the plasmid expressing *fliC*st would produce a strain which could be transformed with two plasmids, each carrying independently tightly regulated wild type and mutant *motA* and *motB*.

fliC of strain YS34 (Δ*motA* Δ*motB* Δ*cheY* Δ*pilA fliC*::*Tn10*) was replaced with *fliC*st in the genomet. It was thought that the presence of Tn10 (Tet^{R}) within *fliC* on the chromosome of YS34 may make replacement of *fliC*::*Tn10* with *fliC*st difficult because the site of integration of the the large transposon (~ 9.3 kb) was unknown. Therefore, at the same time, strain RP5232 (a derivative of wild type strain RP437), which carries a Δ*cheY* deletion, also had *fliC* replaced with *fliC*st. The intention was then to delete chromosomal *motA* and *motB* in RP5232, which could be subsequently used as a background strain in resurrection and de-resurrection experiments.

3.11.1 Constructing a *fliC*st strain

Initially, *fliC*st was amplified by PCR from PS2589 (a gift from Jeffrey Stock, Princeton University) chromosomal DNA using primers PS *Sac*I and PS *Sbf*I which annealed approximately 100 bp from the start and end of *fliC*st respectively (Appendix B). The PCR product was digested with *Sac*I / *Sbf*I and ligated into pUC19 cut with *Sac*I / *Sbf*I; this construct was sequenced to ensure there were no PCR-generated errors. *fliC*st was subsequently excised, the ends were filled in, and ligated into suicide vector pKO3. This construct was called pKO3-PS-*fliC*st and was sequenced and transformed into YS34 and RP5232. However, multiple attempts to replace *fliC*::*Tn10* in YS34 and *fliC* in RP5232 with *fliC*st were unsuccessful.

To confirm that the *fliC* region of the chromosome of RP5232 had the same sequence as strain K-12 (and hence to ensure that there was homology between *fliC* on the chromosome of RP5232 and the suicide vector carrying *fliC*st), primers *fliC* 1 RP and *fliC* 2 RP, which annealed approximately 500 bp from the start and end of *fliC,* were used to amplify the *fliC* region of RP5232 by PCR (Appendix B); this PCR product was sequenced. The sequence of *fliC* of RP5232 was exactly the same as that in the genomic database for strain K-12. Why multiple attempts to replace *fliC* with *fliC*st on the chromosome of RP5232 failed is unknown; it is possible that this region of the chromosome had a high level of secondary structure, impeding recombination.

To determine where the transposon disrupted *fliC* in the chromosome of YS34, the *fliC* region was amplified by PCR using primers *fliC* 1 RP and *fliC* 2 RP, and sequenced. Tn10 was found to interrupt *fliC* approximately 100 bp from the 3' end. Hence, it was reasonable to assume that previous attempts to integrate *fliC*st onto the chromosome of YS34 failed because of the short region of homology (~ 100 bp) between the construct pKO3-PS-*fliC*st and the chromosome at the 5' end of the construct.

A new construct was created (Figure 3.14) in which the *fliC*st region of the PS2589 (not a derivative of RP437) chromosome was amplified using primers PS2589F and PS2589R (Appendix B), which annealed approximately 500 bp from the start and end of *fliC*$^{st.}$ This PCR fragment was digested with *Sph*I / *Sac*I, ligated into pUC19 and sequenced. The *fliC*st region was excised and ligated into *Sph*I / *Sac*I cut suicide vector pDS132 (generating pDS-*fliC*st) which was sequenced and transformed into electrocompetent RP5232 and YS34. This construct (pDS-*fliC*st) carried a larger region of homology which should enhance integration into the genome (see section 2.2.14.1 for detail on pDS132).

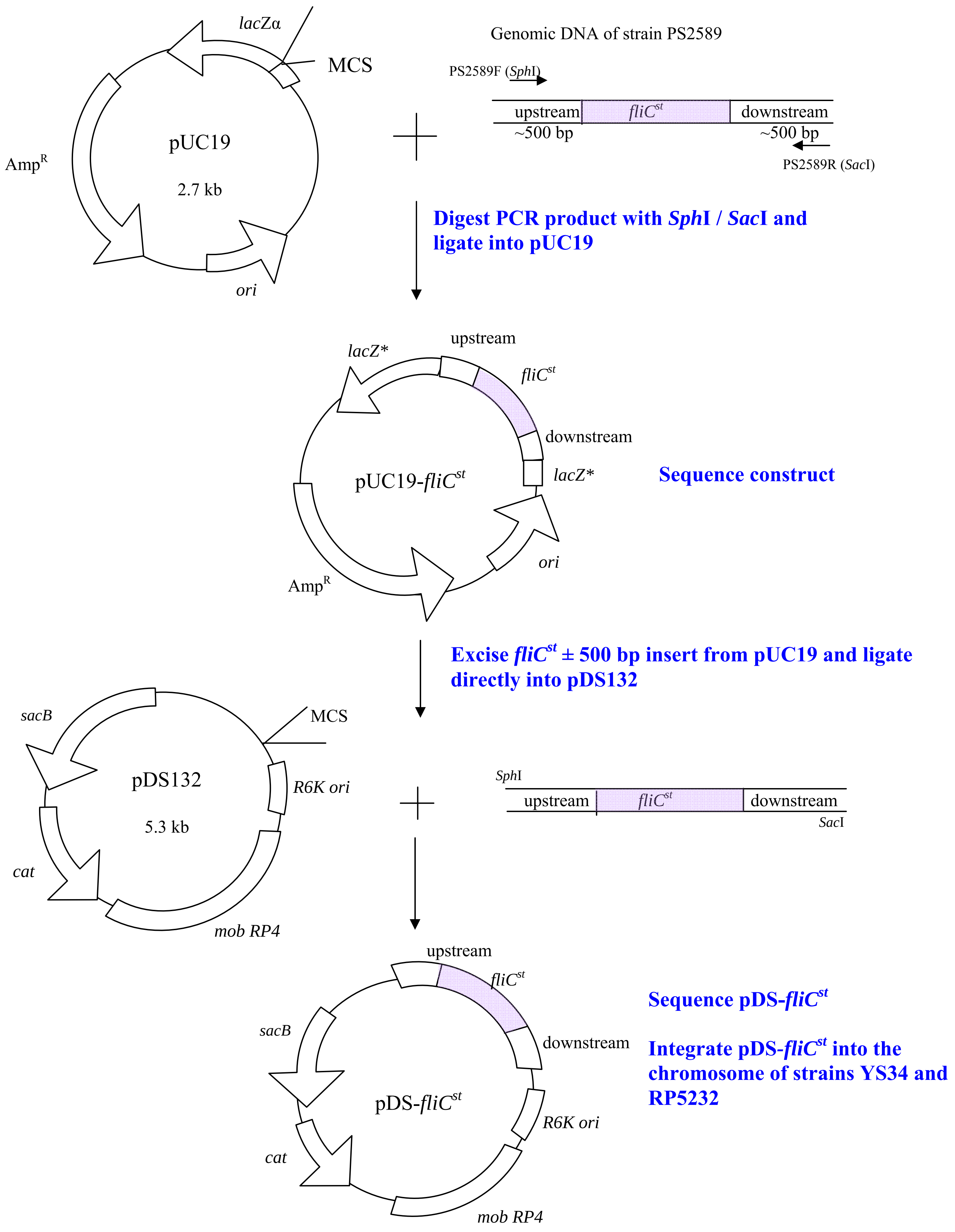

Digest PCR product with *Sph*I / *Sac*I and ligate into pUC19

Sequence construct

Excise *fliC*st ± 500 bp insert from pUC19 and ligate directly into pDS132

Sequence pDS-*fliC*st

Integrate pDS-*fliC*st into the chromosome of strains YS34 and RP5232

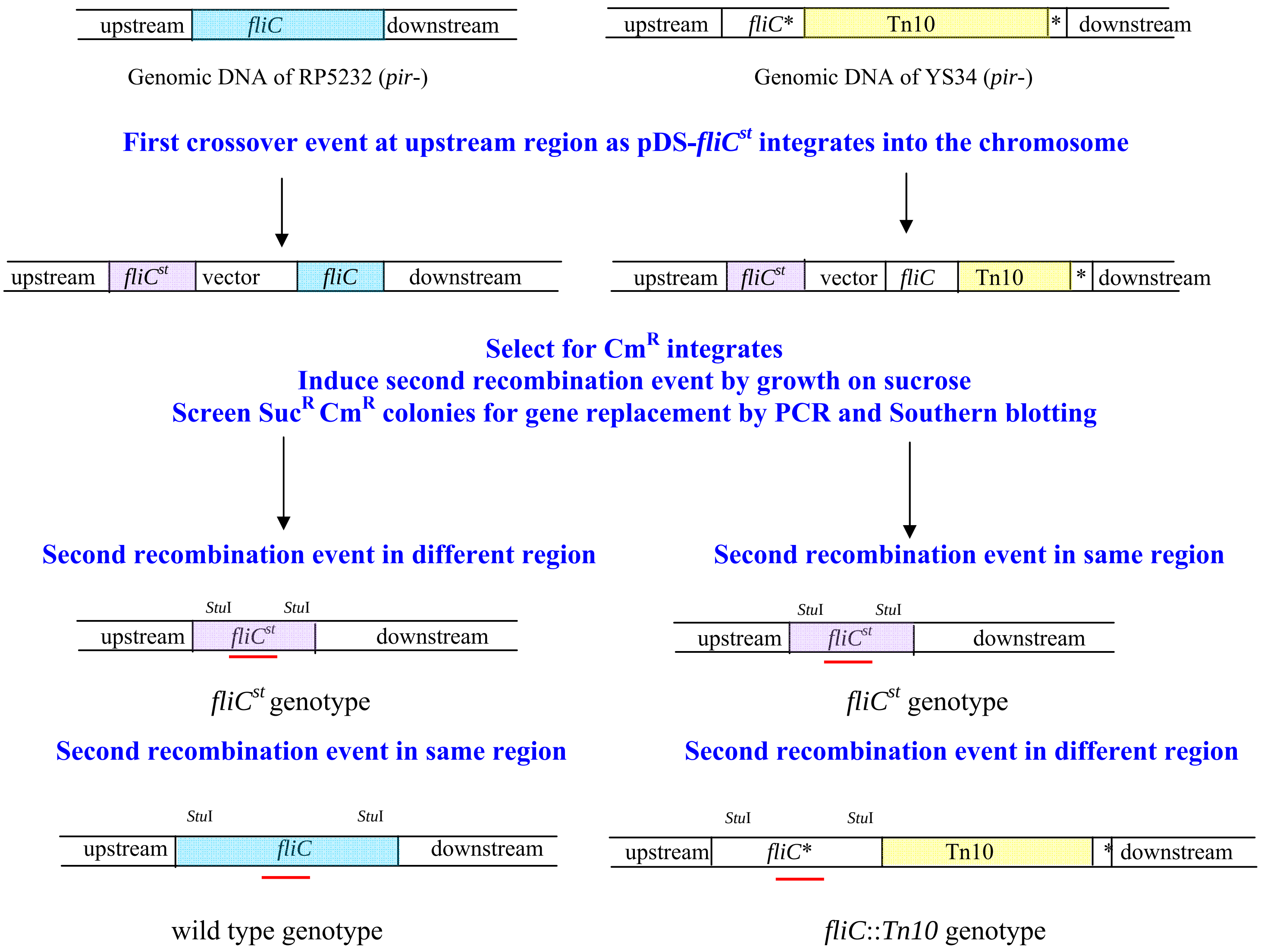

Figure 3.14: Integration of *fliC*st into the genome of strains YS34 and RP5232. The *fliC*st region of the chromosome of PS2589 was amplified by PCR and ligated into pUC19 for sequencing, excised and ligated into the suicide vector pDS132; the resulting construct was called pDS-*fliC*st. pDS-*fliC*st was transformed into YS34 (Δ*motA* Δ*motB* Δ*pilA* Δ*cheY* *fliC*::*Tn10*) and RP5232 (Δ*cheY*) where it integrated into the chromosome by double homologous recombination. *Stu*I sites are indicated; *Stu*I was used to digest chromosomal DNA preparations for Southern blotting to confirm replacement of *fliC* (or *fliC*::*Tn10*) with *fliC*st on the chromosome. Small red lines indicate the site of *fliC*st probe annealing during Southern blotting. MCS = multiple-cloning site; *cat* = Cm^{R}; *fliC** = *fliC* gene (- 100 bp); * = ~ 100 bp of *fliC*.

Cm^{S} Suc^{R} isolates of YS34 transformed with pDS-*fliC*st were replica-plated onto Tet / Cm / LBA and LBA plates to confirm loss of vector backbone and transposon from the chromosome, whilst Cm^{S} Suc^{R} isolates from RP5232 transformed with pDS-*fliC*st were replica-plated onto Cm / LBA and LBA plates.

Genomic DNA preparations of Cm^{S} Suc^{R} colonies from YS34 and RP5232 transformed with pDS-*fliC*st were digested with *Stu*I (sites are indicated on Figure 3.14). DNA digests were subjected to electrophoresis and Southern blotting. Membranes were hybridised with a 500 bp DIG-labelled DNA probe of the central region of *fliC*st cut from pDS-*fliC*st using *Fsp*I / *Nde*I. The site of probe annealing region is indicated on Figure 3.14. A positive control of pFD313 was also run on both gels.

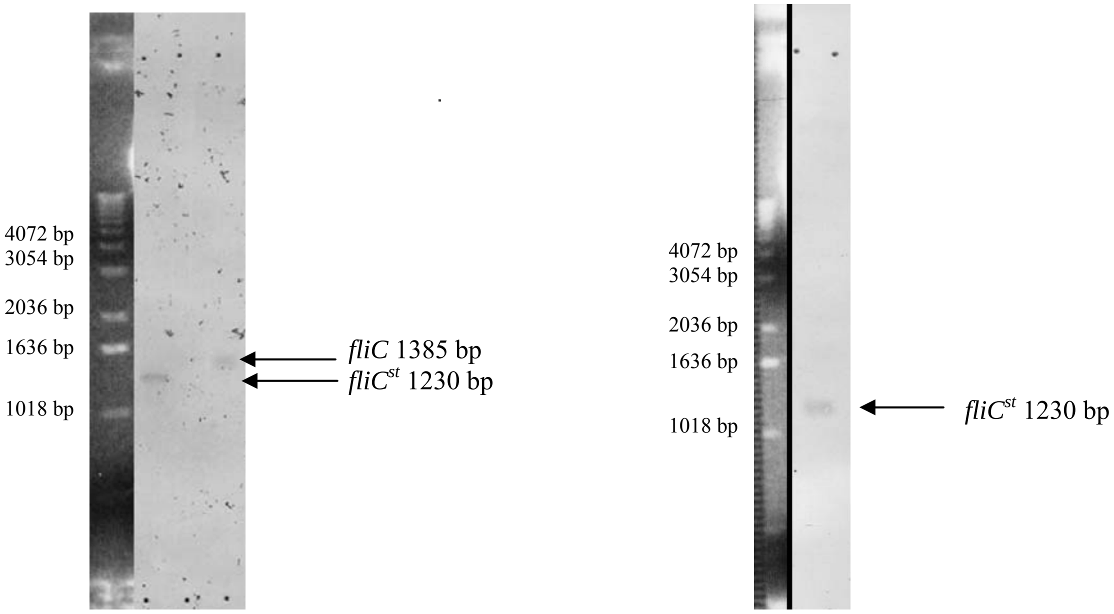

Figure 3.15: A Southern blot of RP5232 (left) and YS34 (right) transformed with pDS-*fliC*st. A positive control of pDS-*fliC*st was also run on both gels (not shown). A band showing unsuccessful replacement of *fliC* with *fliC*st is shown on the RP5232 blot.

Strains JHC36 (parental strain YS34) and JHCE3 (parental strain RP5232) produced a band of the correct size (Figure 3.16), and cultures were subsequently frozen at – 80 ºC.

To confirm that *fliC*st had integrated onto the correct location on the chromosome, the *fliC* region of the chromosome of strains JHC36 and JHCE3 were amplified by PCR using primers *fliC* 1 RP and *fliC* 2 RP, and sequenced.

3.11.2 Phenotypic assessment of *fliC*st strains

In order to assess the tethering ability of JHC36 and JHCE3, JHC36 and YS34 were transformed with pDFB102 (p*lac motA motB*), and grown with shaking in LB-broth containing 0.1 mM IPTG at 30 ºC. The cells were subsequently sheared and prepared in tunnel slides. JHCE3 was not transformed with pDFB102 because it had wild type chromosomal *motA* and *motB*. Strain PS2589 (*fliC*st) was also prepared in a tunnel slide.

JHC36 and JHCE3 displayed similar levels of tethering (and rotating) compared to PS2589; hence, they both had functional sticky filaments. YS34 displayed very low levels of cell tethering compared to JHC36 and PS2589.

3.12 Chapter discussion

Mutant MotB*s tested in this study were dominant-defective proteins, capable of incorporating into a motor containing wild type stator complexes, as determined from swarm plate analysis and the percentage of motile cells grown in the presence of IPTG. The cellular levels of mutant MotB* were significantly higher than the cellular levels of chromosomal (wild type) MotB in strains incubated with IPTG for 30 min or longer, and hence the lack of reduction in the percentage of motile cells was not due to defects in protein expression.

When grown in the presence of IPTG, cells expressing MotB D32E and D32R had the highest percentage of motile cells of all the mutant MotB*s tested, and also showed the highest levels of recovery when resurrecting a stopped (locked) motor. It is possible that MotB D32E and MotB D32R were capable of undergoing low levels of proton-conduction, enabling rotation of the motor; however, such low levels of proton-conduction would be expected to result in slower rotation rates, which were not observed (as seen at low pmf values). Hence, the lack of observable slow and intermediate rotation rates suggests that these two proteins had lower affinities for the motor than the other mutant MotB*s and rarely incorporated into the motor. The introduction of a positive charge in MotB D32R into the stator complex may have disrupted stator complex conformation greatly, resulting in a much lower affinity for the motor; alternatively, the presence of the positive charge may have affected MotB D32R interacting with MotA, and may seldom form a stator complex. D32E may have had a lower affinity for the motor as a result of its larger side chain.

The lack of observable slow and intermediate rotation rates and the lack of any mutant strain to de-resurrect in a step-like manner suggest the possibility that the integration of one mutant stator complex into a functioning motor may be sufficient to lock the motor, which may also explain the observation of brief pauses in rotation. These stops varied in duration between approximately 1 - 20 s. Such pauses were seldom observed in cells expressing MotB D32wt and in cells carrying pJZ18 MotB D32* in the absence of IPTG, and therefore unlikely to be the result of the bead transiently sticking to the glass or other flagella. Perhaps a stopped motor containing one mutant stator complex may only become functional once the mutant stator complex leaves the motor.

Presumably wild type and mutant stator complexes compete for binding in the motor. The cell may be able to distinguish between a mutant and wild type stator complex, and thus have a preference for wild type stator complexes, as evidenced from the lack of any significant decrease in the percentage of motile cells for any cell expressing mutant MotB* when exposed to IPTG for up to 2 h. Mutant stator complexes may have had a lower affinity for the motor than their wild type counterparts, possibly due to a structural change caused by the D32* substitution. Wild type stator complexes may be capable of physically displacing mutant stator complexes from the motor, as seen in the resurrection of stopped motors. Alternatively, the observation of the resurrection of stopped motors may be the result of mutant MotB* degradation during the 2 h incubation in the absence of IPTG.

The ability of motors with apparently defective stators to resurrect after expression of mutant MotB* was stopped and expression of wild type MotB continued suggests that the stator proteins may be exchanging at the motor.

4 Visualising GFP-MotB in the flagellar motor

4.1 Constructing Green Fluorescent Protein (GFP) fusion proteins

GFP is easy to detect by non-invasive fluorescence microscopy, and has the advantages of being relatively small and functions as a monomer. GFP can be fused either N- or C-terminally[237] to other proteins because both termini of GFP are rather flexible and exposed on the surface of the folded protein β-can structure. The structure of GFP is not significantly distorted by fusion to another protein (see section 1.8.1 for more detail on the structure of GFP).

Enhanced GFP (EGFP) is a mutant variant of wild type GFP which is 35 times brighter than wild type GFP when excited at 488 nm (see [238] for a review). The chromophore of wild type GFP contains the residues Ser-65, Tyr-66 and Gly-67. EGFP (BD Biosciences[239]) contains a double substitution of Phe-64 to Leu, which improves folding at 37 ºC, and Ser-65 to Thr to promote chromophore ionisation. EGFP has a single, strong, red-shifted excitation peak at 488 nm (Figure 4.1), making it especially well suited for detection by commonly used equipment.

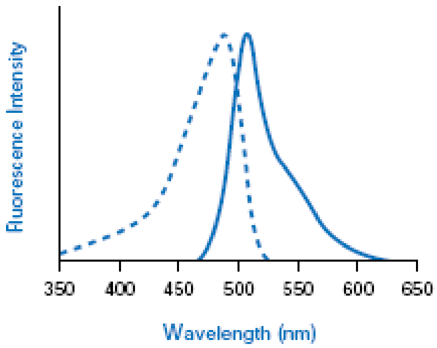

Figure 4.1: Excitation (dashed line) and emission spectra (solid line) of Enhanced GFP (EGFP). The excitation maxima of EGFP is 488 nm and the emission maxima is 507 nm. Taken from www.clontech.com

GFP fusion proteins can be expressed *in vivo* either from an inducible plasmid or by replacing a native gene on the chromosome with the gene fusion. Expression from an inducible plasmid has the advantages of allowing the experimenter to vary the levels of expression and the fusion constructs are relatively easy to create. EGFP has been used in this way to label chemotaxis proteins in *E. coli* (CheA, CheY, CheZ and FliM), which were expressed in the corresponding deletion background[110]. Fusion proteins expressed under native promoters are expressed at wild type levels, however, expression from a single chromosomal copy of the gene fusion may result in low levels of fluorescence, making visualisation difficult.

4.2 GFP-tagging of MotB

MotB was N-terminally fused to EGFP (BD Biosciences) rather than the C-terminus for two reasons: (1) the C-terminus of MotB is located in the periplasm and is believed to anchor the stator complexes to the cell, (2) EGFP is not fluorescent in the periplasm of the bacterial cell if exported unfolded through a Sec transport pathway (Figure 4.2).

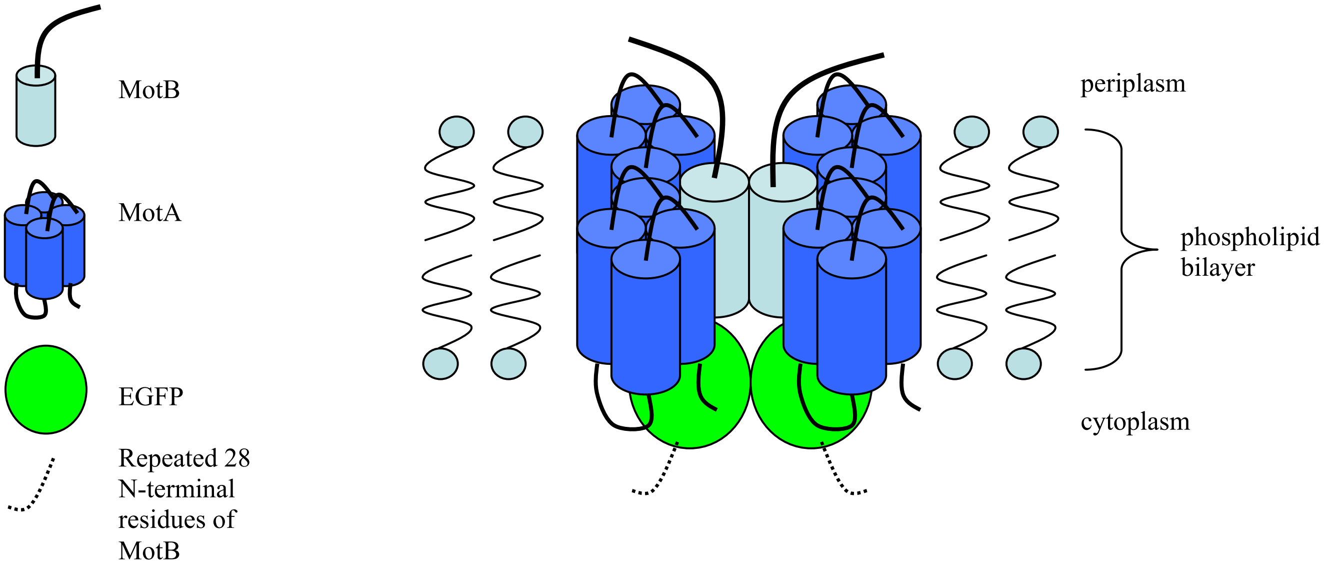

Figure 4.2: An *E. coli* stator complex with a predicted stoichiometry of MotA_4: $(\text{EGFP-MotB})_2$. The sequence encoding the 28 cytoplasmic N-terminal residues of MotB was repeated at the 3' end of *egfp* (see next section for more detail). The molecular weights of EGFP, MotA and MotB are 27kDa, 32 kDa and 34.2 kDa respectively. The diagram is not drawn to scale.

In brief, a *gfp-motB* strain was constructed by linking 500 bp upstream of and including the first 28 codons of *motB* (which may contain a putative membrane-targeting sequence) to *egfp*, followed by the first 500 bp of *motB*. This insert was ligated into a suicide vector which integrated into the chromosome of wild type strain RP437 replacing wild type *motB* by double homologous recombination. This resulted in a single copy of *gfp-motB* under the control of the native *motB* promoter, which should result in wild type expression and regulation.

4.3 Constructing a *gfp-motB* strain

A 550 bp region immediately upstream of and including the first 28 codons of *motB* was amplified by PCR from RP437 chromosomal DNA using primers *motB*A and *motB*B to include a 5' *Eco*RI site (see Appendix D for primer sequences). *egfp* was amplified by PCR from pEGFP-N1 (BD Biosciences) to include a 3' *Xba*I site using primers *motB*C and *motB*D (Figure 4.3). The central primers were designed so that the 3' end of the upstream fragment was complementary to the 5' end of the *egfp* fragment and *vice versa*. The two PCR products were combined and used as templates in overlap-extension PCR with the 5' primer from the original upstream PCR (*motB*A) and the 3' primer from the original *egfp* PCR (*motB*D). This produced a PCR product which contained the region immediately upstream of *motB* fused to *egfp* in such a way as to position the start codon for *egfp* exactly 28 codons into *motB*. This PCR product was cloned into *Eco*RI / *Xba*I cut pUC19. The first 500 bp of *motB* was amplified by PCR from RP437 chromosomal DNA using primers *motB*E and *motB*F (excluding its initial ATG) to include an upstream *Xba*I site and a downstream *Hin*dIII site and cloned into the previous plasmid generating a construct containing the region upstream of *motB*, its start codon and the first 28 codons (encompassing the putative membrane-targeting sequence) fused to *egfp* and then 500 bp of *motB*. The resulting construct (pUC19-*gfp-motB*) was sequenced to ensure there were no PCR-generated errors and cut with *Eco*RI / *Hin*dIII to excise *egfp-motB*. The ends were filled-in and ligated into the *Sma*I cut suicide vector pKO3 [229]. This construct was sequenced to ensure that *egfp-motB* was in-frame (see Appendix E for sequencing primers); this construct was called p*gfp-motB*. For simplicity, from hereon in, *egfp-motB* is referred to as *gfp-motB*.

Wild type strain RP437 was transformed with p*gfp-motB* and plated on LBA / Cm plates overnight at 30 ºC and 43 ºC to select for vector integrates (see section 2.2.14.2 for more detail). Colonies from the 43 ºC plate were grown overnight in LB-broth at 30 ºC and plated on 5 % sucrose at 30 ºC to induce a second recombination event. Colonies were replica-plated onto Cm / LBA and LBA plates at 30 ºC to test for pKO3 backbone excision.

Chromosomal gene replacement of *motB* with *gfp-motB* was confirmed by digesting genomic DNA preparations of Cm^{S} Suc^{R} colonies with *Afl*III, followed by Southern blotting (Figure 4.4). Blots were hybridised with DIG-labelled *egfp* cut from pEGFP-N1 with *Eco*RI / *Xba*I. Replica crosses of colonies that produced a band of the correct size on the Southern blot were picked, grown and frozen at – 80 ºC.

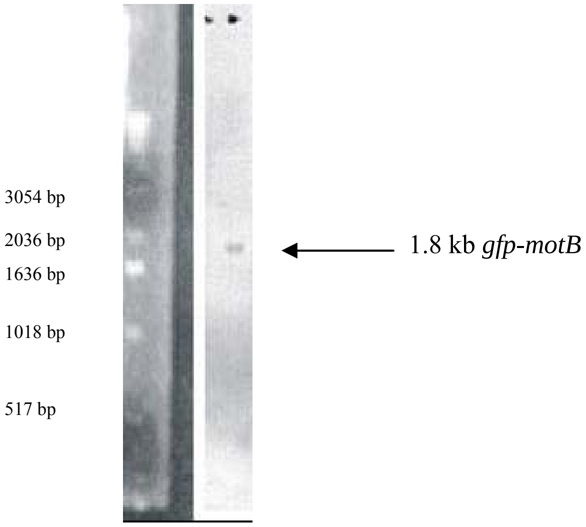

Figure 4.4: Southern blot of RP437 transformed p*gfp-motB* which integrated onto chromosome by double homologous recombination. The membrane was probed with a DIG-labelled *gfp* DNA probe which highlighted bands in two lanes (one is shown). Two cultures produced bands of the correct size, and their genomic DNA was sequenced to confirm the presence of *gfp-motB*. A blank lane to the left of the highlighted band side represents unsuccessful gene replacement. A 1 kb DNA ladder is shown on the left.

To confirm that *gfp-motB* had inserted into the correct location in the chromosome, the *motB* region of the chromosome was amplified by PCR using primers *motA*1 and seqB1 (Appendix F and G) to include the final 500 bp of *motA* through to the end of *motB* (therefore outside the regions cloned into pKO3). The PCR products were sequenced and confirmed perfect replacement of *motB* with *gfp-motB* in-frame in the chromosome in the correct location. One isolate was chosen and named strain JHC1.

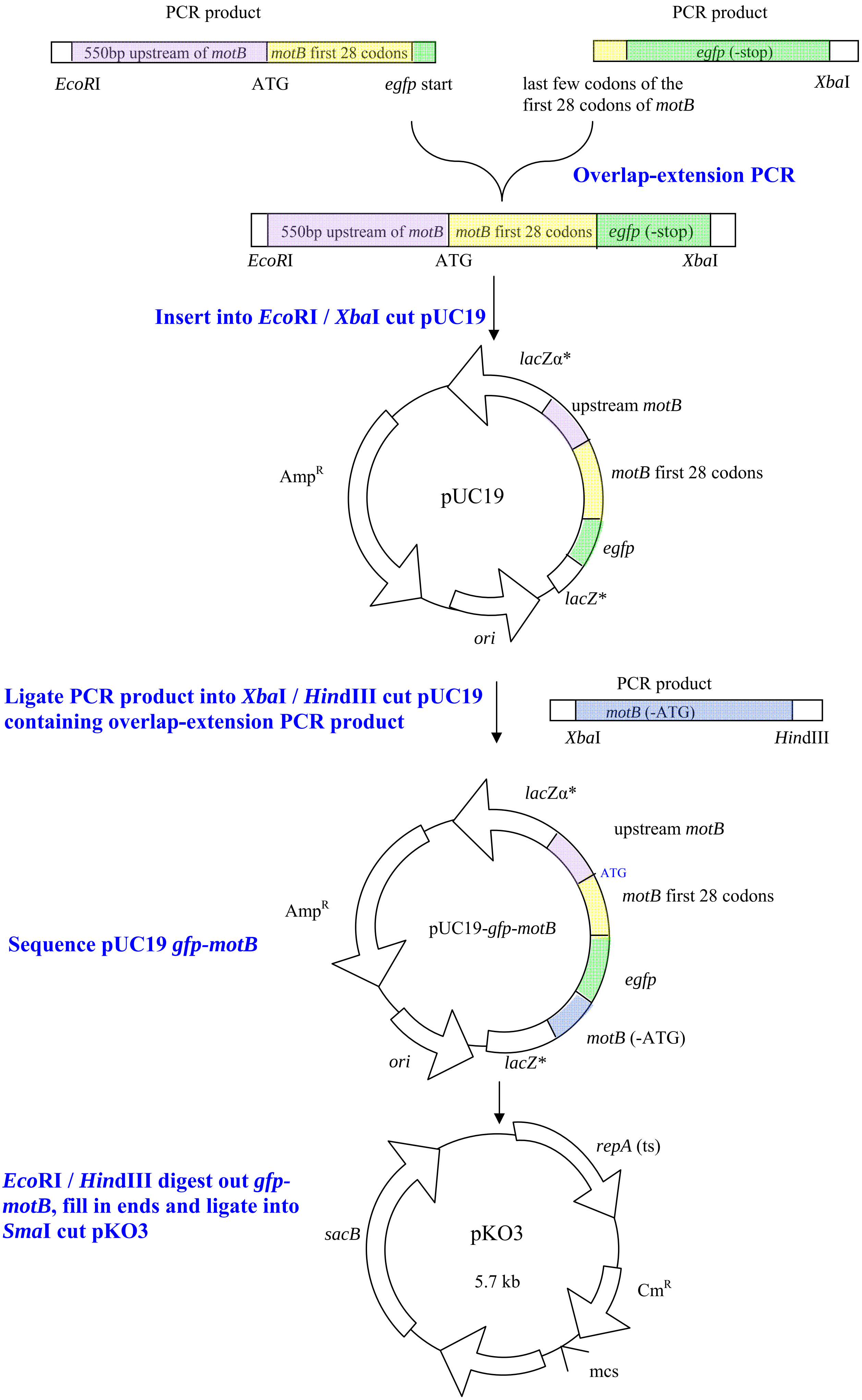

Overlap-extension PCR

Insert into *Eco*RI / *Xba*I cut pUC19

Ligate PCR product into *Xba*I / *Hind*III cut pUC19 containing overlap-extension PCR product

Sequence pUC19 *gfp-motB*

***Eco*RI / *Hind*III digest out *gfp-motB*, fill in ends and ligate into *Sma*I cut pKO3**

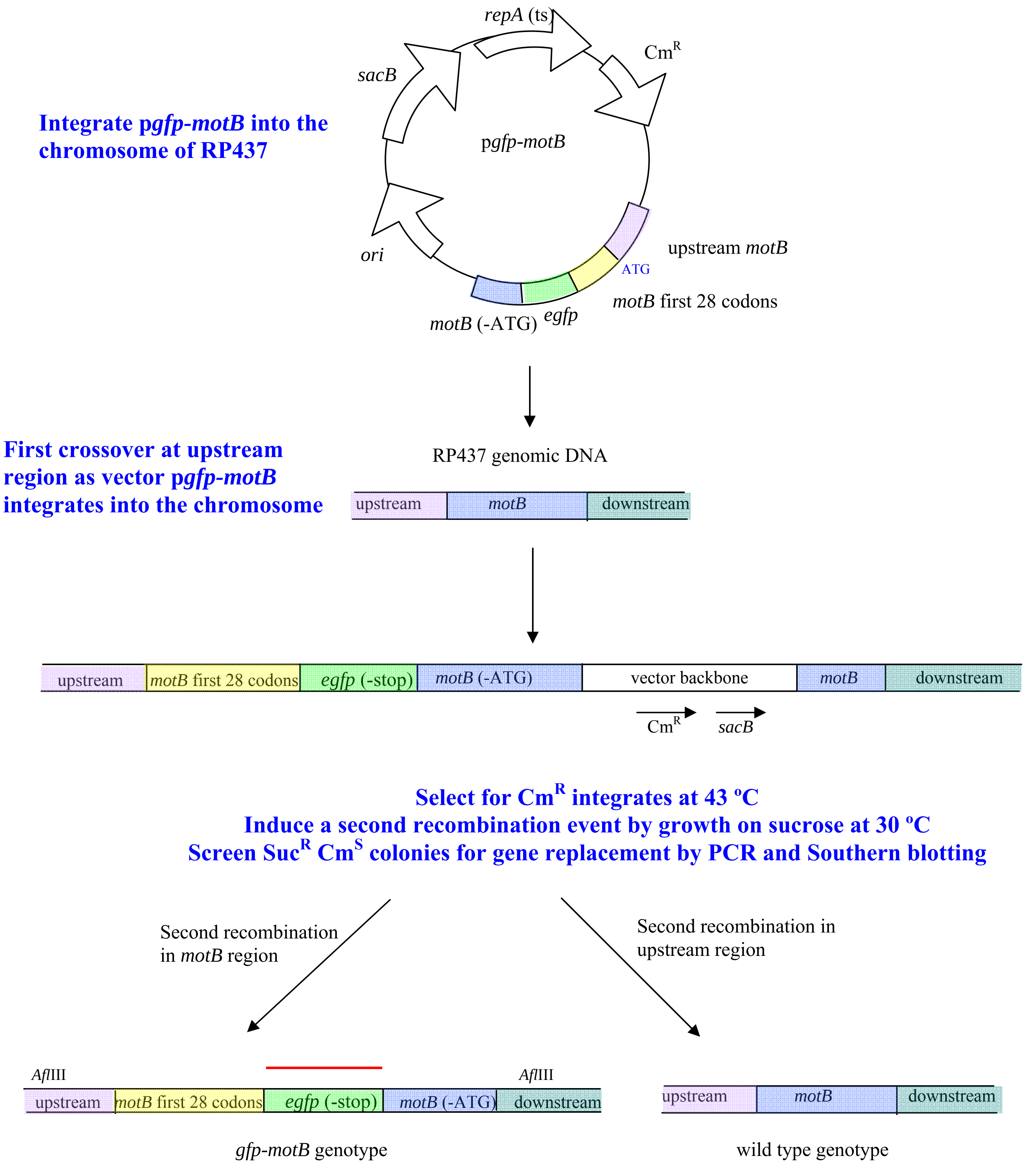

Figure 4.3: Construction of *gfp-motB* strain JHC1. The insert was created by a combination of PCR and overlap-extension PCR, which was ligated into pUC19 for sequencing, and then into suicide vector pKO3. p*gfp-motB* was transformed into RP437 where it integrated into the genome by double homologous recombination. *Afl*III was used to digest chromosomal DNA for Southern blotting, so the sites are indicated, the site of probe annealing is also indicated (red line).

4.4 Western blot analysis of *gfp-motB* strain JHC1

Cell lysate of strain JHC1 (*gfp-motB*), parental strain RP437 and YS34 (Δ*motA* Δ*motB* Δ*cheY* Δ*pilA fliC*::*Tn10*) were subjected to western blotting. Cells were grown in T-broth shaking at 30 ºC until OD_{600} 0.8. ~ 1 ml of each sample was centrifuged (corrections were made for slight variations in the optical density). Cell lysates were subjected to SDS-PAGE and membranes were blotted and hybridised with a 1 / 1000 dilution of anti-MotB antibody (Figure 4.5) (a gift from David Blair, University of Utah). An acetone powder made from strain YS34 was added to the anti-MotB antibody at a 1 / 100 dilution to reduce the levels of background on the membrane.

As Figure 4.5 shows, cell lysate from JHC1 produced a single band with a molecular weight corresponding to the estimated molecular weight of the fusion protein 64.2 kDa (MotB: 34.2 kDa, EGFP: 27 kDa, plus ~3 kDa for the repeated 28 codons). There was no band at 34.2 kDa in JHC1 cell lysate, indicating that the MotB moiety was not selectively cleaved from the N-terminus of the fusion protein.

Cell lysate from parental strain RP437 produced a band corresponding to the molecular weight of MotB (34.2 kDa). As expected, no band(s) were detected in cell lysate from strain YS34.

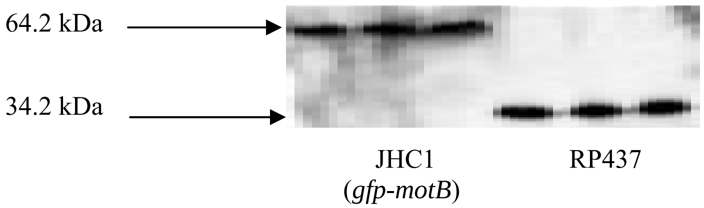

Figure 4.5: Anti-MotB western blot analysis of cell lysates of JHC1 and RP437 (cell lysate from three independent cultures of each strain are shown). Cell lysates were subjected to SDS-PAGE, and membranes were blotted and probed with anti-MotB antibody supplemented with acetone powder made from YS34 (Δ*motAB*), followed by anti-rabbit-HRP-conjugated antibody. Cell lysate of strain YS34 did not produce any bands (not shown).

Band intensities from six independent cultures of JHC1 and RP437 were quantified by scanning membranes and calculating the total pixel intensity within each discrete band (ImageQuant, Molecular Dynamics) (only cell lysates from three independent cultures of each strain are shown in Figure 4.5). The total band pixel intensity for strain for RP437 divided by that for JHC1 was 0.93 ± 0.14 (mean ± s.e., n = 6), consistent with GFP-MotB having similar expression levels to wild type MotB.

4.5 Swarm plate analysis of JHC1

The chemotactic ability of JHC1 was assessed by inoculation onto soft-agar swarm plates. The ability to swarm on swarm plates requires both chemotactic and motile ability.

JHC1 was capable of swarming, albeit to a lesser extent than RP437, indicating that GFP-MotB was functional and capable of generating torque. As expected, swarming was not observed in non-motile and non-chemotactic YS34 (Δ*motA* Δ*motB* Δ*cheY* Δ*pilA* *fliC*::*Tn10*)[227]; and non-chemotactic RP5232 (Δ*cheY*). Mean swarm diameters formed by all four strains on nine separate plates were measured (Figure 4.6B). The ratio of the mean swarm diameter formed by JHC1 to RP437 was 0.37.

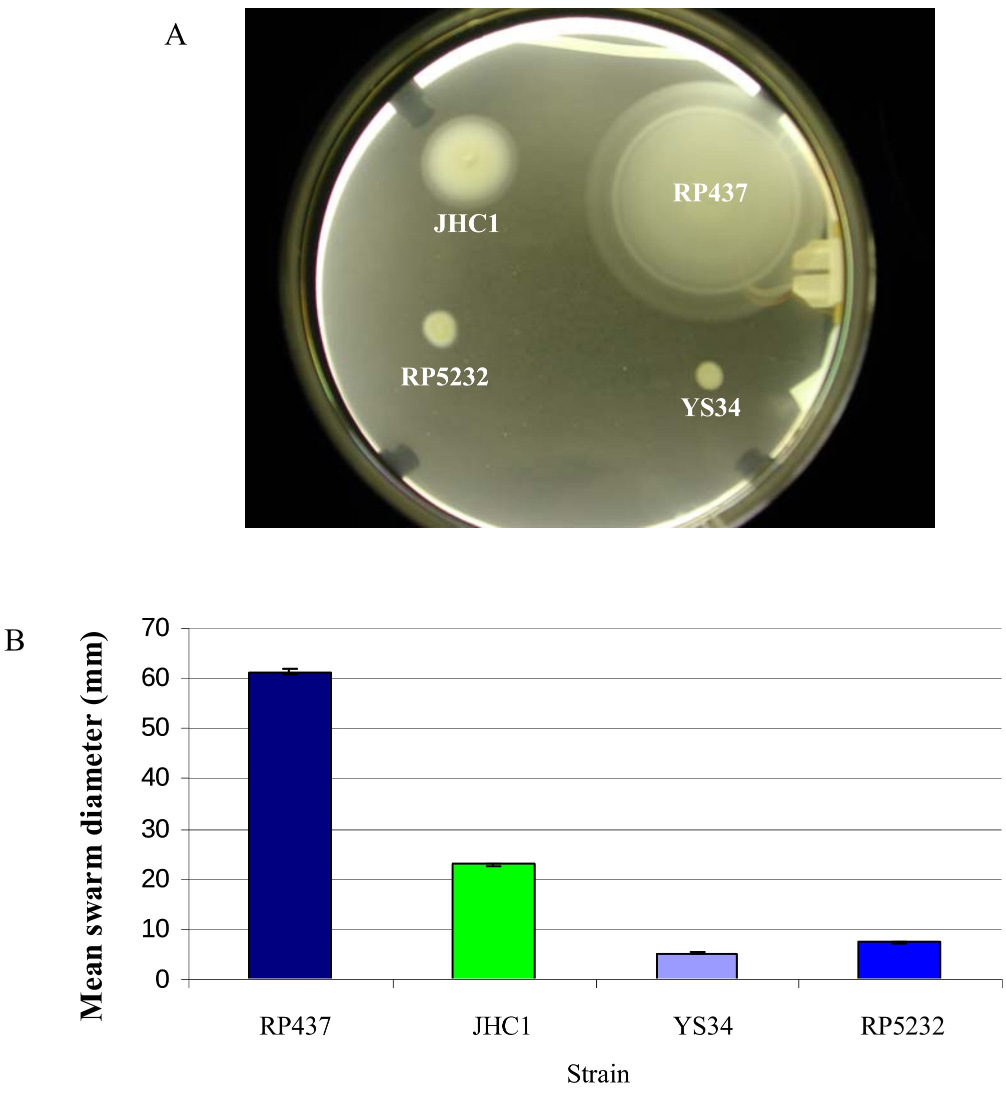
Photo taken at 10 h

Figure 4.6: Assessing the chemotactic ability of JHC1. (A) Swarm plate analysis of JHC1, together with RP437, non-chemotactic RP5232 and non-motile (and non-chemotactic) YS34. JHC1 displayed reduced swarming compared to RP437, indicating that its motile and / or chemotactic ability was impaired in some way by the presence of the GFP-tag on MotB. As expected, non-motile YS34 (Δ*motA* Δ*motB* Δ*pilA* Δ*cheY fliC*::*Tn10*) and non-chemotactic RP5232 (Δ*cheY*) did not swarm. (B) Mean swarm diameters for all four strains. Plates were repeated nine times and standard error bars are shown. Plates were photographed after 10 h at 30 ºC.

4.5.1 Growth rate of JHC1

Growth rates of JHC1 and RP437 were measured in triplicate from three independent samples. There was no measurable difference between the growth rates of JHC1 and RP437 (data not shown).

4.6 Stuck-cell bead analysis of JHC1

To investigate if reduced chemotaxis or motile ability accounted for slower swarm rates observed for JHC1, a stuck-cell bead assay was used to assess flagellar motor activity. JHC1 and RP437 were transformed with pYS7 (Cm^R) carrying *fliC*st. The internal deletion rendered FliC and hence the filament 'sticky', allowing polystyrene beads to adsorb to the filament, which can act as markers of rotation in an optical trap.

Cells were grown in T-broth / Cm until OD_{600} 0.8, sheared, and cell bodies were stuck in a tunnel slide using poly-L-lysine. Polystyrene beads of diameter 0.75 μm were flushed through the tunnel slide and the rotation rates of 21 beads adsorbed onto flagellar stubs as different cells of both strains were measured.

As figure 4.7 shows, there was a wide distribution of rotation rates in both strains. The mean rotation rate of individual JHC1 cells was 23.8 Hz, with a standard deviation of 16.4 and a standard error of 3.6, compared to a mean rotation rate of 75.4 Hz for RP437 with a standard deviation of 10.1 and a standard error of 2.2. Hence, it appears that the presence of the GFP fused to the N-terminus of MotB had in some way affected the torque-generating cycle of the motor.

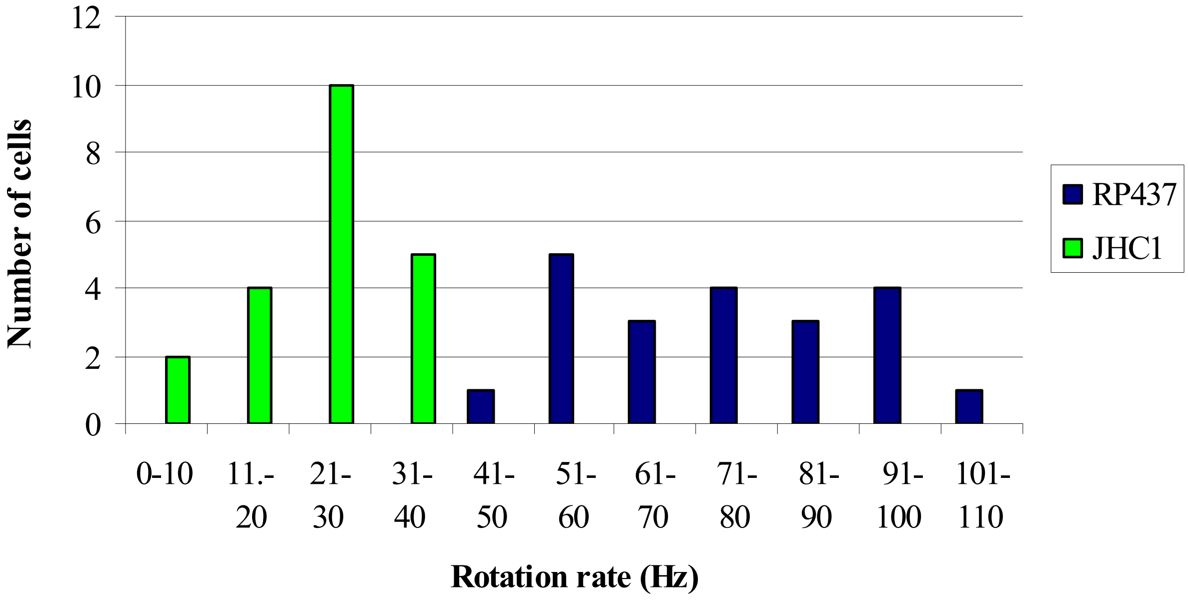

Figure 4.7: Rotation rates of beads (0.75 μm diameter) adsorbed to the filaments of JHC1 and RP437, measured in an optical trap. JHC1 did not rotate above 40 Hz, whilst RP437 did not rotate below 40 Hz. The mean rotation rate for JHC1 was 23.8 Hz, with a standard deviation and standard error of 16.4 and 3.6 respectively. The mean rotation rate of RP437 was 75.4 Hz, with a standard deviation and standard error of 10.1 and 2.2 respectively. The rotation rates of beads adsorbed to 21 cells of each strain were measured.

4.7 Visualising GFP-MotB in the motor

Single colonies of JHC1 and RP437 were picked and grown to stationary phase with shaking in LB-broth at 30 ºC. 200 μl of culture was sub-cultured into 5 ml of T-broth at 30 ºC and grown until OD $_{600}$ 0.8. The cells were sheared and tethered via anti-FliC antibody in tunnel slides.

Motile JHC1 were viewed initially using DIC and epifluorescence microscopy, however the equipment was not sensitive enough to visualise GFP-MotB in the motor. Previous work including electron microscopy and torque-restoration experiments estimate the motor to have ~ 8 stator complexes, with each stator complex containing a MotB dimer, so theoretically, the *E. coli* motor may contain a maximum of 16 MotBs, which would be very difficult to visualise against cell autofluorescence using standard epifluorescence microscopy.

In order to visualise GFP-MotB in the motor, a very sensitive microscopic technique was used, called Total Internal Reflection Fluorescence Microscopy (TIRFM), which is described in detail in section 1.8.4.

4.7.1 TIRFM of JHC1

Cells were sheared and tethered via truncated flagellar filaments to bring the motor close to the coverslip, within the evanescent wave created by TIRF (Figure 4.8A, B). In order to focus on the motor, polystyrene beads 0.2 µm in diameter were flushed through the tunnel slide to act as markers of distance from the coverslip.

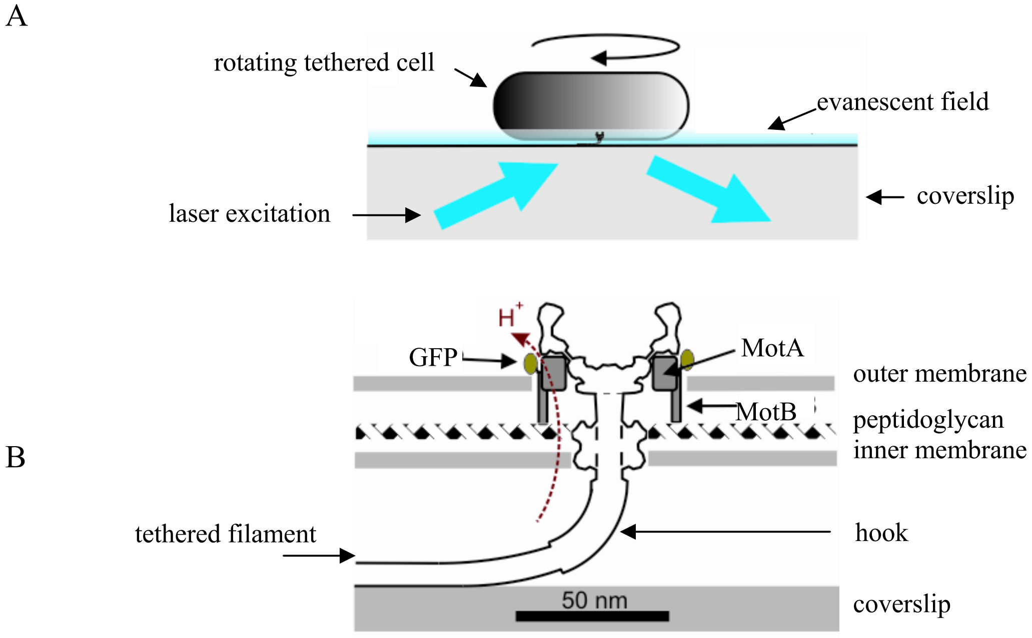

Figure 4.8: TIRFM of JHC1. (A) The anti-FliC antibody tethered cell assay. (B) The motor structure close to the coverslip.

Mid cell-body height from the coverslip was measured for each cell and a video of brightfield images (40 ms exposure, 100 frames) recorded 100 nm above the coverslip. Brightfield videos were used to indicate the centre of cell body rotation, and hence the location of the motor (indicated by a red cross in Figure 4.9A). The frames from the brightfield video shown in Figure 4.9A show two JHC1 cells; the lower cell rotated whilst the upper cell was fixed (it was probably tethered via more than one flagellum). Then false-colour TIRFM images of the cells were taken (Figure 4.9B). In the rotating cells, a fluorescent spot was observed at the centre of cell body rotation, corresponding to the site of the motor (Figure 4.9B). Occasionally, multiple fluorescent spots were seen in non-rotating stuck cells of JHC1, corresponding to multiple flagellar motors within the TIRF excitation field (two fluorescent spots can be seen in the upper fixed cell in Figure 4.9B).

Brightfield videos and TIRFM images of RP437 were also taken, and no fluorescent spots were observed (Figure 4.9C). The dim diffuse fluorescence seen in the TIRFM image is due to cell autofluorescence.

The number of fluorescent spots observed in JHC1 was consistent with the number of randomly distributed flagella per cell (~ six per cell). The cell was modelled as a cylinder, 2 μm in length and 1 μm in diameter, with hemi-spherical ends. It was estimated that approximately one-sixth of the cell surface area was within 100 nm from the coverslip and thus within the TIRF excitation field. An average of 1.0 ± 0.2 (mean ± s.e., n = 63) motors per cell visible in TIRFM images of non-rotating fixed cells corresponded to 6 ± 1.2 motors in total (because one-sixth of the cell surface was estimated to be within the TIRF illumination field), consistent with independent estimates of the total number of motors per cell.

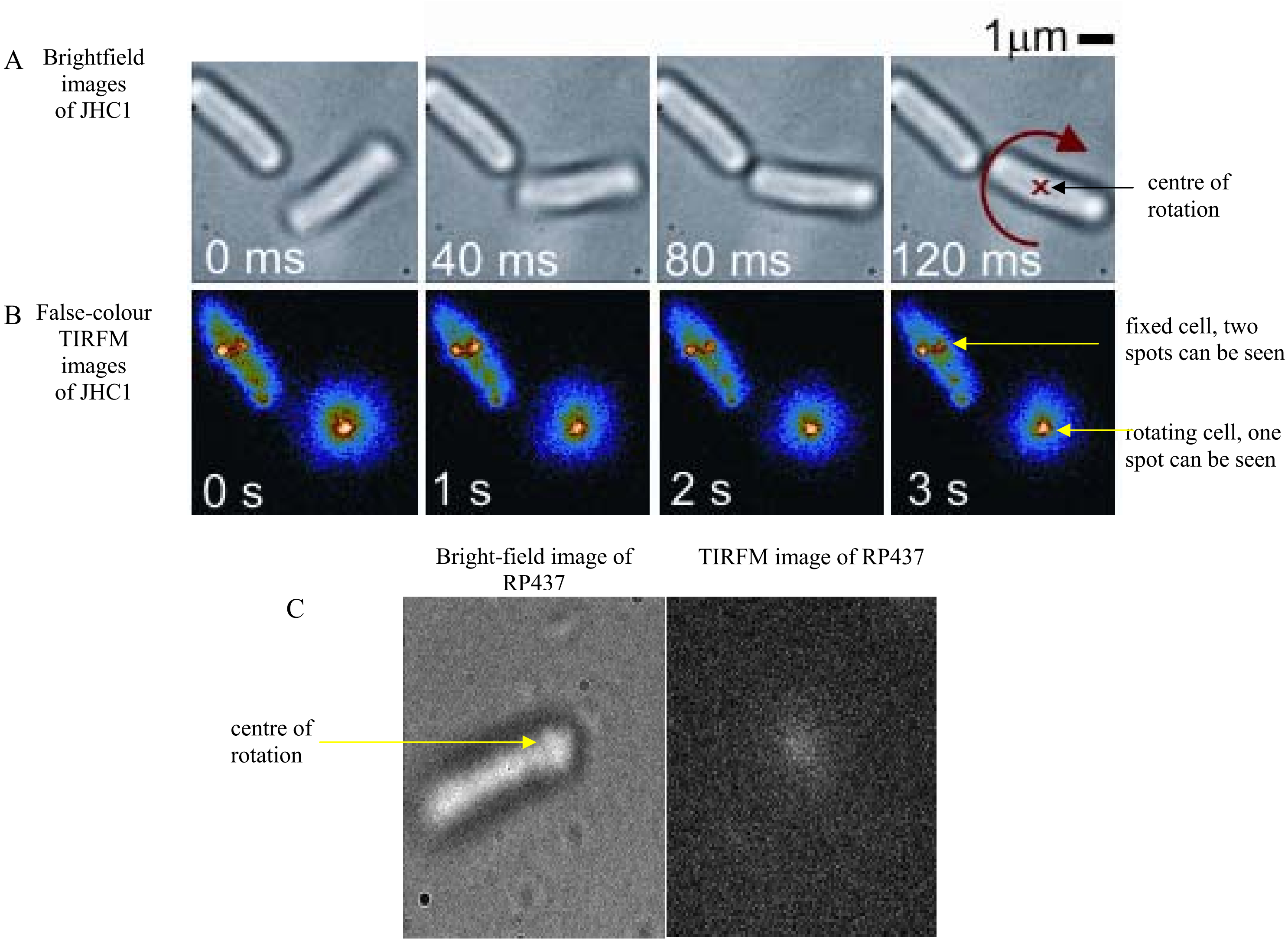

Figure 4.9: TIRFM of JHC1 and RP437. (A) Consecutive brightfield images of a tethered rotating and nearby fixed JHC1 cells. Rotation of the freely-rotating cell is indicated with a red arrow. The red cross corresponds to the centre of cell body rotation, hence the site of the motor. (B) Consecutive false-colour TIRFM images of the same JHC1 cells shown in A. Two spots can be seen in the upper fixed cell, corresponding to two motors within the TIRF excitation field and one fluorescent spot can be seen at the centre of rotation in the rotating cell. (C) Brightfield (left) and TIRFM image (right) of RP437. No fluorescent spots were seen at the centre of rotation. All images had a 1 s exposure time.

4.8 Chapter discussion

A suicide vector was used to replace native chromosomal *motB* in wild type strain RP437 with the gene fusion *gfp-motB*. The suicide vector integrated into the chromosome by double homologous recombination. Gene replacement was confirmed by Southern blotting and DNA sequencing. The fusion protein GFP-MotB was expressed at wild type levels, as determined by quantitative western blotting; hence transcription or translation did not appear to be affected. No degradation products of GFP-MotB were detected on western blots probed with anti-MotB antibody.

The chemotactic ability of JHC1 was assessed by swarm plates, and its motility was assessed by a stuck-cell bead assay. Both swarm and bead rotation rates were reduced to approximately one-third the levels of RP437, suggesting that the reduced swarming ability was due to reduced flagellar rotation rates, implying that the GFP fusion to MotB in some way impairs torque-generation in the motor. Perhaps GFP interfers with the positioning of the large cytoplasmic loop of MotA relative to the rotor protein FliG (believed to be important in torque-generation)[114], or perhaps part of GFP can interact with charged residues on MotA or FliG. It is possible, although unlikely that fewer stator complexes were able to bind at the motor as a result of steric hindrance caused by the GFP-tag. However the number of GFP-MotB molecules at the motor, as measured by TIRFM and FRAP (Fluorescence Recovery After Photobleaching) in Chapter 5 correlate with the number of stator complexes estimated from torque-restoration experiments[192] and electron micrographs of putative stator complexes. Previous work suggested that each motor contains ~ 8 stator complexes, but recent torque-restoration experiments, suggest that each motor contain at least 11 stator complexes. The putative stoichiometry of each complex is $MotA_4$: $MotB_2$, hence, each motor probably contains up to 22 or more GFP-MotBs, too few copies of the fluorophore to visualise using standard epifluorescence microscopy, so TIRFM was used to visualise GFP-MotB in the motor.

TIRFM achieves a very high signal-to-noise ratio, allowing visualisation of single fluorophores within a thin region of the specimen. Fluorescent spots were observed in tethered JHC1, corresponding to the centre of cell body rotation, and hence the site of the motor. The centre of rotation was determined by observing cell body rotation in the corresponding brightfield video.

Occasionally, multiple fluorescent spots were observed in stuck JHC1 cells, corresponding to the presence of multiple motors within the TIRF excitation region. These cells were tethered via more than one flagellum, impeding cell body rotation. Fluorescent spots were not observed in TIRFM images of RP437, indicating that the fluorescent spots observed in JHC1 were GFP-MotB stator complexes.

The GFP fluorophore was able to fold efficiently in the fusion protein GFP-MotB and fluoresce. The presence of the GFP-tag on MotB did not appear to affect localisation of the stator complex to the motor, or insertion into the membrane. This may be because of the repetition of the cytoplasmic N-terminal sequence of MotB at the N-terminus of GFP; although no membrane insertion signal sequence has been identified in these residues. It is not known whether GFP-MotB would have inserted into the membrane if this N-terminal sequence of MotB had not been repeated.

5 Measuring GFP-MotB stoichiometry and exchange in single, functioning motors

5.1 Visualising GFP-MotB in the motor

JHC1 (*gfp-motB*) expressed functional GFP-MotB at wild type levels (Chapter 4). Motile JHC1 were tethered in tunnel slides via truncated flagellar filaments by anti-FliC antibody (a gift from David Blair, University of Utah) and viewed using brightfield microscopy and TIRFM. As shown in Chapter 4, TIRFM images revealed fluorescent spots at the centre of rotation, corresponding to the site of the motor (the centre of rotation was determined by observing cell body rotation in the corresponding brightfield video). The diameter of the fluorescent spots were consistent with a ring of GFP-MotB stator complexes encircling the rotor with a diameter of ~ 50 nm, consistent with observations of rings of studs of putative stator complexes observed in freeze-fracture electron micrographs[89].

5.2 Fluorescence Recovery After Photobleaching (FRAP)

Fluorescence Recovery After Photobleaching (FRAP) is a cellular imaging technique whereby a fluorophore, such as GFP, is deliberately bleached by an intense flash of laser light. Bleaching of the fluorophore renders the protein intact but not fluorescent. This so-called 'photobleaching' is performed in a defined area of a cell and recovery of fluorescence into the photobleached area by the diffusion of unbleached fluorophores is measured. FRAP is often used to study the motion and diffusion of fluorophores within living cells. This technique was used to quantify the number of motor and non-motor GFP-MotBs (see section 1.8.2 for more detail about FRAP).

5.3 Visualising and counting single surface-immobilised GFP molecules

In order to quantify the number of GFP-MotBs in a motor with single-molecule precision, single surface-immobilised GFP molecules needed to be visualised and their photobleaching characterised so that the fluorescence intensity of a single EGFP molecule could be measured. Firstly, GFP had to be over-expressed and purified.

5.3.1 Over-expression and purification of EGFP

egfp was amplified by PCR from pEGFP-N1 (BD Biosciences) (see Appendix E for primers), digested with *Bam*HI / *Hin*dIII and ligated into the expression vector pQE-80 (Qiagen). pQE-80 attached six histidine codons to the N-terminus of EGFP; expression of *egfp* was under the control of an IPTG-inducible *tac* promoter. The resulting construct (pQE-80-*gfp*) was sequenced to ensure there were no PCR-generated errors. pQE-80-*gfp* was transformed into strain M15 pREP4, induced with 100 μM IPTG for 16 h at 18 ºC and over-expressed GFP was purified using an Ni-NTA agarose column (Qiagen).

Purified GFP was bright green to the eye (Figure 5.1A); a Coomassie-stained SDS-PAGE gel of the purified protein revealed a single band at 27 kDa, indicating that the GFP was pure (Figure 5.1B). A Bradford assay was used to determine the concentration of purified GFP, which was 2.24 μg / μl (Figure 5.1C).

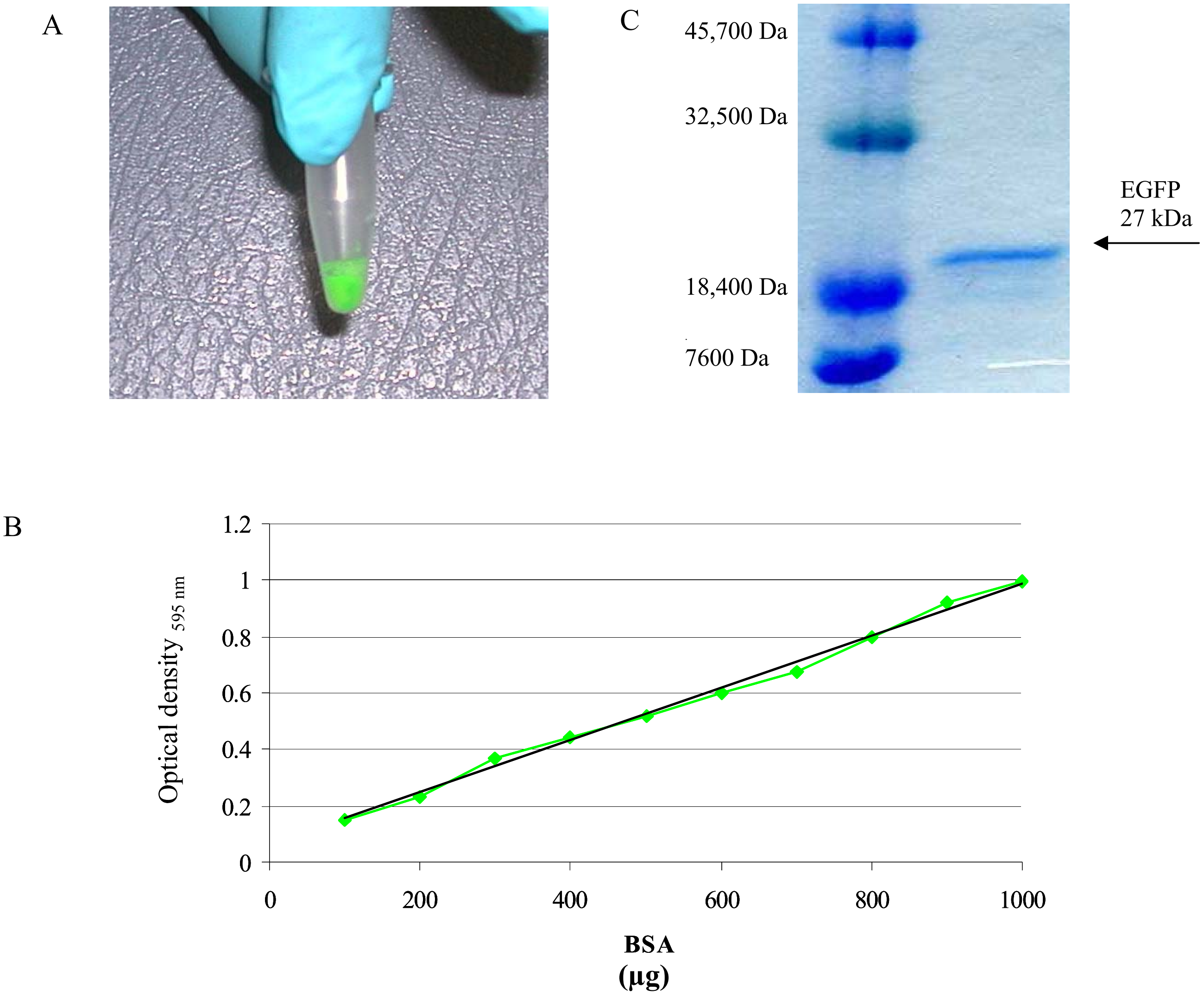

Figure 5.1: Over-expression and purification of EGFP. (A) Purified EGFP in a microfuge tube. (B) The Bradford-assay was used to determine the concentration of purified EGFP. (C) A Coomassie-stained SDS-PAGE gel (12 % polyacrylamide) revealed that the purified protein had a molecular weight the same as GFP (27 kDa); indicating that GFP purified from strain M15 pREP4 was pure (of purified EGFP was loaded onto the gel).

5.3.2 Visualising individual GFP molecules

In order to visualise single GFP molecules to monitor their photobleaching, 5 µg / ml of anti-GFP antibody (BD Biosciences) was flushed through a tunnel slide and allowed to settle for 5 min. Buffer was flushed to remove unbound antibody, then purified GFP (20 ng / ml) was flushed through the slide and allowed to bind to anti-GFP antibody for 5 min. Again, buffer was flushed though to remove unbound GFP. This resulted in 0.1 - 0.3 GFP molecules per μm^2.

5.3.3 Single-step photobleaching of individual GFP molecules

Single surface-immobilised GFP molecules were visualised by TIRF and photobleached in a single step (see section 2.3.6.1); photobleaching of three individual GFP molecules is shown in Figure 5.3.

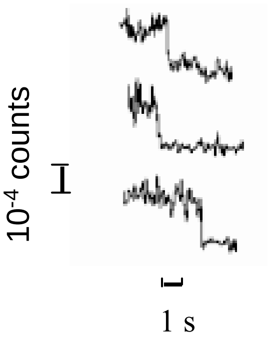

Figure 5.3: Photobleaching of single-surface immobilised GFP molecules by continuous TIRF; single GFP molecules photobleached in a single step.

5.4 Separating motor and background components of fluorescence

Image analysis and modelling was conducted using custom-written software by Dr Mark Leake and Dr Richard Berry in the Clarendon Laboratory, Department of Physics, University of Oxford.

Fluorescent spots at the centre of rotation were 300 nm in diameter. This is consistent with a ring of GFP-MotB stator complexes bordering a rotor of diameter ~ 50 nm, convoluted by the microscope point-spread function. Fluorescence intensity was modelled in a 400 x 400 nm square region of interest (ROI) (8 x 8 pixels) containing a single motor as a uniform background plus a Gaussian spot 300 nm in diameter. A fluorescence intensity centroid was calculated for each fluorescent motor spot. An initial estimate of the location of the motor within the Gaussian spot was based on observing the centre of cell body rotation in the corresponding brightfield video of a rotating cell, whilst motor location in stuck cells was estimated by locating the peak pixel intensity in a given fluorescent motor spot.

Three background components of fluorescence intensity (therefore excluding motor GFP-MotBs) in 400 x 400 ROIs were identified:

1. The mobile membrane pool of GFP-MotBs (observed in JHC1)
2. Non-specific cell autofluorescence (observed in JHC1 and parental strain RP437)
3. Instrumental background

Motor and non-motor contributions to total fluorescence intensity within the 400 x 400 square ROI were calculated as follows:

1. A circular motor mask of radius 240 nm was applied to the ROI, centred on the current motor centroid.
2. Pixel intensities within the motor mask were multiplied by a radially symmetrical 2-dimensional Gaussian mask of fixed half-width (s.d.) 150 nm, and generated a revised estimate for motor centroid weighted by this mask.

3. Steps 1 and 2 were iterated either 10 times or until the motor mask began clipping the side of the original ROI, generally resulting in a final centroid precision of ~ 5 nm.
4. The total background intensity was defined as the mean pixel intensity within the ROI but external to the final motor mask. The motor intensity was defined as the sum of all pixel values within the motor mask after subtraction of the total background intensity from each pixel value. In RP437, the ROI did not contain a motor spot so the total background intensity was defined as the mean intensity of all the pixels within the ROI.
5. The instrumental component of background (the intensity not associated with cells) was defined as the mean pixel intensity in a 400 x 400 nm ROI containing no cells (but close to the observed rotating or fixed cell).

Steps 1-5 were performed separately for each image.

6. The cell autofluorescence component of background fluorescence was defined as the mean pixel intensity from 32 separate RP437 400 x 400 nm ROIs, which obviously did not contain any GFP-MotB. This component of background fluorescence was not expected to contribute to the fluorescence intensity of the motor because only the cell surface adjacent to the coverslip was illuminated by the TIRF excitation field.

The membrane component of background fluorescence (due to a diffusing membrane pool of GFP-MotBs) for each image was defined as the total background intensity minus the autofluorescence component (step 6).

5.5 Step-wise photobleaching of motors

Having shown that GFP photobleaches in a single step, the bleaching of motors was measured. TIRF photobleaching traces of the total fluorescence components in ROIs containing motors for three individual cells of JHC1 (blue) and one RP437 cell (black) are shown in Figure 5.4; total fluorescence components of both strains photobleached exponentially.

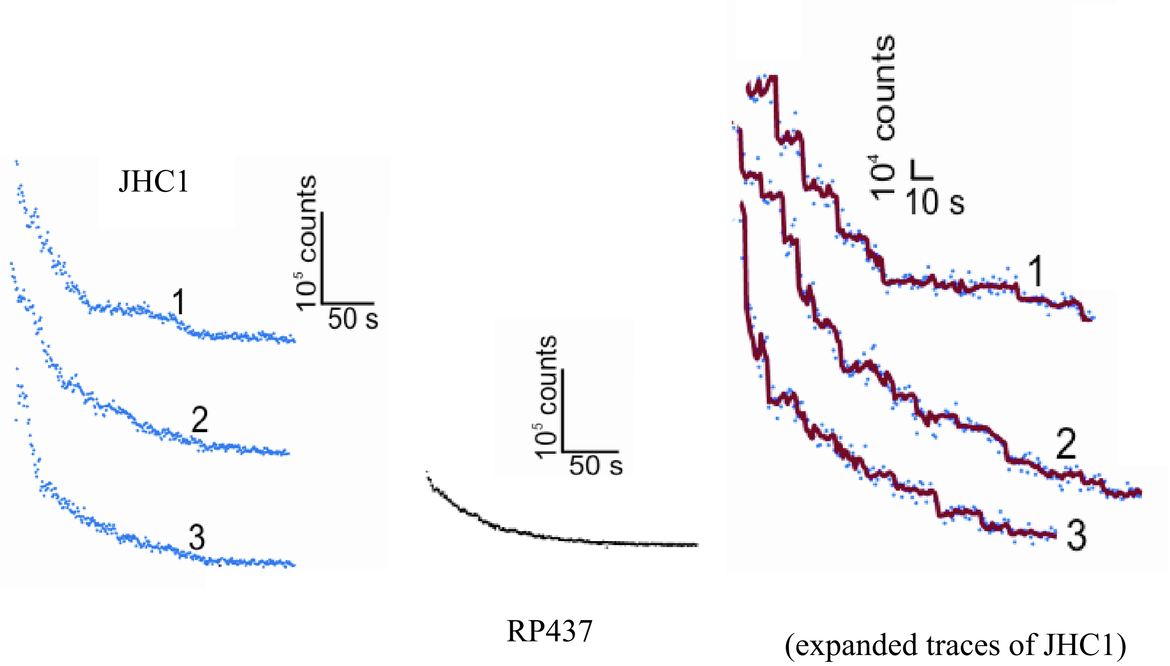

Figure 5.4: Photobleaching by continuous TIRF of total fluorescence intensity (of all cellular components) of JHC1 and RP437. (Left) TIRF photobleaching traces of ROIs containing motors in three JHC1 cells (blue) and one parental RP437 cell (black) showing exponential photobleaching of all cellular components. Autofluorescence background was calculated from the exponential photobleaching of RP437. (Right) Expanded traces of the three JHC1 cells, showing step-wise photobleaching with Chung-Kennedy filtered output overlayered (red).

In JHC1, the GFP-MotB membrane component of fluorescence photobleached considerably more slowly than the motor, which was attributable to diffusion of unbleached GFP-MotBs from outside the TIRF excitation region. The total fluorescence intensity (minus instrumental background) in ROIs containing motors (of JHC1) photobleached in a step-wise manner, which can be seen in expanded traces of Figure 5.4 (left) shown in Figure 5.4 (right). Photobleaching steps were approximately integer values of a unitary level (Figure 5.5) consistent with photobleaching of individual GFP molecules (see Figure 5.3 for single-step photobleaching of single GFP molecules). Photobleaching steps were identified using an edge-preserving algorithm (Chung-Kennedy algorithm) consisting of two adjacent running windows whose output was the mean from the window possessing the smallest variance. Step events in the data were detected by applying a single-tailed Student t-test between the sample means from the two Chung-Kennedy windows, with the criterion for acceptance of a true step being P < 0.001. Each photobleaching step was normalised by dividing the size of the smallest step in each trace, which usually occurred towards the end when only a few GFP-MotB fluorophores remained unbleached. Histograms of normalised step size showed peaks at integer values, confirming the interpretation of larger steps as multiple un-resolved unitary steps (Figure 5.5).

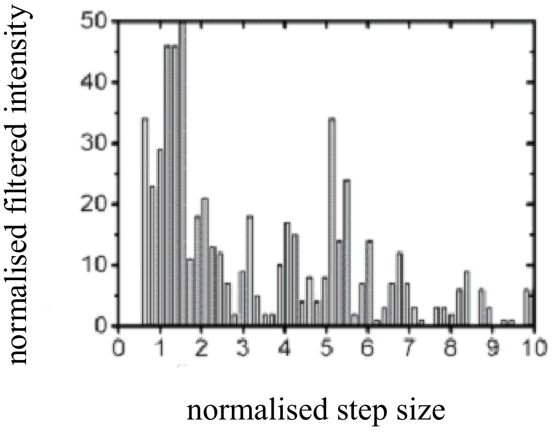

Figure 5.5: Histogram of normalised sizes of all steps found by the Chung-Kennedy algorithm in the total intensity traces shown in Figure 5.4 (left).

Separation into motor and background fluorescence components introduced extra noise (Figure 5.6), so the unitary step size was calculated using the total intensity rather than the motor component alone.

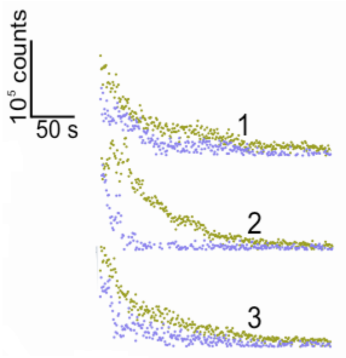

Figure 5.6: TIRF photobleaching traces of three individual JHC1 cells separated into motor (blue) and background (green) components, which introduced extra noise, so the unitary step size was calculated using the total intensity rather than the motor component alone.

5.6 Counting fluorophores

Tests using simulated photobleaching traces with similar noise levels to experimental photobleaching traces indicated that separation into motor and background components recovered the exponential bleach traces without introducing significant errors. However, the separation also generated artifactual fluctuations in intensity at roughly the same level as the noise in the original traces. Since putative single GFP photobleaching events were of a similar size to noise this made the approach for detecting single-molecule GFP photobleaching in either separated component unreliable. Therefore, step-wise photobleaching was detected from the total intensity signal (minus instrumental background) using the Chung-Kennedy edge-preserving algorithm. Step size, mean intensity, noise levels and time intervals between steps were recorded. The size of the smallest detected step was defined in each trace as the 'unitary step size', an estimate of the intensity of a single GFP fluorophore, and the total number of steps as the initial intensity divided by the unitary step size.

5.6.1 Computer simulations

The following was carried out in collaboration with Dr Mark Leake, Clarendon Laboratory, Department of Physics, University of Oxford.

The accuracy of the detection routine was tested by applying the algorithm to Monte-Carlo simulation data. The bleaching process was assumed to be Poisson such that the probability for a given GFP being unbleached after a time t but then bleaching subsequently in a small time interval dt was $\lambda\exp(-\lambda t)dt$ where $1/\lambda = \langle t \rangle$ is the mean unbleached lifetime. In the discrete limit a time-step of $\Delta t \approx dt = 1.0$ ms was chosen. Each unbleached GFP in turn was deemed to have bleached in a given time-step if the bleaching probability was greater than a pseudo-random number in the range 0 - 1. Initial numbers N = 5, 10, 20, 40, 80, 100 of unbleached matured GFP molecules were simulated using a value of $\langle t \rangle = 40$ s similar to the bleach time constant measured for motor intensity. Bleaching traces lasting 300 s were simulated. A value of 5000 counts s^{-1} was assigned to the unitary step size, similar to the experimental value. Image acquisition was simulated at 1 Hz by summing the data in consecutive intervals of size 1.0 s and added Poisson-noise associated with each unbleached GFP (s.d. = 5000 counts s^{-1}); the total noise varying as the square root of unbleached GFP number plus a baseline dark-noise with s.d.= 2000 counts s^{-1}. A range of Chung-Kennedy window width was tried, 3 - 20 s, and found predictions of mean values of N from the steps diction algorithm to be accurate, with a standard deviation of ~ 18 % over this range (10 simulations per parameter set). The best performance occurred with a window size of 10 s (Figure 5.7A) which was used for experimental data. Figure 5.7B shows simulated traces with the output of the Chung-Kennedy filter superimposed. Figure 5.7C shows integer spacing in the histogram of found step sizes normalised to the unitary step size, similar to experimental data. Smaller window sizes gave a higher proportion of over-sized unitary steps whereas larger windows gave a higher proportion of under-sized unitary steps, manifest sometimes as erroneous double-sized step predictions in cases where single steps were never resolved in a particular trace.

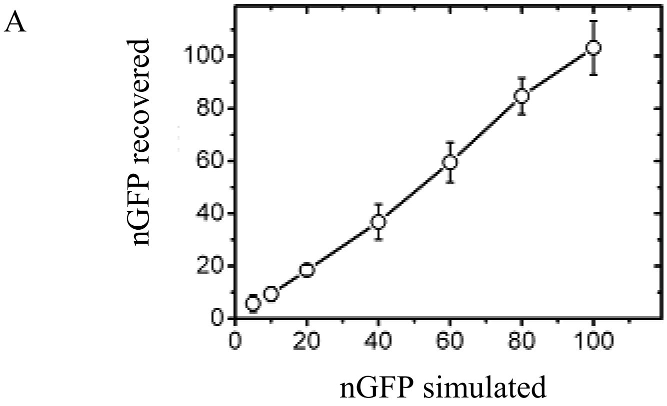

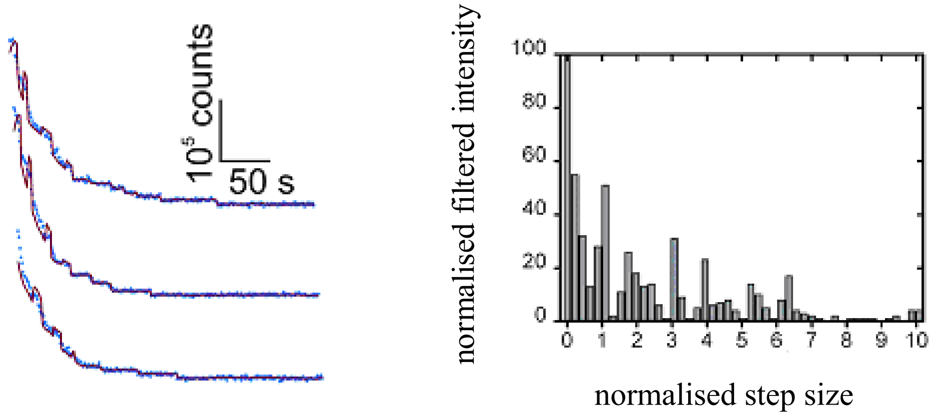

Figure 5.7: Testing fluorophore counting. (A) Recovered number of fluorophores versus true number in Poisson simulated bleaches. 10 simulated traces per data point, error bars are one standard deviation. (B) Three Poisson bleach simulations, raw (blue) and Chung-Kennedy filtered (red) data, 60 initially unbleached GFP molecules, bleach time constant of 40 s. (C) Histogram of recovered step sizes for the traces of B normalised to the recovered unitary step size for each.

A negative control was simulated for the algorithm: smooth exponential decay traces with bleach time constants and noise similar to experimental data. These traces are shown in Figure 5.8A. There is no clear integer spacing in the histogram of normalised step sizes (Figure 5.8B), demonstrating the validity of this method of assigning the unitary step size and thus the number of unitary steps.

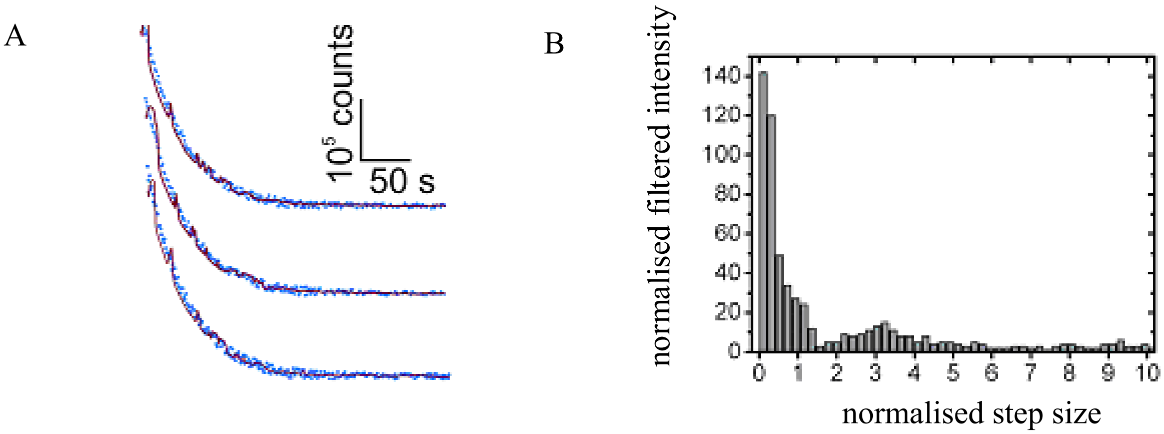

Figure 5.8: Testing fluorophore counting using simulated data. (A) Three examples of smooth exponential photobleach data simulations. (B) The corresponding normalised step size histogram.

The distribution of unitary step sizes and initial motor intensities respectively, for 134 traces from different cells is shown in Figure 5.8. The widths probably reflect different distances from the motor to the coverslip, as a result of slight variation in the tightness of the cell tether. TIRF intensity falls exponentially with distance over 100 nm, giving a ~ 4–fold variation over the measured range of cell heights, ~ 150 nm. Step-wise photobleaching of single surface-immobilised GFP molecules (Figure 5.3) showed an average step size of 13,000 counts s^{-1}, after correcting for differences in laser power and exposure time, thus the average unitary step size is consistent with motors ~ 90 nm from the coverslip.

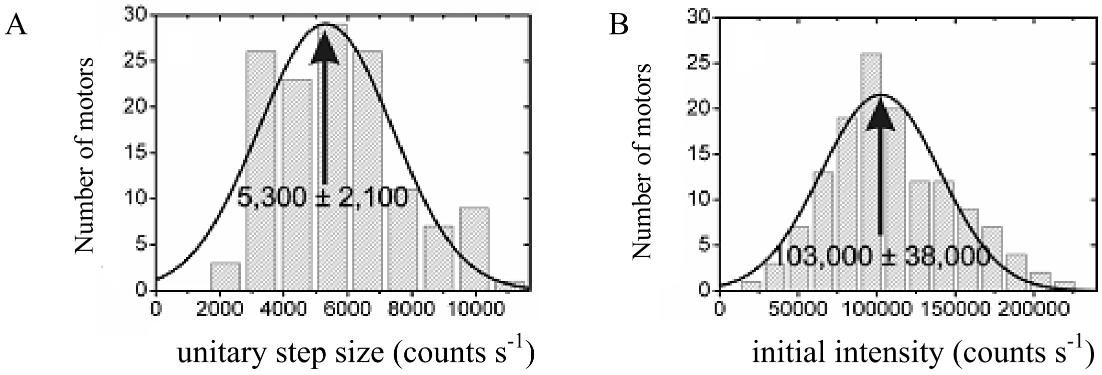

Figure 5.8: Histograms for pooled tethered and fixed cells data (134 bleaches). (A) Unitary photobleaching step size. (B) Initial motor spot fluorescence intensity. The ratio of the peaks in A and B gives an estimate of the average number of GFP-MotBs per motor. Gaussian fits are shown with mean ± s.d. indicated.

The total number of GFP-MotB molecules per motor was estimated by dividing I_0 by the unitary step size for each trace (Figure 5.9). The peak at 22 ± 7 compares well with the ratio of peaks in Figures 5.8A and B (19 ± 10). Dividing the initial membrane component of background intensity by the unitary step size gave an average of 0.052 ±

0.022 molecules per pixel. The cell was modeled as a cylinder, 2 μm in length, and 1 μm in diameter, with hemispherical ends:

$$4 \pi r^2 = 4 \times \pi \times 0.5 \times 0.5 = 3.142\ \mu m^2$$

$$2 \pi r l = 2 \times \pi \times 0.5 \times 2 = 6.283\ \mu m^2$$

$$\text{Total surface area} = 9.43\ \mu m^2$$

The cell surface area was estimated as 3700 ± 500 pixels (each pixel is 50 nm x 50 nm) and thus the total number of non–motor GFP-MotB molecules per cell was estimated as 190 ± 80.

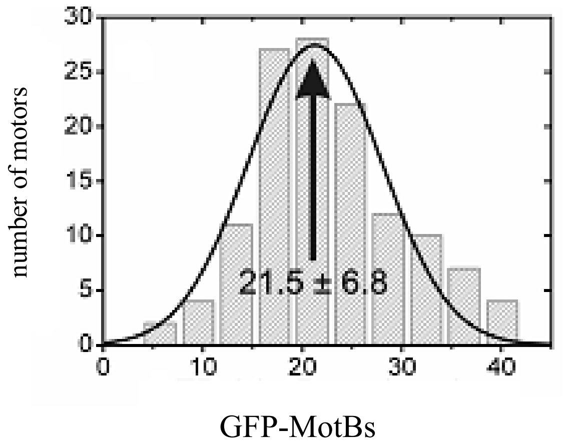

Figure 5.9: A histogram estimating the number of GFP-MotB molecules per motor.

5.7 Recovery of fluorescence in the motor

FRAP was used to determine whether there was GFP-MotB exchange in the motor. If fluorescence returned to the site of a photobleached motor, this would imply that there is GFP-MotB exchange. Fluorescence recovery would be the result of either the diffusion of a mobile membrane pool of unbleached GFP-MotBs and / or synthesis of new (and therefore, unbleached) GFP-MotBs. To determine whether GFP-MotBs exchange at the motor, and what proportion of (any) fluorescence recovery would be the result of diffusion of a membrane pool of unbleached GFP-MotBs and new protein synthesis, the following experiments were undertaken using JHC1:

1. The region adjacent to the coverslip and containing the motor was photobleached using TIRF; any fluorescence recovery would be the result of diffusion of a membrane pool of unbleached GFP-MotBs from outside the bleach region or newly synthesized GFP-MotBs incorporating into the motor.
2. The whole cell was photobleached using wide-field epifluorescence. Any fluorescence recovery in the motor would be the result of new protein synthesis because all the membrane pool of GFP-MotBs would be photobleached.
3. JHC1 were incubated with chloramphenicol (50 μg / ml) (to inhibit protein synthesis) and then the motor was photobleached using TIRF; any fluorescence recovery would be the result of diffusion of the unbleached membrane pool of GFP-MotBs.
4. Finally, the whole cell (after incubation with chloramphenicol) was photobleached using wide-field epifluorescence. No significant recovery of fluorescence would be expected because protein synthesis is inhibited and the entire membrane-pool of GFP-MotBs would be photobleached. However, GFP maturation may result in a low level of fluorescence recovery.

5.7.1 Photobleaching and image acquisition

Continuous TIRF photobleaching was initiated by opening a mechanical shutter simultaneously with the start of fluorescence data acquisition. Images were sampled continuously for 300 s at 1 Hz resulting in > 90 % photobleaching within range of the TIRF field ~ 100 nm from the coverslip. Wide-field epifluorescence photobleaching was performed for a further 300 s to photobleach the entire cell (when required).

Image files were read into custom-written analysis software written by Dr Mark Leake and Dr Richard Berry (Lab View 7.1, National Instruments, Austin, Texas). Lateral sample drift was measured by comparing time–stamped pre- and post-photobleach brightfield images (typically < 400 nm per hour), applying a correction to all subsequent image frames by linear interpolation with time.

5.7.2 GFP-MotB exchange in the motor

TIRF images of JHC1 prior to photobleaching showed a fluorescent spot at the site of tethering (Figure 5.10, top). The cell was photobleached using TIRF (experiment 1 above) and single false-colour TIRF images were taken 0, 30, 60 and 90 min after photobleaching to monitor fluorescence recovery at the motor (Figure 5.10, bottom panel). The photobleached fluorescent spot recovered with its original position and intensity profile (note the different intensity scales). The fluorescence intensity of the motor of this particular cell after 90 min had recovered ~ 55 % of the initial pre-bleach fluorescence intensity of the motor. Hence, there must be GFP-MotB exchange in the motor.

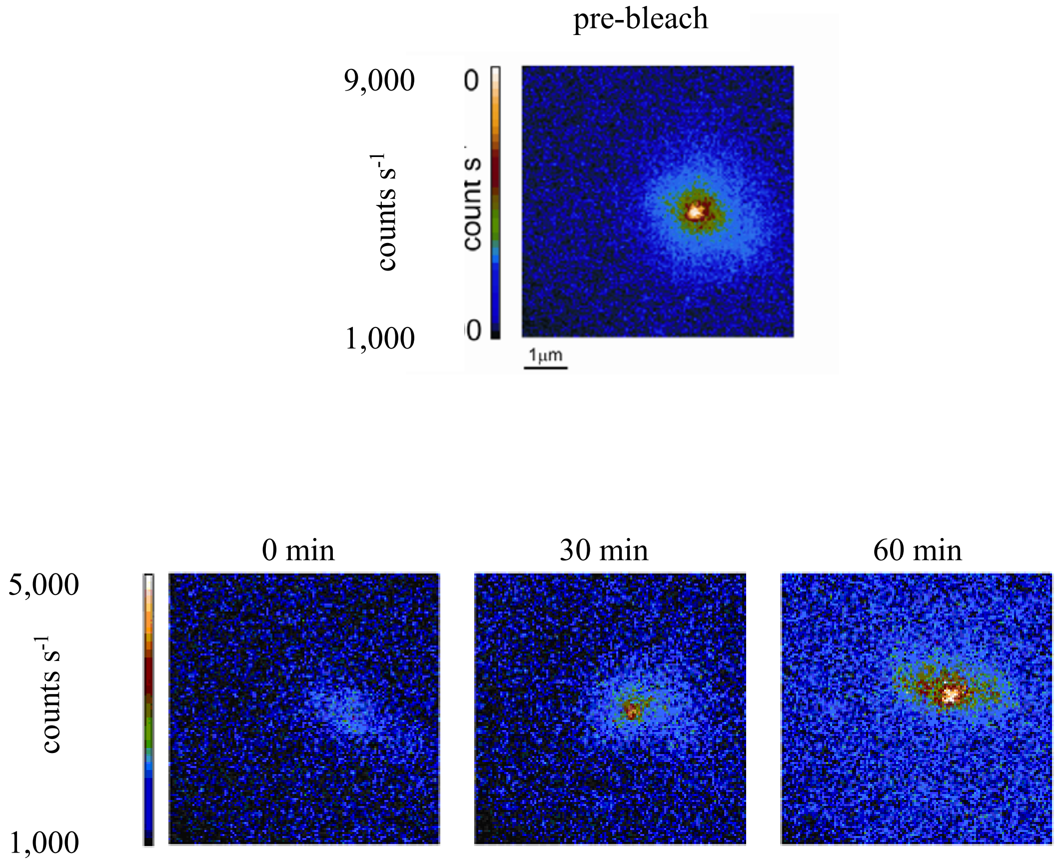

Figure 5.10: Slow fluorescence recovery in the motor of JHC1 after whole-cell photobleaching by TIRF. (Top) A false-colour TIRFM image of a tethered rotating JHC1 cell prior to photobleaching. (Bottom panel) TIRF images of the same cell, 0, 30, and 60 min after TIRF photobleaching. The fluorescent spot at the centre of rotation, corresponding to the site of motor, was photobleached. Fluorescence returned at the site of the photobleached motor, albeit to a lower fluorescence intensity than the pre-bleach fluorescence intensity of the motor. Note the different intensity scales.

5.8 Fluorescence recovery in the motor in the absence and presence of nutrient

Fluorescence recovery in the motor after TIRF photobleaching was measured in both the motor and background components of JHC1. As shown in Figure 5.11, fluorescence recovery was higher in both the motor and background components in JHC1 incubated in motility buffer supplemented with 10 % T-broth (up to 75 % of the initial pre-bleach fluorescence intensity recovered) (Figure 5.11B), compared to JHC1 incubated in motility buffer without nutrient (Figure 5.11A). This was attributable to higher levels of new GFP-MotB synthesis.

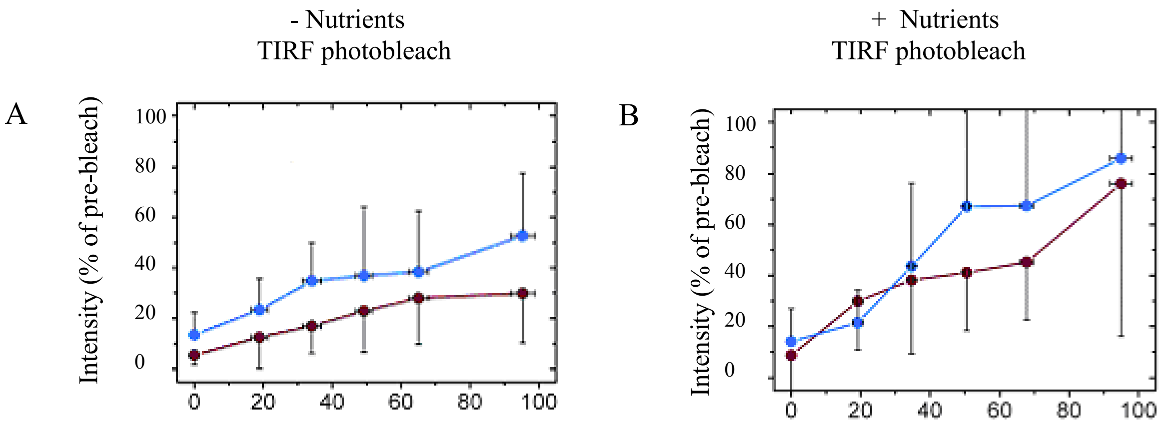

Figure 5.11: Fluorescence recovery in both the motor and background components of fluorescence of JHC1 after TIRF photobleaching. (A) Fluorescence recovery in motility buffer measured as a percentage of the pre-bleach fluorescence intensity of the motor and background components. (B) Fluorescence recovery in motility buffer supplemented with 10 % T-broth. Fluorescence recovery in the motor is shown in red and fluorescence recovery in the total background components is shown in blue. Error bars are one standard deviation; there were four cells in each data set.

5.9 Fluorescence recovery when protein synthesis is inhibited

JHC1 incubated with chloramphenicol (50 μg / ml) for 30 min prior to tethering in a tunnel slide were photobleached using wide-field epifluorescence (experiment 4 above) (Figure 5.12A) or TIRF (experiment 3 above) (Figure 5.12B). Fluorescence recovery in the motor and background components was low in cells photobleached using wide-field epifluorescence (Figure 5.13A) probably because both synthesis of new GFP-MotB was suppressed and the existing mobile pool of GFP-MotBs was photobleached. The 7 % recovery of fluorescence intensity (of the pre-bleach fluorescence intensity) had a 1 / e time of 22 min, which was close to the measured maturation time for GFP *in vivo*, this represents maturation of existing but immature GFP and also implies that a similar percentage of GFP may be initially non-photoactive in the experimental TIRF photobleaches.

A small percentage of fluorescence recovery was observed in both the motor and background components of JHC1 incubated with chloramphenicol when TIRF-photobleached (Figure 5.13B). This small amount of fluorescence recovery was attributable to the fraction of mobile GFP-MotBs that do not diffuse into the TIRF excitation region during the 300 s TIRF photobleach exposure.

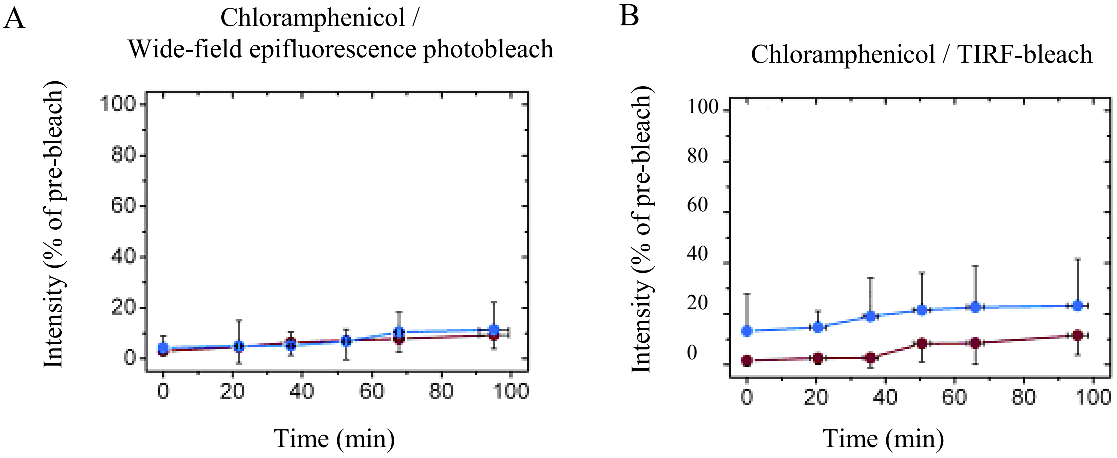

Figure 5.13: Fluorescence recovery in the motor and background components of JHC1 when protein synthesis is inhibited. Cells were incubated with 50 μg / ml chloramphenicol for 30 min prior to tethering in a tunnel slide to suppress new protein synthesis. (A) Photobleaching using wide-field epifluorescence (whole-cell bleaching) of JHC1, fluorescence recovery in both components was very low. The small amount of fluorescence recovery (7 %) was attributable to GFP maturation. (B) TIRF photobleaching of JHC1 when protein synthesis is suppressed. Fluorescence recovery of the motor component is shown in red, whilst the fluorescence recovery of the background components is shown in blue. Error bars of one standard deviation are shown; four cells were tested in each dataset.

These results show that when a motor is photobleached, fluorescence recovers at the site of the original fluorescent spot indicating that there is GFP-MotB exchange at the motor, largely with a mobile membrane pool of GFP-MotBs, and to a lesser extent from new protein synthesis.

Only minor differences in fluorescence recovery in the motor were observed between experiments 1 and 2, indicating that the majority of GFP-MotBs in the membrane pool diffuse through the TIRF excitation region (and are subsequently photobleached) during the 300 s photobleaching exposure. The proportion of the membrane pool of GFP-MotBs that are photobleached during TIRF excitation depends upon the rate of GFP-MotB diffusion and the duration of the TIRF photobleach.

5.10 Fast exchange of GFP-MotB in the motor

GFP-MotB exchange between the membrane and motor components was investigated by using focussed laser exposures of 0.5 s to photobleach all GFP-MotBs in regions of width ~ 1 µm (see section 2.3.6.1 for details on intensity). Figure 5.14 shows a FRAP / FLAP (Fluorescence Loss After Photobleaching) experiment. FRAP of both the motor and background components of fluorescence intensity in the photobleached area were monitored as photobleached GFP-MotBs diffused and exchanged with non-photobleached GFP-MotBs from the membrane pool (and to a lesser extent from new protein synthesis). At the same time, FLAP was monitored at the other end of the cell, fluorescence of this area decreased as photobleached GFP-MotBs diffused into the area from the photobleached ~1 µm diameter area.

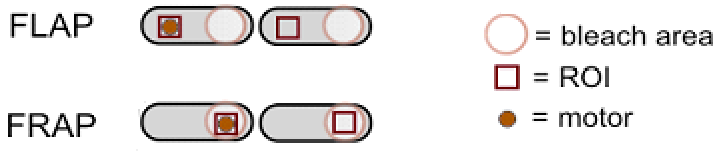

Figure 5.14: Focussed laser FRAP and FLAP. FRAP is monitored in the photobleached area containing a motor as the membrane pool of non-photobleached GFP-MotBs diffuse into the motor area. At the same time, FLAP is monitored in the non-photobleached area of the cell; fluorescence decreases as result of photobleached motor GFP-MotBs diffusing into this area.

Figure 5.15 shows TIRFM images of a JHC1 cell containing two motors before and after photobleaching of a 1 µm diameter area containing one of the motors. Fluorescence recovery (FRAP) of both the motor and background components in the photobleached area is visible, as is loss of fluorescence at the other end of the cell.

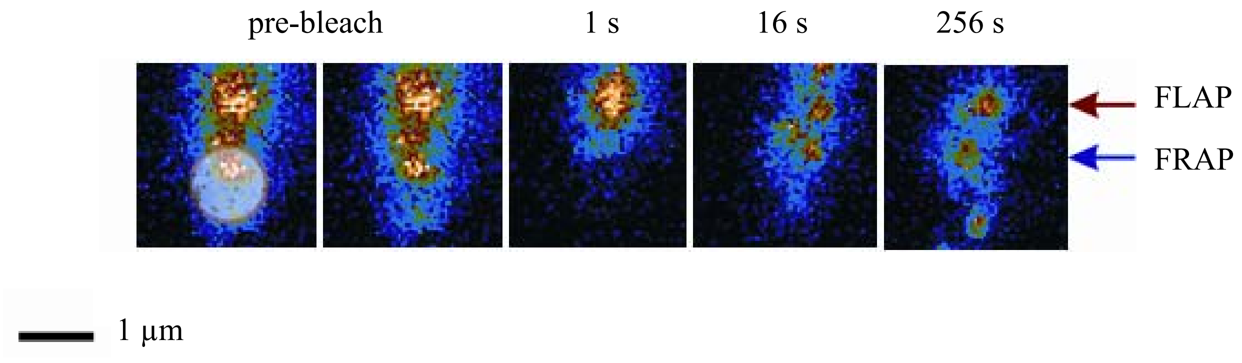

Figure 5.15: Successive TIRFM images of a JHC1 cell before and after photobleaching. The two pre-photobleach images are identical with the left panel indicating the position of the laser spot (opaque circle). Arrows on the right of the figure indicate the positions of two motors, one showing FLAP (red) and the other showing FRAP (blue).

5.10.1 Photobleaching in FRAP and FLAP experiments

For FRAP and FLAP experiments, single exposures were taken in TIRF mode at intervals up to 256 s after bleaching with the focussed laser for 0.5 s, centered either over a fluorescent spot of a putative motor (FRAP) or > 1 µm distant from a motor (FLAP), using both fixed and tethered cells in motility buffer containing 50 µg / ml chloramphenicol. Average curves were generated for FRAP and FLAP of both motor and membrane components, with all measurements of intensity components corrected for photobleaching during observation by multiplication with a cumulative factor exp (t_{total} / t_0) where t_{total} is the total accumulated time under TIRF observation and t_0 is the appropriate bleach time constant (Table 1). A final brightfield video was taken to assess lateral sample drift.

FRAP of the motor and FLAP of the membrane components averaged over 19 - 38 cells, are shown in Figure 5.16A, B. Fluorescence recovered in both components over the course of a few minutes with motor recovery slightly delayed compared to membrane recovery. FLAP occurred on the same timescale in both components. Fitting all membrane FRAP data from ROIs lacking motors to a model of a diffusing pool of GFP-MotB in the membrane gave a diffusion co-efficient of $D = 0.0075 \pm 0.0013\ \mu m^2\ s^{-1}$ (calculated by Dr Mark Leake, Department of Physics, Oxford University). Fitting all motor FRAP and FLAP data to a model of binding and unbinding at the motor gave rate constants of $0.02 \pm 0.01\ s^{-1}$ and $0.03 \pm 0.02\ s^{-1}$ respectively. The large uncertainty in rate constant estimates is a consequence of the small difference between recovery rates of motor and membrane components relative to noise.

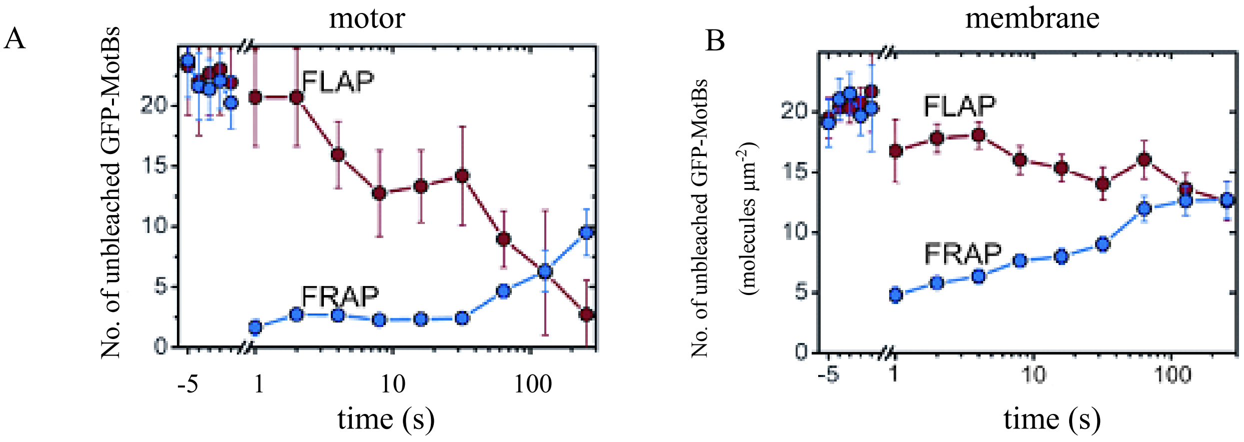

Figure 5.16: Focussed laser FRAP and FLAP to determine the number of unbleached GFP-MotBs in the motor (A) and membrane components (B) versus time. Averages of 19 (motor, FLAP), 30 (motor, FRAP) and 38 (membrane) ROIs. The error bars shown are one standard deviation.

5.11 Chapter discussion

motB was replaced with *gfp-motB* using a suicide vector which integrated into the genome by double homologous recombination, resulting in *gfp-motB* under the control of the native promoter. GFP-MotB was shown to be expressed at wild type levels allowing investigation into GFP-MotB stoichiometry and dynamics under physiological conditions.

Previous research suggests that each flagellar motor has ~ 8 stator complexes, with each stator complex having a stoichiometry of $MotA_4$: $MotB_2$. In recent torque-restoration experiments[192], at least 11 discrete speed increments were observed following induced expression of functional Mot protein in a defective background, correlating with freeze-fracture and electron micrograph studies which observed on average 11 putative stator complexes. The estimate from this study of 22 ± 7 GFP-MotB molecules per motor (i.e. ~ 11 stator complexes per motor), obtained by monitoring the step-wise photobleaching of the motor, is in close agreement with these estimates. As described in section 5.6, whole-cell photobleaches of JHC1 incubated in chloramphenicol prior to photobleaching resulted in fluorescence recovery levels of 7 % with a 1 / e time of 22 min, which is close to the measured maturation time for GFP *in vivo*, suggesting that a similar percentage of GFP may be non-photoactive in the photobleaches using TIRF, thus the estimate of ~ 22 GFP-MotBs in the motor may be an underestimate by only ~ 1 – 2 molecules. The varying numbers in the estimates of the number of GFP-MotBs may reflect natural variation in the number of stators in a motor, as well as noise due to background fluorescence, GFP blinking and instrumental limitations.

FRAP and FLAP showed active turnover of GFP-MotB, an anchored component of a multi-protein complex, between a membrane pool of ~ 200 molecules and the motor. This rapid exchange had a rate constant of the order of 0.03 s^{-1} and a diffusion co-efficient of $D \approx 0.008$ μm^2 s^{-1}. This measurement is ~ 40 % slower than measured for free membrane proteins of comparable size to a GFP-MotB dimer, but only ~ 20 % slower than a $MotA_4$: $(GFP\text{-}MotB)_2$ stator, assuming Stokes radius r scales to the 1 / 3 power with molecular weight and D scales as l / r. A relatively high diffusion co-efficient indicates that MotB in the membrane pool does not bind significantly to the cell wall but is freely diffusing.

The dwell time of a given stator in the motor was only ~ 30 s. 11 stators each with a rate constant of order 0.03 s^{-1} for leaving the motor gives an overall exchange rate of ~ 0.33 stator s^{-1}. Speed fluctuations seen in rotating wild type motors (Chapter 3) may reflect stator exchange. Rapid exchange of GFP-MotBs between the membrane pool and the functioning motor could imply that biological components may wear out and need to be replaced just as they do in man-made machines.

6 Fluorophore tagging of motor components MotA, FliG and FliM

6.1 Fluorescence Resonance Energy Transfer (FRET)

FRET (described in detail in section 1.8.1) can be used to monitor and quantify protein-protein interactions, conformational changes and protein-complex formation. CFP (Cyan Fluorescent Protein) and YFP (Yellow Fluorescent Protein) are the most popular pair of fluorophores used in FRET, both of which are variants of GFP, which are well suited for FRET because the emission spectrum of CFP partially overlaps the excitation spectrum of YFP.

6.2 Tagging MotA, FliG and FliM with fluorophores

MotA, FliG and FliM were fused to YFP with the aim of measuring FRET between various combinations of motor proteins, including MotB (which would be re-tagged with CFP using the strategy described in Chapter 4). The intention was to monitor stator complex formation between CFP-MotB and MotA-YFP to determine whether stator complexes form at the motor, or if they form prior to intergration into the motor, and to also determine molecular distances between the rotor and the stator.

A suicide vector (pDS132) was used to replace *motA*, *fliG* and *fliM* with the corresponding gene fusion in the genome, resulting in a single copy under the control of the native promoter. pDS132 was used in Chapter 3 to replace chromosomal *fliC* with *fliC^st^*. Suicide vector pKO3 was used in Chapter 4 to replace chromosomal *motB* with *gfp-motB*, but it is a very low-copy number plasmid which made cloning steps difficult, so pDS132 was used to fuse *motA*, *fliG* and *fliM* to *xfp* (encoding cyan, green or yellow fluorescent protein).

6.3 Fluorophore-labelling of MotA

The N- and C- termini of the membrane protein MotA are postulated to lie in the cytoplasm (Figure 6.1). It is unknown whether MotA contains a membrane-insertion signal sequence; the N-terminus is hydrophobic, which is consistent with a role as a membrane-insertion signal sequence, but the absence of arginine and lysine residues suggests the contrary. However, fusing the N-terminus of MotA with YFP could hinder insertion of MotA into the membrane.

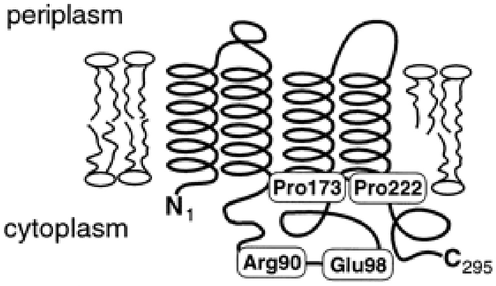

Figure 6.1: The structure of MotA. The C- and N–termini of the membrane protein MotA are thought to lie in the cytoplasm. Taken from [168].

6.3.1 N-terminal GFP-labelling of MotA

The N-terminus of MotA was fused to EGFP (if MotA-GFP proved functional and fluorescent it would have been re-tagged with EYFP).

In order to fuse *motA* with *egfp*, a construct was made by PCR and overlap-extension PCR which contained approximately 500 bp upstream of *motA* (stopping at the base before the start codon) linked directly to the start codon of *egfp*, followed by the entire length of *egfp* minus the stop codon, joined to the first 500 bp of *motA*, minus the start codon. This construct contained an 8-codon linker from pEGFP-N1 (BD Biosciences) between *motA* and *egfp*.

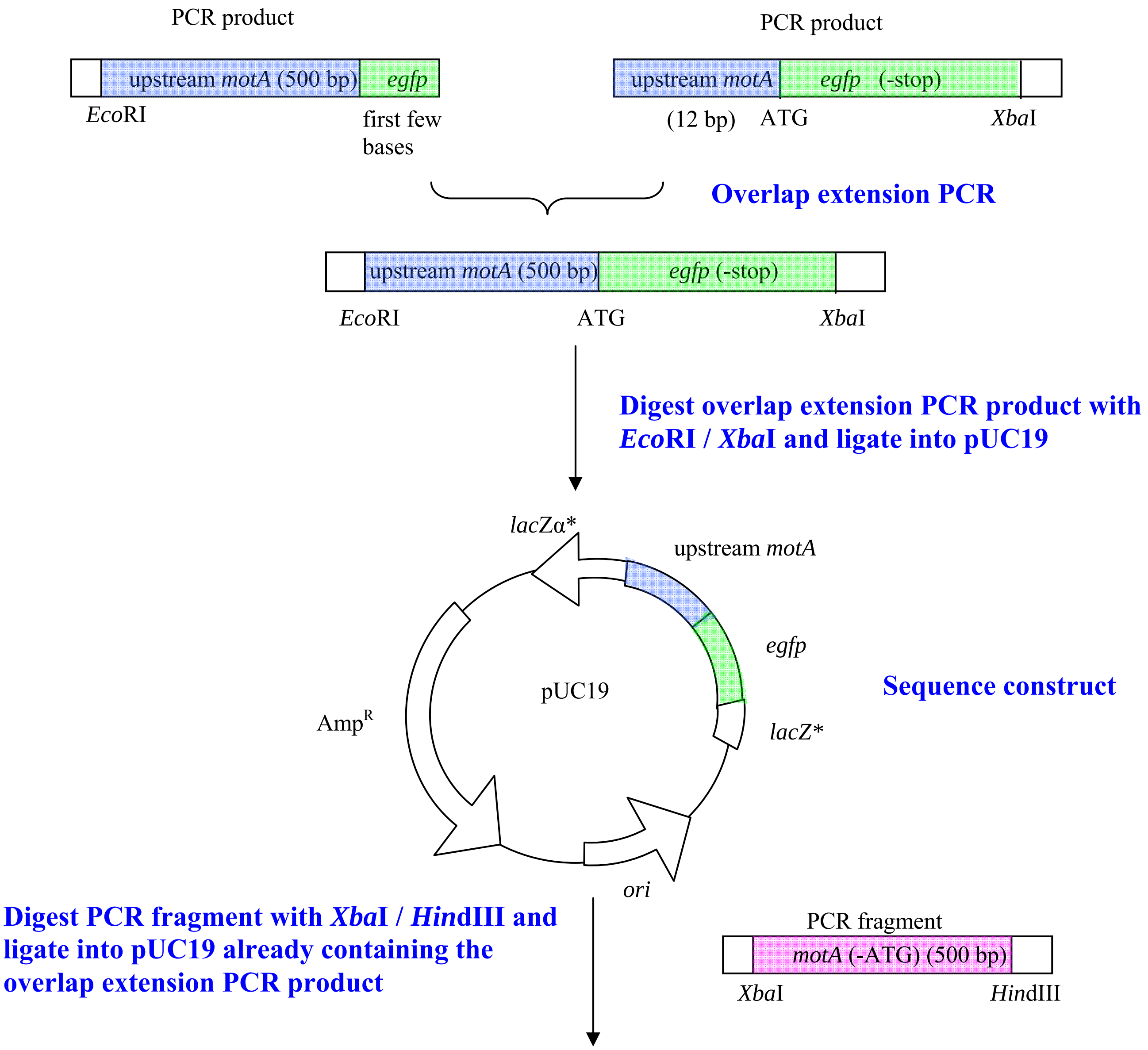

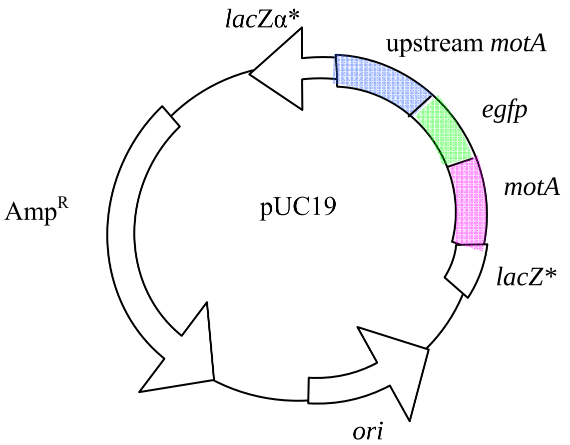

Sequence construct

Excise insert with *Eco*RI / *Xba*I, fill in ends and ligate into pDS132

Sequence construct

Integrate into the chromosome of strain RP437

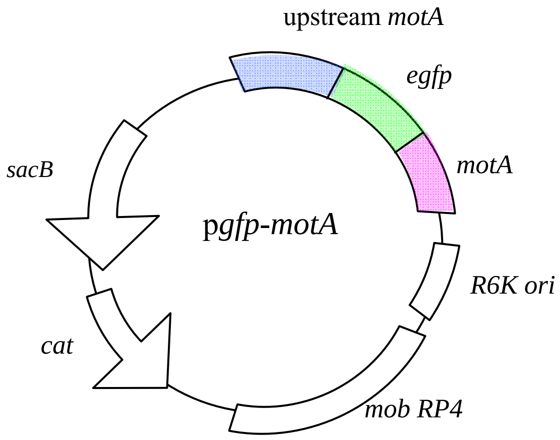

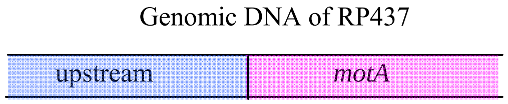

First crossover event as p*gfp-motA* integrates into the chromosome

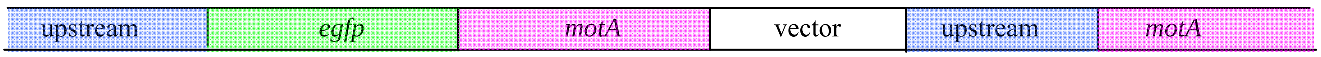

Select for Cm^R integrates
Induce second recombination event by growth on sucrose
Screen Suc^R Cm^R colonies for gene replacement by PCR and Southern blotting

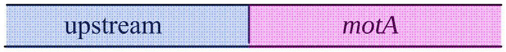

wild type genotype

gfp-motA genotype

Figure 6.3: Replacement of chromosomal *motA* with *egfp-motA* in RP437. The *egfp-motA* insert was created by a combination of PCR and overlap-extension PCR and was originally cloned into the cloning vector pUC19, then excised and ligated into the suicide vector pDS132 and electroporated into RP437. The insert integrated into the chromosome by double homolgous recombination. An 8-codon linker connected 3' *egfp* to 5' *motA*. The red line indicates the site of probe annealing during Southern blotting.

The upstream region of the *egfp-motA* insert started with a primer-encoded 5' *Eco*RI site, followed by approximately 500 bp of *motA* as far as the base before the start codon, which was amplified by PCR from RP437 chromosomal DNA using primers *motA*A1 and *motA*A2 (see Appendix H for primers), ending in the first 15 bp of *egfp* in the primer (Figure 6.2). The *egfp* sequence was amplified by PCR from pEGFP-N1 (BD Biosciences) by PCR using primers *motA*A3 and *motA*A4. The forward primer, *motA*A3, started with 12 bp homologous to genomic DNA upstream of *motA*, followed by the first 12 bp of *egfp*. The reverse primer, *motA*A4, started with a primer-encoded *Xba*I site, and amplified back into *egfp*, excluding the stop codon. The upstream and *egfp* fragments were joined together by overlap-extension PCR using the forward primer of the upstream fragment (*motA*A1) and the reverse primer of the *egfp* section (*motA*A4). Overlap-extension PCR was used so that the start codon of *egfp* remained the same distance from the Shine-Dalgarno site as in wild type genomic DNA. This fragment was digested with *Eco*RI / *Xba*I and ligated into pUC19.

The downstream fragment was amplified from RP437 chromosomal DNA using a forward primer containing a primer-encoded *Xba*I site (*motA*A5), followed by *motA* (minus the start codon), and a reverse primer which bound approximately 500 bp into *motA*, and contained a primer-encoded *Hin*dIII site (*motA*A6). This fragment was ligated into pUC19 already containing the upstream and *egfp* regions, using the *Xba*I and *Hin*dIII sites (Figure 6.2). This construct was sequenced to ensure there were no PCR-generated errors. The entire insert was excised from pUC19 using *Eco*RI / *Hin*dIII, the ends were filled in and the *egfp-motA* nsert was ligated into *Sma*I cut pDS132, and sequenced (see Appendices C and G for primers); this construct was called p*gfp-motA*. From hereon in, *egfp-motA* is referred to as *gfp-motA* for simplicity.

RP437 was electroporated with p*gfp-motA* and plated onto Cm / LBA plates. Cm^R colonies were serially-diluted and spread-plated onto LBA plates containing 5 % sucrose (without NaCl), which selected for pDS132 backbone excision from the chromosome following a second crossover event, because sucrose is lethal to cells carrying *sacB*. Cm^S Suc^R colonies were replica-plated onto Cm / LBA plates and LBA plates containing 5 % sucrose (without NaCl) to confirm a second crossover event and loss of vector backbone from the chromosome.

6.3.2 C-terminal YFP-labelling of MotA

The C-terminus of MotA was fused to EYFP.

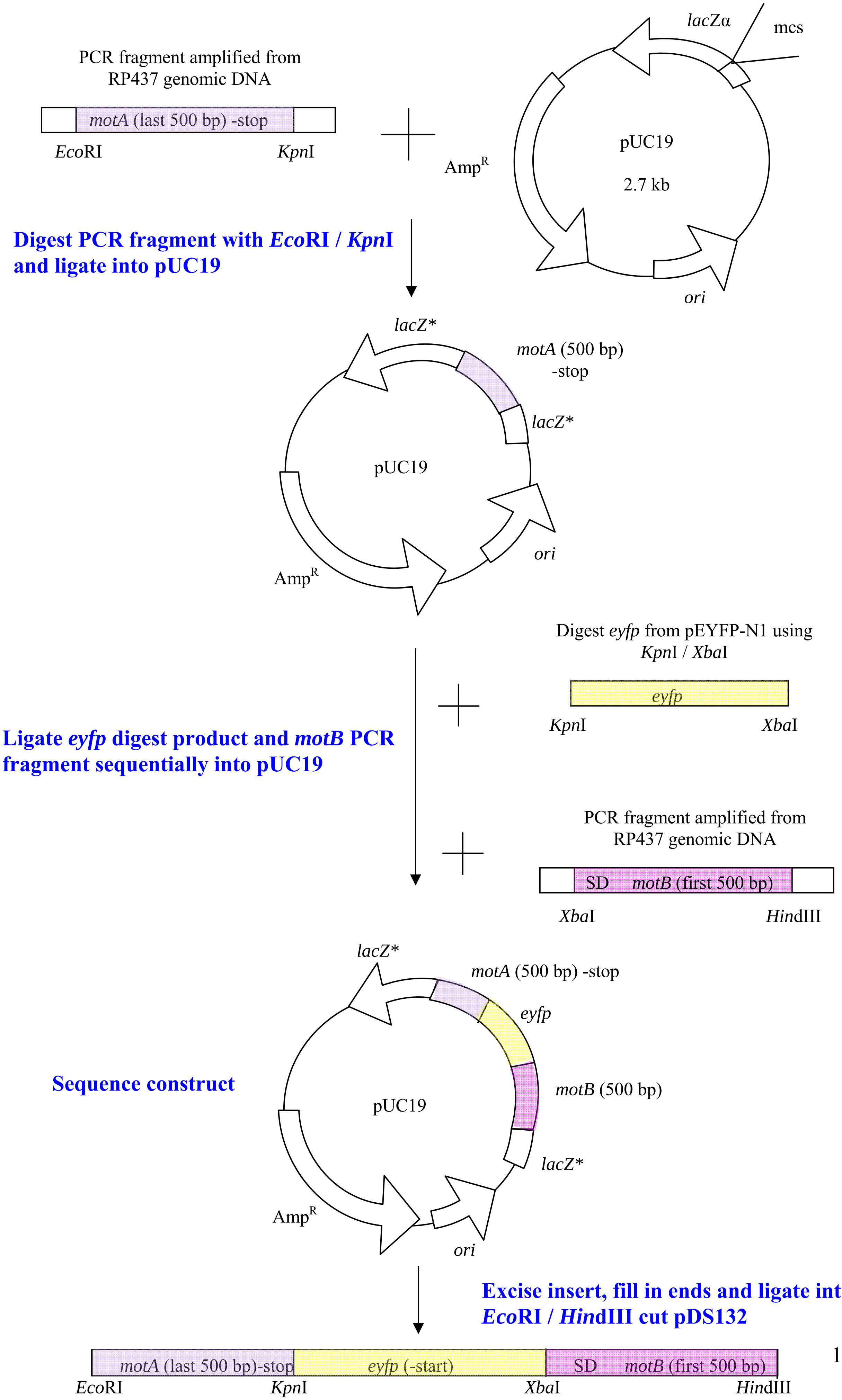
PCR fragment amplified from
RP437 genomic DNA
motA (last 500 bp) -stop
EcoRI
KpnI
lacZα
mcs
pUC19
2.7 kb
AmpR
ori
Digest PCR fragment with EcoRI / KpnI and ligate into pUC19
lacZ*
motA (500 bp) -stop
lacZ*
pUC19
ori
AmpR
Digest eyfp from pEYFP-N1 using KpnI / XbaI
eyfp
KpnI
XbaI
Ligate eyfp digest product and motB PCR fragment sequentially into pUC19
PCR fragment amplified from
RP437 genomic DNA
SD motB (first 500 bp)
XbaI
HindIII
lacZ*
motA (500 bp) -stop
eyfp
motB (500 bp)
Sequence construct
pUC19
lacZ*
AmpR
ori
Excise insert, fill in ends and ligate into EcoRI / HindIII cut pDS132
motA (last 500 bp)-stop
eyfp (-start)
SD motB (first 500 bp)
EcoRI
KpnI
XbaI
HindIII

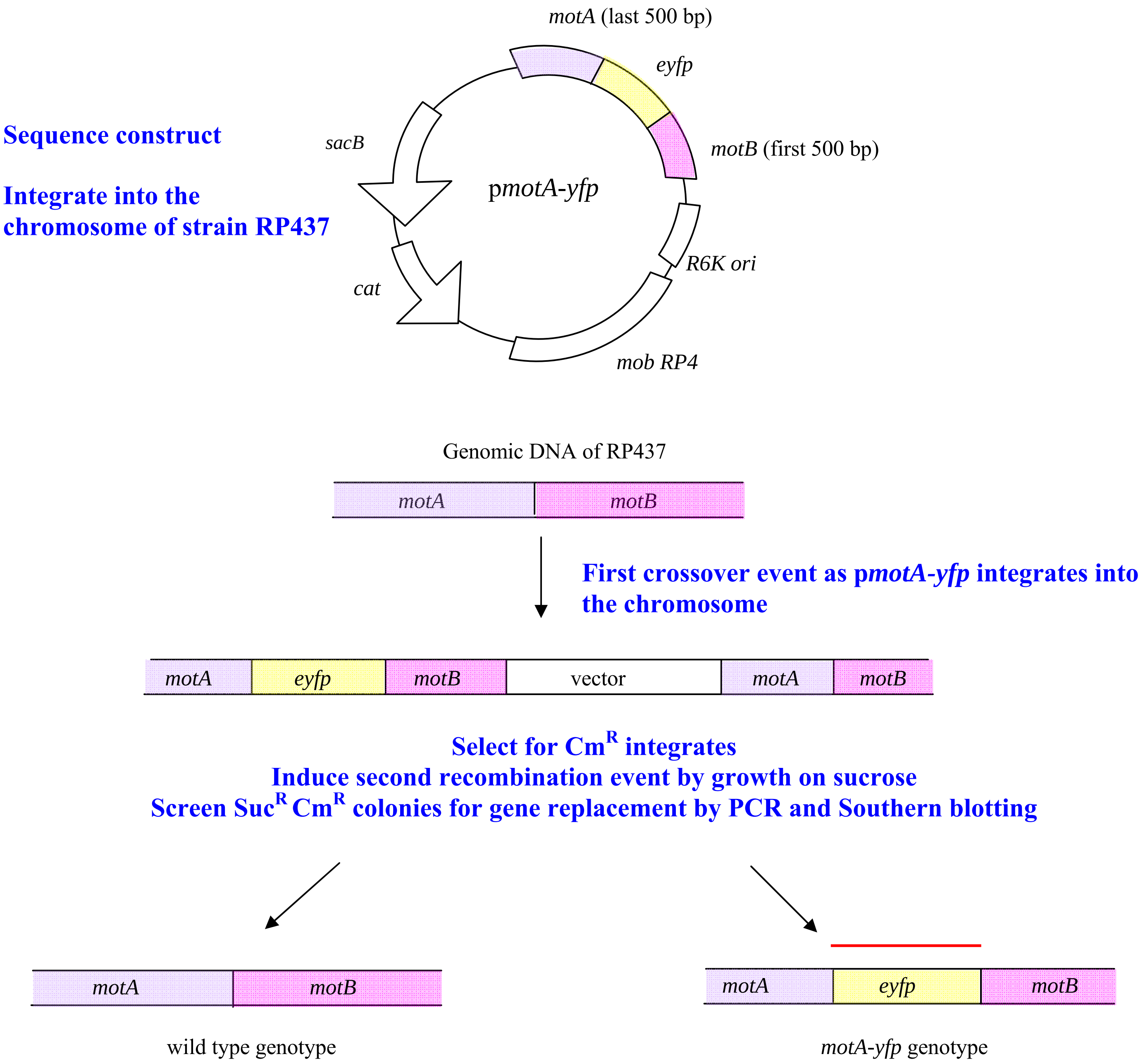

Figure 6.3: Construction of the *motA-eyfp* insert used to replace *motA* in the chromosome of RP437. The *motA-eyfp* insert was created by PCR, ligated into the cloning vector pUC19, excised and ligated into the suicide vector pDS132 and electroporated into RP437. *motA-eyfp* integrated into the genome by double homologous recombination. The Shine-Dalgarno site of *motB* (SD) was repeated after *motA-eyfp* because of the 3 bp overlap between *motA* and *motB*. An 11-codon linker separated the 3' end of *motA* and the 5' end of *eyfp*. The red line indicates the site of probe annealing during Southern blotting (see section 6.3.3).

The upstream fragment was amplified from RP437 chromosomal DNA, using a forward primer (*motA*1) that bound approximately 500 bp from the end of *motA* and contained a primer-encoded *Eco*RI site (see Appendix I for primers) (Figure 6.3). The reverse primer (*motA*2) bound at the end of *motA* 2 bp into the stop codon and contained a primer-encoded *Kpn*I site. pEYFP-N1 (BD Biosciences) was digested with *Kpn*I / *Xba*I to create the *eyfp* fragment. The downstream fragment was amplified from RP437 chromosomal DNA using a forward primer containing a primer-encoded *Xba*I site (*motA*3), and amplified the region directly downstream of *motA*. Primer *motA*3 contained a 15 bp repeat of the Shine-Dalgarno site of *motB* (to affect translation of *motB* as little as possible). The reverse primer (*motA*4) had a primer-encoded *Hin*dIII site, and amplified back from approximately 500 bp downstream of *motA*. The fragments were ligated sequentially into pUC19, which was sequenced to ensure there were no PCR-generated errors. The *motA-eyfp* insert was excised using *Eco*RI / *Hin*dIII; the ends were filled in and ligated into *Sma*I cut pDS132. The final construct, called p*motA-yfp*, contained the 3' region of *motA*, an 11-codon linker region, then *eyfp* in frame with *motA*, then 500 bp of genomic DNA downstream of *motA*, directly after the stop codon. p*motA-yfp* was sequenced (for primers see Appendices C and G) and electroporated into RP437 as before (see section 6.3.1). From hereon in, *motA-eyfp* is referred to as *motA-yfp* for simplicity.

6.4 Confirming genomic replacement of *motA* with *gfp-motA or motA-yfp*

Chromosomal DNA preparations from Cm^S Suc^R colonies resulting from RP437 electroporation with p*gfp-motA* were digested with *Bgl*II / *Pst*I, whilst Cm^S Suc^R colonies resulting from RP437 electroporation with p*motA-yfp* were digested with *Bgl*II / *Nsi*I.

Chromosomal DNA digests were electrophoresed and Southern-blotted. Southern blots were hybridised with a DIG-labelled DNA probe of *eyfp* cut from pEYFP-N1 with *Eco*RI / *Xba*I. Blank lanes can be seen in both Southern blots, which were the result of unsuccessful gene replacement (Figure 6.4).

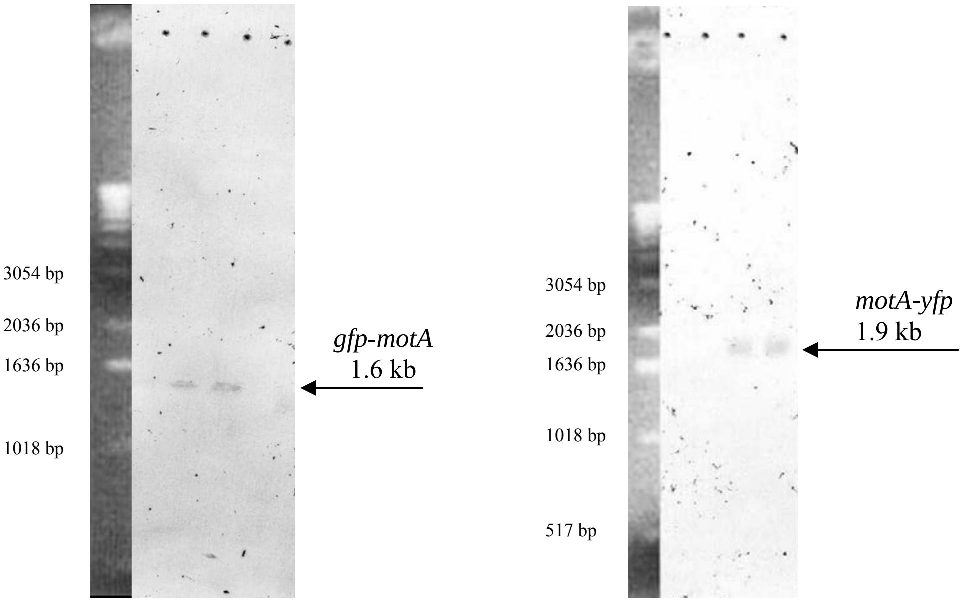

Figure 6.4: Southern blots of Cm^{S} Suc^{R} isolates resulting from electroporation of RP437 with either p*gfp-motA* (left) or p*motA-yfp* (right), which integrated into the chromosome by double homologous recombination. Membranes were probed with a DIG-labelled *eyfp* DNA probe which highlighted bands of the correct size in many lanes in both blots. A 1 kb DNA ladder is shown on the left of both blots. Blank lanes can be seen on both blots which are the result of unsuccessful gene replacement.

To confirm that *gfp-motA* and *motA-yfp* had integrated at the correct location on the chromosome, the *motA* region was amplified by PCR to include 200 bp upstream and downstream of the regions cloned into p*gfp-motA* and p*motA-yfp*. The *gfp-motA* region of the chromosome was amplified using primers 1975855 and 1974478 (see Appendix J), whilst the *motA-yfp* region of the chromosome was amplified using primers 1973579 and 1974878 (see Appendix J); both PCR fragments were sequenced.

One *motA-yfp* isolate ('JHC2.27') was sequenced, and three *gfp-motA* isolates ('JHC3.72', 'JHC3.81' and 'JHC3.82') were sequenced. All four strains had the correct sequence of *gfp-motA* or *motA-yfp* in-frame on the chromosome at the correct location.

6.5 Phenotypic analysis of *gfp-motA* and *motA-yfp* strains

Cultures were grown until stationary phase in LB-broth with shaking at 30 ºC. 5 µl of culture was inoculated onto soft-agar swarm plates and incubated at 30 ºC.

motA-yfp (JHC2.27) and *gfp-motA* strains (JHC3.72, JHC3.81 and JHC3.82) were non-motile (Figure 6.5A). However, after 14 h incubation on the swarm plates, flares were visible emerging from JHC2.27 (*motA-yfp*) (Figure 6.5B). These mutants were picked and grown to stationary phase in LB-broth with shaking at 30 ºC and re-inoculated onto fresh swarm plates (Figure 6.5C). Further flares formed and the process of growing cultures to stationary phase in LB-broth and re-inoculating onto fresh swarm plates was repeated many times until swarm rates comparable to parental strain RP437 were observed (see later Figure 6.6).

All non-motile *motA-yfp* and *gfp-motA* strains (JHC2.27, JHC3.72, JHC3.81 and JHC3.82) were tethered in tunnel slides, but no rotating tethered cells were observed, indicating that the initial lack of swarming was a result of a defect(s) in motility, rather than chemotaxis.

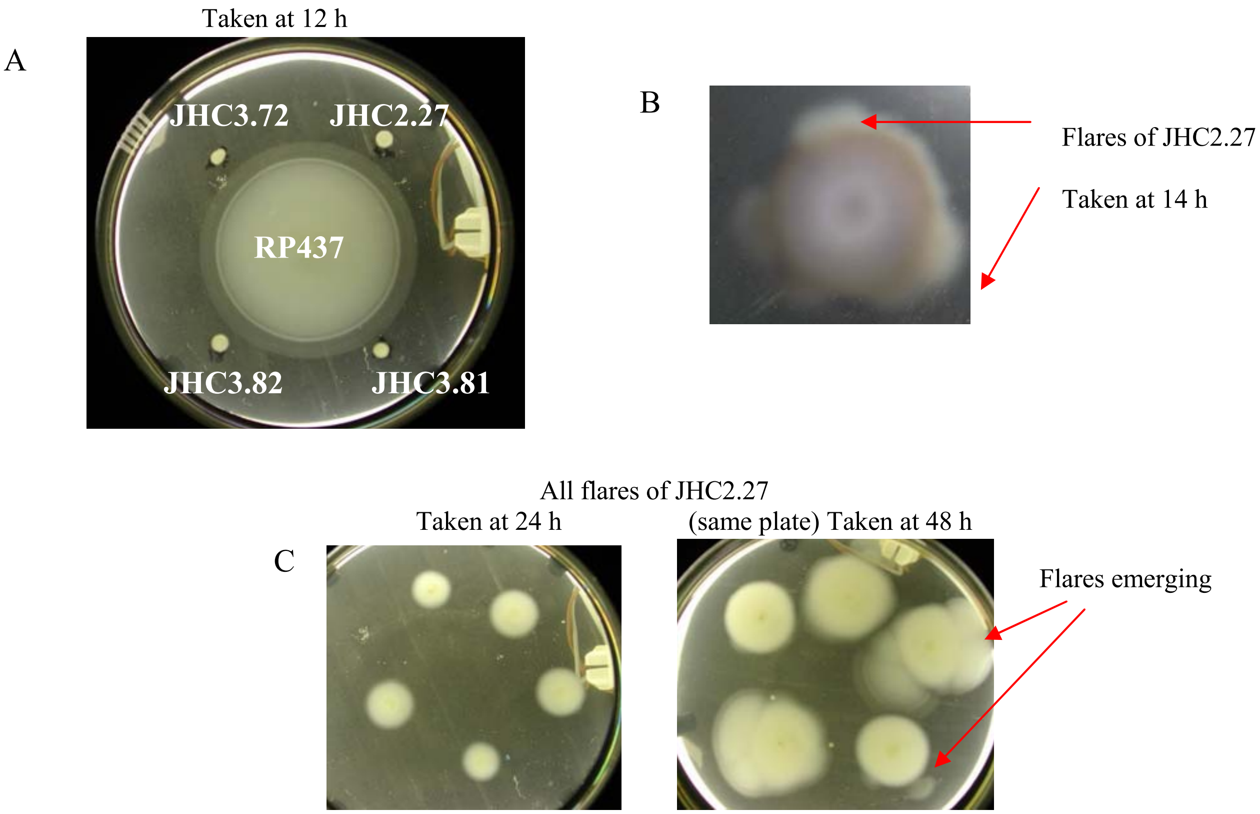

Figure 6.5: Swarm plate analysis of *motA-yfp* and *gfp-motA* strains. (A) Swarming phenotypes of three original *gfp-motA* strains (JHC3.72, JHC3.81, and JHC3.82) and one *motA-yfp* strain (JHC2.27); together with parental strain RP437. This photo was taken at 12 h. (B) A close-up of *motA-yfp* JHC2.27 which produced flares after ~ 14 h incubation at 30 ºC. These flares were subsequently grown to stationary phase in LB-broth and re-inoculated on fresh swarm plates shown in C. (C) The photo on the left was taken at 24 h; the swarm plate inoculated with parental RP437 strain is not shown at this time point because it had swarmed over the entire surface of the plate after 20 h. The photo on the right was taken at 48 h and further flares can be seen emerging.

The *motA* region of the chromosome of cells from four flares of JHC2.27 (*motA-yfp*) were amplified by PCR to include 700 bp upstream of *motA* and 700 bp into *motB,* and sequenced. Strangely, flares JHC2.27.O and JHC2.27.M (Figure 6.6A), which had swarm rates approximately one-fifth the rate of RP437 had the perfect sequence of *motA-yfp* in-frame on the chromosome. Flare JHC2.27.27, which also had the perfect sequence of *motA-yfp* in-frame on the chromosome swarmed at approximately three-quarters the rate of RP437 (Figure 6.6B). Flare JHC2.27.21 which had a wild type swarm rate had excised all but ~ 100 bp of the 3’ end of *yfp* from the chromosome (Figure 6.6C).

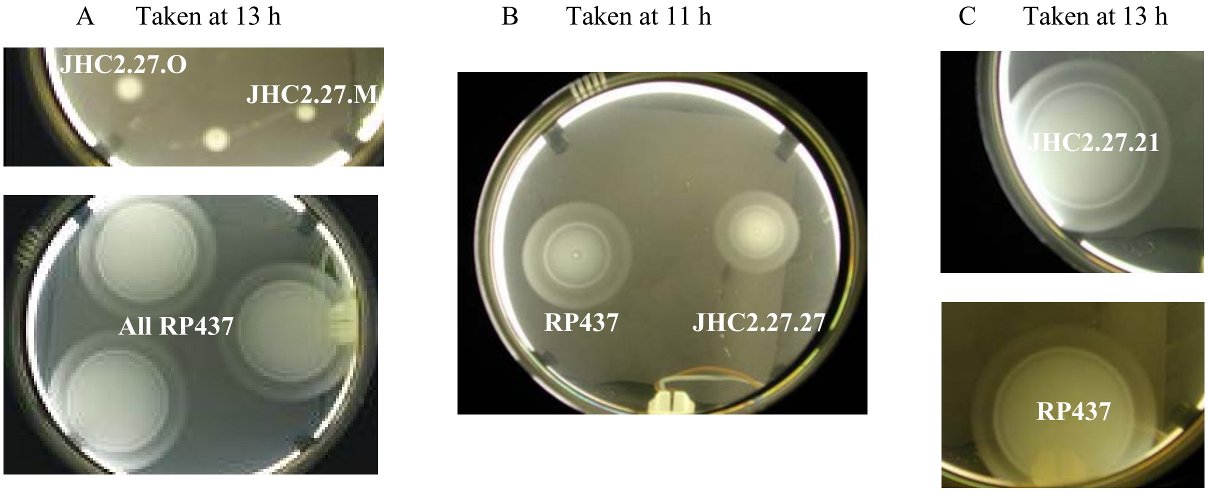

Figure 6.6: Swarm plate analysis of flares produced from *motA-yfp* strain JHC2.27. (A) Flares JHC2.27.O and JHC2.27.M on the top plate, and RP437 on the lower plate, both taken at 13 h. (B) Flare JHC2.27.27 and RP437 were inoculated on the same swarm plate; the photo was taken at 11 h. (C) Swarm plates of flare JHC2.27.21 on top plate and RP437 on the lower plate, both photos were taken at 13 h. All four flares had the *motA* region of the chromosome sequenced.

6.6 Epifluorescence and TIRFM of *gfp-motA* and *motA-yfp* strains

RP437, non-motile *gfp-motA* strains JHC3.72, JHC3.81 and JHC3.82, non-motile *motA-yfp* strain JHC2.27 and cells taken from flares formed from JHC2.27 were grown at 30 ºC with shaking in LB-broth until OD $_{600}$ 0.8 and viewed using epifluorescence and TIRF microscopy (only epifluorescence images are shown in Figure 6.7). No fluorescent spots were visible in any *gfp-motA* or *motA-yfp* strain. The levels of cytoplasmic fluorescence of *gfp-motA* and *motA-yfp* isolates were the same as RP437, indicating that neither the fusion proteins nor XFP were expressed.

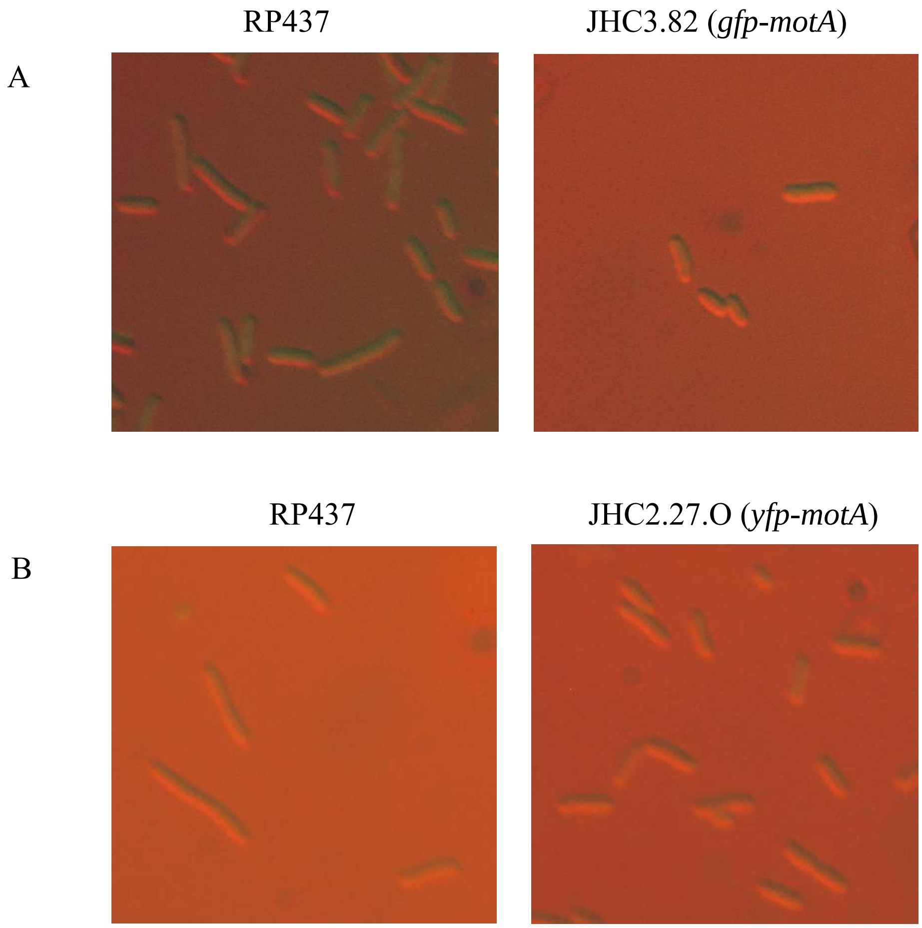

RP437

JHC3.82 (*gfp-motA*)

RP437

JHC2.27.O (*yfp-motA*)

Figure 6.7: Epifluorescence images of RP437, *gfp-motA* and *yfp-motA* strains. (A) RP437 and non-motile JHC3.82 (*gfp-motA*). (B) RP437 and flare JHC2.27.O (*motA-yfp*). JHC2.27.O was a flare produced from JHC2.27. JHC2.27.O had the perfect sequence of *motA-yfp* in-frame on the chromosome. No fluorescence spots were observed in any *gfp-motA* or *yfp-motA* strain, and the level of cellular fluorescence was the same as parental strain RP437, indicating that neither the fusion proteins nor XFP were expressed.

6.7 Western blot analysis of *gfp-motA* and *motA-yfp* strains

To confirm that the fusion proteins GFP-MotA and MotA-YFP were not expressed, cell lysates of *gfp-motA* strains JHC3.72, JHC3.81 and JHC3.82 and *motA-yfp* strain JHC2.27, flares of JHC2.27, RP437 and YS34 (Δ*motA* Δ*motB* Δ*pilA* Δ*cheY* *fliC*::*Tn10*) were subjected to western blot analysis. Cells were grown in LB-broth with shaking at 30 ºC until an OD_{600} 0.8. 1 ml of culture was centrifuged and resuspended in

50 μl of SDS-PAGE buffer. Gels were blotted and hybridised with either a 1 / 1000 dilution of anti-MotA antibody, a 1 / 1000 dilution of anti-MotB antibody or a 1 / 50 dilution of anti-GFP antibody (anti-GFP antibody can bind to CFP, GFP and YFP) (Figure 6.8).

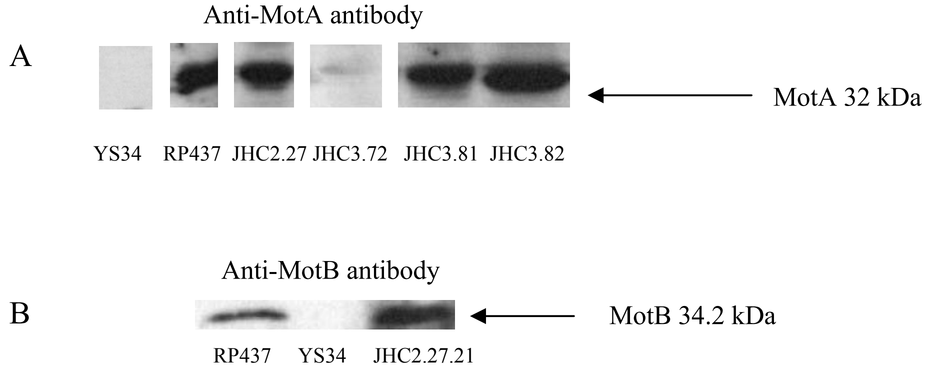

Figure 6.8: Western blot analysis of *gfp-motA* and *motA-yfp* strains. (A) Anti-MotA antibody western blot of cell lysate from YS34 (Δ*motA* Δ*motB* Δ*pilA* Δ*cheY fliC*::*Tn10*), RP437, three non-motile *gfp-motA* strains JHC3.72, JHC3.81 and JHC3.82 and non-motile *motA-yfp* strain JHC2.27 were subjected to SDS-PAGE, blotted and probed with 1 / 1000 dilution of anti-MotA antibody. All flares of JHC2.27 did not produce any bands corresponding to MotA or the fusion protein, so data is not shown. (B) Anti-MotB antibody western blot of cell lysate of RP437, YS34 and flare JHC2.27.21. All other isolates tested did not produce any bands, so data is not shown. A 1 / 1000 dilution of anti-MotB antibody was used. The anti-GFP antibody western blot is not shown because no bands were detected in cell lysate from any *gfp-motA* or *motA-yfp* strain.

A band corresponding to MotA is clearly visible in the cell lysate of RP437 and non-motile JHC2.27 (*motA-yfp*), JHC 3.81 (*gfp-motA*) and JHC3.82 (*gfp-motA*). Non-motile JHC3.72 (*gfp-motA*) produced a very faint band corresponding to MotA (Figure 6.8A). No bands corresponding to the predicted molecular weight of GFP-MotA and YFP-MotA were detected in cell lysate of any strain. Intriguingly, cultures from cells taken from flares produced from JHC2.27 did not produce any (detectable) bands corresponding to either YFP-MotA or MotA. As expected, no MotA was detected in cell lysate of YS34.

Western blots hybridised with anti-GFP antibody (BD Biosciences) (which can detect CFP, GFP and YFP) failed to detect any band(s) corresponding to either the predicted molecular weight of the fusion protein or XFP in any isolate (data not shown).

Anti-MotB antibody (Figure 6.8B) detected a band corresponding to the molecular weight of MotB in only one strain taken from a flare JHC2.27.21. All other strains tested failed to produce any bands (data not shown). All cells taken from flares are motile by definition, yet no MotB was detected; presumably MotB expression was down-regulated to such an extent that it was undetectable using western blotting. Cells from flare JHC2.27.21 which expressed MotB at a level comparable to RP437 had excised all but ~ 100 bp of *yfp* from the chromosome, yet strangely, no MotA was detected in the anti-MotA antibody blot. As expected, no MotB was detected in cell lysate of YS34.

In summary, even though the sequence of *gfp-motA* and *motA-yfp* (± 700 bp upstream and downstream) was perfect and in-frame in all four original non-motile strains (JHC3.72, JHC3.81, JHC3.82 and JHC2.27) and in all motile flares produced from JHC2.27 (with one exception), no detectable fusion protein or XFP was detected in cell lysate of any strain. This suggests distant suppressor mutations may have occurred to allow motility, but time did not permit further investigation.

6.8 YFP-labelling of FliM and FliG

The strategy used to construct *fliM-yfp* and *fliG-yfp* strains was the same as that used to make the *motA-yfp* strain. EYFP was fused to the C-terminus of both FliM and FliG because when Berg and Sourjik[110] over-expressed FliM-YFP from an inducible plasmid, FliM-YFP was better at complementing a null *fliM* mutant in swarm plates than YFP-FliM.

The *fliM-yfp* and *fliG-yfp* inserts were cloned initially into the cloning vector pUC19, excised and ligated into the suicide vector pDS132 and electroporated into RP437 where they integrated into the chromosome by double homologous recombination.

6.8.1 Constructing a *fliM-yfp* strain

The upstream fragment of the *fliM-yfp* insert used to replace chromosomal *fliM* contained the last 500 bp of *fliM* minus the stop codon which were amplified by PCR from RP437 chromosomal DNA using a forward primer that contained a primer-encoded *Sac*I site (*fliM*1, Appendix K) (Figure 6.9). The reverse primer (*fliM*2) bound at the end of *fliM* 2 bp into the stop codon and contained a primer-encoded *Xma*I site. pEYFP-N1 (BD Biosciences) was digested with *Xma*I / *Sac*I to create the *eyfp* fragment. The downstream fragment was amplified by PCR from RP437 chromosomal DNA using a forward primer containing a primer-encoded *Xba*I site (*fliM*3), and amplified the region directly downstream of *fliM*. Primer *fliM*3 contained a 15 bp repeat of the Shine-Dalgarno site of *fliN* (to disrupt expression of downstream *fliN* as little as possible). The reverse primer (*fliM*4) had a primer-encoded *Sph*I site, and amplified back from approximately 500 bp downstream of *fliM*. The fragments were ligated sequentially into pUC19 which was sequenced to ensure there were no PCR-generated errors. *fliM-eyfp* was excised using *Sac*I / *Sph*I and ligated directly into pDS132. The final construct contained the 3' region of *fliM*, an 8-codon linker region from pEGFP-N1, *eyfp* in frame with *fliM*, then 500 bp of genomic DNA downstream of *fliM,* directly after the stop codon (Figure 6.9). This construct was sequenced and called p*fliM-yfp*. From hereon in, *fliM-eyfp* is referred to as *fliM-yfp* for simplicity.

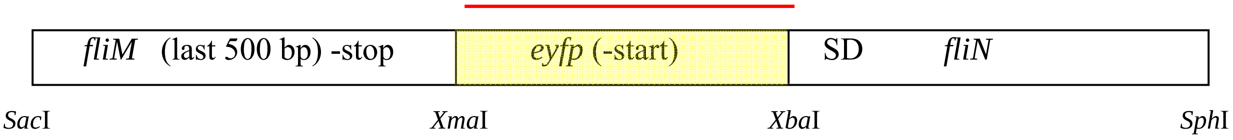

Figure 6.9: The *fliM-eyfp* construct used to replace *fliM* in the chromosome of RP437. This construct was made in the cloning vector pUC19, excised and ligated directly into the suicide vector pDS132 which integrated into the chromosome by double homologous recombination. The Shine-Dalgarno site (SD) of *fliN* was repeated because of a 3 bp overlap between *fliM* and *fliN*. An 8-codon linker connected *fliM* to *eyfp*. The red line indicates site of probe annealing in Southern blotting (see section 6.5.3).

6.8.2 Constructing a *fliG-yfp* strain

The *fliG-yfp* insert was created in the same way as the *fliM-yfp* insert using the same restriction sites (Figure 6.10) (see Appendix L for primers). The resulting construct was sequenced and called p*fliG-yfp*. From hereon in, *fliG-eyfp* is referred to as *fliG-yfp* for simplicity.

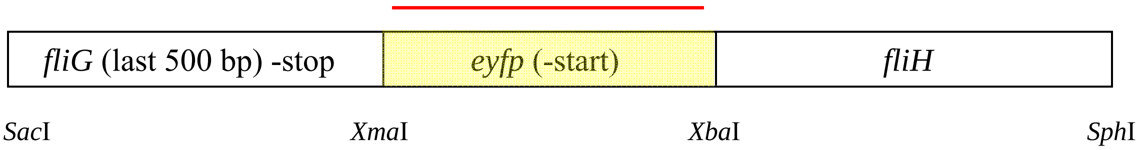

Figure 6.10: The *fliG-eyfp* insert used to replace *fliG* in the chromosome of RP437. This insert was constructed in the cloning vector pUC19, excised and directly ligated into *Sac*I / *Sph*I cut suicide vector pDS132. *fliG-yfp* integrated into the chromosome by double homologous recombination. The red line indicates site of probe annealing in Southern blotting (see section 6.4.3).

6.9 Confirming chromosomal gene replacement

Chromosomal DNA preparations of Cm^S Suc^R colonies of RP437 resulting from electroporation with p*fliM-yfp* were digested with *Acl*I; whilst Cm^S Suc^R colonies of RP437 resulting from electroporation with p*fliG-yfp* were digested with *Bgl*II. All chromosomal DNA digests were electrophoresed and Southern-blotted (Figure 6.12). Membranes were hybridised with a DIG-labelled DNA probe of *eyfp* cut from pEYFP-N1 with *Eco*RI / *Xba*I. Replica-crosses of colonies that produced bands of the correct size were picked and frozen at – 80 ºC. Blank lanes can be seen in both Southern blots, which were the result of unsuccessful gene replacement (Figure 6.11).

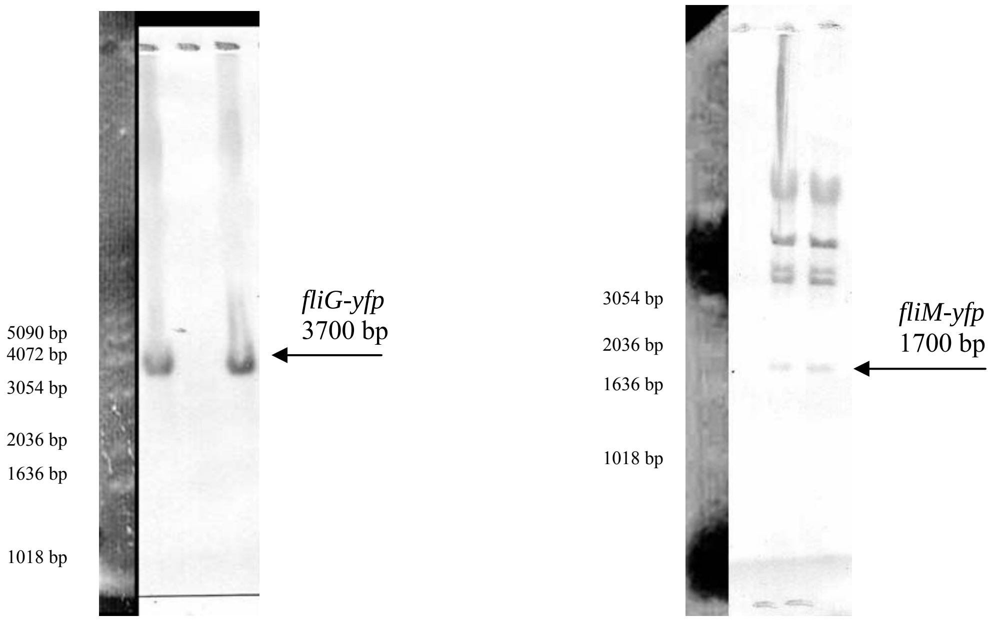

Figure 6.11: Southern blots of Cm^S Suc^R colonies resulting from electroporation of RP437 with either p*fliG-yfp* (left) or p*fliM-yfp* (right). A 1 kb ladder is shown on the left-hand side of each Southern blot. The expected size of the band is indicated. Multiple bands of higher molecular weights are visible in the *fliM-yfp* Southern blot as a result of incomplete chromosomal DNA digestion with *Acl*I. Blank lanes can be seen in both blots, which were the result of unsuccessful gene replacement.

To confirm that *fliM-yfp* and *fliG-yfp* had integrated at the correct location in the genome, the *fliM* or *fliG* regions of the chromosome amplified by PCR and sequenced. The *fliM* region of the chromosome was amplified using primers 2018316 and 2019784 (Appendix M) which annealed outside the upstream and downstream regions cloned into p*fliM-yfp*. The *fliG* region of the chromosome was amplified using primers 2013146 and 2014624 (Appendix N).

Sequenced *fliM-yfp* strains were called JHC4.25, JHC4.26, JHC4.31 and JHC4.32. All four had the perfect sequence of *fliM-yfp* in-frame in the chromosome at the correct location. Sequenced *fliG-yfp* strains were called JHC5.8, JHC5.42 and JHC5.44; and again, all three had the perfect sequence of *fliG-yfp* in-frame at the correct location in the chromosome.

6.10 Swarm plate analysis of *fliM-yfp* strains

JHC4.25, JHC4.26, JHC4.31 and JHC4.32 were grown to stationary phase with shaking in LB-broth at 30 ºC. 5 µl of culture was inoculated onto soft-agar swarm plates (0.25 % agar in LB-broth).

All four *fliM-yfp* strains were non-motile, however, after 40 h flares were visible emerging from JHC4.25 and JHC4.32, isolates were called JHC4.25.1 and JHC4.31.1 respectively; JHC4.26 and JHC4.32 did not produce any flares (Figure 6.12A). Isolates JHC4.25.1 and JHC4.31.1 were grown to stationary phase with shaking in LB-broth and re-inoculated onto fresh swarm plates (Figure 6.12B). After 24 h, flares formed from JHC4.25.1 (Figure 6.12C), which were grown to stationary phase with shaking in LB-broth and subsequently inoculated onto fresh swarm plates (Figure 6.13D), which had swarm rates similar to RP437. No further flares formed from isolates JHC4.25.1.1, JHC4.25.1.2 and JHC4.25.1.3.

All four non-motile *fliM-yfp* strains (JHC4.25, JHC4.26, JHC4.31 and JHC4.32) were tethered via anti-FliC antibody in tunnel slides. No rotating cells were observed, indicating that the initial lack of swarming was a result of a defect(s) in motility, rather than chemotaxis.

The *fliM* region of the chromosome of isolates JHC4.25.1, JHC4.25.1.1, JHC4.25.1.2 and JHC4.25.1.3 were sequenced, and all four had the perfect *fliM-yfp* sequence in-frame on the chromosome. Isolate JHC4.31.1 was sequenced and had excised *yfp* completely from the chromosome, yet it had a slightly slower swarm rate compared to RP437.

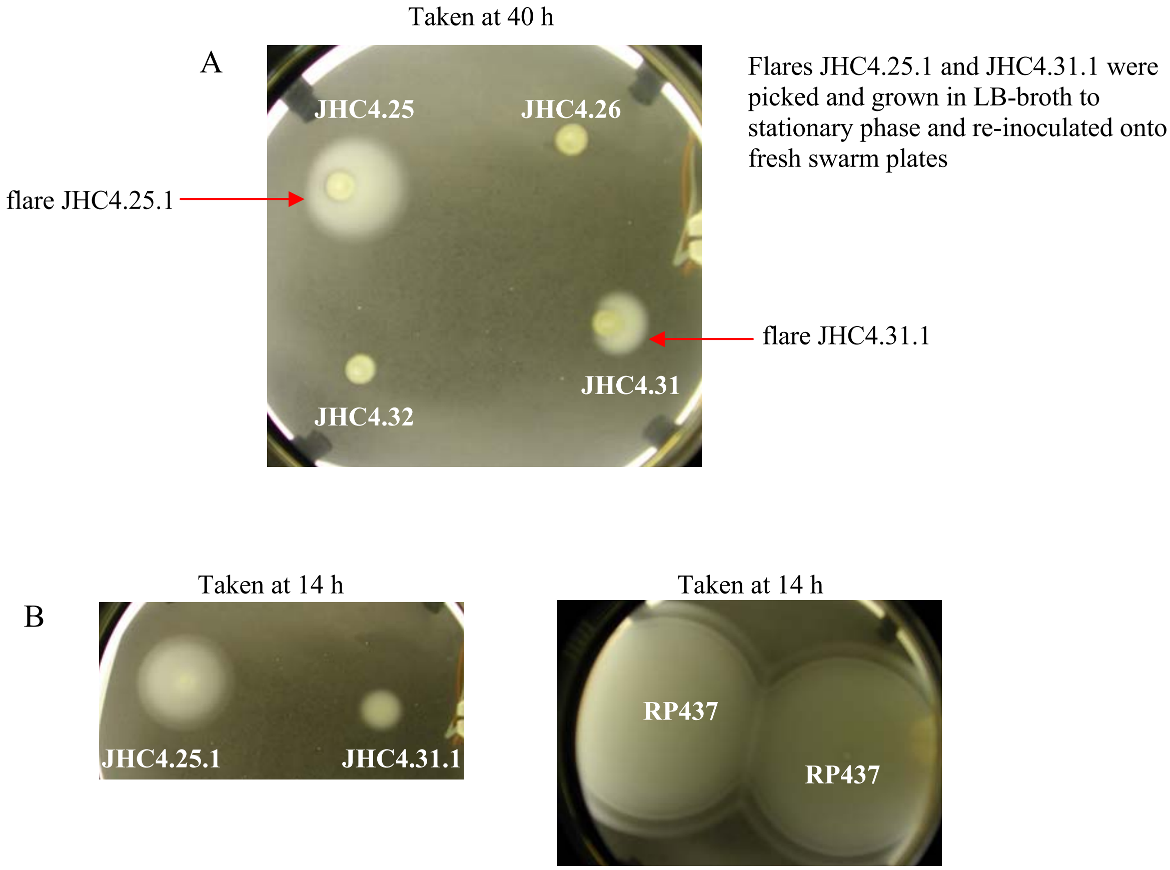

Flares JHC4.25.1 and JHC4.31.1 were picked and grown in LB-broth to stationary phase and re-inoculated onto fresh swarm plates

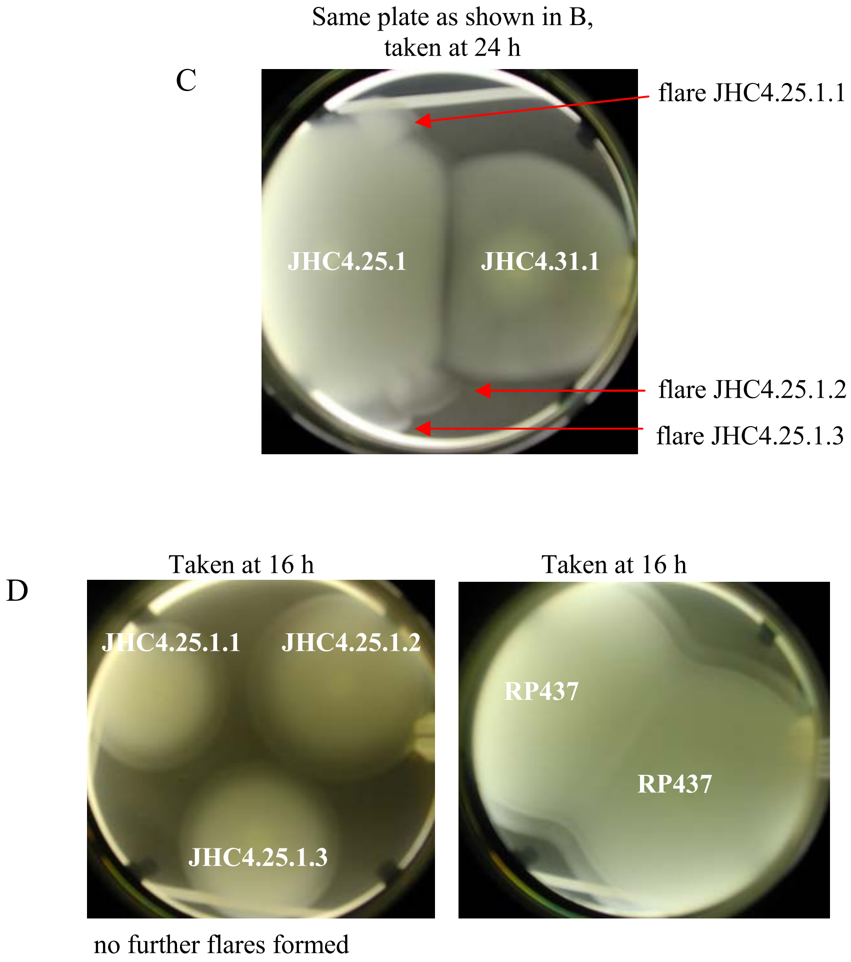

Figure 6.12: Swarm plate analysis of *fliM-yfp* strains. (A) Flares formed from non-motile strains JHC4.25 and JHC4.31; JHC4.26 and JHC4.32 did not produce any flares. This photo was taken at 40 h, by about 18 h, RP437 had swarmed over the entire plate, so is not shown. (B) Flares JHC4.25.1 (and JHC4.31.1, not shown) were picked from the plate shown in A and grown to stationary phase in LB-broth and re-inoculated onto fresh swarm plates. These photos were taken at 14 h, and RP437 is shown. (C) This plate is the same plate as that shown in B, taken at 24 h. Further flares were produced from JHC4.25.1. Again, RP437 is not shown because it had swarmed over the entire plate by 18 h. (D) Flares formed in C (JHC4.25.1.1, JHC4.25.1.2 and JHC4.25.1.3.) were grown to stationary phase in LB-broth at 30 ºC and re-inoculated onto fresh swarm plates. These photos were taken at 16 h; RP437 is shown. No further flares were produced.

6.11 Epifluorescence and TIRF microscopy of *fliM-yfp* strains

Non-motile *fliM-yfp* strains JHC4.25, JHC4.26, JHC4.31 and JHC4.32, and isolates from flares formed from JHC4.25 were observed using epifluorescence and TIRF microscopy. Fluorescent spots were observed in all *fliM-yfp* strains (motile and non-motile) that had the perfect sequence of *fliM-yfp* in-frame on the chromosome. Fluorescent spots can be seen in the epifluorescence images shown in Figure 6.13 in isolate JHC4.25.1.2; no fluorescent spots were observed in RP437.

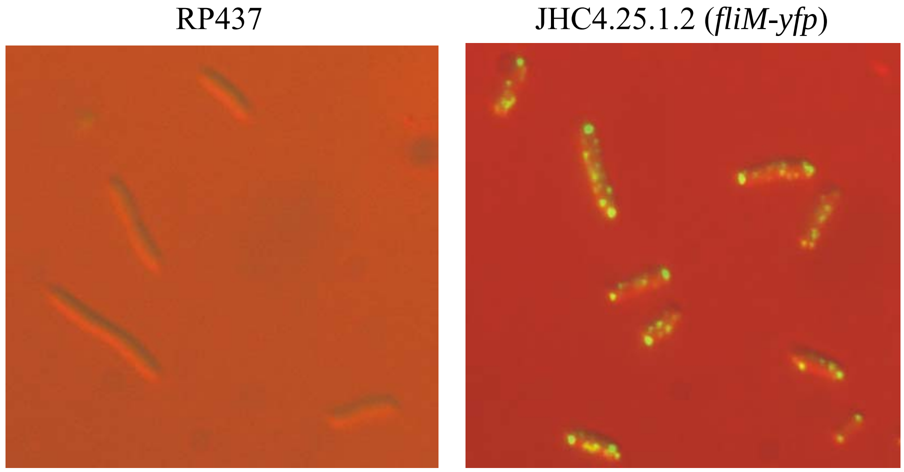
RP437

JHC4.25.1.2 (*fliM-yfp*)

Figure 6.13: Epifluorescence images of RP437 (left) and *fliM-yfp* flare JHC4.25.1.2 (right). Fluorescent spots were visible in all *fliM-yfp* strains, both motile and non-motile, that had the perfect sequence of *fliM-yfp* in-frame on the chromosome. No fluorescent spots were observed in the parental strain RP437.

To determine whether the fluorescent spots observed using epifluorescence microscopy were motor localised, cells were tethered using anti-FliC antibody in tunnel slides and observed using TIRFM. As Figure 6.14 shows, the fluorescent spots observed in all *fliM-yfp* strains corresponded to the site of tethering, and hence the motor. Multiple fluorescent spots correspond to the presence of multiple flagellar motors within the TIRF illumination field.

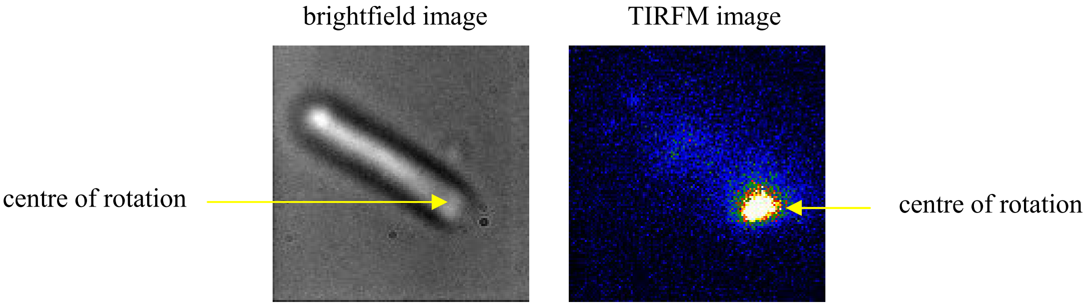
brightfield image

TIRFM image

centre of rotation

centre of rotation

Figure 6.14: TIRFM and brightfield images of *fliM-yfp* flare JHC25.1.2. (A) The centre of cell body rotation was assessed from a brightfield video of a rotating JHC25.1.2 cell (left). (B) A false-colour TIRFM image of JHC25.1.2; a fluorescent spot corresponded to the centre of rotation, and hence the motor. Multiple fluorescent spots correspond to multiple flagellar motors within the TIRF illumination field.

6.11.1 Swarm plate analysis of *fliG-yfp* strains

Three *fliG-yfp* strains (JHC5.8, JHC5.42 and JHC5.44), which had the perfect sequence of *fliG-yfp* in-frame in the chromosome, were grown to stationary phase with shaking in LB-broth at 30 ºC and inoculated onto soft-agar swarm plates (0.25 % agar in LB-broth) to assess their chemotactic ability.

Cells from flares produced from non-motile *fliG-yfp* strain JHC5.8 were isolated and called JHC5.8.1, JHC5.8.2 and JHC5.8.3 (Figure 6.15A). All cultures were grown to stationary phase with shaking in LB-broth at 30 ºC and re-inoculated onto fresh swarm plates (Figure 6.15B); however, no further flares were produced. Isolates JHC5.8.1, JHC5.8.2 and JHC5.8.3 had swarm rates comparable to RP437. Non-motile strains JHC5.42 and JHC5.44 also produced flares, as shown in Figure 6.15A, which also had similar swarm rates to RP437 (data not shown).

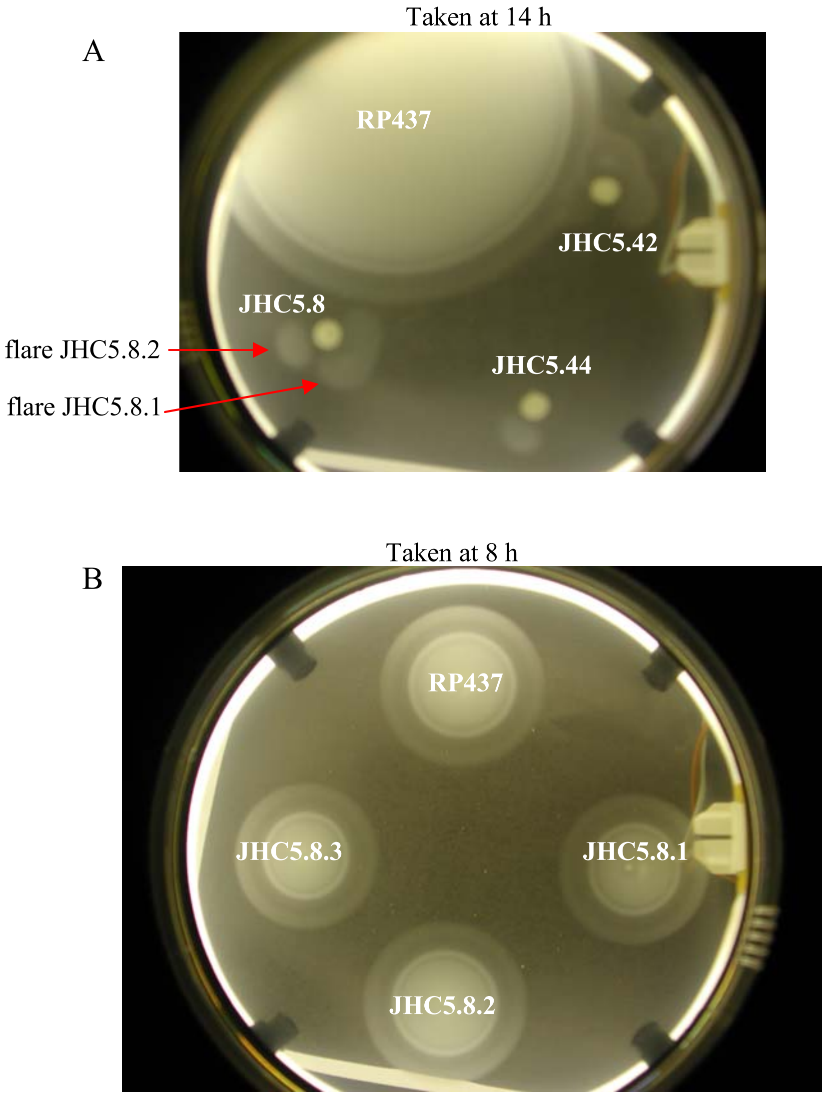

Figure 6.15: Swarm plate analysis of *fliG-yfp* strains. (A) JHC5.8, JHC5.42 and JHC5.44 and RP437 were inoculated onto swarm plates. Flares formed from all three cultures (only those formed from JHC5.8 are shown). Flares were grown to stationary phase with shaking in LB-broth and inoculated onto fresh swarm plates shown in B. (B) No further flares were produced from flares JHC5.8.1, JHC5.8.2, and JHC5.8.3.

Non-motile *fliG-yfp* strains JHC5.8, JHC5.42 and JHC5.44 were tethered in tunnel slides using anti-FliC antibody but no rotating cells were observed, indicating that the initial lack of swarming was a result of a defect(s) in motility, rather than chemotaxis.

All motile *fliG-yfp* isolates had excised *yfp* completely from the chromosome.

6.12 Epifluorescence and TIRF microscopy of *fliG-yfp* strains

Non-motile *fliG-yfp* strains JHC5.8, JHC5.42 and JHC5.44 were observed using epifluorescence and TIRF microscopy; isolates from flares were not tested because they had excised *yfp* completely from the chromomsome. Fluorescent spots were observed in all three strains. Figure 6.16 shows epifluorescence images of RP437 (which did not contain any fluorescent spots) and JHC5.42.

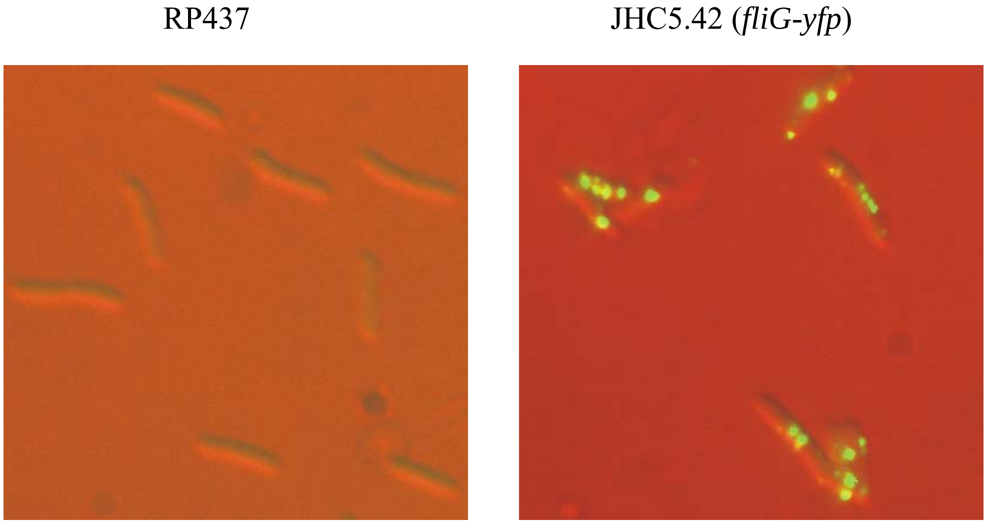

Figure 6.16: Epifluorescence images of RP437 (left) and non-motile *fliG-yfp* strain JHC5.42 (right). Fluorescent spots were observed in JHC5.42 and similar images were observed for JHC5.8 and JHC5.44 (not shown). Flares were not observed using epifluorescence (or TIRF) microscopy because they had excised *yfp* completely from the chromosome.

TIRFM images confirmed that the fluorescent spots observed using epifluorescence microscopy were motor-localised (Figure 6.17). *fliG-yfp* strains were non-motile, so the centre of rotation was deduced by observing Brownian motion about the site of tethering.

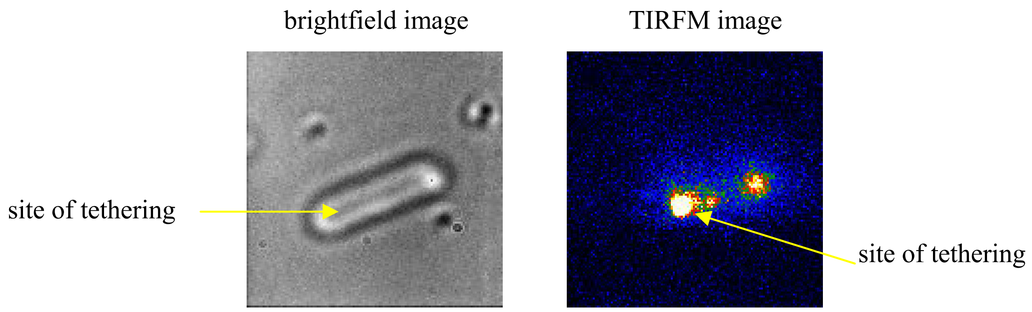

Figure 6.17: TIRFM images of non-motile *fliG-yfp* strain JHC5.42. (A) A brightfield image of non-motile JHC5.42; the site of tethering was deduced from observing Brownian motion. (B) Fluorescent spots can be seen in the false-colour TIRFM image, which corresponded to the site of tethering, and hence the motor. Three fluorescent spots can be seen in the TIRF image, corresponding to the presence of three motors within the TIRF illumination region.

6.13 Chapter discussion

motA, *fliG* and *fliM* were individually replaced in the genome with *motA-yfp* (and *gfp-motA*), *fliG-yfp* and *fliM-yfp* respectively, in separate wild type RP437 backgrounds, using a suicide vector which integrated into the chromosome by double homologous recombination. Gene replacement was confirmed by Southern blotting and sequencing.

6.13.1 N-terminal labelling

The *gfp-motA* isolates were non-motile as assessed by swarm plates and tethering via anti-FliC antibody in tunnel slides, and no flares formed on swarm plates even when left for 72 h. The absence of any free-swimming or rotating cells indicated that defect(s) in motility, rather than chemotaxis were the result of the lack of swarming. All isolates had the perfect sequence of *gfp-motA* in-frame in the chromosome, yet no fusion protein was detected using western blotting; MotA was expressed at wild type levels in two of the three strains tested, but no MotB or GFP were detected.

It is possible that a protease (or mutated protease) may have recognised some sequence within *gfp-motA*, perhaps in the linker region between GFP and MotA, resulting in cleavage of the fusion protein. GFP may have been excised from the fusion protein immediately after translation, and subsequently degraded so it was not detected using western blotting, but in that case MotA would have been expected to incorporate into the motor. All *gfp-motA* strains had the perfect sequence of *gfp-motA* in-frame in the chromosome, so the lack of detectable GFP was not due to the introduction of a stop codon. No fluorescence was detected using epifluorescence microscopy of TIRFM in any *gfp-motA* strain, suggesting that GFP was not expressed, or if it was, it was degraded rapidly. As *motB* is part of the same operon, the lack of detectable MotB may however explain the non-motile phenotype, or it is possible that MotB was expressed at very low (undetectable) levels.

The non-motile phenotype could result from the GFP-tag on MotA affecting insertion of GFP-MotA into the membrane. MotA does not have a characteristic membrane-insertion signal sequence and it is possible that the first transmembrane helix of MotA is itself the membrane-insertion signal sequence. Alternatively, GFP-MotA may have been unable to form a complex with MotB, and the lack of stator complex formation would explain the lack of motility. It is possible that MotA had several residues of GFP attached to its N-terminus, or some residues of MotA were missing, which could have affected stator complex formation or torque-generation, which may explain the non-motile phenotype.

N-terminal labelling of MotB was successful (Chapter 4), resulting in a fluorescent, functional protein, capable of forming complexes with MotA. However, with GFP-MotB, the 28 N-terminal cytoplasmic residues of MotB were repeated at the N-terminus of GFP, indicating that repetition of any putative membrane-insertion signal sequences may be critical when tagging membrane proteins with reporter proteins.

6.13.2 C-terminal labelling of motor components MotA, FliG and FliM

Initially, all *motA-yfp, fliG-yfp* and *fliM-yfp* strains were non-motile, as assessed by swarm plates and tethering via anti-FliC antibody in tunnel slides. The lack of any observable rotating tethered cells indicated that defect(s) in motility, rather than chemotaxis were the result of the lack of swarming.

Swarm plates of *motA-yfp, fliG-yfp* and *fliM-yfp* when incubated for many hours, (by which time RP437 had swarmed significantly) resulted in the formation of flares from all three strains. Cells from flares of *motA-yfp* and *fliM-yfp* were sub-cultured and re-inoculated onto swarm plates many times (at least five rounds each) until swarm rates comparable to wild type were observed, whereas isolates from flares of *fliG-yfp* had wild type levels of swarming, and had excised *yfp* completely from the chromosome. Isolates of flares of *motA-yfp* and *fliM-yfp* strains had varying lengths of *yfp* remaining on the chromosome, ranging from full-length *motA-yfp* and *fliM-yfp*, to partial excision of *yfp*, to full excision of *yfp* from the chromosome.

No fusion protein could be detected in cells isolated from any *motA-yfp* strain. No MotA was detected in any strain isolated from *motA-yfp* flares, yet they were motile, so is possible that expression of MotA was too low to be detected. No MotA-YFP or excised YFP was detected using epifluorescence or TIRF microscopy. As mentioned with the *gfp-motA* strains, even though MotA appeared to have the same molecular weight as MotA from wild type RP437 in western blotting, it is possible that MotA expressed in *motA-yfp* strains had some residues of YFP attached, or had some residues missing which may have affected stator complex formation or torque-generation.

MotB was detected (by western blotting) in only one *motA-yfp* flare, which had excised all but 100 bp from the 3'end of *yfp* from the chromosome. It is possible that regulatory elements upstream of *motB* (therefore within *motA*) may exist which may require as little sequence disruption between *motA* and *motB* in order to achieve translational coupling. These results suggest that the translation of *motB* was somehow affected by the presence of *yfp* fused to *motA*. Isolates from flares were obviously motile, and motility cannot be achieved without MotB, hence it is possible that MotB was expressed at very low levels, which were undetectable using western blotting.

FliM-YFP and FliG-YFP expression was not confirmed by western blotting because anti-FliM and anti-FliG antibodies were not available and the commericially available anti-GFP antibody (BD Biosciences) is non-specific.

Some isolates from *motA-yfp* flares which had perfect integration of *motA-yfp* in-frame in the genome, swarmed at less than one-fifth the rate of RP437, while another *motA-yfp* motile isolate which again had the perfect sequence of *motA-yfp* in-frame in the genome swarmed at over three-quarters the rate of RP437, yet no MotA was detected in these flares using western blotting, suggesting that the level of MotA expression in RP437 far exceeds the level of MotA required to achieve wild type levels of swarming. Why these flares, which produced similar banding patterns on western blots, varied so much in their swarm rates is unknown. It is possible that transcription and / or translation of genes upstream or downstream from *motA,* which were not sequenced, were affected by the presence of *yfp* attached to *motA*.

Fluorescent spots were observed in *fliM-yfp* (motile and non-motile) and *fliG-yfp* (non-motile) strains, using epifluorescence microscopy. TIRFM confirmed that these fluorescent spots were motor-localised. No fluorescent spots were observed in the parental strain RP437. These can therefore be used in future experiments to investigate rotor proteins and their interactions with the stator complexes.

C-terminal labeling of MotA, FliG and FliM involved repetition of the Shine-Dalgarno sites of the genes downstream of *motA*, *fliG* and *fliM* (*motB, fliH* and *fliN* respectively). The repeat was 15 bp long in the *motA-yfp* and *fliM-yfp* constructs and 41 bp in the *fliG-yfp* construct. Flares of *fliM-yfp* and *fliG-yfp* which had excised all of *yfp* from the chromosome may have achieved this by homologous recombination between the regions of repeated sequence either side of *yfp*. The large regions of repeated sequence in *fliG-yfp* isolates may explain why no intermediary flares were observed; only one set of flares were produced which swarmed at wild type levels.

These results suggest that when tagging various proteins at the C-terminus, if the corresponding gene overlaps with a gene downstream, it is important to repeat enough sequence so that transcription and / or translation of the downstream gene is minimally affected, but too much repetition of sequence can result in homologous recombination and excision of the reporter gene.

7 Discussion

7.1 De-resurrection experiments

The exact number and stoichiometry of the torque-generating stator complexes of the bacterial flagellar motor is unknown. To determine the number of stator complexes in the flagellar motor, various dominant-defective mutant MotB*s were expressed from an inducible plasmid in a wild type background. When cells were grown in the presence of the inducer, the ratio of mutant to wild type MotB was very high, resulting in stopped (locked) motors containing mutant MotB* stator complexes. However, motile cells were observed in cells expressing MotB D32E and MotB D32R, indicating these proteins had much lower affinities for the motor than the other MotB* point mutants, rather than the suggestion that MotB D32E and MotB D32R were capable of low levels of proton-conduction, as cells expressing these point mutant proteins had bead rotation rates comparable to wild type. The low percentage of motile cells expressing the other mutant MotB*s also had bead rotation rates comparable to wild type, suggesting that the integration of just one mutant stator complex may be sufficient to lock the motor; the observation of brief stops in rotation rate in individual cells expressing mutant MotB* supports this suggestion.

When cells were exposed to the inducer for a short period sufficient to express an excess of mutant MotB*, the bead rotation rate was expected to decrease in a step-wise manner as successive mutant stator complexes incorporated into the motor. However, this was not observed, the bead rotation rate either remained approximately constant or it decreased in a manner suggestive of de-energisation. Hence, various modifications were made, including the use of flow-cells and supplementing the buffers with nutrient, but no individual functioning motors de-resurrected in a step-wise manner. Even though the ratio of mutant MotB* to wild type MotB was high in the flow-cell when exposed to the inducer, it is possible that mutant MotB* could not form stable stator complexes with MotA, or the mutant stator complexes were not stable within the motor.

Non-functional motors could be made to resurrect in all point mutants, however this was monitored over a population, so whether these resurrections were step-wise is unknown and will need future investigation. Hence, the number of stator complexes in the flagellar motor could not be determined using this technique.

7.2 Fluorophore tagging of motor components

MotA, FliG and FliM were fused to XFP in the hope of doing FRET. Unfortunately, MotA-YFP and GFP-MotA were not detected using western blotting, epifluorescence and TIRF microscopy. It is possible that the levels of expression were too low to be detected using these techniques (but sufficient to result in the levels of motility observed) because many strains carried the perfect sequence of *gfp-motA* or *motA-yfp* in-frame in the genome. *gfp-motA* strains did not form any flares on swarm plates, whilst flares did form from *motA-yfp* strains.

FliG-YFP was non-functional, but it was fluorescent and motor-localised. Flares of *fliG-yfp* had excised all of *yfp* from the chromosome. FliM-YFP was fluorescent, functional and motor-localised. As with cells expressing GFP-MotB, multiple fluorescent spots were observed in many cells expressing FliG-YFP or FliM-YFP which corresponds to the presence of multiple motors within the TIRF illumination field. Flares of *fliM-yfp* which had the perfect sequence of *fliM-yfp* in-frame on the chromosome had swarm rates up to 70 % that of the parental strain. Flares of *fliM-yfp* and *motA-yfp* had varying levels of *yfp* excised from the chromosome, ranging from full-length to complete excision.

Hence it will be possible to perform FRET between Mot-CFP and FliM-YFP (and possibly FliG-YFP, even though expression results in non-functioning motors).

7.3 Determining the number of stator complexes by TIRFM and FRAP

gfp-motB in the genome was under the control of the native *motB* promoter and was subsequently expressed at wild type levels. Using TIRFM, fluorescent spots were observed at the centre of cell body rotation of motile tethered *gfp-motB*, corresponding to the site of the motor; such spots were not observed in the parental wild type strain. Multiple spots were often observed in cells that were tethered via more than one flagellum, corresponding to the presence of more than one motor within the TIRF illumination field. This is the first *in vivo* observation of proteins in a functioning motor.

GFP-MotB stoichiometry, dynamics and turnover were measured with single-molecule precision in functioning motors *in vivo*. Counting fluorophores by utilising the step-wise photobleaching of single surface-immobilised molecules of GFP, revealed that each motor contained ~ 22 copies of GFP-MotB, consistent with each motor having ~ 11 stator complexes each containing a GFP-MotB dimer. This estimate is consistent with estimates from previous torque-restoration and electron microscopy experiments[89,156,183,188], but is the first direct observational measurement of protein number. The reduced motility observed in *gfp-motB* cells (which had swarm and bead rotation rates approximately one-third that of wild type) was probably caused by some aspect of torque-generation being affected by the presence of the GFP-tag on MotB, possibly affecting the interaction of charged residues between the cytoplasmic loop of MotA and FliG, rather than the result of fewer stator complexes binding in the motor as the numbers measured were similar to the number measured by alternative methods. The broad distribution in counting estimates of GFP-MotB may include natural variation in the number of stators per motor as well as noise due to background fluorescence, GFP blinking and instrumental limitations.

GFP-MotB was observed within the motor but also in a freely diffusing membrane pool. Unexpectedly, FRAP and FLAP showed active and rapid turnover of GFP-MotB between the membrane pool and the motor with a rate constant on the order of 0.03 s^{-1}. The dwell time of a given stator in the motor was only ~ 30 s. A membrane pool of ~ 200 GFP-MotB molecules was also measured, with a diffusion co-efficient of 0.008 μm^{-2} s^{-1}, which is 40 % slower than measured for free membrane proteins of comparable size to a GFP-MotB dimer, and only 20 % slower than a $MotA_4$: $(GFP\text{-}MotB)_2$ stator. A relatively high diffusion co-efficient indicates that MotB in the membrane pool does not bind significantly to the cell wall. The large uncertainty in rate constant estimates is a consequence of the small different between recovery rates of motor and membrane components relative to noise.

These data are invaluable if we are to start to understand and be able to recreate biological systems *in vitro* with a view to constructing bionano devices and also in the emerging field of systems biology. In designing artificial motors based on these design principles, the durability and copy numbers of motor components may need to be considered. Unexpectedly, GFP-MotBs were exchanging in a functioning biological machine, meaning that bionano devices may require a constant supply of new components to function for long periods efficiently. However the data from the mutant MotB* and other motor fusions suggests that rate of exchange may depend on an available pool and it may be possible to increase or decrease the rate of exchange by regulating expression.

8 Publications

Leake, M., Chandler, J. H., Wadhams, G. H., Berry, R. M. & Armitage, J. P. Measurement of protein stoichiometry and turnover in single, functioning membrane protein complexes. Submitted to *Nature* 2006 (in revision).

Reid, S. W., Leake, M. C., Chandler, J. H., Lo, C. J., Armitage, J. P. & Berry, R. M. The maximum number of torque-generating units in the flagellar motor of *Escherichia coli* is at least 11.
Published online 23/05/2006 http://www.pnas.org/cgi/content/abstract/103/21/8066

9 References

1. Boyer, P. D. The ATP synthase-a splendid molecular machine. *Ann. Rev. Biochem.* **66**, 717-749 (1997).

2. Sabbert, D., Engelbrecht, S. & Junge, W. Functional and idling rotatory motion within F_1-ATPase. *Proc. Natl. Acad. Sci. U. S. A.* **94**, 4401-4405 (1997).

3. Noji, H., Yasuda, R., Yoshida, M. & Kinosita, K. Direct observation of the rotation of F1-ATPase [see comments]. *Nature* **386**, 299-302 (1997).

4. Foster, D. L. & Fillingame, R. H. Stoichiometry of subunits in the H^+-ATPase complex of *Escherichia coli*. *J. Biol. Chem.* **257**, 2009-2015 (1982).

5. Fillingame, R. H., Jones, P. C., Jiang, W., Valiyaveetil, F. I. & Dmitriev, O. Y. Subunit organization and structure in the F_0 sector of *Escherichia coli* F_1F_0 ATP synthase. *Biochimica et Biophysica Acta-Bioenergetics* **1365**, 135-142 (1998).

6. Schemidt, R. A., Qu, J., Williams, J. R. & Brusilow, W. S. A. Effects of carbon source on expression of F_0 genes and on the stoichiometry of the c subunit in the F_1F_0 ATPase of *Escherichia coli*. *J. Bacteriol.* **180**, 3205-3208 (1998).

7. Schemidt, R. A., Hsu, D. K. W., Deckershebestreit, G., Altendorf, K. & Brusilow, W. S. A. The effects of an ATP ribosome-binding site mutation on the stoichiometry of the c-subunit in the F_1F_0 ATPase of *Escherichia coli*. *Arch. Biochem. Biophys.* **323**, 423-428 (1995).

8. Kaim, G. & Dimroth, P. Voltage-generated torque drives the motor of the ATP synthase. *Embo Journal* **17**, 5887-5895 (1998).

9. Takeyasu, K., Omote, H., Nettikadan, S., Tokumasu, F., IwamotoKihara, A. & Futai, M. Molecular imaging of *Escherichia coli* F_0F_1-ATPase in reconstituted membranes using atomic force microscopy. *FEBS Letts.* **392**, 110-113 (1996).

10. Singh, S., Turina, P., Bustamante, C. J., Keller, D. J. & Capaldi, R. Topographical structure of membrane-bound *Escherichia coli* F_1F_0 ATP synthase in aqueous buffer. *FEBS Letts.* **397**, 30-34 (1996).

11. Vik, S. B., Patterson, A. R. & Antonio, B. J. Insertion scanning mutagenesis of subunit a of the F1F0 ATP synthase near His(245) and implications on gating of the proton channel. (vol 273, pg 16229, 1998). *J. Biol. Chem.* **273**, 22159 (1998).

12. Valiyaveetil, F. I. & Fillingame, R. H. On the role of Arg-210 and Glu-219 of subunit alpha in proton translocation by the *Escherichia coli* F_0F_1-ATP synthase. *J. Biol. Chem.* **272**, 32635-32641 (1997).

13. Fillingame, R. H. Subunit-c of F_1F_0 ATP Synthase - structure and role in transmembrane energy transduction. *Biochimica et Biophysica Acta* **1101**, 240-243 (1992).

14. Junge, W., Lill, H. & Engelbrecht, S. ATP synthase: an electrochemical transducer with rotatory mechanics. *Trends Biochem. Sci.* **22**, 420-423 (1997).

15. Boyer, P. D. The binding change mechanism for ATP synthase - some probabilities and possibilities. *Biochimica et Biophysica Acta* **1140**, 215-250 (1993).

16. Abrahams, J. P., Leslie, A. G. W., Lutter, R. & Walker, J. E. Structure at 2.8-angstrom resolution of F_1-ATPase from bovine heart-mitochondria. *Nature* **370**, 621-628 (1994).

17. Shimabukuro, K., Yasuda, R., Muneyuki, E., Hara, K. Y., Kinosita, K. & Yoshida, M. Catalysis and rotation of F-1 motor: Cleavage of ATP at the catalytic site occurs in 1 ms before 40 degrees substep rotation. *Proc. Natl. Acad. Sci. U. S. A.* **100**, 14731-14736 (2003).

18. Sabbert, D. & Junge, W. Stepped versus continuous rotatory motors at the molecular scale. *Proc. Natl. Acad. Sci. U. S. A.* **94**, 2312-2317 (1997).

19. Stock, D., Leslie, A. G. W. & Walker, J. E. Molecular architecture of the rotary motor in ATP synthase. *Science* **286**, 1700-1705 (1999).

20. Berry, S. & Rumberg, B. H^+/ATP coupling ratio at the unmodulated F_0F_1-ATP synthase determined by proton flux measurements. *Biochimica et Biophysica Acta-Bioenergetics* **1276**, 51-56 (1996).

21. VanWalraven, H. S., Strotmann, H., Schwarz, O. & Rumberg, B. The H^+/ATP coupling ratio of the ATP synthase from thiol-modulated chloroplasts and two cyanobacterial strains is four. *FEBS Letts.* **379**, 309-313 (1996).

22. Junge, W. ATP synthase and other motor proteins. *Proc. Natl. Acad. Sci. U. S. A.* **96**, 4735-4737 (1999).

23. Nakamoto, R. K., Ketchum, C. J. & Al-Shawi, M. K. Rotational coupling in the F_0F_1 ATP synthase. *Annual Review of Biophysics and Biomolecular Structure* **28**, 205-234 (1999).

24. Dmitriev, O. Y., Jones, P. C. & Fillingame, R. H. Structure of the subunit c oligomer in the F_1F_0 ATP synthase: Model derived from solution structure of the monomer and cross-linking in the native enzyme. *Proc. Natl. Acad. Sci. U. S. A.* **96**, 7785-7790 (1999).

25. Scholey, J. M. Intraflagellar transport. *Annual Review of Cell and Developmental Biology* **19**, 423-443 (2003).

26. Mitchell, D. R. Speculations on the evolution of 9+2 organelles and the role of central pair microtubules. *Biology of the Cell* **96**, 691-696 (2004).

27. Margulis, L. *Origin of eukaryotic cells*. Yale University Press, New Haven, CT (1970).

28. Margulis, L. *Symbiosis in cell evolution*. W.H.Freeman Company, New York (1993).

29. Macnab, R. M. Genetics and biogenesis of bacterial flagella. *Annu. Rev. Genet.* **26**, 131-158 (1992).

30. Segall, J. E., Block, S. M. & Berg, H. C. Temporal comparisons in bacterial chemotaxis. *Proc. Natl. Acad. Sci. U. S. A.* **83**, 8987-8991 (1986).

31. Macnab, R. M. Bacterial flagella rotating in bundles: a study in helical geometry. *Proc. Natl. Acad. Sci. U. S. A.* **74**, 221-225 (1977).

32. Block, S. M., Fahrner, K. A. & Berg, H. C. Visualization of bacterial flagella by video-enhanced light microscopy. *J. Bacteriol.* **173**, 933-936 (1991).

33. Larsen, S. H., Reader, R. W., Kort, E. N., Tso, W.-W. & Adler, J. Change in direction of flagellar rotation is the basis of the chemotactic response in *Escherichia coli*. *Nature* **249**, 74-77 (1974).

34. Macnab, R. M. & Ornston, M. K. Normal-to-curly flagellar transitions and their role in bacterial tumbling.Stabilization of an alternative quaternary structure by mechanical force. *J. Mol. Biol.* **112**, 1-30 (1977).

35. Turner, L., Ryu, W. S. & Berg, H. C. Real-time imaging of fluorescent flagellar filaments. *J. Bacteriol.* **182**, 2793-2801 (2000).

36. Bourret, R. B., Borkovich, K. A. & Simon, M. I. Signal transduction pathways involving protein phosphorylation in prokaryotes. *Annu. Rev. Biochem.* **60**, 401-441 (1991).

37. Hess, J. F., Bourret, R. B. & Simon, M. I. Histidine phosphorylation and phosphoryl group transfer in bacterial chemotaxis. *Nature* **336**, 139-143 (1988).

38. Sanders, D. A., Gillece-Castro, B. L., Stock, A. M., Burlingame, A. L. & Koshland, D. E., Jr. Identification of the site of phosphorylation of the chemotaxis response regulator protein, CheY. *J. Biol. Chem.* **264**, 21770-21778 (1989).

39. Bourret, R. B., Hess, J. F. & Simon, M. I. Conserved aspartate residues and phosphorylation in signal transduction by the chemotaxis protein CheY. *Proc. Natl. Acad. Sci. U. S. A.* **87**, 41-45 (1990).

40. Hess, J. F., Oosawa, K., Kaplan, N. & Simon, M. I. Phosphorylation of three proteins in the signalling pathway of bacterial chemotaxis. *Cell* **53**, 79-87 (1988).

41. Turner, L., Caplan, S. R. & Berg, H. C. Temperature-induced switching of the bacterial flagellar motor. *Biophys. J.* **71**, 2227-2233 (1996).

42. Ishihara, A., Segall, J. E., Block, S. M. & Berg, H. C. Co-ordination of flagella on filamentous cells of *Escherichia coli*. *J. Bacteriol.* **155**, 228-237 (1983).

43. Macnab, R. M. & Han, D. P. Asynchronous switching of flagellar motors on a single cell. *Cell* **32**, 109-117 (1983).

44. Berg, H. C. *Cell motility*. Goldman, R., Pollard, T. & Rosenbaum, J. (eds.), pp. 47-56 (Cold Spring Harbor, New York,1976).

45. Kudo, S., Magariyama, Y. & Aizawa, S.-I. Abrupt changes in flagellar rotation observed by laser dark-field microscopy. *Nature* **346**, 677-680 (1990).

46. Springer, W. R. & Koshland, D. E. Jr. Identification of a protein methyltransferase as the *cheR* gene product in the bacterial sensing system. *Proc. Natl. Acad. Sci. U. S. A.* **74**, 533-537 (1977).

47. Djordjevic, S. & Stock, A. M. Structural analysis of bacterial chemotaxis proteins: Components of a dynamic signaling system. *J. Struct. Biol.* **124**, 189-200 (1998).

48. West, A. H., Djordjevic, S., Martinez-Hackert, E. & Stock, A. M. Purification, crystallization, and preliminary X-ray diffraction analyses of the bacterial chemotaxis receptor modifying enzymes. *prot* **21**, 345-350 (1995).

49. Stock, J. B. & Koshland, D. E. Jr. A protein methylesterase involved in bacterial sensing. *Proc. Natl. Acad. Sci. U. S. A.* **75**, 3659-3663 (1978).

50. Lupas, A. & Stock, J. Phosphorylation of an N-terminal regulatory domain activates the CheB methylesterase in bacterial chemotaxis. *J. Biol. Chem.* **264**, 17337-17342 (1989).

51. Anand, G. S., Goudreau, P. N., Lewis, J. K. & Stock, A. M. Evidence for phosphorylation-dependent conformational changes in methylesterase CheB. *Protein Sci.* **9**, 898-906 (2000).

52. Falke, J. J., Bass, R. B., Butler, S. L., Chervitz, S. A. & Danielson, M. A. The two-component signaling pathway of bacterial chemotaxis: A molecular view of signal transduction by receptors, kinases, and adaptation enzymes. *Annual Review of Cell and Developmental Biology* **13**, 457-512 (1997).

53. Macnab, R. M. The bacterial flagellum: reversible rotary propellor and type III export apparatus. *J. Bacteriol.* **181**, 7149-7153 (1999).

54. Tomich, M., Herfst, C. A., Golden, J. W. & Mohr, C. D. Role of flagella in host cell invasion by *Burkholderia cepacia*. *Infec. Immun.* **70**, 1799-1806 (2002).

55. Morooka, T., Umeda, A. & Amako, K. Motility as an intestinal colonization factor for *Campylobacter jejuni*. *J. Gen. Microbiol.* **131**, 1973-1980 (1985).

56. Eaton, K. A., Morgan, D. R. & Krakowka, S. Motility as a factor in the colonisation of gnotobiotic piglets by *Helicobacter pylori*. *J. Med. Microbiol.* **37**, 123-127 (1992).

57. Feldman, M., Bryan, R., Rajan, S., Scheffler, L., Brunnert, S., Tang, H. & Prince, A. Role of flagella in pathogenesis of *Pseudomonas aeruginosa* pulmonary infection. *Infect. Immun.* **66**, 43-51 (1998).

58. Montie, T. C., Doyle-Huntzinger, D., Craven, R. C. & Holder, I. A. Loss of virulence associated with absence of flagellum in an isogenic mutant of *Pseudomonas aeruginosa* in the burned-mouse model. *Infect. Immun.* **38**, 1296-1298 (1982).

59. Yao, R. J., Burr, D. H., Doig, P., Trust, T. J., Niu, H. Y. & Guerry, P. Isolation of motile and nonmotile insertional mutants of *Campylobacter jejuni* - the role of motility in adherence and invasion of eukaryotic cells. *Mol. Microbiol.* **14**, 883-893 (1994).

60. Arora, S. K., Ritchings, B. W., Almira, E. C., Lory, S. & Ramphal, R. The *Pseudomonas aeruginosa* flagellar cap protein, FliD, is responsible for mucin adhesion. *Infec. Immun.* **66**, 1000-1007 (1998).

61. Foynes, S., Dorrell, N., Ward, S. J., Stabler, R. A., McColm, A. A., Rycroft, A. N. & Wren, B. W. *Helicobacter pylori* possesses two CheY response regulators and a histidine kinase sensor, CheA, which are essential for chemotaxis and colonization of the gastric mucosa. *Infect. Immun.* **68**, 2016-2023 (2000).

62. Visick, K. L. & Fall-Ngai, M. J. An exclusive contract: Specificity in the *Vibrio fischeri Euprymna scolopes* partnership. *J. Bacteriol.* **182**, 1779-1787 (2000).

63. Fall-Ngai, M. J. Consequences of evolving with bacterial symbionts: Insights from the squid-vibrio associations. *Annual Review of Ecology and Systematics* **30**, 235-256 (1999).

64. Graf, J., Dunlap, P. V. & Ruby, E. G. Effect of transposon-induced motility mutations on colonization of the host light organ by *Vibrio fischeri*. *J. Bacteriol.* **176**, 6986-6991 (1994).

65. Pratt, L. A. & Kolter, R. Genetic analysis of *Escherichia coli* biofilm formation:roles of flagella, motility, chamotaxis and type 1 pili. *Mol. Microbiol.* **30**, 285-293 (1998).

66. Watnick, P. I., Lauriano, C. M., Klose, K. E., Croal, L. & Kolter, R. The absence of a flagellum leads to altered colony morphology, biofilm development and virulence in *Vibrio cholerae* O139. *Mol. Microbiol.* **39**, 223-235 (2001).

67. O'Toole, G. A. & Kolter, R. Flagellar and twitching moltility are necessary for *Pseudomonas aeruginosa* biofilm development. *Mol. Microbiol.* **30**, 295-304 (1998).

68. Kubori, T., Shimamoto, N., Yamaguchi, S., Namba, K. & Aizawa, S.-I. Morphological pathway of flagellar assembly in *Salmonella typhimurium*. *J. Mol. Biol.* **226**, 433-446 (1992).

69. Macnab, R. M. *Escherichia coli and Salmonella:Cellular and Molecular Biology*. Neidhardt, F. C. *et al.* (eds.), pp. 123-145 (ASM, Washington,1996).

70. Kalir, S., McClure, J., Pabbaraju, K., Southward, C., Ronen, M., Leibler, S., Surette, M. G. & Alon, U. Ordering genes in a flagella pathway by analysis of expression kinetics from living bacteria. *Science* **292**, 2080-2083 (2001).

71. Berg, H. C. The rotary motor of bacterial flagella. *Ann. Rev. Biochem.* **72**, 19-54 (2003).

72. Homma, M. & Iino, T. Excretion of unassembled hook-associated proteins by *Salmonella typhimurium*. *J. Bacteriol.* **164**, 1370-1372 (1985).

73. Homma, M., Fujita, H., Yamaguchi, S. & Iino, T. Excretion of unassembled flagellin by *Salmonella typhimurium* mutants defective in hook associated proteins. *J. Bacteriol.* **159**, 1056-1059 (1984).

74. Maki, S., Vonderviszt, F., Furukawa, Y., Imada, K. & Namba, K. Plugging interactions of HAP2 pentamer into the distal end of flagellar filament revealed by electron microscopy. *J. Mol. Biol.* **277**, 771-777 (1998).

75. Asakura, S. Polymerization of flagellin and polymorphism of flagella. *Adv. Biophys.* **1**, 99-155 (1970).

76. Vonderviszt, F., Aizawa, S.-I. & Namba, K. Role of the disordered terminal regions of flagellin in filament formation and stability. *J. Mol. Biol.* **221**, 1461-1474 (1991).

77. Trachtenberg, S. & DeRosier, D. J. Conformational switching in the flagellar filament of *Salmonella typhimurium*. *J. Mol. Biol.* **226**, 447-454 (1992).

78. Imada, K., Vonderviszt, F., Furukawa, Y., Oosawa, K. & Namba, K. Assembly characteristics of flagellar cap protein HAP2 of *Salmonella*: decamer and pentamer in the pH-sensitive equilibrium. *J. Mol. Biol.* **277**, 883-891 (1998).

79. Yonekura, K., Maki, S., Morgan, D. G., DeRosier, D. J., Vonderviszt, F., Imada, K. & Namba, K. The bacterial flagellar cap as the rotary promoter of flagellin self-assembly. *Science* **290**, 2148-2152 (2000).

80. Berry, R. M. & Armitage, J. P. The bacterial flagella motor. *Adv. Microb. Physiol.* **41**, 291-337 (1999).

81. Sosinsky, G. E., Francis, N. R., DeRosier, D. J., Wall, J. S., Simon, M. N. & Hainfeld, J. Mass determination and estimation of subunit stoichiometry of the bacterial hook-basal body flagellar complex of *Salmonella typhimurium* by scanning transmission electron microscopy. *Proc. Natl. Acad. Sci. U. S. A.* **89**, 4801-4805 (1992).

82. Emerson, S. U., Tokuyasu, K. & Simon, M. I. Bacterial flagella: polarity of elongation. *Science* **169**, 190-192 (1970).

83. Ikeda, T., Homma, M., Iino, T., Asakura, S. & Kamiya, R. Localization and stoichiometry of hook-associated proteins within *Salmonella typhimurium* Flagella. *J. Bacteriol.* **169**, 1168-1173 (1987).

84. Iino, T. Polarity of flagellar growth in *Salmonella*. *J. Gen. Microbiol.* **56**, 227-239 (1969).

85. DePamphilis, M. L. & Adler, J. Purification of intact flagella from *Escherichia coli* and *Bacillus subtilis*. *J. Bacteriol.* **105**, 376-383 (1971).

86. Cohen-Bazire, G. & London, J. Basal organelles of bacterial flagella. *J. Bacteriol.* **94**, 458-465 (1967).

87. DePamphilis, M. L. & Adler, J. Fine structure and isolation of the hook-basal body complex from flagella of *Escherichia coli* and *Bacillus subtilis*. *J. Bacteriol.* **105**, 384-395 (1971).

88. Aizawa, S.-I., Dean, G. E., Jones, C. J., Macnab, R. M. & Yamaguchi, S. Purification and characterization of the flagellar hook-basal body complex of *Salmonella typhimurium*. *J. Bacteriol.* **161**, 836-849 (1985).

89. Khan, S., Dapice, M. & Reese, T. S. Effects of *mot* gene expression on the structure of the flagellar motor. *J. Mol. Biol.* **202**, 575-584 (1988).

90. Khan, S., Khan, I. H. & Reese, T. S. New structural features of the flagellar base in *Salmonella typhimurium* revealed by rapid-freeze electron microscopy. *J. Bacteriol.* **173**, 2888-2896 (1991).

91. Khan, I. H., Reese, T. S. & Khan, S. The cytoplasmic component of the bacterial flagellar motor. *Proc. Natl. Acad. Sci. U. S. A.* **89**, 5956-5960 (1992).

92. Francis, N. R., Sosinsky, G. E., Thomas, D. & DeRosier, D. J. Isolation, characterization and structure of bacterial flagellar motors containing the switch complex. *J. Mol. Biol.* **235**, 1261-1270 (1994).

93. Driks, A. & DeRosier, D. J. Additional structures associated with bacterial flagellar basal body. *J. Mol. Biol.* **211**, 669-672 (1990).

94. Suzuki, H., Yonekura, K. & Namba, K. Structure of the rotor of the bacterial flagellar motor revealed by electron cryomicroscopy and single-particle image analysis. *J. Mol. Biol.* **337**, 105-113 (2004).

95. Zhao, R., Pathak, N., Jaffe, H., Reese, T. S. & Khan, S. FliN is a major structural protein of the C-ring in the *Salmonella typhimurium* flagellar basal body. *J. Mol. Biol.* **261**, 195-208 (1996).

96. Zhao, R., Amsler, C. D., Matsumura, P. & Khan, S. FliG and FliM distribution in the *Salmonella typhimurium* cell and flagellar basal bodies. *J. Bacteriol.* **178**, 258-265 (1996).

97. Welch, M., Oosawa, K., Aizawa, S.-I. & Eisenbach, M. Phosphorylation-dependent binding of a signal molecule to the flagellar switch of bacteria. *Proc. Natl. Acad. Sci. U. S. A.* **90**, 8787-8791 (1993).

98. Welch, M., Oosawa, K., Aizawa, S.-I. & Eisenbach, M. Effects of phosphorylation, Mg^{2+}, and conformation of the chemotaxis protein CheY on its binding to the flagellar switch protein FliM. *Biochemistry* **33**, 10470-10476 (1994).

99. Toker, A. S. & Macnab, R. M. Distinct regions of bacterial flagellar switch protein FliM interact with FliG, FliN and CheY. *J. Mol. Biol.* **273**, 623-634 (1997).

100. Bren, A. & Eisenbach, M. The N terminus of the flagellar switch protein, FliM, is the binding domain for the chemotactic response regulator, CheY. *J. Mol. Biol.* **278**, 507-514 (1998).

101. Zhou, J., Sharp, L. L., Tang, H. L., Lloyd, S. A., Billings, S., Braun, T. F. & Blair, D. F. Function of protonatable residues in the flagellar motor of *Escherichia coli*: a critical role for Asp 32 of MotB. *J. Bacteriol.* **180**, 2729-2735 (1998).

102. Sockett, H., Yamaguchi, S., Kihara, M., Irikura, V. M. & Macnab, R. M. Molecular analysis of the flagellar switch protein FliM of *Salmonella typhimurium*. *J. Bacteriol.* **174**, 793-806 (1992).

103. Tang, H. & Blair, D. F. Regulated underexpression of the FliM protein of *Escherichia coli* and evidence for a location in the flagellar motor distinct from the MotA/MotB torque generators. *J. Bacteriol.* **177**, 3485-3495 (1995).

104. Tang, H., Billings, S., Wang, X., Sharp, L. & Blair, D. F. Regulated underexpression and overexpression of the FliN protein of *Escherichia coli* and evidence for an interaction between FliN and FliM in the flagellar motor. *J. Bacteriol.* **177**, 3496-3503 (1995).

105. Clegg, D. O. & Koshland, D. E. Jr. Identification of a bacterial sensing protein and effects of its elevated expression. *J. Bacteriol.* **162**, 398-405 (1985).

106. Vogler, A. P., Homma, M., Irikura, V. M. & Macnab, R. M. *Salmonella typhimurium* mutants defective in flagellar filament regrowth and sequence similarity of FliI to F_0F_1, vacuolar, and archaebacterial ATPase subunits. *J. Bacteriol.* **173**, 3564-3572 (1991).

107. Bischoff, D. S. & Ordal, G. W. Identification and characterization of FliY, a novel component of the *Bacillus subtilis* flagellar switch complex. *Mol. Microbiol.* **6**, 2715-2723 (1992).

108. Thomas, D. R., Morgan, D. G. & DeRosier, D. J. Rotational symmetry of the C ring and a mechanism for the flagellar rotary motor. *Proc. Natl. Acad. Sci. U. S. A.* **96**, 10134-10139 (1999).

109. Young, H. S., Dang, H. Y., Lai, Y. M., DeRosier, D. J. & Khan, S. Variable symmetry in *Salmonella typhimurium* flagellar motors. *Biophys. J.* **84**, 571-577 (2003).

110. Sourjik, V. & Berg, H. C. Localization of components of the chemotaxis machinery of *Escherichia coli* using fluorescent protein fusions. *Mol. Microbiol.* **37**, 740-751 (2000).

111. Lloyd, S. A., Tang, H., Wang, X., Billings, S. & Blair, D. F. Torque generation in the flagellar motor of *Escherichia coli*: Evidence for a direct role for FliG but not for FliM or FliN. *J. Bacteriol.* **178**, 223-231 (1996).

112. Lloyd, S. A., Whitby, F. G., Blair, D. F. & Hill, C. P. Structure of the C-terminal domain of FliG, a component of the rotor in the bacterial flagellar motor. *Nature* **400**, 472-475 (1999).

113. Brown, P. N., Hill, C. P. & Blair, D. F. Crystal structure of the middle and C-terminal domains of the flagellar rotor protein FliG. *Embo Journal* **21**, 3225-3234 (2002).

114. Lloyd, S. A. & Blair, D. F. Charged residues of the rotor protein FliG essential for torque generation in the flagellar motor of *Escherichia coli*. *J. Mol. Biol.* **266**, 733-744 (1997).

115. Tang, H., Braun, T. F. & Blair, D. F. Motility protein complexes in the bacterial flagellar motor. *J. Mol. Biol.* **261**, 209-221 (1996).

116. Lowder, B. J., Duyvesteyn, M. D. & Blair, D. F. FliG subunit arrangement in the flagellar rotor probed by targeted cross-linking. *J. Bacteriol.* **187**, 5640-5647 (2005).

117. Jones, C. J., Macnab, R. M., Okino, H. & Aizawa, S.-I. Stoichiometric analysis of the flagellar hook-(basal-body) complex of *Salmonella typhimurium*. *J. Mol. Biol.* **212**, 377-387 (1990).

118. Francis, N. R., Irikura, V. M., Yamaguchi, S., DeRosier, D. J. & Macnab, R. M. Localization of the *Salmonella typhimurium* flagellar switch protein FliG to the cytoplasmic M-ring face of the basal body. *Proc. Natl. Acad. Sci. U. S. A.* **89**, 6304-6308 (1992).

119. Oosawa, K., Ueno, T. & Aizawa, S.-I. Overproduction of the bacterial flagellar switch proteins and their interactions with the MS ring complex *in vitro*. *J. Bacteriol.* **176**, 3683-3691 (1994).

120. Marykwas, D. L., Schmidt, S. A. & Berg, H. C. Interacting components of the flagellar motor of *Escherichia coli* revealed by the two-hybrid system in yeast. *J. Mol. Biol.* **256**, 564-576 (1996).

121. Thomas, D., Morgan, D. G. & DeRosier, D. J. Structures of bacterial flagellar motors from two FliF-FliG gene fusion mutants. *J. Bacteriol.* **183**, 6404-6412 (2001).

122. Kihara, M., Francis, N. R., DeRosier, D. J. & Macnab, R. M. Analysis of a FliM-FliN flagellar switch fusion mutant of *Salmonella typhimurium*. *J. Bacteriol.* **178**, 4582-4589 (1996).

123. Macnab, R. M. *Two-component signal transduction*. Hoch, J. A. & Silhavy, T. J. (eds.), pp. 181-199 (ASM, Washington,1995).

124. Blair, D. F. & Berg, H. C. The MotA protein of *Escherichia coli* is a proton-conducting component of the flagellar motor. *Cell* **60**, 439-449 (1990).

125. Garza, A. G., Harris-Haller, L. W., Stoebner, R. A. & Manson, M. D. Motility protein interactions in the bacterial flagellar motor. *Proc. Natl. Acad. Sci. U. S. A.* **92**, 1970-1974 (1995).

126. Sharp, L. L., Zhou, J. D. & Blair, D. F. Features of MotA proton channel structure revealed by tryptophan-scanning mutagenesis. *Proc. Natl. Acad. Sci. U. S. A.* **92**, 7946-7950 (1995).

127. Stolz, B. & Berg, H. C. Evidence for interactions between MotA and MotB, torque- generating elements of the flagellar motor of *Escherichia coli*. *J. Bacteriol.* **173**, 7033-7037 (1991).

128. Garza, A. G., Bronstein, P. A., Valdez, P. A., HarrisHaller, L. W. & Manson, M. D. Extragenic suppression of *motA* missense mutations of *Escherichia coli*. *J. Bacteriol.* **178**, 6116-6122 (1996).

129. Braun, T. F. & Blair, D. F. Targeted disulfide cross-linking of the MotB protein of *Escherichia coli:* Evidence for two H^+ channels in the stator complex. *Biochemistry* **40**, 13051-13059 (2001).

130. Ridgway, H. F., Silverman, M. & Simon, M. I. Localization of proteins controlling motility and chemotaxis in *Escherichia coli*. *J. Bacteriol.* **132**, 657-665 (1977).

131. Dean, G. E., Macnab, R. M., Stader, J., Matsumura, P. & Burks, C. Gene sequence and predicted amino acid sequence of the *motA* protein,a membrane associated protein required for flagellar rotation in *Escherichia coli*. *J. Bacteriol.* **159**, 991-999 (1984).

132. Blair, D. F. & Berg, H. C. Mutations in the MotA protein of *Escherichia coli* reveal domains critical for proton conduction. *J. Mol. Biol.* **221**, 1433-1442 (1991).

133. Zhou, J. D., Fazzio, R. T. & Blair, D. F. Membrane topology of the MotA protein of *Escherichia coli*. *J. Mol. Biol.* **251**, 237-242 (1995).

134. Stader, J., Matsumura, P., Vacante, D., Dean, G. E. & Macnab, R. M. Nucleotide sequence of the *Escherichia coli motB* gene and site limited incorporation of its product into the cytoplasmic membrane. *J. Bacteriol.* **166**, 244-252 (1986).

135. Chun, S. Y. & Parkinson, J. S. Bacterial motility - membrane topology of the *Escherichia coli* MotB protein. *Science* **239**, 276-278 (1988).

136. Demot, R. & Vanderleyden, J. The C-terminal sequence conservation between OmpA-related outer membrane proteins and MotB suggests a common function in both Gram-positive and Gram-negative bacteria, possibly in the interaction of these domains peptidoglycan. *Mol. Microbiol.* **12**, 333-336 (1994).

137. Berg, H. C. Dynamic properties of bacterial flagellar motors. *Nature* **249**, 77-79 (1974).

138. Sharp, L. L., Zhou, J. & Blair, D. F. Tryptophan-scanning mutagenesis of MotB, an integral membrane protein essential for flagellar rotation in *Escherichia coli*. *Biochemistry* **34**, 9166-9171 (1995).

139. Imae, Y. *New Era of Bioenergetics*. Mukohata, Y. (ed.), pp. 197-221 (Academic Press, Tokyo,1991).

140. Imae, Y. & Atsumi, T. Na^+-Driven Bacterial Flagellar Motors. *Journal of Bioenergetics and Biomembranes* **21**, 705-716 (1989).

141. Hirota, N. & Imae, Y. Na^+-driven flagellar motors of an alkalophilic *Bacillus* strain YN-1. *J. Biol. Chem.* **258**, 10577-10581 (1983).

142. Liu, J. Z., Dapice, M. & Khan, S. Ion selectivity of the *Vibrio alginolyticus* flagellar motor. *J. Bacteriol.* **172**, 5236-5244 (1990).

143. Atsumi, T., McCarter, L. & Imae, Y. Polar and lateral flagellar motors of marine *Vibrio* are driven by different ion-motive forces. *Nature* **355**, 182-184 (1992).

144. Asai, Y., Kojima, S., Kato, H., Nishioka, N., Kawagishi, I. & Homma, M. Putative channel components for the fast-rotating sodium-driven flagellar motor of a marine bacterium. *J. Bacteriol.* **179**, 5104-5110 (1997).

145. Yorimitsu, T., Kojima, M., Yakushi, T. & Homma, M. Multimeric structure of the PomA/PomB channel complex in the Na^+-driven flagellar motor of *Vibrio alginolyticus*. *Journal of Biochemistry* **135**, 43-51 (2004).

146. Sugiyama, S., Cragoe, E. J. & Imae, Y. Amiloride, A specific inhibitor for the Na^+-driven flagellar motors of alkalophilic *Bacillus*. *J. Biol. Chem.* **263**, 8215-8219 (1988).

147. Atsumi, T., Sugiyama, S., Cragoe, E. J., Jr. & Imae, Y. Specific inhibition of the Na^+-driven flagellar motors of alkalophilic *Bacillus* strains by the amiloride analog phenamil. *J. Bacteriol.* **172**, 1634-1639 (1990).

148. Gosink, K. K. & Hase, C. C. Requirements for conversion of the Na^+-driven flagellar motor of *Vibrio cholerae* to the H^+-driven motor of *Escherichia coli*. *J. Bacteriol.* **182**, 4234-4240 (2000).

149. Okabe, M., Yakushi, T., Asai, Y. & Homma, M. Cloning and characterization of *motX,* a *Vibrio alginolyticus* sodium-driven flagellar motor gene. *Journal of Biochemistry* **130**, 879-884 (2001).

150. Asai, Y., Yakushi, T., Kawagishi, I. & Homma, M. Ion-coupling determinants of Na^+-driven and H^+-driven flagellar motors. *J. Mol. Biol.* **327**, 453-463 (2003).

151. Rizzotti, M. *Early evolution from the appearance of the first cell to the first modern organisms*. Birkhauser Verlag, Boston (2000).

152. Kojima, S. & Blair, D. F. Conformational change in the stator of the bacterial flagellar motor. *Biochemistry* **40**, 13041-13050 (2001).

153. Cascales, E., Lioubes, R. & Sturgis, J. N. The ToIQ-ToIR proteins energize ToIA and share homologies with the flagellar motor proteins MotA-MotB. *Mol. Microbiol.* **42**, 795-807 (2001).

154. Coulton, J. W. & Murray, R. G. E. Cell envelope associations of *Aquaspirillum serpens* flagella. *J. Bacteriol.* **136**, 1037-1049 (1978).

155. Khan, S., Ivey, D. M. & Krulwich, T. A. Membrane ultrastructure of alkaliphilic *Bacillus* species studied by rapid-freeze electron-microscopy. *J. Bacteriol.* **174**, 5123-5126 (1992).

156. Blair, D. F. & Berg, H. C. Restoration of torque in defective flagellar motors. *Science* **242**, 1678-1681 (1988).

157. Blair, D. F., Kim, D. Y. & Berg, H. C. Mutant MotB proteins in *Escherichia coli*. *J. Bacteriol.* **173**, 4049-4055 (1991).

158. Zhou, J. & Blair, D. F. Residues of the cytoplasmic domain of MotA essential for torque generation in the bacterial flagellar motor. *J. Mol. Biol.* **273**, 428-439 (1997).

159. Wilson, M. L. & Macnab, R. M. Overproduction of the MotA protein of *Escherichia coli* and estimation of its wild type level. *J. Bacteriol.* **170**, 588-597 (1988).

160. Wilson, M. L. & Macnab, R. M. Co-overproduction and localization of the *Escherichia coli* motility proteins MotA and MotB. *J. Bacteriol.* **172**, 3932-3939 (1990).

161. Van Way, S. M., Hosking, E. R., Braun, T. F. & Manson, M. D. Mot protein assembly into the bacterial flagellum: A model based on mutational analysis of the *motB* gene. *J. Mol. Biol.* **297**, 7-24 (2000).

162. Meister, M., Lowe, G. & Berg, H. C. The proton flux through the bacterial flagellar motor. *Cell* **49**, 643-650 (1987).

163. Berg, H. C., Manson, M. D. & Conley, M. P. *Prokaryotic and eukaryotic flagella*. Amos, W. B. & Duckett, J. G. (eds.), pp. 1-31 (Cambride University Press, Cambridge,1982).

164. Khan, S., Meister, M. & Berg, H. C. Constraints on flagellar rotation. *J. Mol. Biol.* **184**, 645-656 (1985).

165. Khan, S. & Macnab, R. M. Proton chemical potential, proton electrical potential and bacterial motility. *J. Mol. Biol.* **138**, 599-614 (1980).

166. Khan, S. & Berg, H. C. Isotope and thermal effects in chemiosmotic coupling to the flagellar motor of *Streptococcus*. *Cell* **32**, 913-919 (1983).

167. Fung, D. C. & Berg, H. C. Powering the flagellar motor of *Escherichia coli* with an external voltage source. *Nature* **375**, 809-812 (1995).

168. Braun, T. F., Poulson, S., Gully, J. B., Empey, J. C., Van, W. S., Putnam, A. & Blair, D. F. Function of proline residues of MotA in torque generation by the flagellar motor of *Escherichia coli*. *J. Bacteriol.* **181**, 3542-3551 (1999).

169. Zhou, J., Lloyd, S. A. & Blair, D. F. Electrostatic interactions between rotor and stator in the bacterial flagellar motor. *Proc. Natl. Acad. Sci. U. S. A.* **95**, 6436-6441 (1998).

170. Blair, D. F. Flagellar movement driven by proton translocation. *FEBS Letts.* **545**, 86-95 (2003).

171. Togashi, F., Yamaguchi, S., Kihara, M., Aizawa, S. I. & Macnab, R. M. An extreme clockwise switch bias mutation in *fliG* of *Salmonella typhimurium* and its suppression by slow-motile mutations in *motA* and *motB*. *J. Bacteriol.* **179**, 2994-3003 (1997).

172. Asai, Y., Kawagishi, I., Sockett, R. E. & Homma, M. Coupling ion specificity of chimeras between H^+ and Na^+ driven motor proteins, MotB and PomB, in *Vibrio* polar flagella. *EMBO J.* **19**, 3639-3648 (2000).

173. Okabe, M., Yakushi, T., Kojima, M. & Homma, M. MotX and MotY, specific components of the sodium-driven flagellar motor, colocalize to the outer membrane in *Vibrio alginolyticus*. *Mol. Microbiol.* **46**, 125-134 (2002).

174. McCarter, L. L. MotY, a component of the sodium-type flagellar motor. *J. Bacteriol.* **176**, 4219-4225 (1994).

175. McCarter, L. L. MotX, the channel component of the sodium-type flagellar motor. *J. Bacteriol.* **176**, 5988-5998 (1994).

176. McCarter, L. L. Genetic and molecular characterization of the polar flagellum of *Vibrio parahaemolyticus*. *J. Bacteriol.* **177**, 1595-1609 (1995).

177. Asai, Y., Kawagishi, I., Sockett, R. E. & Homma, M. Hybrid motor with H^+ and Na^+-driven components can rotate *Vibrio* polar flagella by using sodium ions. *J. Bacteriol.* **181**, 6332-6338 (1999).

178. Sato, K. & Homma, M. Multimeric structure of PomA, a component of the Na^+-driven polar flagellar motor of *Vibrio alginolyticus*. *J. Biol. Chem.* **275**, 20223-20228 (2000).

179. Silverman, M. & Simon, M. Operon controlled motility and chemotaxis in *Escherichia coli*. *Nature* **264**, 577-580 (1976).

180. Sato, K. & Homma, M. Functional reconstitution of the Na^+-driven polar flagellar motor component of *Vibrio alginolyticus*. *J. Biol. Chem.* **275**, 5718-5722 (2000).

181. Braun, T. F., Al-Mawsawi, L. Q., Kojima, S. & Blair, D. F. Arrangement of core membrane segments in the MotA/MotB proton-channel complex of *Escherichia coli*. *Biochemistry* **43**, 35-45 (2004).

182. Silverman, M., Matsumura, P. & Simon, M. Identification of Mot gene product with *Escherichia coli* lambda hybrids. *Proc. Natl. Acad. Sci. U. S. A.* **73**, 3126-3130 (1976).

183. Block, S. M. & Berg, H. C. Successive incorporation of force generating units in the bacterial rotary motor. *Nature* **309**, 470-472 (1984).

184. Muramoto, K., Sugiyama, S., Cragoe, E. J., Jr. & Imae, Y. Successive inactivation of the force-generating units of sodium-driven bacterial flagellar motors by a photoreactive amiloride analog. *J. Biol. Chem.* **269**, 3374-3380 (1994).

185. Silverman, M. & Simon, M. Flagellar rotation and the mechanism of bacterial motility. *Nature* **249**, 73-74 (1974).

186. Berg, H. C. & Turner, L. Torque generated by the flagellar motor of *Escherichia coli*. *Biophys. J.* **65**, 2201-2216 (1993).

187. Washizu, M., Kurahashi, Y., Iochi, H., Kurosawa, O., Aizawa, S.-I., Kudo, S., Magariyama, Y. & Hotani, H. Dielectrophoretic measurement of bacterial motor characteristics. *IEEE Trans. Ind. Applications* **29**, 286-294 (1993).

188. Ryu, W. S., Berry, R. M. & Berg, H. C. Torque-generating units of the flagellar motor of *Escherichia coli* have a high duty ratio. *Nature* **403**, 444-447 (2000).

189. Ashkin, A. Trapping of atoms by resonance radiation pressure. *Physical Review Letters* **40**, 729-732 (1978).

190. Berry, R. M., Turner, L. & Berg, H. C. Mechanical limits of bacterial flagellar motors probed by electrorotation. *Biophys. J.* **69**, 280-286 (1995).

191. Sowa, Y., Rowe, A. D., Leake, M. C., Yakushi, T., Homma, M., Ishijima, A. & Berry, R. M. Direct observation of steps in rotation of the bacterial flagellar motor. *Nature* **437**, 916-919 (2005).

192. Reid, S. W., Leake, M. C., Chandler, J. H., Lo, C. J., Armitage, J. P. & Berry, R. M. The maximum number of torque-generating units in the flagellar motor of *Escherichia coli* is at least 11. *Proc. Natl. Acad. Sci. U. S. A.* **103**, 8066-8071 (2006).

193. Ashkin, A., Dziedzic, J. M., Bjorkholm, J. E. & Chu, S. Observation of a single-beam gradient force optical trap for dielectric particles. *Optics Letters* **11**, 288-290 (1986).

194. Ashkin, A., Dziedzic, J. M. & Yamane, T. Optical trapping and manipulation of single cells using infrared laser beams. *Nature* **330**, 769-771 (1987).

195. Liu, Y., Sonek, G. J., Berns, M. W. & Tromberg, B. J. Physiological monitoring of optically trapped cells: Assessing the effects of confinement by 1064-nm laser tweezers using microfluorometry. *Biophys. J.* **71**, 2158-2167 (1996).

196. Chu, S. Laser manipulation of atoms and particles. *Science* **253**, 861-866 (1991).

197. Aufderheide, K. J., Du, Q. & Fry, E. S. Directed positioning of micronuclei in *Paramecium tetraurelia* with laser tweezers - absence of detectable damage after manipulation. *Journal of Eukaryotic Microbiology* **40**, 793-796 (1993).

198. Kuo, S. C. & Sheetz, M. P. Force of single kinesin molecules measured with optical tweezers. *Science* **260**, 232-234 (1993).

199. Meister, M., Caplan, S. R. & Berg, H. C. Dynamics of a tightly coupled mechanism for flagellar rotation. *Biophys. J.* **55**, 905-914 (1989).

200. Zhou, J., Lloyd, S. A. & Blair, D. F. Electrostatic interactions between rotor and stator in the bacterial flagellar motor. *Proc. Natl. Acad. Sci. U. S. A.* **95**, 6436-6441 (1998).

201. Chen, X. & Berg, H. C. Torque-speed relationship of the flagellar rotary motor of *Escherichia coli*. *Biophys. J.* **78**, 1036-1041 (2000).

202. Armstrong, J. B., Adler, J. & Dahl, M. M. Non-chemotactic mutants of *Escherichia coli*. *J. Bacteriol.* **93**, 390-398 (1967).

203. Berry, R. M. & Berg, H. C. Torque generated by the flagellar motor of *Escherichia coli* while driven backward. *Biophys. J.* **76**, 580-587 (1999).

204. Lowe, G., Meister, M. & Berg, H. C. Rapid rotation of flagellar bundles in swimming bacteria. *Nature* **325**, 637-640 (1987).

205. Berry, R. M. & Berg, H. C. Absence of a barrier to backwards rotation of the bacterial flagellar motor demonstrated with optical tweezers. *Proc. Natl. Acad. Sci. U. S. A.* **94**, 14433-14437 (1997).

206. Chen, X. & Berg, H. C. Solvent-isotope and pH effects on flagellar rotation in *Escherichia coli*. *Biophys. J.* **78**, 2280-2284 (2000).

207. Berg, H. C. & Khan, S. *Mobility and recognition in cell biology*., pp. 485-497 (Walter de Gruyter, Berlin,1983).

208. Iwazawa, J., Imae, Y. & Kobayasi, S. Study of the torque of the bacterial flagellar motor using a rotating electric field. *Biophys. J.* **64**, 925-933 (1993).

209. Khan, S., Dapice, M. & Humayun, I. Energy transduction in the bacterial flagellar motor. Effects of load and pH. *Biophys. J.* **57**, 779-796 (1990).

210. Shapiro, L. & Losick, R. Dynamic spatial regulation in the bacterial cell. *Cell* **100**, 89-98 (2000).

211. Fishov, I. & Woldringh, C. L. Visualization of membrane domains in *Escherichia coli*. *Mol. Microbiol.* **32**, 1166-1172 (1999).

212. Mileykovskaya, E. & Dowhan, W. Visualization of phospholipid domains in *Escherichia coli* by using the cardiolipin-specific fluorescent dye 10-N-nonyl acridine orange. *J. Bacteriol.* **182**, 1172-1175 (2000).

213. Yang, F., Moss, L. G. & Phillips, G. N. The molecular structure of green fluorescent protein. *Nature Biotechnology* **14**, 1246-1251 (1996).

214. Prasher, D. C., Eckenrode, V. K., Ward, W. W., Prendergast, F. G. & Cormier, M. J. Primary structure of the *Aequorea victoria* green-fluorescent protein. *Gene* **111**, 229-233 (1992).

215. Cody, C. W., Prasher, D. C., Westler, W. M., Prendergast, F. G. & Ward, W. W. Chemical-structure of the hexapeptide chromophore of the *Aequorea* green-fluorescent protein. *Biochemistry* **32**, 1212-1218 (1993).

216. Ray, N., Nenninger, A., Mullineaux, C. W. & Robinson, C. Location and mobility of twin arginine translocase subunits in the *Escherichia coli* plasma membrane. *J. Biol. Chem.* **280**, 17961-17968 (2005).

217. Sarcina, M., Tobin, M. J. & Mullineaux, C. W. Diffusion of phycobilisomes on the thylakoid membranes of the cyanobacterium *Synechococcus* 7942 - Effects of phycobilisome size, temperature, and membrane lipid composition. *J. Biol. Chem.* **276**, 46830-46834 (2001).

218. Sarcina, M., Murata, N., Tobin, M. J. & Mullineaux, C. W. Lipid diffusion in the thylakoid membranes of the cyanobacterium *Synechococcus* sp.: effect of fatty acid desaturation. *FEBS Letts.* **553**, 295-298 (2003).

219. Kruse, K. A dynamic model for determining the middle of *Escherichia coli*. *Biophys. J.* **82**, 618-627 (2002).

220. Meinhardt, H. & de Boer, P. A. J. Pattern formation in *Escherichia coli*: A model for the pole-to-pole oscillations of Min proteins and the localization of the division site. *Proc. Natl. Acad. Sci. U. S. A.* **98**, 14202-14207 (2001).

221. Deich, J., Judd, E. M., McAdams, H. H. & Moerner, W. E. Visualization of the movement of single histidine kinase molecules in live *Caulobacter* cells. *Proc. Natl. Acad. Sci. U. S. A.* **101**, 15921-15926 (2004).

222. Elowitz, M. B., Surette, M. G., Wolf, P. E., Stock, J. B. & Leibler, S. Protein mobility in the cytoplasm of *Escherichia coli*. *J. Bacteriol.* **181**, 197-203 (1999).

223. Kusumi, A., Sako, Y. & Yamamoto, M. Confined Lateral Diffusion of Membrane-Receptors As Studied by Single-Particle Tracking (Nanovid Microscopy) - Effects of Calcium-Induced Differentiation in Cultured Epithelial-Cells. *Biophys. J.* **65**, 2021-2040 (1993).

224. Simson, R., Sheets, E. D. & Jacobson, K. Detection of Temporary Lateral Confinement of Membrane-Proteins Using Single-Particle Tracking Analysis. *Biophys. J.* **69**, 989-993 (1995).

225. Harms, G. S., Cognet, L., Lommerse, P. H. M., Blab, G. A., Kahr, H., Gamsjager, R., Spaink, H. P., Soldatov, N. M., Romanin, C. & Schmidt, T. Single-molecule imaging of L-type Ca2+ channels in live cells. *Biophys. J.* **81**, 2639-2646 (2001).

226. Vrljic, M., Nishimura, S. Y., Brasselet, S., Moerner, W. E. & McConnell, H. M. Translational diffusion of individual class II MHC membrane proteins in cells. *Biophys. J.* **83**, 2681-2692 (2002).

227. Lo, C. J., Leake, M. C. & Berry, R. M. Fluorescence measurement of intracellular sodium concentration in single *Escherichia coli* cells. *Biophys. J.* **90**, 357-365 (2006).

228. Kuwajima, G. Construction of a minimum-size functional flagellin of *Escherichia coli*. *J. Bacteriol.* **170**, 3305-3309 (1988).

229. Link, A. J., Phillips, D. & Church, G. M. Methods for generating precise deletions and insertions in the genome of wild-type *Escherichia coli*: Application to open reading frame characterization. *J. Bacteriol.* **179**, 6228-6237 (1997).

230. Philippe, N., Alcaraz, J. P., Coursange, E., Geiselmann, J. & Schneider, D. Improvement of pCVD442, a suicide plasmid for gene allele exchange in bacteria. *Plasmid* **51**, 246-255 (2004).

231. Sambrook, J. & Russell, J. B. *Molecular Cloning: A laboratory manual*. Cold Spring Harbor Laboratory Press, New York (2001).

232. Giuliano, G., Pollock, D., Stapp, H. & Scholnick, P. A. A genetic-physical map of the *Rhodobacter capsulatus* carotenoid biosynthesis gene cluster. *Mol. Gen. Genet.* **213**, 78-83 (1988).

233. Sambrook, J., Fritsch, E. F. & Maniatis, T. *Molecular Cloning: a laboratory manual*. Cold Spring Harbour Laboratory Press, (1989).

234. Morrison, T. B. & Parkinson, J. S. Liberation of an interaction domain from the phosphotransfer region of CheA, a signaling kinase of *Escherichia coli*. *Proc. Natl. Acad. Sci. U. S. A.* **91**, 5485-5489 (1994).

235. Gittes, F. & Schmidt, C. F. Interference model for back-focal-plane displacement detection in optical tweezers. *Optics Letters* **23**, 7-9 (1998).

236. Rowe, A. D., Leake, M. C., Morgan, H. & Berry, R. M. Rapid rotation of micron and submicron dielectric particles measured using optical tweezers. *Journal of Modern Optics* **50**, 1539-1554 (2003).

237. Chalfie, M. Green Fluorescent Protein. *Photochem. Photobiol.* **62**, 651-656 (1995).

238. Cormack, B. P., Valdivia, R. H. & Falkow, S. FACS-optimized mutants of the green fluorescent protein (GFP). *Gene* **173**, 33-38 (1996).

239. Yang, T. T., Cheng, L. Z. & Kain, S. R. Optimized codon usage and chromophore mutations provide enhanced sensitivity with the green fluorescent protein. *Nucleic Acids Research* **24**, 4592-4593 (1996).

10 Appendices

Appendix A

Blocking buffer (2.2.16 SDS-PAGE / western blotting)

milk powder in PBS	5 % (w/v)

Blotting buffer (10 X) (2.2.16 SDS-PAGE / western blotting)

glycine	144.1 g
tris	30.3 g
made up to 1 l with dH_20	

Coomassie Brilliant Blue solution (2.2.16 SDS-PAGE / western blotting)

Coomassie Brilliant Blue	2.5 g
methanol	400 ml
acetic acid	100 ml
dH_2O	500 ml

De-staining solution (2.2.16 SDS-PAGE / western blotting)

methanol	400 ml
acetic acid	100 ml
dH_2O	500 ml

DISH 1 (2.2.1 Preparing plasmid DNA)

glucose	50 mM
tris (pH 8.0)	25 mM
EDTA	10 mM

DISH II (2.2.1 Preparing plasmid DNA)

SDS	10 %
NaOH	200 mM

DISH III (2.2.1 Preparing plasmid DNA)

potassium acetate (pH 5.0)	3 M

5 X DNA loading dye (2.2.5 DNA electrophoresis)

glycerol	70 % (w/v)
TE	30 % (w/v)
bromophenol blue	0.25 % (w/v)
xylene cyanol	0.25 % (w/v)

Elution buffer (2.2.15 Over-expressing and purifying EGFP)

NaCl	150 mM
glycerol	10 %
tris HCl (pH 8.0)	50 mM
DTT	1 mM
imidazole	500 mM

Hybridisation buffer (2.2.12 Southern blotting)

SSC	5 X
blocking reagent (Roche)	2 %
sarkosyl	0.1 %
SDS	0.02 %

LB Agar (LBA)

Bacto-tryptone	10 g/l
yeast extract	5 g/l
NaCl	5 g/l
agar	20 g/l
pH 7.0	

LB-broth

Bacto-tryptone	10 g/l
yeast extract	5 g/l
NaCl	5 g/l
pH 7.0	

Lysis buffer (2.2.2 Preparing chromosomal DNA)

tris (pH 8.0)	10 mM
EDTA	1 mM
SDS	1%
preheated to 65 ºC prior to use	

Lysis buffer (2.2.15 Over-expressing and purifying EGFP)

NaCl	150 mM

glycerol	10 %
tris-HCl (pH 8.0)	50 mM
DTT	1 mM
imidazole	10 mM

Motility buffer

potassium phosphate	10 mM
EDTA	0.1 mM
pH 7.0	

Resolving gel (SDS-PAGE / western blotting)

polyacrylamide 30 %	4 ml
1.5 M tris-HCl (pH 8.0)	2.6 ml
10 % SDS	0.1 ml
APS	0.1 ml
TEMED	4 µl
dH_2O	3.2 ml

SDS-PAGE loading dye

tris-HCl (pH 6.8)	0.09 M
glycerol	20 %
SDS	2 %
bromophenol blue	0.02 %
DTT	0.1 M

SDS-PAGE running buffer (1X)

glycine	188 g
tris	30.2 g
SDS	10 g
made up to 10 l with dH_2O	

SOB media

NaCl	0.5 g/L
tryptone	20 g/L
yeast extract	5 g/L
pH 7.0	

SOC media

glucose	20 mM
MgCl	10 mM

MgSO4	10 mM
NaCl	10 mM
tryptone	20 g/l
yeast extract	5 g/l
pH 7.0	

Stacking gel (2.2.16 SDS-PAGE / western blotting)

polyacrylamide 30 %	2.5 ml
tris-HCl 0.5 M (pH 6.8)	5 ml
10 % SDS	0.2 ml
dH_2O	10 ml

add 25 µl 10 % APS and 2 µl TEMED per 1 ml of the above solution.

10 X TBE (2.2.5 DNA electrophoresis)

tris base	108 g
boric acid	55 g
EDTA, pH 8.0	7.4 g
made up to 1 l, pH 8.3	

T-broth

tryptone	10 g/l
NaCl	5 g/l
pH 7.0	

2YT

trytone	16 g/l
yeast extract	10 g/l
NaCl	5 g/l
glycerol	50 %

Appendix B

Primers used in Chapter 3; restriction sites are underlined.
PS *Sac*I and PS *Sbf*I were used to make pKO3-PS-*fliC*st.
fliC 1 RP and *fliC* 2 RP were used to sequence the *fliC* region of the chromosome (± 500 bp) of strain RP5232 and the *fliC* region of strains JHC36 and JHCE3.
SEQ1-8 were used to sequence pDS-*fliC*st and *fliC* of RP5232.
SEQ1-8 and Tn10 *Sal*I were used for sequencing *fliC* of YS34 to determine where the transposon (Tn10) had integrated.
PS2589F and PS2589R were used to make pDS-*fliC*st.

Primer name	Target sequence	Primer sequence	Restriction site
PS *Sac*I	*fliC*	AGTAGAGCTCGACGGCGATTGAGCCGACGGGTGG	*Sac*I
PS *Sbf*I		GATCCCTGCAGGTTGCAATTCAACTTGTAGGCCTG	*Sal*I
fliC 1 RP		GATCAAGCTTGGTGCTGCTGGTGGTGCTGGTG	*Hind*III
fliC 2 RP		ATCGGCATGCAATGCCGTTCCTTGTAGGGCGTG	*Sph*I
SEQ1		GCACAAGTCATTAATACC	-
SEQ2		AGTTGTTGTTGATTTCGG	-
SEQ3		ACGGCGTGAACGTGCTGG	-
SEQ4		ACCCTCAATTGAAGCTGG	-
SEQ5		GGTGGTGATAACGATGGG	-
SEQ6		AGTTTCATTCACATCCGC	-
SEQ7		CCGTTCTTCCCTCGGTGC	-
SEQ8		GCCAACACGGAGTTACCG	-
Tn10 *Sal*I		GATCGTCGACCAAGTTCGGTAAGAGTGAGAG	*Sal*I
PS2589F		CTAGGCATGCAGTTGTAAATGCCGTTCCTTG	*Sph*I
PS2589R		GACTGAGCTCGCAGTGGTGGCACTGAACGC	*Sac*I

Appendix C

Primers used to sequence constructs pDS132: pDS-*fliC*st in Chapter 3, and p*gfp-motA*, p*motA-yfp*, p*fliG-yfp* and p*fliM-yfp* in Chapter 6.

Primer name	Primer sequence
DS132F	CAGGTCGACGGATCTG
DS132R	CACATGTGGAATTGTG

Appendix D

PCR primers used to construct strain JHC1 (*gfp-motB*) in Chapter 4. Plasmid midi-preparations of pJZ18 D32wt and pEGFP-N1 (Clontech) were used as templates for PCR. Restriction sites are underlined.

Primer name	Target sequence	Primer sequence	Restriction site
motB A	*motB*	CCGGAATTCTACCCACGCATCCTCGC	*Eco*RI
motB B		CTTGCTCACCATAATCTTCCACGATC	-
motB C		GATCGTGGAAGATTATGGTGAGCAAG	-
motB D		CTAGTCTAGACTTGTACAGCTCGTCC	*Xba*I
motB E		CTAGTCTAGAAAGAATCAAGCGCATCCG	*Xba*I
motB F		CCCAAGCTTGCATTGGCCCGATCGGC	*Hind*III

Appendix E

Primers used to sequence p*gfp-motB* in Chapter 3. PCR primers *gfp*F and *gfp*R were used to amplify *egfp* from pEGFP-N1 to make pQE-80-*gfp* for expression of EGFP protein in Chapter 6.

Primer name	Target sequence	Primer sequence	Restriction site
KO3-L	-	AGGGCAGGGTCGTTAAATAGC	-
KO3-R	-	TTAATGCGCCGCTACAGGGCG	-
*gfp*F	*egfp*	CGCGGATCCGTGAGCAAGGGCGAGGAGC	*Bam*HI
*gfp*R		CCCAAGCTTTTACTTGTACAGCTCGTC	*Hind*III

Appendix F

Primers used to sequence the *motB* region of the chromosome of strain JHC1 to confirm *gfp-motB* integration onto the chromosome, outside of the regions cloned into suicide vector pKO3 (Chapter 3).

Primer name	Target sequence	Primer sequence
*motA*1	*motA*	CCGGAATTCCTGCGCCTGATTATCAGCGG
seqB1	*motB*	CGGGATCCCCTCGGTTCGGCTGATGG

Appendix G

Primers used to sequence constructs p*gfp-motB* (Chapter 4), p*yfp-motA*, p*motA-yfp*, p*fliG-yfp* and p*fliM-yfp* (Chapter 6).

Primer name	Target sequence	Primer sequence
yfp 1	*ecfp / egfp / eyfp*	TCCAGCTCGACCAGGATG
yfp 2		CACATGGTCCTGCTGGAG
yfp 3		GTCGTGCTGCTTCATGTG
yfp 4		GGTGTTCTGCTGGTAGTG
yfp 5		GTAAACGGCCACAAGTTC
yfp 6		CAGAAGAACGGCATCAAG

Appendix H

PCR primers used to make p*gfp-motA* in Chapter 6.

Primer name	Target sequence	Primer sequence	Restriction site
motA A1	*motA*	CCGGAATTCCGTTCATGCTTCGATGTTCTG	*Eco*RI
motA A2		TGGAAGGATGATGTCATGGTGAGCAAGGGC	-
motA A3		GCCCTTGCTCACCATGACATCATCCTTCCAC	-
motA A4			*Xba*I
motA A5		CTAGTCTAGACTTATCTTATTAGGTTACCTGG	*Xba*I
motA A6		ATATAAGCTTAGCGCCAGACTGTTCGC	*Hin*dIII

Appendix I

PCR primers used to make p*motA-yfp* in Chapter 6.

Primer name	Target sequence	Primer sequence	Restriction site
*motA*1	*motA*	CCGGAATTCCTGCGCCTGATTATCAGCGG	*Eco*RI
*motA*2		CGGGGTACCGTTCGTTCCTCGGTTGTCG	*Kpn*I
*motA*3		CTAGTCTAGAGACAACCGCGGAAGCATGAAG	*Xba*I
*motA*4		ATATAAGCTTACTGCCGGTTCTAAACATCGGG	*Hin*dIII

Appendix J

Primers used to sequence the *motA* region of the chromosome of isolates transformed with p*gfp-motA* (1975855 and 1974478) and p*motA-yfp* (1973579 and 1974878).

Primer name	Target sequence	Primer sequence

1975855	*motA*	GCATTGTTCAGGAAGCGCGGGATATTC
1974478		TGACGTAAAACAGTCGCTAATGGGGAAA
1973579		GCCGCTATCCAACCCTCCGACCATCAGTTC
1974878		TCGCTGGAACGTGATATTGAA

Appendix K

PCR primers used to construct p*fliM-cfp* in Chapter 6.

Primer name	Target sequence	Primer sequence	Restriction site
fliM 1	*fliM*	TCGTGAGCTCTGGAAGGCGATTAATCCGCTGG	*Sac*I
fliM 2		ACTGCCCGGGGTTTGGGCTGTTCCTCGTTC	*Xma*I
fliM 3		CTAGTCTAGACGAGGAACAGCCCAAATGAGTAC	*Xba*I
fliM 4		ACGTGCATGCTAATGGCGATGAGTGCGCCGC	*Sph*I

Appendix L

PCR primers used to construct p*fliG-yfp* in Chapter 6.

Primer name	Target sequence	Primer sequence	Restriction site
fliG 1	*fliG*	TCGAGAGCTCCGACGTGATGTTGCGTATCG	*Sac*I
fliG 2		ACTGCCCGGGGGACATAGGTATCCTCGCCG	*Xma*I
fliG 3		CTAGTCTAGAGGCGAGATGGTAATTGGCAG	*Xba*I
fliG 4		ACGTGCATGCGTTTACCGCTGAATAACGGT	*Sph*I

Appendix M

Primers used to sequence the *fliM* region of the chromosome of isolates transformed with p*fliM-yfp* in Chapter 6.

Primer name	Target sequence	Primer sequence
2018316	*fliM*	CTGTTCAACCTGCTGCGTCGTAGCC
2019784		TGACCTGCGGTAACGCCGAGCACCAG

Appendix N

Primers used to sequence the *fliG* region of the chromosome of isolates transformed with p*fliG*-*yfp* in Chapter 6.

Primer name	Target sequence	Primer sequence
2013146	*fliG*	GGTCAAAGCTCTGGGTGAAGAACGTG
2014624		TCAAAGTTATCCAGCGTGGTTGGC